Self-assembly of diketopyrrolopyrrole semiconductors : impact of H-bonds on electronic properties

Swann Militzer

▶ **To cite this version:**

Swann Militzer. Self-assembly of diketopyrrolopyrrole semiconductors : impact of H-bonds on electronic properties. Other. Université de Strasbourg, 2019. English. NNT : 2019STRAE048 . tel-02503132

HAL Id: tel-02503132
https://theses.hal.science/tel-02503132v1

Submitted on 9 Mar 2020

HAL is a multi-disciplinary open access archive for the deposit and dissemination of scientific research documents, whether they are published or not. The documents may come from teaching and research institutions in France or abroad, or from public or private research centers.

L'archive ouverte pluridisciplinaire **HAL**, est destinée au dépôt et à la diffusion de documents scientifiques de niveau recherche, publiés ou non, émanant des établissements d'enseignement et de recherche français ou étrangers, des laboratoires publics ou privés.

UNIVERSITÉ DE STRASBOURG

ÉCOLE DOCTORALE de Physique et Chimie-Physique

Institut Charles Sadron – UPR 22

THÈSE présentée par :

Swann MILITZER

soutenue le : **4 Décembre 2019**

pour obtenir le grade de : **Docteur de l'université de Strasbourg**

Discipline/ Spécialité : Chimie Physique

Auto-assemblages de dicétopyrrolopyrrole semiconducteurs : impact des liaisons H sur les propriétés électroniques

THÈSE dirigée par :

Mr. MESINI Philippe — Directeur de recherche, ICS, Université de Strasbourg

RAPPORTEURS :

Mr. ACHELLE Sylvain — Maître de conférence, Université de Rennes 1

Mr. SALLÉ Marc — Professeur, Université d'Angers

AUTRES MEMBRES DU JURY :

Mme HEITZ Valérie — Professeur, Université de Strasbourg

Remerciements

Cette thèse a été effectuée à l'Institut Charles Sadron (ICS) au sein de l'équipe Systèmes Complexes Moléculaires et Macromoléculaires Organisés (SYCOMMOR) sous la direction de Philippe Mésini et d'Amparo Ruiz-Caretero.

Tout d'abord je tiens à remercier le Pr. Valérie Heitz, le Dr. Sylvain Achelle et le Pr. Marc Sallé pour avoir accepté d'examiner ce travail de thèse.

Je souhaite remercier Philippe Mésini pour m'avoir donné l'opportunité d'effectuer mon doctorat au sein de l'équipe SYCOMMOR. Je le remercie surtout pour ses conseils et sa disponibilité qu'il a pu m'accorder au cours de cette période.

Je voudrais remercier Amparo Ruiz-Careterro qui m'a pris sous son aile et qui s'est beaucoup investie pour moi en me faisant découvrir un usage des pigments organiques, qui m'était inconnu avant mon arrivée à l'ICS. Merci pour m'avoir encadré, pris le temps de m'expliquer et me conseiller sur tout ce qu'il me fallait pour mener à bien ce travail.

Je remercie également les différentes personnes ayant collaborés sur la réalisation de ce projet : Dominique Collin pour les analyses en Rhéologie, Turbidimétrie et en microscopie optique. Marc Schmutz et Alain Carvahlo pour les analyses en CRYO-TEM et CRYO-MEB. Jérôme Combet et Guillaume Fleith pour les analyses en SAXS.

Je tiens à dire un grand merci à Jean Philippe Lamps pour tous ses conseils pratiques pour les manipes de chimie organique et son aide concernant la synthèse de certains produits.

Merci à tous les membres de l'équipe SYMMOR pour leur accueil chaleureux au sein de l'équipe SYCOMMOR et leurs conseils qu'ils ont pu me donner.

Je dis aussi merci cordialement à tous mes dorénavant anciens collègues de bureaux ainsi que tous les doctorants et post-doctorants que j'ai pu rencontrer au cours de cette période. Nos conversations au cours de nos pauses cafés vont me manquer, je vous souhaite à tous une bonne continuation dans vos projets.

Je souhaite remercier sincèrement les organismes Région alsace Champagne Ardenne Lorraine et L'IRTG pour le financement de cette thèse.

Table of Contents

Abbreviation list

AFM: Atomic Force Microscopy

BHJSC: bulk heterojunction solar cells

CD: Circular dichroism

DFT: density functional theoretical

DSC: differential scanning calorimetry

DMF: Dimethylformamide

DNA: Deoxyribonucleic acid

DMSO: Dimethyl sulfoxide

DPP: Diketopyrrolopyrrole

FET: Field Effect Transistor

GIWAXS: grazing incidence wide-angle X-ray scattering

GIXD: grazing incidence X-ray diffraction

GIXS: grazing incidence X-ray scattering

HOMO: highest occupied molecular orbital

LDA: Lithium diisopropylamide

LET: light-emitting transistor

LMWG: low molecular weigh

LUMO: lowest unoccupied molecular orbital

MEB: microscopie électronique à balayage

MET: microscopie électronique à transmission

NDI: naphthalene diimides

NIR: near-infrared

NMR: Nuclear Magnetic Resonance spectroscopy

OFETs: organic field effect transistors

OLEDs: organic light emitting diodes

OPV: organic photovoltaic

OM: optical microscopy

OSCs: organic solar cells

$PC_{61}BM$: Phenyl-C61-butyric acid methyl ester

PCE: power conversion efficiency

PDMS: polydimtehylsiloxane

PDI: perylene diimide

Rf: retardation factor

SAXS: Small angle X-ray scattering

SLD: scattering length density

TEM: Transmission electron microscopy

TFA: trifluroacetic acid

TGA: thermal gravimetric analysis

THF: Tetrahydrofuran

TLC: thin layer chromatography

TOE: ton of oil equivalent

UV-Vis: Ultraviolet–visible

XRD: X-ray diffraction

Résumé du manuscrit

I. Introduction générale

Les pigments organiques, utilisés de tous temps par l'homme comme colorants peuvent être employés aujourd'hui comme semi-conducteurs. Ces produits possèdent des mobilités de charge pouvant atteindre les 10 $cm^2V^{-1}s^{-1}$. Ils sont donc une alternative possible aux semi-conducteurs inorganiques actuellement utilisés dans les cellules photovoltaïques, tels le silicium ou bien le germanium. Car ils sont moins couteux et plus faciles à produire.

Les molécules de type dicétopyrrolopyrrole (**DPP**) déjà très utilisés en tant que biomarqueurs pour leur fluorescence, peuvent être utilisés comme semi-conducteurs : ils sont très recherchés pour leur propriétés optoélectroniques pour la conception de diodes électroluminescentes (OLED), de transistors à effet de champs (OFET), et les cellules solaires.

La plupart des semi-conducteurs organique sont des polymères. Néanmoins, l'intérêt envers les petites molécules ne cessent de croître, car elles s'auto-assemblent par interactions non covalentes, généralement les interactions π-π ou liaisons hydrogène (H). Les liaisons H modulent les propriétés optoélectroniques, mais elles ne les améliorent pas toujours. C'est pourquoi notre équipe à entreprit une étude systématique sur l'influence des liaisons H sur les propriétés d'auto-assemblage et optoélectroniques. Des petites molécules à base de **DPP** servent de modèles pour cette enquête.

Nous avons développé une librairie de molécules de **DPP** qui se distinguent par plusieurs paramètres tels le nombre de liaisons hydrogène généré, leurs positions, et la nature des fonctions chimiques utilisées. Des chaines allyliques de différentes tailles sont également introduites ainsi que des centres chiraux. Ces travaux de doctorat sont le commencement de cette étude systématique et seront focalisés sur la synthèse et l'étude de l'influence des liaisons H sur l'auto-assemblage et les propriétés optoélectroniques. Des études de transfert de charges ont également été entreprise.

Ce manuscrit est composé en quatre chapitres :

Le premier chapitre est une introduction générale sur les propriétés des semi-conducteurs organiques. Il se focalise ensuite sur les études trouvées dans la littérature concernant les **DPP** avec des liaisons H pour l'organique électronique.

Le deuxième chapitre expose nos résultats obtenus des **DPP** possédant des fonctions semicarbazones. Leur propriété optoélectronique et leur morphologie ont été étudié.

Le troisième chapitre concerne l'étude de **DPP** bisamides. L'influence de la chiralité a aussi été étudié.

Le quatrième chapitre est consacré au développement de nouveaux organogels à base de **DPP** monoamide ayant des chaines alkyles de différentes tailles. La structure et les propriétés thermodynamique sont décrites et un diagramme de phase a été établi.

II. Chapitre 1: Introduction

L'étude de semi-conducteurs est vitale pour développer des outils capables d'absorber et de convertir la lumière en électricité.

Il existe plusieurs paramètres auxquels les semi-conducteurs doivent répondre à différents critères. Ils doivent avoir une bonne conductivité (entre 10^{-5} et 10^{-2} $S.cm^{-1}$; Figure 1a) et une différence d'énergie LUMO-HOMO appropriée (1,5 eV). Cette différence d'énergie peut également être modulé en ajoutant des impuretés qui introduisent des niveaux d'énergies proche de la bande valence ou de la bande de conduction (Figure 1b). Les matériaux doivent également adopter une structure supramoléculaire bien organisée et orientée en fonction de la nature du dispositif que l'on souhaite développer. Concernant les cellules photovoltaïques, on cherche idéalement à obtenir une couche active où les semi-conducteurs donneur/accepteur adoptent une configuration d'échiquier (Figure 1c). Cette configuration facilite le transfert de charge.

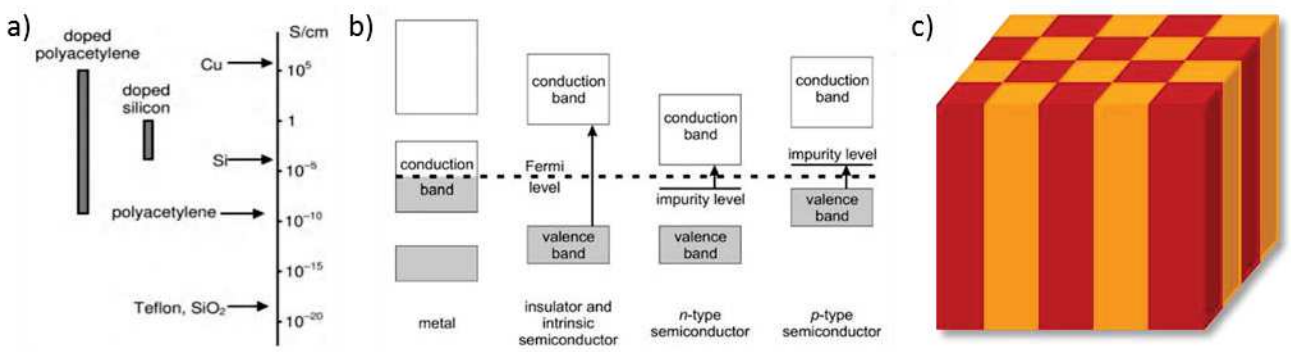

***Figure 1**: a) Conductivité des matériaux semiconducteurs ; b) Comparaison des bandes d'énergie des métaux, isolants et semi-conducteurs de type p et n ; c) structure idéale pour la conception de cellule solaire.*

Notre étude s'est portée sur les **DPP** qui sont des pigments très utilisés pour diverses applications dans différents domaines. Ils sont aussi très étudiés en tant que semi-conducteurs pour développer des cellules solaires. La voie de synthèse la plus répandue est la condensation entre le succinate de diethyle et une molécule aromatique ayant une fonction nitrile (Schéma 1a). Dans notre cas il s'agit du 2-thiopheneacetonitrile. Une fois la structure obtenue, elle peut être modifiée par halogénation. Des lithiations peuvent être également réalisées pour ajouter des groupements électrophiles et former des aldéhydes ou des ester boronique (Schéma 1b). Ces fonctions sont ensuite utilisées pour ajouter des chaines alkyles ou des groupements aromatiques.

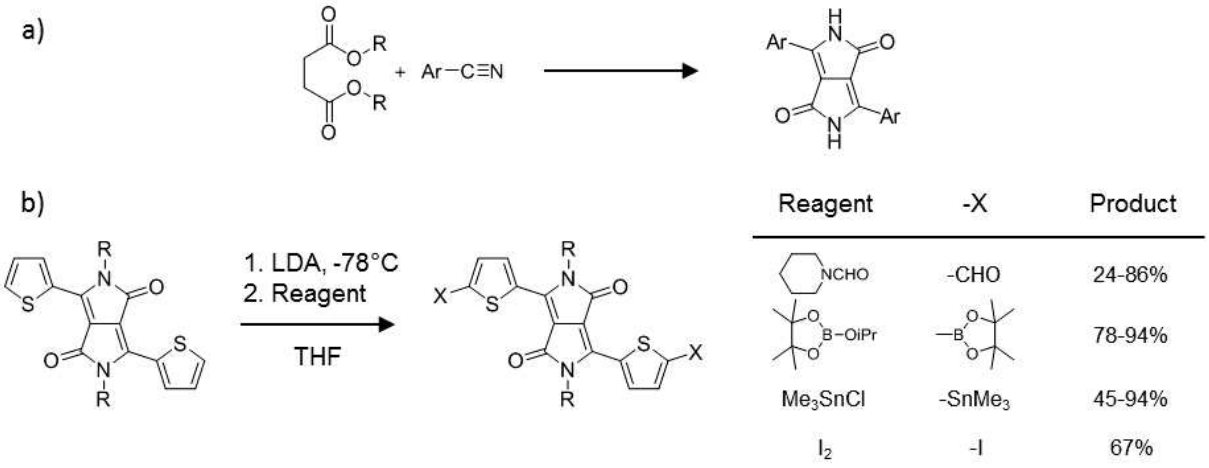

Schéma 1: *a) Synthèse d'une structure de DPP par condensation entre le* succinate de diéthyle *et un dérivé aromatique ayant une fonction nitrile ; b) Différentes fonctionnalisations possible suite à une lithiation de* ***DPP***

Notre objectif est de développer une librairie de petites molécules à base de **DPP** et d'étudier les structures supramoléculaires qu'ils forment par liaisons H. Les auto-assemblages résultant peuvent être utilisées dans des cellules solaires. Cependant il n'y a jusqu'à présent aucun accord quant au rôle des liaisons H en raison de travaux contradictoires trouvés dans la littérature : pour des dérivés dithienosiloles et dithienothiophenes (Figure 2a) les interactions H diminuent les performances des cellules solaires et des transistors fabriqués ; pour des quaterthiophenes (Figure 2b) l'efficacité augmente.

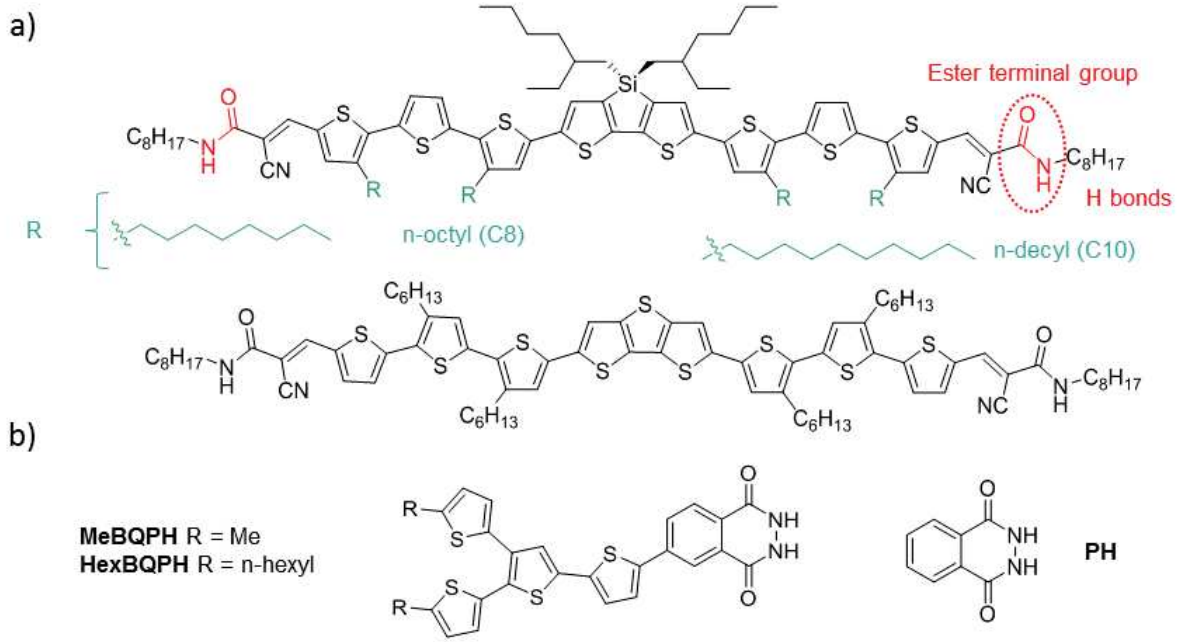

Figure 2: *exemples de molécules semi-conductrices générant des liaisons de H à effet a) néfaste et b) bénéfique pour le développement de cellules solaire.*

Concernant les **DPPs**, plusieurs études structurales ont été effectuées sur des molécules avec des interactions H formés sur différentes positions. Quand les liaisons

H se forment entre les lactames, les monomères s'arrangent dans une configuration ''head to tail'' provoquant un déplacement bathochromique et améliorant la mobilité de charge. La nature des groupements aromatiques ou la présence de groupement halogènes (Figure 3a) modifient la structure cristalline des **DPPs** (Figure 3b et c) et donc leurs propriétés optoélectroniques.

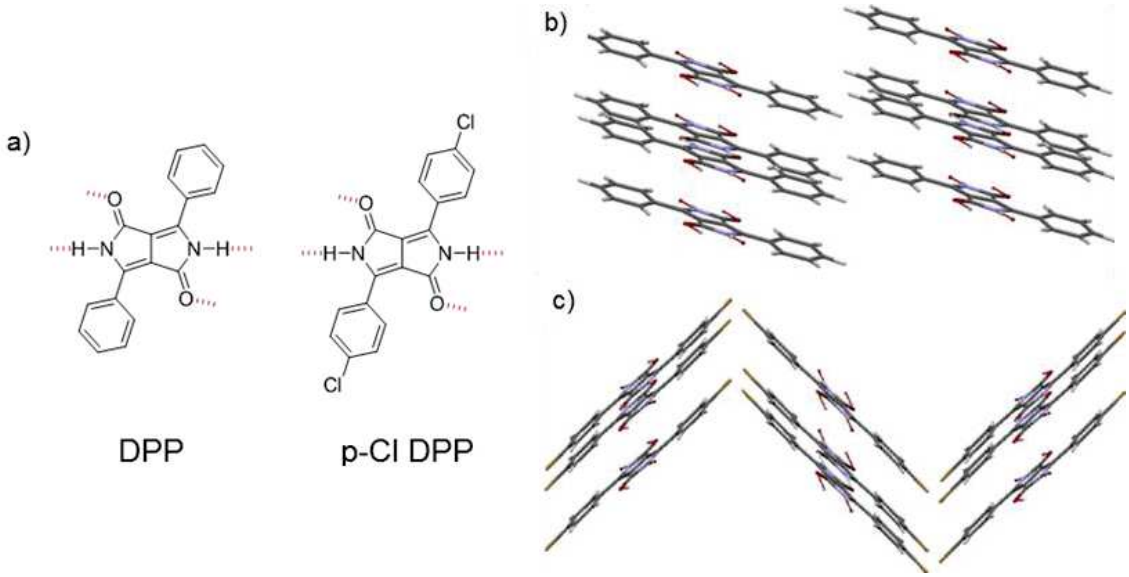

Figure 3: *Structure moléculaire de (a)* ***DPP****,* ***p-Cl DPP*** *and* ***p-Br DPP****, (b) Structures cristallines de* ***PhDPP*** *et (c)* ***p-Cl DPP****.*

L'inconvénient majeur de ces molécules formant les liaisons H est leur solubilité. On peut y remédier avec des groupes protecteurs t-Boc. Le produit protégé est soluble et est déposé sur un support solide. Puis le groupement protecteur est éliminé par traitement thermique provoquant l'auto-assemblage des **DPPs** (Figure 4).

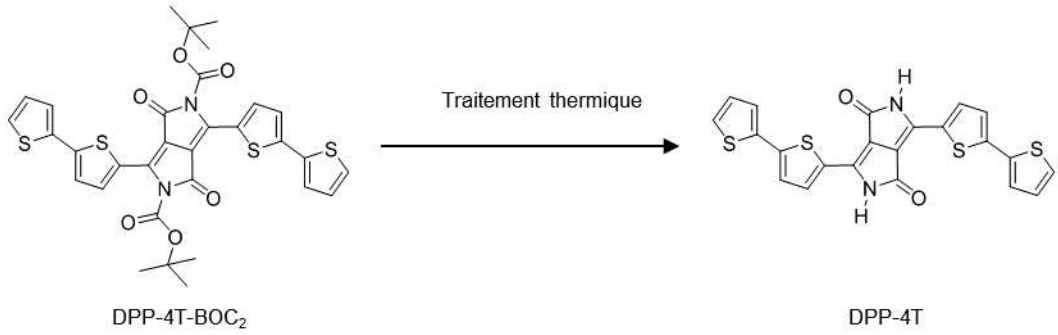

Figure 4: *a) Principe de l'auto-assemblage par élimination du groupement protecteur t-boc ;*

Une autre solution pour améliorer la solubilité est d'ajouter une chaine alkyl sur l'un des azotes des cycles lactames. Beaucoup d'exemples de molécules ont été développés avec des fonctions amides sur la périphérie de la structure principale (Figure 5).

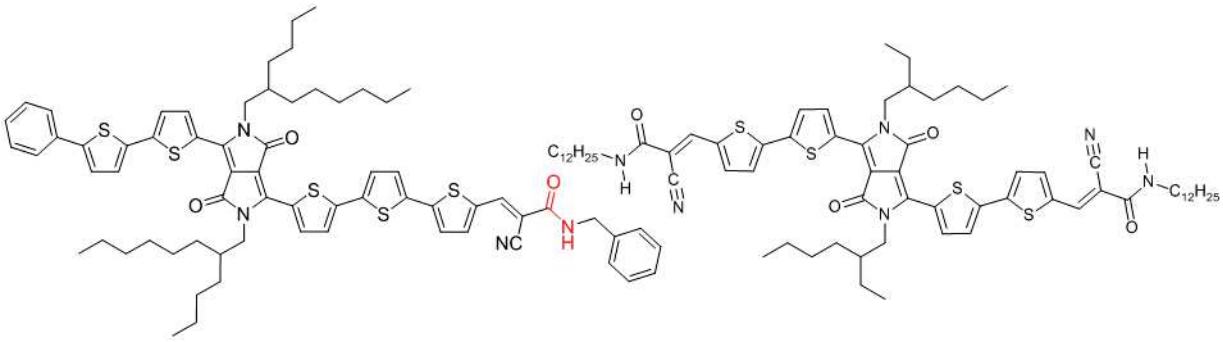

Figure 5: *Exemples de molécules de* ***DPP*** *avec des fonctions amides en périphérie.*

III. Chapitre 2: Dicétopyrrolopyrrole Semicarbazone

Dans ce chapitre, l'incorporation de liaison H sur la périphérie des cycles thiophènes a été exploré. Les molécules développées présentent une fonction semicarbazone générant 2 liaisons H. Afin d'améliorer la solubilité de ces composants, deux chaines ethylhexyl ou butyloctyl sont attachées sur les azotes des cycles lactames (Figure 6).

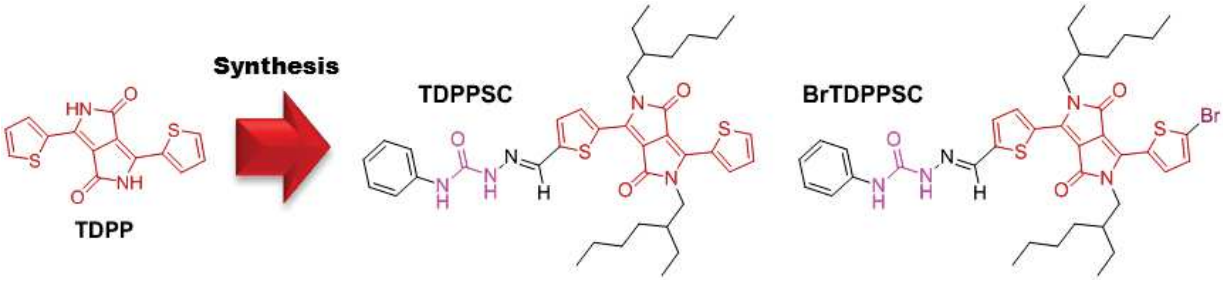

Figure 6: *Structure chimique des molécules de* ***DPP*** *semicarbazone développées*

Les semicarbazones ont jusqu'à présent des applications biologiques et catalytiques. Récemment, un exemple d'une molécule **DPP** ayant deux semicarbazones a été utilisée en tant que senseur pour des composés ioniques (Figure 7).

Figure 7: *Structure de la molécule* ***DPP*** *détectrice d'ions fluorés.*

La famille des **DPPs** semicarbazones a été synthétisée selon le schéma 2.

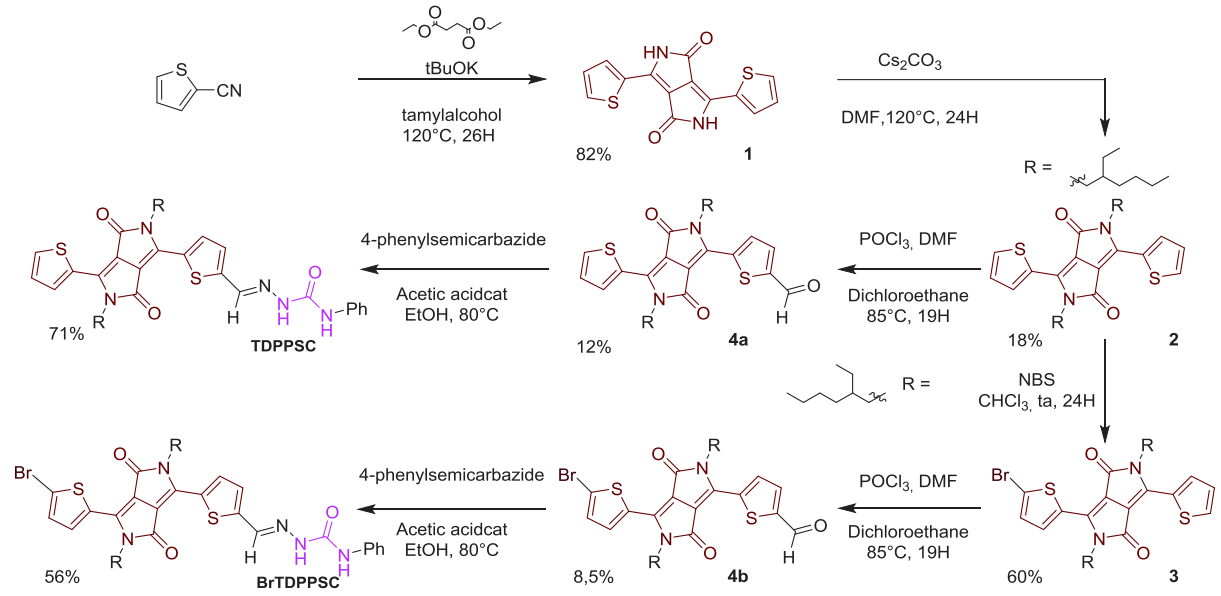

***Schéma 2** : Synthèse multi-étape des **DPP** semicarbazones*

Au cours de ces synthèses, certaines réactions ont été optimisées afin d'améliorer les rendements de réaction faibles. Pour la N-alkylation (1 à 2, schéma 2), le rendement initial de 18% a été porté à 28% après avoir optimisé les proportions des réactifs, la température et le temps de réaction. La réaction de formylation (2 à 4a et 3 à 4b, schéma 2) a également été modifiée cette fois-ci en changeant le solvant, les réactifs, la température et le temps de réaction. Le rendement initial de 12% a augmenté à 27%. Des sous-produits de ces synthèses ont aussi été isolés et identifiés pour être utilisé ultérieurement dans la formation de nouveaux produits (Figure 8).

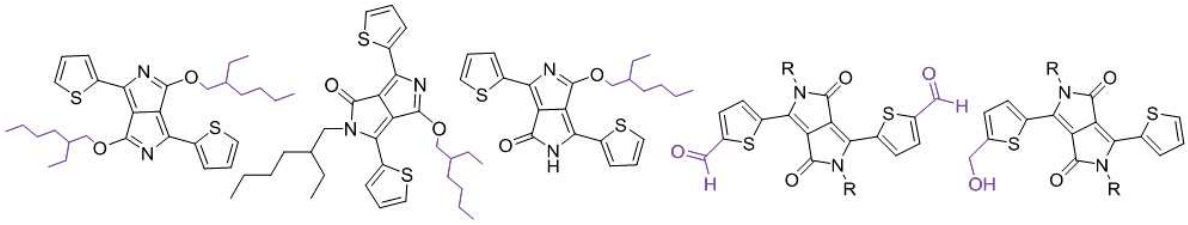

***Figure 8**: Sous-produits de **DPPs** obtenus au cours des synthèses*

L'auto assemblage de **TDPPSC** et **BrTDPPSC** a été étudié par spectroscopie UV-visible, en solution (Figure 9a et b) et sur films solides préparés par spin-coating (Figure 9c) à partir de solution dans différents solvants. Tous les échantillons présentent, une zone d'absorption large de 450 à 650 nm caractéristique du cœur **DPP**. Dans le chloroforme, bon solvant, l'absorption s'arrête à 650 nm (Figure 9a et b, courbes verte). Dans les autres solvants, notamment l'acétate d'éthyle, d'autres bandes sont détectées au-delà de 650 nm (Figure 9a et b courbes noire rouge et bleue). Elles peuvent atteindre la région du proche infrarouge et caractérisent la formation d'agrégats de type J. Ces bandes sont plus intenses à l'état solide (Figure 9c).

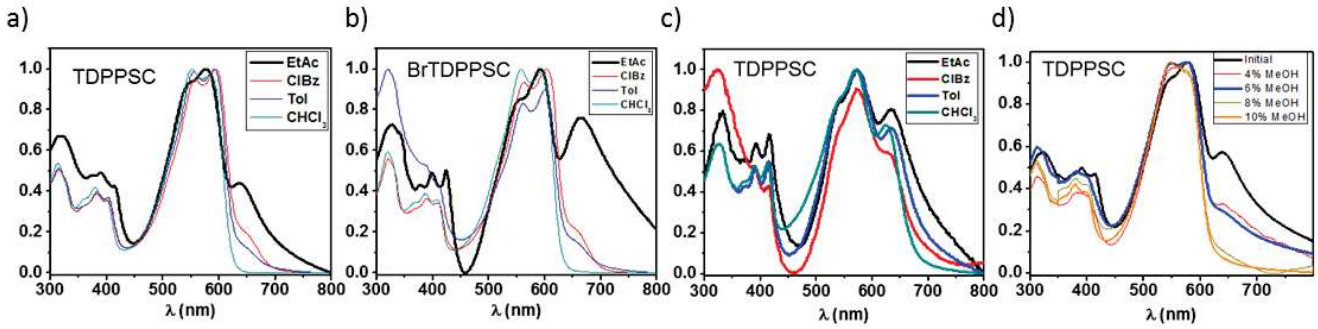

Figure 9: *a) et b) Spectres d'absorption UV en solution le chloroforme, le chlorobenzène, le toluène et l'acétate d'éthyle de TDPPSC et BrTDPPSC; c) Spectres d'absorption UV d'échantillons spin-coatés de TDPPSC; d) Spectre d'absorption UV de TDPPSC en solution d'acétate d'éthyle avec des additions progressives de méthanol*

Pour montrer la présence de liaisons H, on a mesuré les spectres IR des composés à l'état solide, en solution dans des solvants générant des agrégats ou pas (Figure 10). A l'état solide et dans les solutions générant des agrégats, les spectres possèdent deux pics caractérisant les fonctions semicarbazones liées. Pour les échantillons ne générant pas d'agrégats, ces signaux laissent place à un signal indiquant que les fonctions semicarbazones sont libres. Nous avons aussi mesuré les spectres UV de solutions où du méthanol a été ajouté (Figure 9d). Quand la proportion de MeOH augmente, l'intensité des agrégats J diminue. Ces résultats montrent que ces agrégats sont assemblés par des liaisons H intermoléculaire, en accord avec les études antérieures sur les **DPP.**

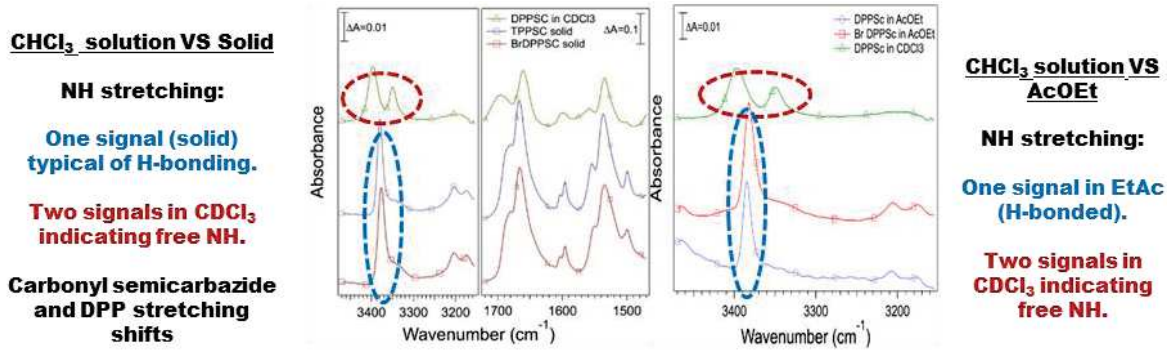

Figure 10: *Comparaison des spectres IR de TDPPSC à l'état solide et en solution dans le chloroforme (à gauche) et de* ***TDPPSC*** *dans le chloroforme et* ***TDPPSC*** *et* ***BrTDPPSC*** *dans l'acétate d'éthyle (à droite).*

La morphologie des échantillons spin-coatés a été étudiée par microscopie électronique à balayage (MEB). Les structures varient avec le solvant de dépôt utilisé (Figure 11).

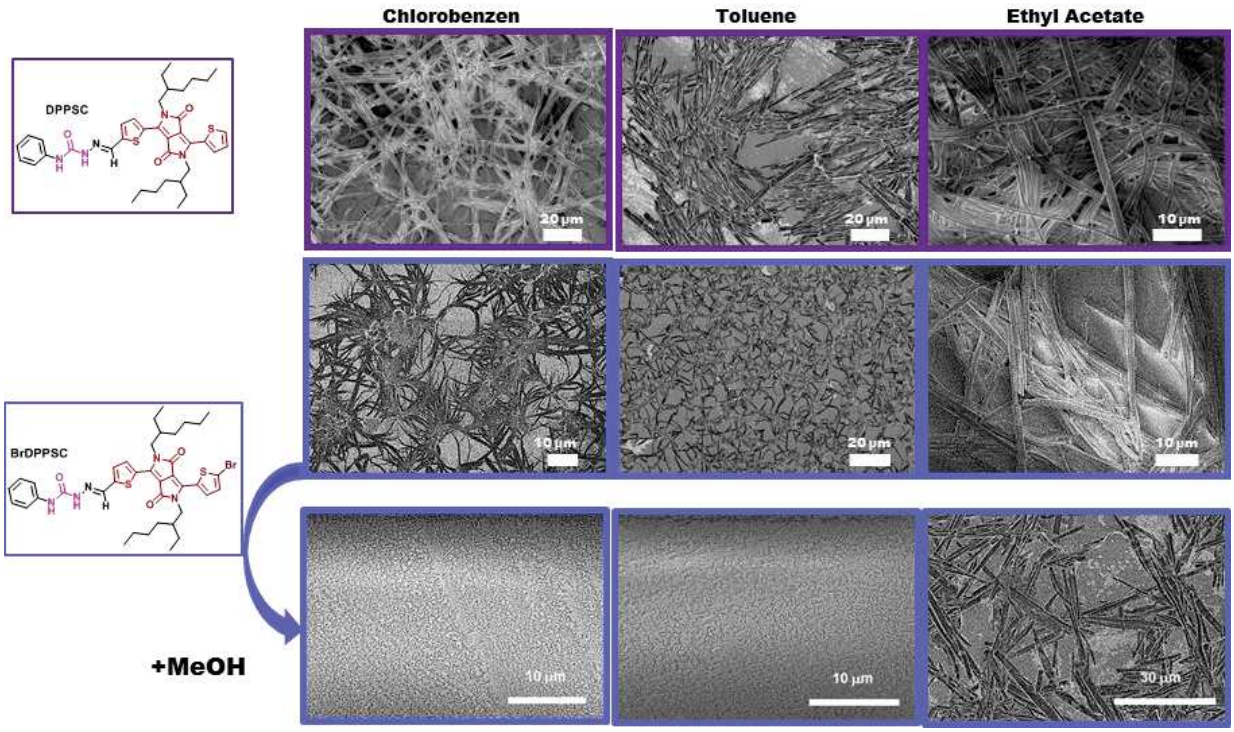

Figure 11: *Images MEB d'échantillons spin-coatés de* ***TDPPSC*** *et* ***BrTDPPSC*** *préparés à partir de solutions de chlorobenzène, de toluène, et d'acétate d'éthyle; C = 2.5 mg/m*

On observe des structures fibrillaires ou lamellaires. Les échantillons avec le rapport d'aspect le plus élevé ont des épaisseurs de l'ordre du nanomètre et des longueurs de plusieurs micromètres. Ces structures disparaissent ou se raréfient quand du méthanol est ajouté dans la solution de drop-casting. Cette expérience confirme bien le lien entre la formation de liaison H et des agrégats de type-J.

Les valeurs des niveaux d'énergie HOMO et LUMO ont été déterminé par cyclovoltamétrie : pour **TDPPSC** et **BrTDPPSC** HOMO de -5,18 eV et -5,26 eV, LUMO de -3,43 eV et -3,5 eV respectivement. La différence d'énergies est par conséquent de 1.75 eV. Ces composés sont donc de bon candidats pour des dispositifs électroniques tels que les transistors ou les cellules solaires. La méthode de déposition des structures est en cours d'optimisation.

IV. Chapitre 3: Dicétopyrrolopyrrole Bisamide

Au cours de notre étude précédente, l'auto-assemblage de DPP et les propriétés optiques étaient gouvernés par la formation d'interactions non covalentes proches du cœur principal. Ici nous étudions l'influence de la chiralité sur l'agrégation et les propriétés résultantes.

Dans ce chapitre, deux **DPP** bisamide, chiral (**DPPBA**) et achiral (**(S)-DPPBA**) sont été synthétisés et étudiés (Figure 12). Les amides utilisés pour générer des liaisons H sont situés sur les chaines alkyles attachées sur les azotes de la structure principale. Concernant **(S)-DPPBA**, deux centres chiraux sont localisés à côté des groupements amide.

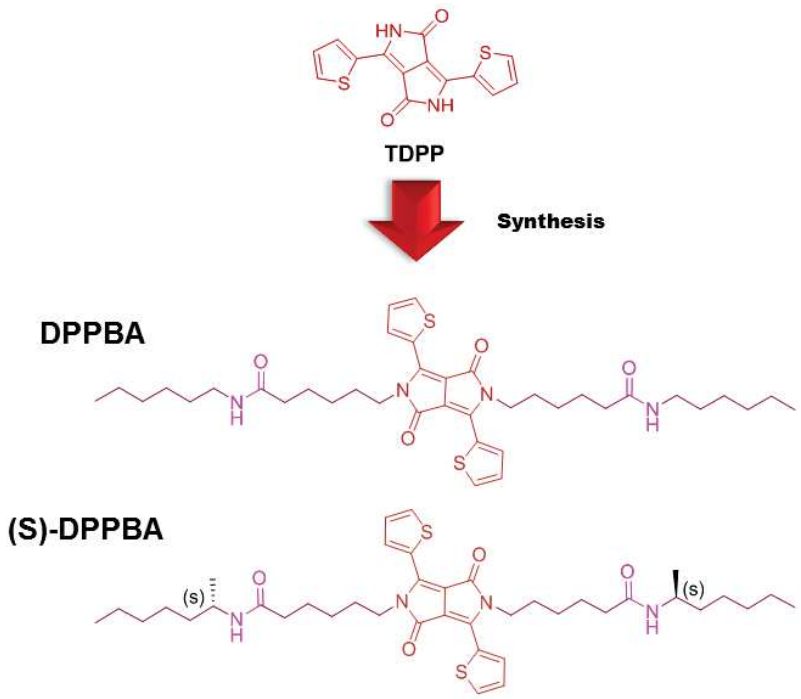

Figure 12: *Structure chimique des molécules de* ***DPP*** *bisamide développées*

Ces composés ont été synthétisés selon le Schéma 3a. La molécule de **DPP** est N-alkylé avec ces intermédiaires pour former **DPPBA** et **(S)-DPPBA**. Des sous-produits ont également été isolés et identifiés par RMN (Schéma 3b).

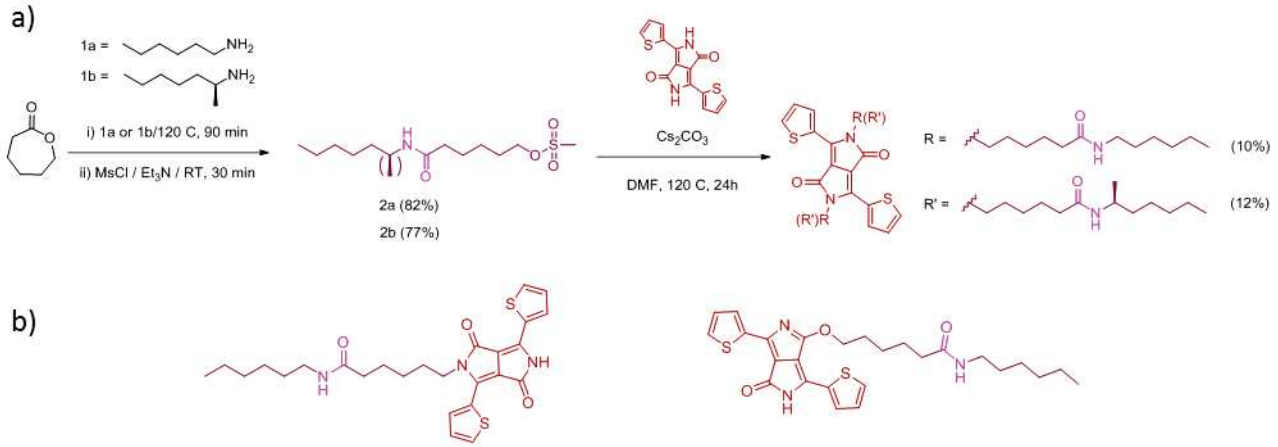

Schéma 3: *a) Synthèse de* ***DPPBA*** *et* ***(s)-DPPBA*** *; b) Sous-produits de* ***DPP*** *obtenus*

Les spectres d'absorption des deux produits montrent des bandes d'agrégats de type J plus intenses que les **DPP** semicarbazone et s'étendant vers le proche infrarouge (Figure 13). Ces bandes sont aussi présentes dans les solutions de **(S)-DPPBA** dans le chloroforme, mais absentes de celles de **DPPBA,** qui reste dissocié dans le chloroforme. Des analyses en spectroscopie IR et des analyses UV avec ajout de méthanol ont confirmé la formation de liaisons H avec la formation des signaux d'agrégats J.

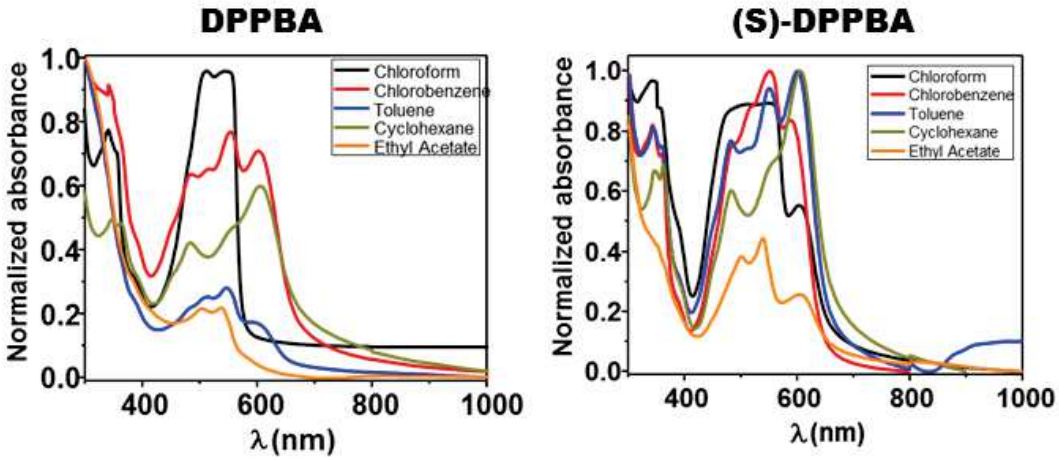

Figure 13: *a) Spectres d'absorption UV en solution le chloroforme, le chlorobenzène, le toluène et l'acétate d'éthyle de* ***DPPBA*** *and* ***(S)-DPPBA****.*

Les structures formées dans les solutions ont été examinées par microscopie électronique (MET) à transmission. Différentes structures ont été observées selon la nature du solvant, et selon la chiralité. **DPPBA** forme des structures petites et rigides ; les **(S)-DPPBA** forme des structures plus longues et hélicoïdale dans certains solvants (Figure 14).

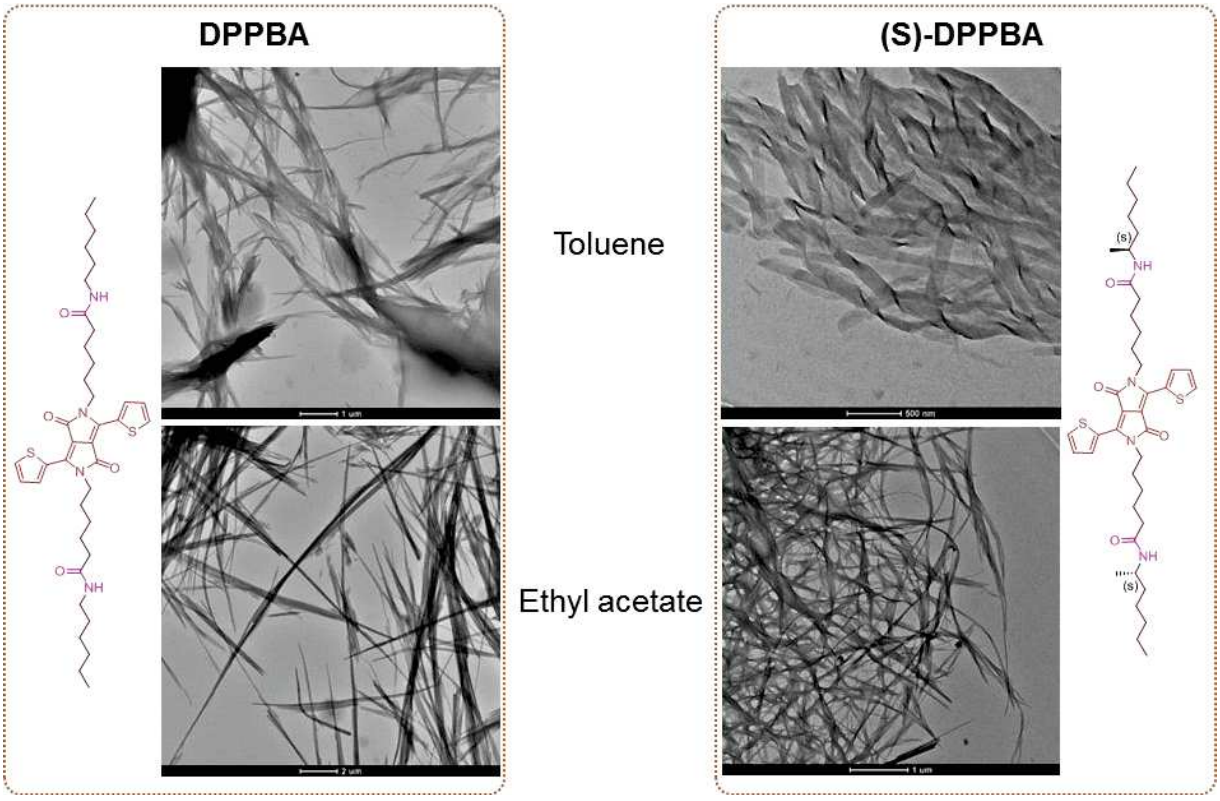

Figure 14: *Images TEM de* ***TDPPBA*** *and* ***(S)-DPPBA*** *dans le toluène et l'acétate d'éthyle.*

Le dichroïsme circulaire montre un effet Coton pour certains des signaux de **(S)-TDPPBA** (Figure 15a). Ces signaux sont situés dans les mêmes régions que les

signaux d'agrégats J observés sur les spectres UV. Aucun signal n'a été observé pour **TDPPBA** (Figure 15b).

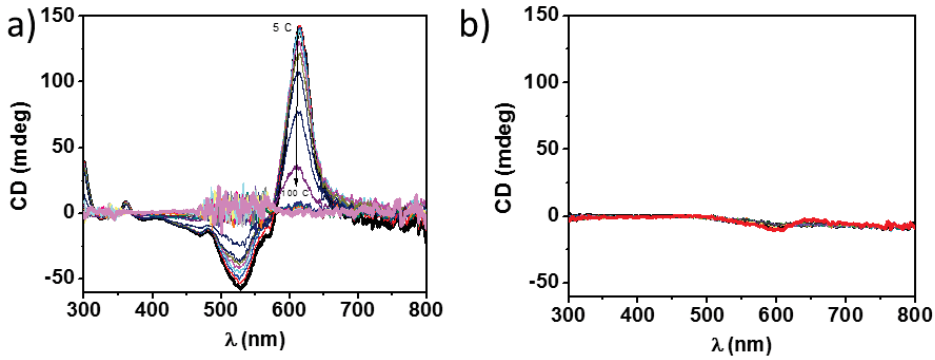

Figure 15: *Spectres CD de (S)-DPPBA (a) et DPPBA (b) avec variation de température*

Des premières mesures de photoconductivités par FP-TRMC (Flash photolysis time resolved microwave conductivity) ont également été effectuées via une collaboration avec l'équipe dirigée par le professeur Seki (Tokyo). Les résultats préliminaires ont révélé que **TDPPBA** possède une photoconductivité plus élevée et un temps de recombinaison de charges plus long que le dérivé chiral (Figure 16). La proximité des centres chiraux avec les amides peut expliquer ce résultat **(S)-TDPPBA.**

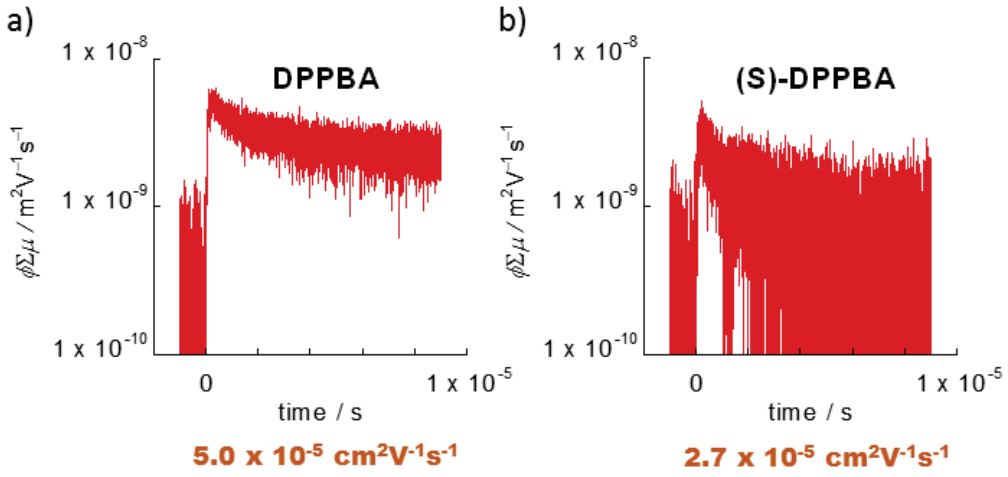

Figure 16: *Suivi cinétique de la conductivité d'échantillons de DPPBA (a) et DPPBA (b) drop-castés après excitation à 355 nm et des impulsions laser à 4.5 × 10^{15} photons cm^{-2}.*

L'exposition des échantillons à des vapeurs de solvant formant les agrégats J, augmente la photoconductivité et la durée de vie des charges. Ces valeurs ne changent pas après exposition à des vapeurs de méthanol, mais diminuent après immersion dans du méthanol. Les spectres UV mesurés avant et après trempage ne montrant aucun changement structural, d'autres analyses sont en cours afin de comprendre ce résultat.

V. Chapitre 4: Dicétopyrrolopyrrole Monoamide

Les organogelateurs sont des composés qui s'assemblent en agrégats fibrillaires formant un réseau fibrillaire. Cette morphologie facilite les transports de charges et peut être exploitée pour former la couche active d'un dispositif, pour peu qu'on dispose d'un organogélateur semi-conducteur.

Concevoir un gélateur semi-conducteur de novo est difficile car il n'y a aucune règle permettant de prédire la formation d'organogels et de contrôler les structures supramoléculaires formées. Néanmoins plusieurs molécules tels les oligothiophenes, les tétrathiafulvènes, les naphtalènes et pérylènes diimides sont de bons gélateurs (Figure 17) ayant des propriétés de conductivité et de transfert de charges intéressantes pour les cellules photovoltaïques.

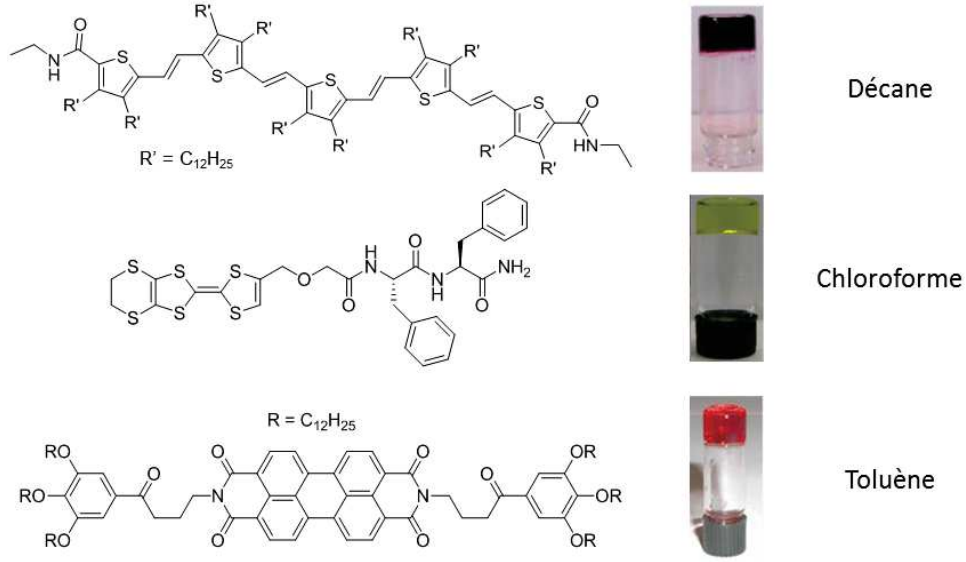

Figure 17: *Exemples de molécules semiconductrices formant des organogels dans différents solvants*

Dans la littérature, seuls trois organogels et un hydrogel à base de **DPP** ont été développés. Nous avons cherché à agrandir cette petite librairie. Nous avons proposé deux nouvelles molécules (**EHTDPPma** et **BOTDPPma**, Figure 18) développées à partir d'un sous-produit isolé et identifié lors de la synthèse des DPP semicarbazones (chapitre 2).

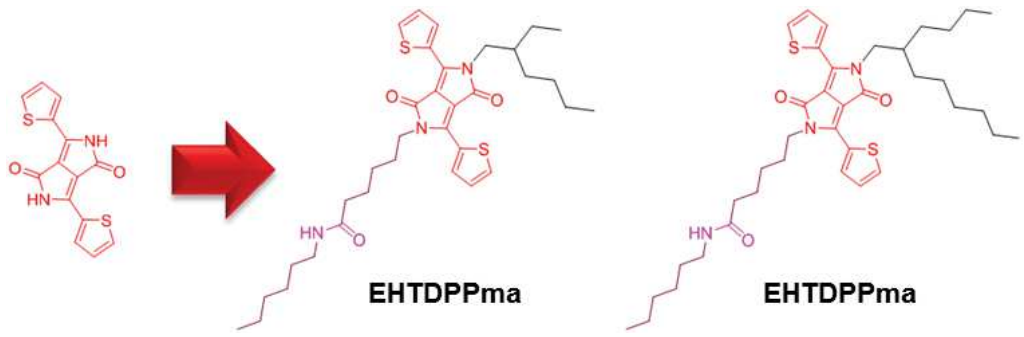

Figure 18: *Structure chimique des molécules de DPP monoamide développées.*

Ces molécules ont été synthétisées selon le même schéma que les molécules bisamides (chapitre 3). Les chaines ethylhexyl ou butyloctyl sont d'abord attachées sur les **DPPs** avant les bras amides (Schéma 4).

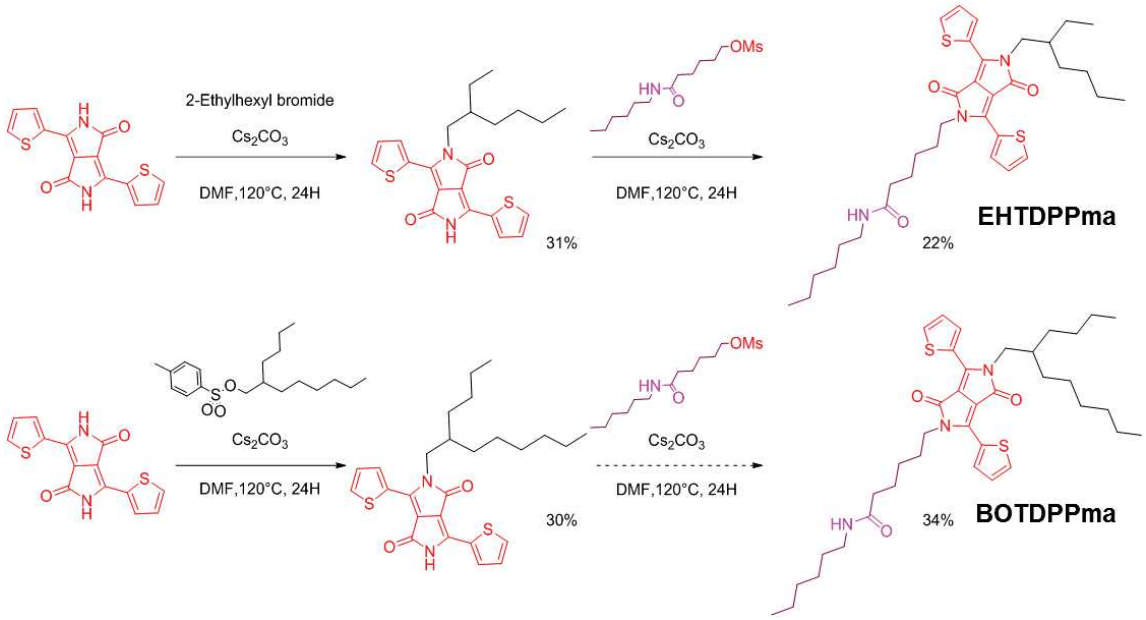

Schéma 4: *Synthèse de* ***EHTDPPma*** *et* ***BOTDPPma****.*

Ces composés forment des gels dans le cyclohexane et la *trans*-décaline à des concentrations > 0.5 % en masse. La mesure des modules élastiques et de pertes (G' et G'') en fonction de la fréquence confirment que les matériaux formés sont des gels (G' > G'' à toutes fréquences, Figure 19). Les températures de transitions sol-gel sont déterminées par la mesure de G' et G'' en fonction de la température.

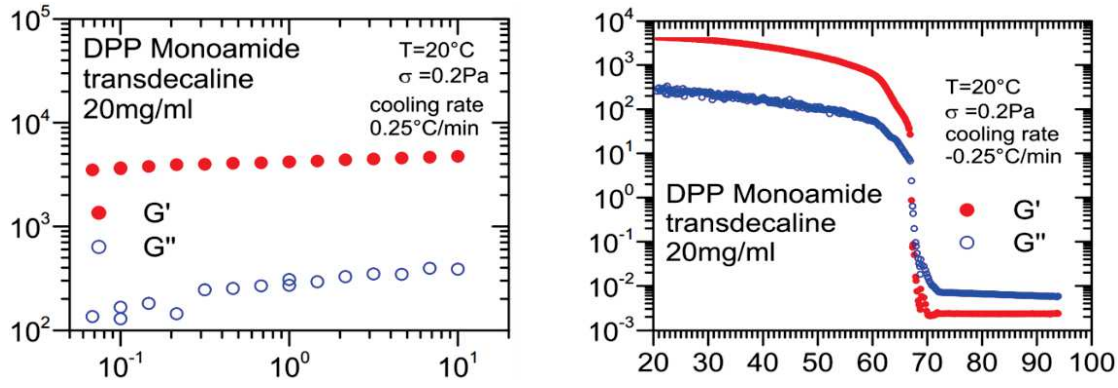

Figure 19: *Mesure rhéologiques de G' et G'' en fonction de la fréquence (à gauche) et de la température (à droite) de gel de* ***BOTDPPma*** *gel dans la trans-décaline*

Les transitions dans le gel ont également été suivies par turbidimétrie. (Figure 19a). Pour les gels très concentrés, lors du refroidissement cette technique détecte une seconde transition à une températures plus basse que la température sol-gel mesurées par rhéologie (Figure 20a). Par microscopie optique à température variable, on montre que cette deuxième transition correspond à l'apparition de sphérulites, identifiées par des croix de maltes en lumière polarisée (Figure 20b).

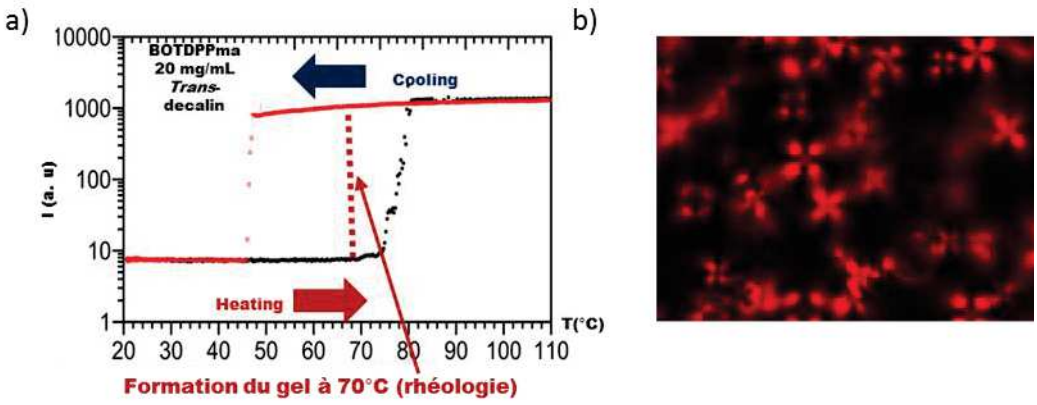

Figure 20: *a) Mesure optique en fonction de la température (vitesse de chauffe/ refroidissement : 0,3°C/min) ; b) Image de microscopie optique à lumière polarisée montrant la présence de sphérulites.*

Par cryo-TEM, on a étudié la morphologie des gels dans le cyclohexane et la *trans*-décaline (Figure 21). Les deux gels sont des réseaux fibrillaires. Les fibres mesurent plusieurs centaines de nanomètre de long et ont un diamètre de 7 nm en moyenne.

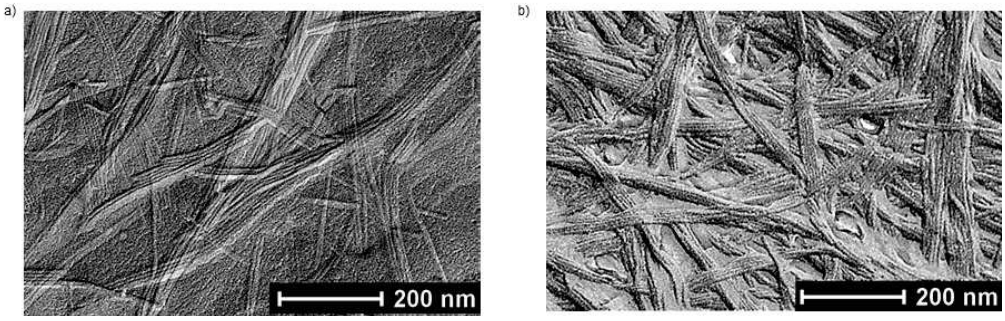

Figure 21: *Images TEM de (a)* ***BOTDPPma*** *dans la trans-décaline (C= 2.22 mg/ml) et de (b)* ***BOTDPPma*** *dans le cyclohexane (C= 20 mg/ml).*

Un diagramme de phase a été établi à partir des mesures de rhéologie et de turbidité pour différentes concentrations (Figure 22a).

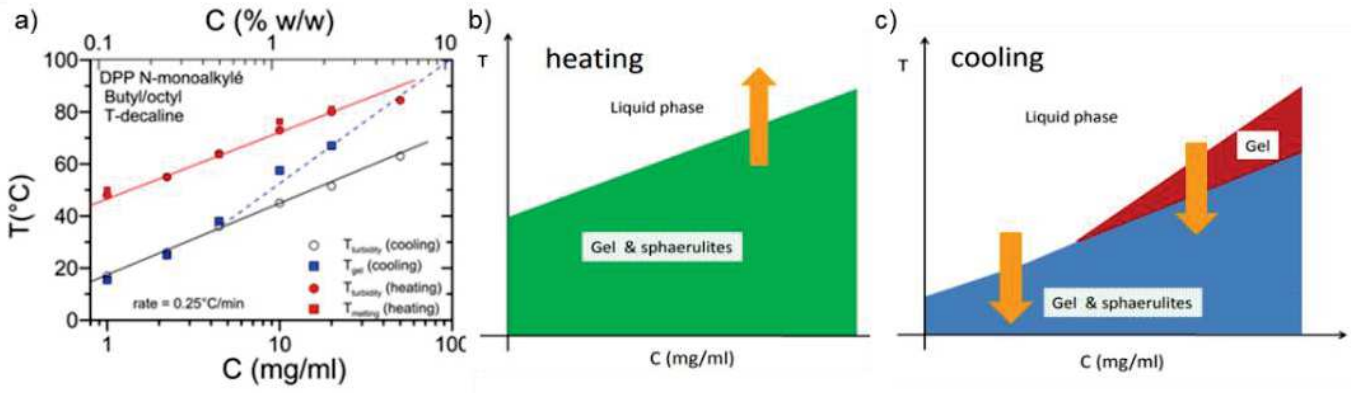

Figure 22: *a) Diagramme de phase de* ***BOTDPPma*** *dans la trans-decaline b) Schémas Simplifiés du diagramme de phase pendant le cycle b) de chauffage et c) de refroidissement*

Lors de la chauffe, on observe une seule transition gel-liquide (Figure 22b) ; lors du refroidissement, on observe les deux transitions au-dessus de C = 10 mg/mL, (Figure 22c). Dans ce régime, les fibres se forment dans un premier temps. Les sphérulites se forment ensuite. En revanche pour C < 10 mg/mL, nanofibres et sphérulites semblent se former simultanément.

La structure des fibres au sein des organogels a été étudiée par SAXS (Small angle X-ray scattering) (Figure 23a). Les intensités mesurées peuvent être ajustées par un modèle cylindrique à 3 couches. On détermine les épaisseurs des trois couches et leur densité de longueur de diffusion.

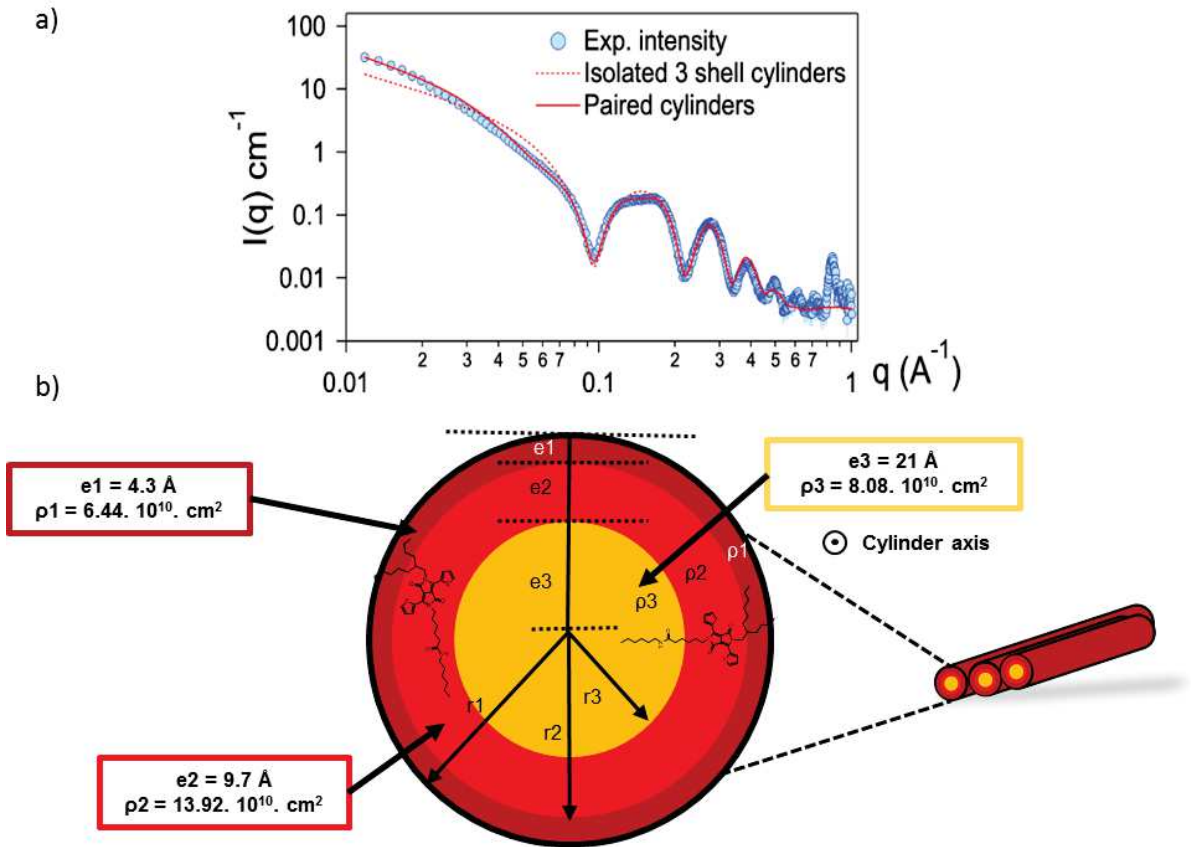

Figure 23: *a) Diffractogramme montrant la courbe expérimentale obtenue (sphères bleue), le modèle d'une structure cylindrique à trois couches (pointillés rouge) et la fusion des deux courbes (ligne continue rouge)*

En comparant les densités de matière trouvées à celles estimées pour les différentes parties de **BOTDPPma**, on peut proposer deux structures. La molécule peut être disposée de façon à ce que le bras amide occupe la couche centrale tandis la structure **DPP** et la chaine butyloctyl occupent la couche centrale et externe respectivement (Figure 23b). Cependant, la densité de matière obtenue pour la couche centrale est similaire à celle de la *trans*-décaline. Par conséquent une configuration où la structure **DPP** et le bras amide occupent la couche intermédiaire et où du solvant remplirait la couche centrale est aussi envisageable (Figure 22b). Des analyses SANS (small angle neutron scattering) sont en cours afin de déterminer la bonne configuration.

VI. Conclusion générale et perspectives

En conclusion, une librairie de petites molécules à base de **DPP** a été développée pour étudier l'influence des liaisons H sur leur propriétés d'auto-assemblage et optoélectroniques. Ces molécules sont différentiées par plusieurs paramètres tels le nombre et la nature des fonctions générant les liaisons H. La solubilité et la chiralité ont également été étudiées.

Les analyses de spectroscopie UV-visible ont révélées la présence de signaux caractéristiques d'agrégats de type J. Ces signaux sont plus ou moins intense en fonction de différents paramètres. Ils peuvent atteindre la région du proche infrarouge bénéfique pour fabriquer des cellules solaires. L'addition de méthanol et les analyses de spectroscopie infra-rouge ont confirmé l'implication des liaison H dans la formation des agrégats.

Une étude morphologique des agrégats a été effectuée par microscopie MET et MEB. Différentes structures ont pu être observé en fonction des structures des molécules, des solvants et des méthodes de déposition utilisées. Ces structures seront étudiées pour développer des cellules photovoltaïques ou des transistors à effets de champs.

Les transports de charges ont été étudié par des mesures FP-TRMC. Le dérivé achiral avait des mesures de photoconductivité plus élevé et des temps de recombinaisons de charges plus longues que le dérivé chiral. Les mesures de photoconductivité ont également été améliorées après exposition des échantillons à des vapeurs de solvants promouvant la formation d'agrégats alors qu'aucun changement n'a été observé après exposition des échantillons des vapeurs de méthanol.

Des gels ont pu être formés dans le cyclohexane et la *trans*-décaline avec les **DPP** monoamides. Les images TEM ont révélés la présence de de réseau nano fibrillaire avec un diamètre moyen de 10 nm. Les mesures de turbidités ont également montré une seconde transition dut à la formation de sphérulites une fois l'échantillon exposé à la lumière polarisée.

Un diagramme de phase a été établit en comparant les mesures de turbidité de rhéologie et montrent deux cas de figures : A faible concentrations, le gel forme uniquement un réseau fibrillaire tandis qu'à forte concentrations, les sphérulites se forment en supplément.

Ce projet sera poursuivi selon plusieurs perspectives. La première concerne l'agrandissement de la librairie de molécules de **DPP** développées. Suite aux résultats en photoconductivité montrant l'influence du positionnement des fonctions générant les liaisons H, des molécules où les amides seraient localisés sur différentes positions des bras alkyles devraient être synthétisé. Des molécules ayant des centres chiraux à différents endroits devraient aussi voir le jour (Figure 24).

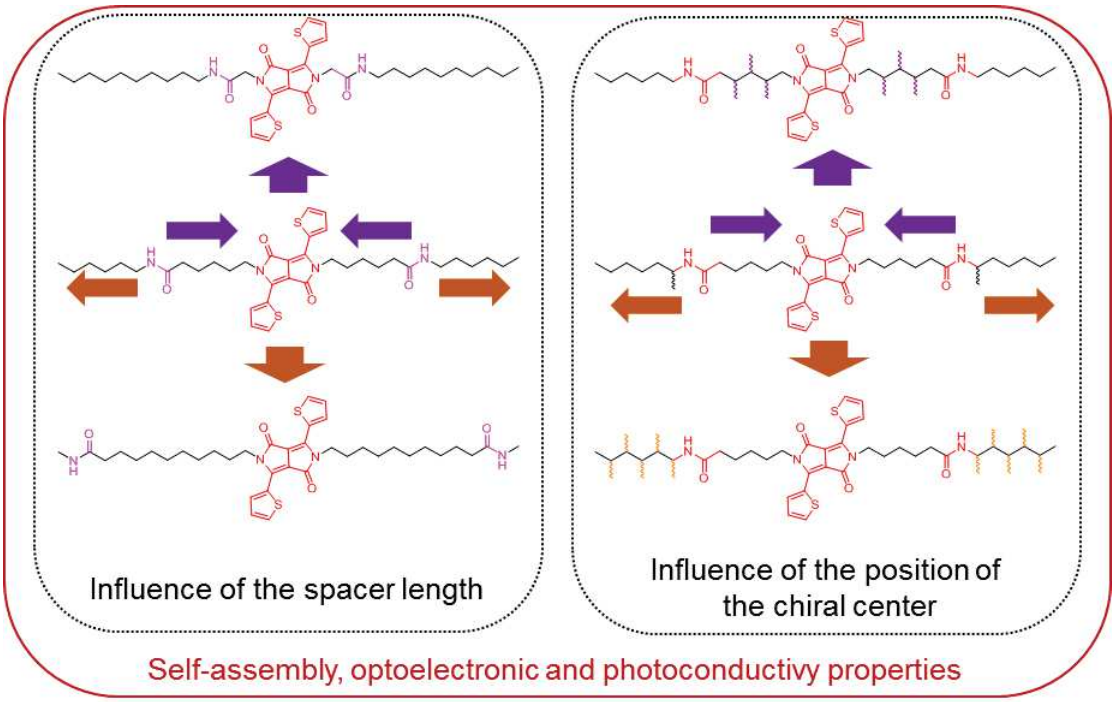

Figure 24: *Nouvelles molécules de DPP bisamide*

Pour le développement de nouveaux organogelateurs, des **DPPs** monoamides où le bras amide serait attaché sur différentes positions peuvent être développés. Il a été démontré sur des études cristallographique que la position de chaines alkyle sur les thiophènes pouvait influencer l'auto-assemblage des monomères entre eux et par conséquence les performances des cellules solaires développées. Des molécules avec le bras amide attaché sur les positions 2,3 et 4 sur une des thiophènes serait intéressant à étudier pour former des gels (Figure 25a). La solubilité étant aussi important, les chaines alkyles attachées sur les pyrroles doivent être ajustées. Concernant les molécules déjà étudiées, leur solubilité pourraient être améliorées en attachant des chaines alkyles. L'amélioration de la solubilité pourrait permettre à ces composés de former des gels (Figure 25b).

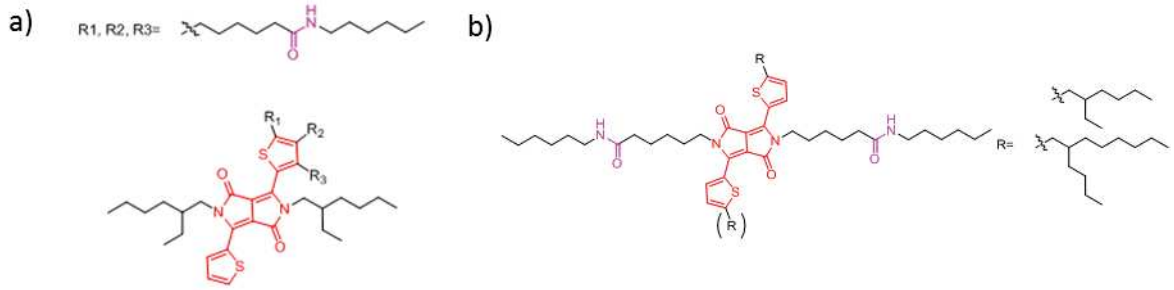

Figure 25: *a) Nouveaux organogelateurs de DPP monoamide pouvant être développés; c) Nouvelles molécules de DPP bisamide pouvant être développées à partir des molécules étudiées.*

Parmi les molécules étudiées, **DPPBA** semble être un candidat intéressant pour faire des cellules solaires en raison des mesures de photoconductivité effectuées. Ce composé forme des structures fibrillaire longues adéquates pour le transfert de charge. La méthode de déposition doit être cependant optimisée.

General Introduction

Since the prehistoric ages, colours have always been important in our everyday life. They have a deep psychological, aesthetic, functional and economic impact on our society. Colourants can either be dye or pigments. Organic pigments are usually destined for bulk coloration of plastics and synthetic fibers. They are also applied to coatings as paints and inks. Then, over time, new properties of these compounds were discovered. Consequently, the use of organic pigments raised in several technological industrial sectors such as photo-reprographics, optoelectronic devices and optical data storage. If the pigments are still employed for their color in some of these applications, they can also be used for other purposes.

Today, organic pigments such as isoindigo, squaraines, perylene and naphthalene diimide are produced and used as organic semiconductors. According to the literature, for most of these products, the charge carrier mobilities exceed 1 $cm^2V^{-1}s^{-1}$. Perylene and naphthalene diimide pigments draw most attention since their electron mobility values are close to 10 $cm^2V^{-1}s^{-1}$. Therefore, organic semiconductors can play a major role in the development of organic electronic devices such as photovoltaics displays. Solar cells today attract a huge interest for the production of energy. The energy consumption continues to increase, which has a negative impact in the environment: most of the energy production relies on fossil fuels, which are drying off. Furthermore, greenhouse gas released during the combustion of fossil fuels is mainly responsible for global warming. Most of the solar panels commercialized nowadays are based on inorganic materials such as silicon or germanium. These compounds are for now the most efficient materials but they remain costly to process. Organic solar cells are therefore attracting more attention due to their easy and low cost production. They are also light and highly flexible.

Diketopyrrolopyrrole (**DPP**) figures amongst the well-known organic pigments used today. They are distinguished for their red coloration, particularly the E 254 pigment famously known as the Ferrari red pigment. These pigments can also be used as biomarkers in biology. They can be coupled with therapeutic products and hence, form theranostic agents for the development of pharmaceutics. **DPP** molecules also havea huge interest in the development of organic semiconductors. They are highly sought for their interesting optoelectronic properties suitable for organic light emitting diodes (OLEDs), organic field effect transistors (OFETs) and organic solar cells (OSCs).

Most of the organic semiconductors used in electronic devices are polymers. However, small semiconducting molecules recently started to gain interest. They are easier to produce and can self-assemble into supramolecular structures with the help of non-covalent interactions mostly π-π stacking through their aromatic structures. Hydrogen bonds (H-bonds) are also used to make complex systems. However, there is no consensus whether their presence improves or worsens device performance. It is for this reason that our group underwent a systematic study of the influence of H-bonds in the self-assembly and the optoelectronic properties of small organic semiconducting molecules. Thiophene- capped **DPP** molecules are the model for this study.

We developed a library of small **DPP** molecules, which are distinguished by several parameters: the number of H-bonding groups, the position and the nature of these groups. The molecules are also composed of different branched alkyl chains to investigate solubility. One molecule has also one chiral center. This PhD project is the very beginning of this systematic study and will be focused on the synthesis and the study of the influence of H-bonds in the self-assembly and optoelectronic properties (Figure 1). We have also started to study the effects of the chemical structures on the charge transport properties.

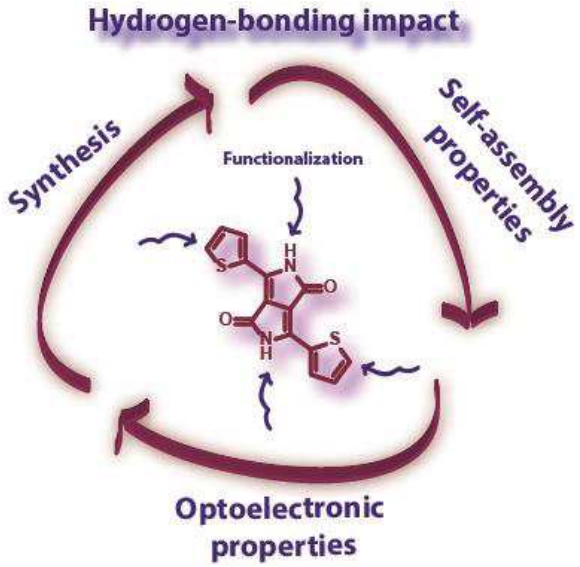

Figure 1: *Aim of this PhD project*

This manuscript is composed of four chapters :

The first chapter is devoted to a broad introduction on energy and supramolecular strategies applied in organic electronics. It continues with a survey of the literature about H-bonded **DPP**, and their use in organic electronic devices.

The second chapter exposes our results on semicarbazone-based **DPP** molecules. This is the part of the library where the H-bonds are covalently attached to the semiconducting segment, and varying the alkyl tails for solubility. We have explored their optoelectronic properties and their morphology in order to see if they are suitable candidates for organic electronic devices.

The third chapter is a study of amide-based **DPP** molecules. In this case, the H-bonding functionalities are connected to the **DPP** core through the lactam rings and having flexible alkyl linkers. In this part the influence of chirality was also studied.

The fourth and last chapter deals with the synthesis and study of new organogelators based on **DPP** with mono amide arms and branched carbon chains. The structure of the gels and their thermodynamic properties are described, as well as the elaboration of the phase diagram.

Chapter 1: Introduction

Summary

This chapter is a collection of global information presented in the literature and in relation with the notions and concepts used in this PhD work. It is divided in four parts:

The first part describes the economical context motivating scientists for solar energy conversion and transfer. This part will then give general information about semiconductors: their nature, their use in electronic devices, their electronic and morphology properties in electronic devices, such as organic solar cells and organic field effect transistors. The second part will give a brief description about diketopyrrolopyrrole (**DPP**) dye, how to synthesize and modify their chemical structure. The following part presents some achievements of supramolecular chemistry improving organic device performance. It is also here that we debate whether the H-bonds improve or worsen devices. We will then present most of the work done so far on polymers and small molecules based on **DPP** used for organic electronic studies. The final part will present studies made on **DPP** organogelators, which self-assemble due to H-bonding interactions

I. The importance of supramolecular chemistry in organic electronics

1. Energy consumption, issues and alternatives

The increasing world population originates a constant rise in the energy demand. It has been estimated that over 13 trillion watts are consumed worldwide in a year and that it should double by 2050[1] (Figure 1). Most of the energy production relies on fossil fuels such as oil, gas and coal, which are being rapidly drained and are the main causes of global warming since they release huge amounts of CO_2 into the atmosphere. As technology evolves, so does the energy demand, being the search of renewable energy sources one of the most important topics in scientific research. Several challenges need to be addressed to obtain sufficient energy that meets the demand in a sustainable and inexpensive manner. In this sense, solar light seems to be a great alternative energy source as one hour of sun light can be transformed into the energy consumed by the entire world population in one year[2].

Therefore, the research on semiconducting materials is crucial for the efficient absorption of light and conversion into electricity. The next paragraphs contain an overview on the requirements a semiconductor must have, more specifically organic semiconductors, and the optimal device morphology to achieve high efficiency on different types of devices. The strategies pursued to achieve connection among semiconductors in order to transport charges efficiently will be discussed. In this sense, we will focus on strategies based on supramolecular chemistry and more particularly, in the incorporation of hydrogen bonds in the molecular structures of organic semiconductors.

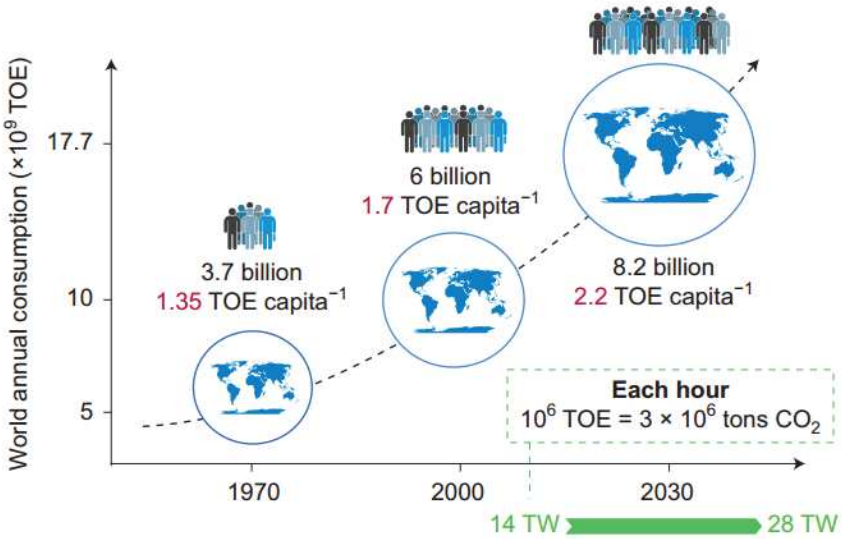

Figure 1: *Past, present and forecast of the world's energy needs up to 2050; TOE = ton of oil equivalent.*

2. Semiconducting materials

Semiconductors can be categorized in two families, inorganic and organic, even though hybrid materials can be also found. Inorganic semiconductors were discovered

first, and are still the most used in electronic devices. The most famous inorganic semiconductors in electronic industry are silicon (Si) and germanium (Ge). Semiconductors materials made from binary compounds such as gallium arsenide (GaAs)[3] or zinc blends (ZnS)[4,5] can also be used for device making. Another category of inorganic semiconductors are the oxide compounds, such as cuprous oxide (Cu_2O)[6] or zinc oxide (ZnO)[7,8]. Organic semiconductors are different from inorganic semiconductors in several aspects. They are π-conjugated organic small molecules or polymers where the charge carriers (polarons) move freely in the conjugated backbone[9]. Because of their high absorption coefficient[10], organic semiconductors can be applied in thin layers to fully absorb incident photons, which is very useful for developing photovoltaics and photodetectors. Organic semiconductors can have high photoluminescence quantum efficiency, hence making them suitable candidates for light emitting diodes (OLEDs)[11]. Furthermore, organic semiconductors also have small energy band gaps which allow efficient charge transfer of positive (holes) and negative (electrons) charges. Such characteristic is very promising for the development of all types of organic electronic devices.

The first mention of organic semiconductors appeared in the late 50's[12] and it was in 1977 when polyacetylene was discovered as the first conductive polymer by Shirakawa *et al*.[13] (Figure 2). They found the conductivity of these compounds could increase 10^9 times higher when doped with halogen vapors (Figure 2).

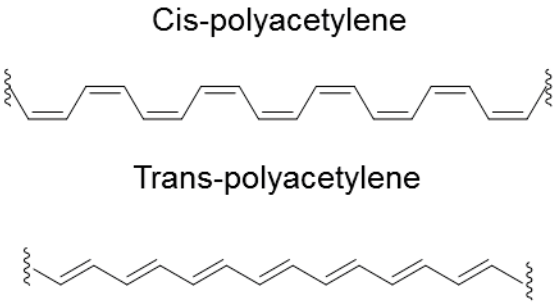

Figure 2: *Polyacetylene in cis or trans configurations.*

Several polymers were then examined for possible thin film applications in industrial production. Current research concentrates on compounds with bandgaps around 1.6 eV absorbing in the near-infrared (NIR) to develop efficient organic photovoltaic (OPV) devices. Several families of polymers are currently investigated as organic semiconductors with potential applications in organic electronics. The main structures of these organic semiconductors are shown in figure 3.

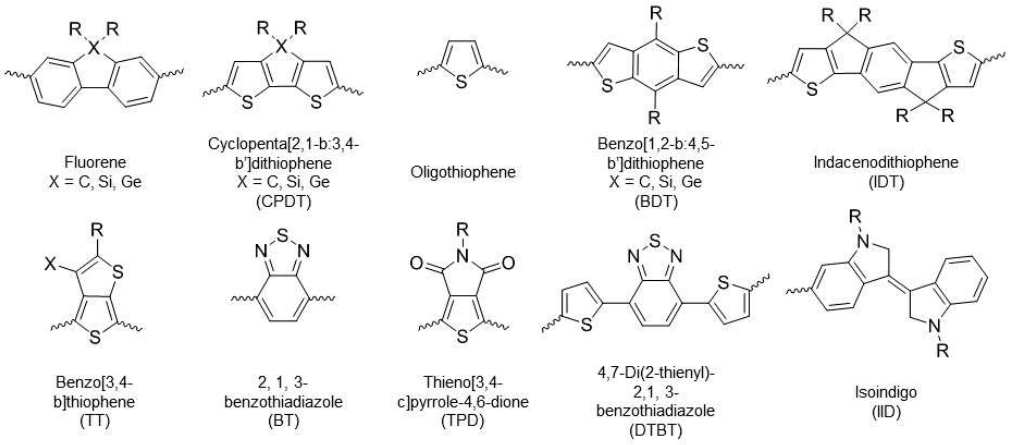

***Figure 3**: Structure of organic semiconductors used for organic electronic devices.*

Some of these polymers are well suited for OPV[14,15] devices, FETs[14,16] and LEDs[17]. Although semiconducting polymers can present interesting properties similar to inorganic semiconductors, they do present some drawbacks. Regarding their synthesis, polymers are occasionally difficult to purify and to optimize because of their molecular weight, their polydispersity and regioregularity. These reasons have pushed scientists to turn their attention to small organic molecules[18,19] based on the same main structures shown above.

In this thesis, we have focused on the diketopyrrolopyrrole (**DPP**) dye (Figure 4). It is a great semiconducting segment with multiple functionalization options and excellent optoelectronic properties. The next paragraphs are dedicated to a full description of this dye that will be used in this thesis.

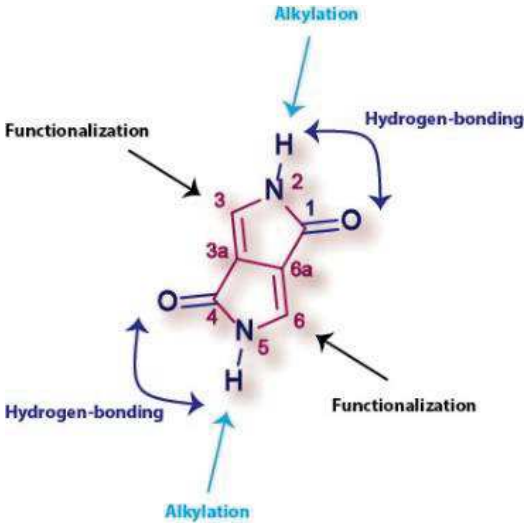

***Figure 4:** Structure of the main core of the diketopyrrolopyrrole molecule.*

3. Electronic requirements

In order to implement semiconducting materials in devices, their electronic properties and self-assembly must meet some requirements which will be discussed

now. The first property considered is their conductivity. This quantity represents the amount of electrical charges that can travel in a material in a given distance, being possible to distinguish between semiconducting and insulating materials. Metal conductivity is usually around 10^6 S.cm^{-1}, semiconductors conductivity from 10^{-5} to 10^{-2} S.cm^{-1} and insulators materials have a much lower conductivity of 10^{-14} S.cm^{-1} (Figure 5).

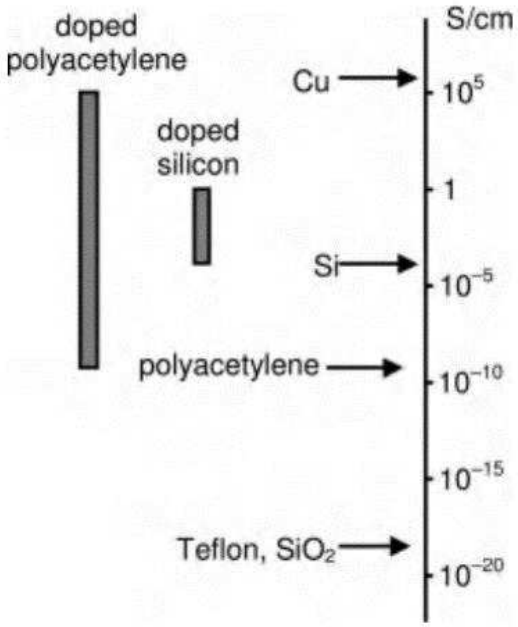

Figure 5: *Conductivity scale of several major materials used for electronics.*

Other parameters that need to be addressed are the band structure and the energy levels of the highest occupied molecular orbital (HOMO) and the lowest unoccupied molecular orbital (LUMO). The difference of these two levels is the band gap. It reveals whether the material is insulating or conductive. The energy band gap also influences the optical properties of a conductive material, such as its color and luminescence. The HOMO and LUMO energy levels establish whether a semiconductor compound can be reduced or oxidized classifying them respectively as n-type or p-type material.

According to the bands theory illustrated in figure 6, a metal has a conduction band partially filled; a semiconductor has a filled valence band and an empty conduction band. Semiconductors are insulators at T = 0 K, but when the temperature is elevated, electrons are excited from the valence band to the conduction band allowing conductivity. The main difference between an insulator and a semiconductor is the energy band gap separating the valence from the conduction band; it is higher in an insulator (6 eV), preventing any electron migration. It is much lower in semiconductors (around 1 eV) and can also be tuned with the addition of small impurities, a process known as doping. This process consists on either introducing energy levels close to the conduction band or the valence band, which are processes respectively known as n-type doping or p-type doping

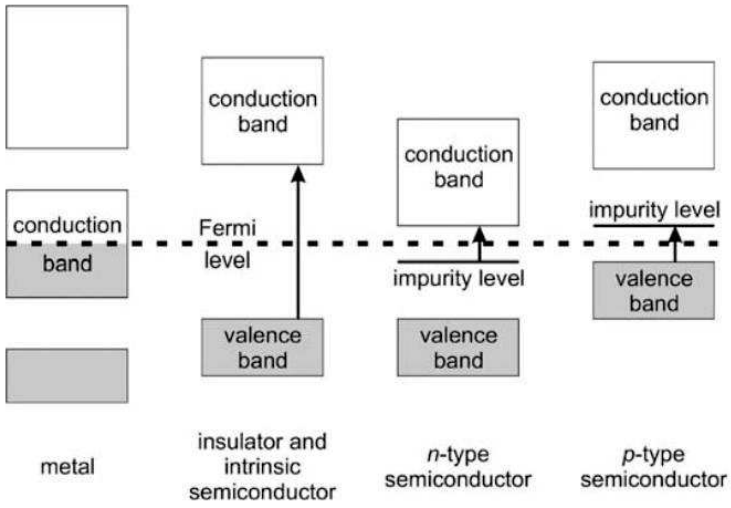

Figure 6: *Comparison of energy bands between metals, insulators, n and p-type semiconductors.*

4. Morphology in organic electronic devices

Although organic semiconductors are the main elements of solar cells or transistors, the later devices are differentiated in several aspects, starting with their structures. An OFET is composed of three parts: an insulator, three electrodes and a thin layer made of semiconductors (Figure 7a and b). One electrode (the gate) is in contact with the insulator, the two other (the source and the drain) are directly in contact with the semiconducting layer.

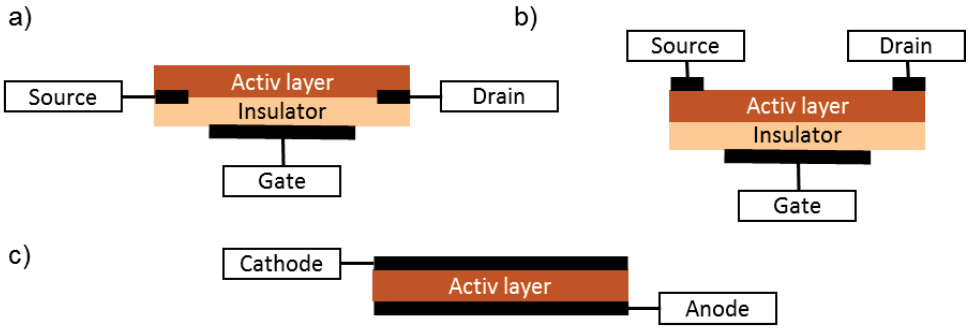

Figure 7: *General structure of a) a top-gated, b) a bottom contact transistors and c) solar cells.*

The fabrication of these devices consists of piling up thin films of the different components. Since organic semiconducting materials are fragile, there are usually deposited on the insulator. The source and the gate electrodes can be placed either on the insulator (bottom contact) or on top of the semiconducting layer (top contact). In solar cells, the semiconducting layer is sandwiched between two electrodes[20]

The organic semiconductors layer of both transistor and solar cell devices need to be perfectly connected to guaranty optimal charge transport. However, the

semiconducting layer made with these materials should have different morphology and orientation depending on the type of device. OFETs need one type of organic semiconductor electron donor (**D**) or electron acceptor (**A**), while a solar cell requires the presence of both. Regarding OFET devices, the semiconductors should arrange with parallel orientation with respect to the electrodes. On the other hand, according to previous studies, the energy transfer is optimal when, in the active layer, both semiconductors are organized in a checkboard configuration[21] (Figure 8a) in a solar cell with perpendicular orientation of the molecules with respect to the electrodes. To reach such configurations, the layer is processed by spin-coating[22], chemical vapor deposition[23] or using additives[24]. After deposition, thermal treatment can improve the morphology of the active layer.[25,26] However, these procedures rely on phase separation and do not perfectly organize both **D** and **A** components in the optimal "checkerboard" morphology. Instead, the semiconducting molecules are randomly organized (Figure 8b). Another strategy consists in using organic semiconductors able to self-assemble into supramolecular structures by using noncovalent interactions by a bottom up approach. Such tool improves the binding between **D** and **A** compounds[27,28] and may yield an active layer morphology closer to the ideal checkerboard structure (Figure 8c). Therefore, the design of well-ordered nanostructures using noncovalent interaction such as π-π stacking or hydrogen bonding has become of great interest for the development of organic electronics.

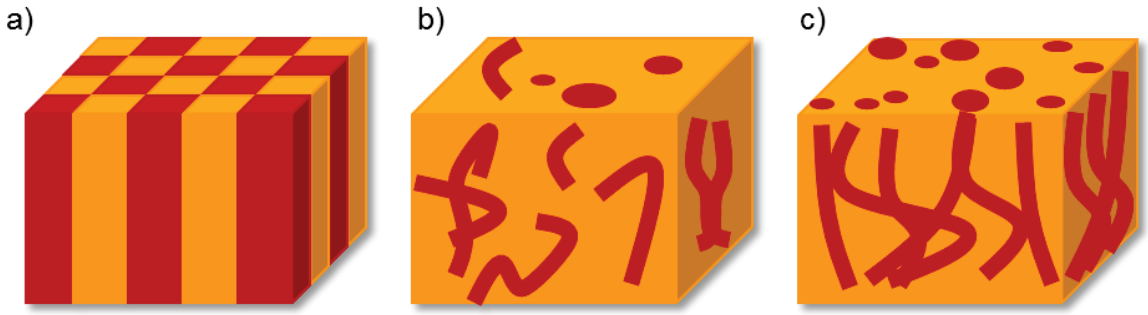

Figure 8: *a) Checkerboard morphology with donor D (red) and acceptor A (orange) molecules according Monte Carlo modelling; b) Morphology obtained after phase-separation; c) Morphology obtained by molecular recognition using hydrogen-bonding and π- π stacking.*

Another parameter that needs to be taken in account is the packing orientation of the molecules. It has been established that the optoelectronic properties and the devices performances are influenced by the organization of the molecules. Previous studies revealed organic field effect transistors are highly efficient when the oligomers or polymers are assembled in an edge-on organization[29–31] with respect to the substrate whereas face-on packing is advantageous for solar cells devices[32–34] (Figure 9).

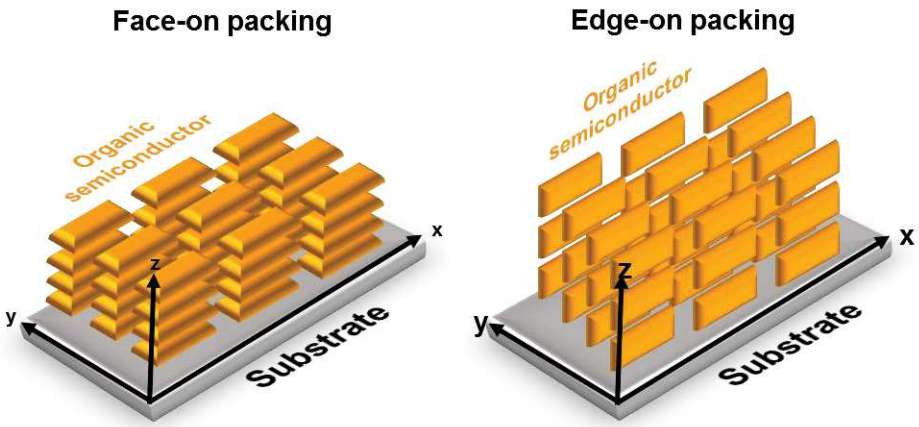

Figure 9: *Illustration of face-on and edge-on orientation of organic semiconductors.*

Therefore the control over the supramolecular assembly of organic semiconductors for obtaining either face-on or edge-on organization remains until now a great challenge. Many methods for orienting organic semiconductors in a specific direction onto the substrate have been reported in the literature. The most efficient approach to this aim is rational design of the molecular structure using several alkyl chains[35–38] and aromatic[39–41], which can provide a preprogrammed architecture. However, the influence of solvents[42,43], the use of solvent additives and thermal and/or solvent vapor annealing have also been studied to guide the packing of the molecules.

II. Diketopyrrolopyrrole dye

1. Description

Since their discovery by Farnum in 1974[44], diketopyrrolopyrroles (**DPP**) are a famous class of organic pigments used for many purposes. Their color, high stability and low solubility are well adapted for paints, varnishes and inks. The famous Ferrari red color is based on a **DPP** molecule[45]. Several years later, it was discovered that these compounds could also be converted into soluble dyes by N-alkylation[46]. These properties have attracted a lot of interest from the scientific community who developed many **DPP** derivatives for several applications. Besides applications in biology as biomarkers for microscopy[47,48], most scientific articles or patents are related to organic electronics for semiconducting devices. **DPPs** can be used as sensors[49,50] or probes for detecting for detecting ionic and non-ionic compounds but also for making organic LEDs, OFETs[51,52] and solar cells[53].

2. Synthesis

The chemical structure for **DPP** molecules is a conjugated bicyclic γ-lactam ring. It is generally substituted in positions 3- and 6- by aryl or heteroaryl groups, and more rarely by aliphatic groups[54,55]. Both amide groups can be unsubstituted or alkylated to improve solubility, even with aryl or acyl groups. Several synthetic strategies are known

to obtain **DPP** molecules that can be either symmetric or asymmetric. The most common route to these compounds is the condensation of nitriles and succinic acid esters[56–60], which will be used for making our molecules.

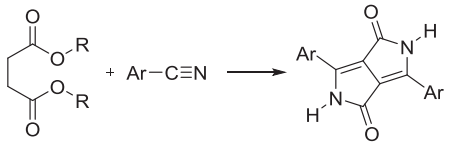

Scheme 1: *Synthesis of a **DPP** core by a condensation reaction between diethyl succinic and an aromatic nitrile.*

3. Reactivity

Once the main core is formed, the compounds can be easily modified. The compounds can be alkylated on the nitrogen or oxygen atoms, depending on the reaction conditions. The aromatic substituents attached to positions 3- and 6- of the **DPP** core can also undergo transformations such as halogenation or formylation. Thiopene-capped **DPP** can also undergo lithiation with lithium diisopropylamide (LDA), and can then be used to introduce new substituents in reaction with various electrophiles such as formamides (DMF, N-formylpiperidine) forming aldehydes[61,62] (scheme 2).The reaction of lithiated **DPP** with 2-isopropoxy-4,4,5,5-tetramethyl-1,3,2-dioxaborolane is used to produce boronic diesters[63], and organotin derivatives with trimethyltin chloride[64,65] (scheme 2). The reaction of **DPP** with LDA and iodine gives diiodinated derivatives[63].

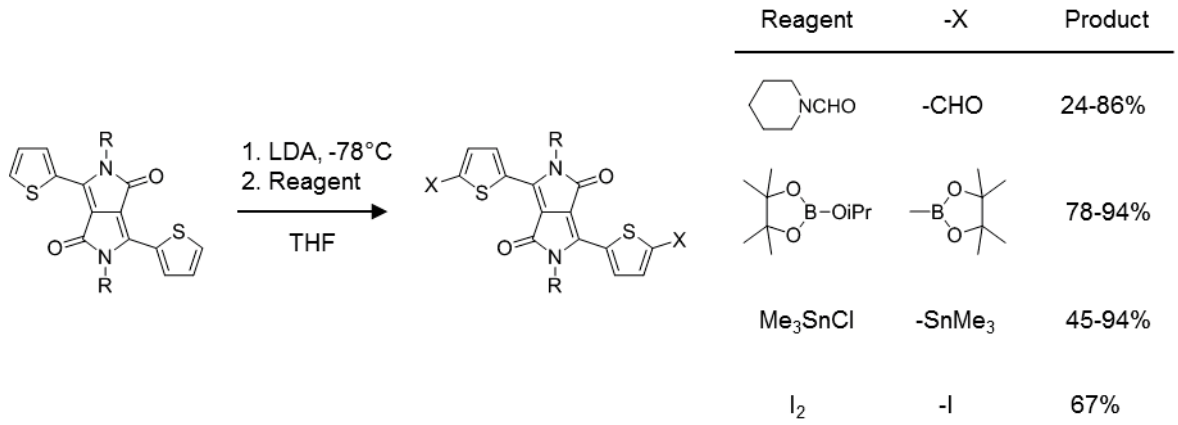

Scheme 2: *Possible functionalization of **DPP** by lithiation.*

Many examples of polymer and small molecules based **DPP** were reported for organics electronics applications. The aim of this PhD project is to develop new small **DPP** molecules with potential applications in electronic devices. One of the major criteria essential for making efficient devices is the organization of the monomer units in the active layers. For this reason, the interest of this project is to focus in supramolecular chemistry strategies to develop and study supramolecular structure formed with our **DPP** library, which will be presented in the following chapters of this

manuscript. In the next paragraph we will discuss about the importance of the application of supramolecular strategies in organic electronics to achieve the appropriate morphology and to tune the optoelectronic properties by controlling the self-assembly processes.

III. Supramolecular chemistry strategies applied in organic electronics

As previously explained, not only the electronic parameters are important to achieve good device performance. The morphology is equally important and in many cases, molecules designed with the optimal electronic properties do not result in performing devices due to the wrong morphology and packing on thin films. In the next paragraphs, supramolecular strategies applied in the field of organic electronics are described.

1. Supramolecular chemistry

Also known as “chemistry beyond the molecules”, supramolecular chemistry relies on the making and study of molecules capable of forming complex structures using of noncovalent interactions[66,67]. Even if this discipline started in the early 1900s with the studies of molecular natural or synthetic complexes[68–70], supramolecular chemistry was coined by Lehn, Cram and Pederson in 1978 who were awarded the Nobel prize of chemistry in 1987. Since then, this field was explored in several areas combining chemistry, physics and biology. In this sense, supramolecular chemistry can be very useful to design organic semiconductors equipped with noncovalent interactions able to guide the assembly and the required packing. Several noncovalent interactions have been introduced into the molecular structures of organic semiconductors. π-π stacking is naturally present between the aromatic units and conjugated segments of these compounds. It addition, other noncovalent interactions, such as H-bonding, metalophillic[71] or electrostatic interactions can be used to achieve directionality to the supramolecular structures formed.

In this thesis, the study of the influence of H-bonding in organic electronic materials has been investigated and therefore, special attention is given to this type of noncovalent interaction.

2. Supramolecular chemistry and hydrogen-bonding in organic electronics

H-bonding[72] interactions inspired scientist to develop complex systems mimicking natural process, such as catalysis or photosynthesis. In organic electronics, H-bonds have been explored to build supramolecular structures suitable for the fabrication of OLEDs, OFETs and solar cells.[73–76] These interactions are influenced by several physico-chemical parameters such as temperature, concentration, solvent or chirality. Therefore, these parameters can tune the aggregation state, the molecular packing, and the electronic properties. Many studies are mentioned in the literature where scientists used H-bonds to develop fiber[77], rosette [78], helical[79] or columnar[80]

structures that cannot be formed without them and that show interesting electronics properties that could be used for device fabrication.

However, there is no real consensus on the influence of H-bonds in the final outcome of organic electronic devices. While some works are focused on studying the supramolecular structures formed by H-bonding, the electronic properties are not well investigated. On the other hand, other examples found in literature do not perform an exhaustive study of the self-assembly properties of the H-bonded semiconductors. Therefore, systematic studies where electronic and supramolecular parameters are included should be performed. To illustrate the lack of consensus in this topic, the example of the work of Bumjoon *et al.* [81] is here explained. The authors studied the influence of H-bonding interactions on dithienosilole-based small molecules and incorporated them in OEFT and solar cell devices. They synthesized several derivatives either with ester or with amide as the end groups, and with different alkyl side, chains (Figure 10).

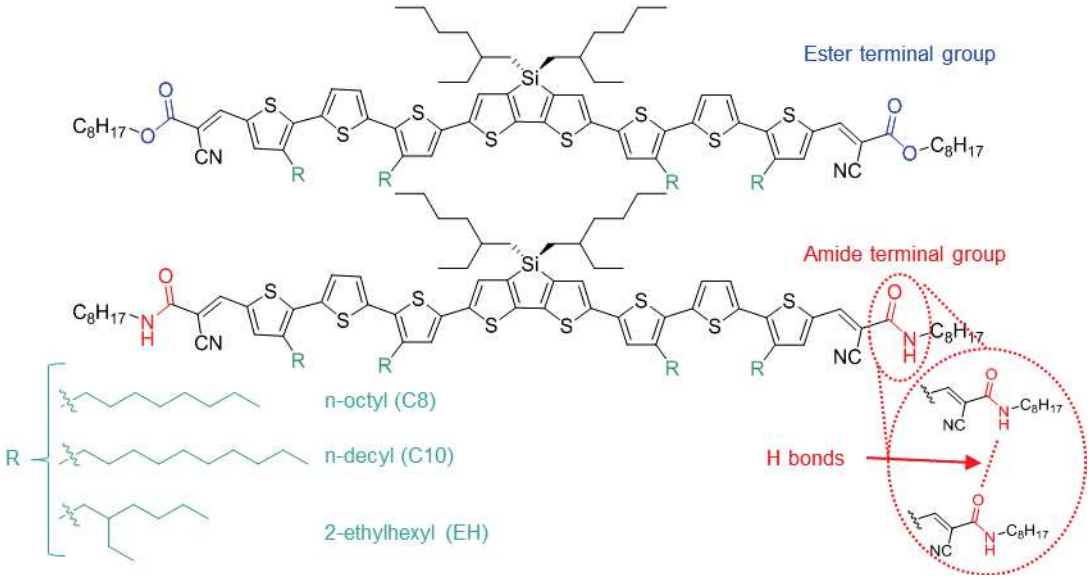

Figure 10: *Chemical structure of six molecule donors with various alkyl side chains and ester or amide groups.*

In UV absorption spectra in solution and on thin film, the ester analogs had absorption signals slightly more red-shifted than those of their amide analogs. The molecules with amide terminal functions exhibited stronger intermolecular interactions than the ester analogs according to domain spacing measured by grazing incidence X-ray scattering (GIXS). However in the GIXS diffractograms, the presence of (010) reflections for the ester molecules proved a well-ordered ‘’edge-on’’ molecular orientation. As a result, charge carrier mobility measurements performed on OFETs were higher for devices made with the ester derivatives than those of the amide analogs. OPV devices were also fabricated and revealed lower device performance for the amide molecules than those made with the ester derivatives.

a)

Sample	$\mu_{h,max}$ ($cm^2 V^{-1} s^{-1}$)
C8-Ester	1.37×10^{-2}
C10-Ester	2.82×10^{-2}
EH-Ester	2.70×10^{-4}
C8-Amide	2.18×10^{-3}
C10-Amide	2.99×10^{-3}
EH-Amide	6.54×10^{-6}

b)

Active layer	V_{OC} (V)	J_{SC} (mA cm^{-2})	FF	PCE (%)	Integrated J_{SC}[a] (mA cm^{-2})
C8-Ester	0.82	9.79	0.54	4.31	9.67
C10-Ester	0.82	9.30	0.57	4.31	9.19
EH-Ester	0.94	7.75	0.41	3.00	7.63
C8-Amide	0.87	7.94	0.47	3.22	7.83
C10-Amide	0.86	8.38	0.52	3.75	8.23
EH-Amide	0.64	1.25	0.26	0.21	1.22

[a] Calculated by integration of EQE curves.

Table 1: *a) The maximum mobility of the FET devices; b) Characteristics measurement obtained by OPVs made with dithienosilole-based small molecules and PCBM as electron acceptor.*

The active layers were analyzed by Transmission Electron Microscopy (TEM) and Atomic Force Microscopy (AFM) microscopy studies revealing that ester molecules blended with Phenyl-C61-butyric acid methyl ester (PCBM) forming an interpenetrating bi-continuous morphology. Active layers made with **PCBM** and the amide molecules showed less distinct features in the phase separated morphology. This study shows the amide derivatives present lower results than those of the ester analogs suggesting an unfavorable influence of the H-bonds interactions. However, the authors confirm these results are due to the influence of the alkyl chains: When the carbon chains are branched, it disturbs the packing of the molecules and affects the active layer of OPV and OFET devices. It is important to remark that the devices were fabricated with only one solvent, which makes difficult the study of the supramolecular structures that are heavily influenced by the solvent. Furthermore, solubility could have been an issue since H-bonded derivatives are generally less soluble than their ester analogs.
Schülze *et al*. synthesized quaterthiophenes bearing phthalhydrazide (BQPH, Figure11), able to self-assemble with H-bonds. They also synthesize the ester analogues unable to form H-bonds (BQPME, and BQPNMe, Figure 11). They compared their behavior in organic photovoltaic materials[82].

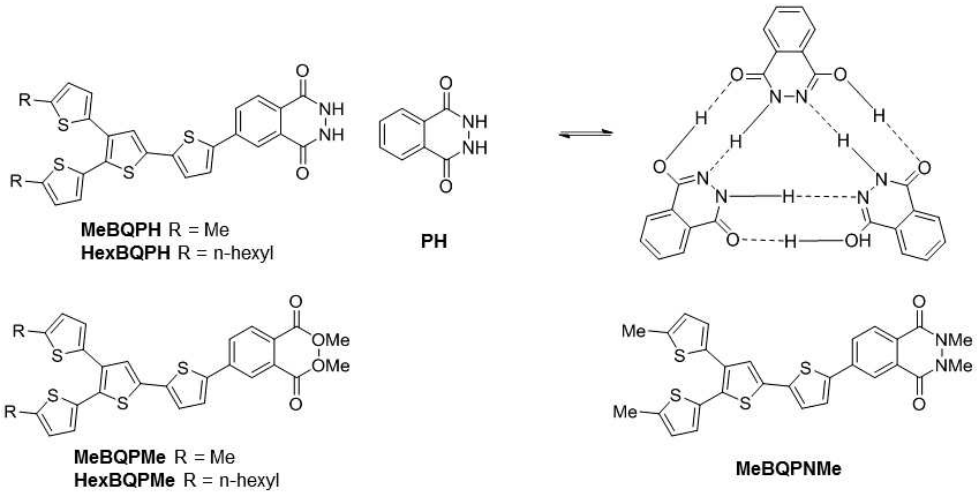

Figure 11: *Molecular structures of MeBQPH, HexBQPH, MeBQPME, HexBQPME, MeBQPNMe and phthalhydrazide (PH).*

The formation of H-bonds was confirmed in solution and in bulk films by FTIR. It was also supported by thermal gravimetric analysis (TGA) and differential scanning calorimetry (DSC): the H-bonded compounds melt and degrade at higher temperatures than the control analogs with ester or alkylated amide functions. The formation of H-bonds also generated red-shifted absorption bands according to UV spectra study compared to the analogs without primary amide. Photovoltaics devices were developed with BQPH and the non-hydrogen bonding analogs, both blended with C60. The power conversion efficiency increases from 0.49% for the control molecules to 1.04% for the H-bonded ones. In this example, the hydrogen bonds revealed to be beneficial. However, a few months later Xiao *et al*. published a study that shows also that the presence of amide functions generating H-bonds is detrimental[83] (Figure 12). They studied dithienothiophene derivatives having terminal groups of either octyl cyanoacetate or octyl cyanoacetamide.

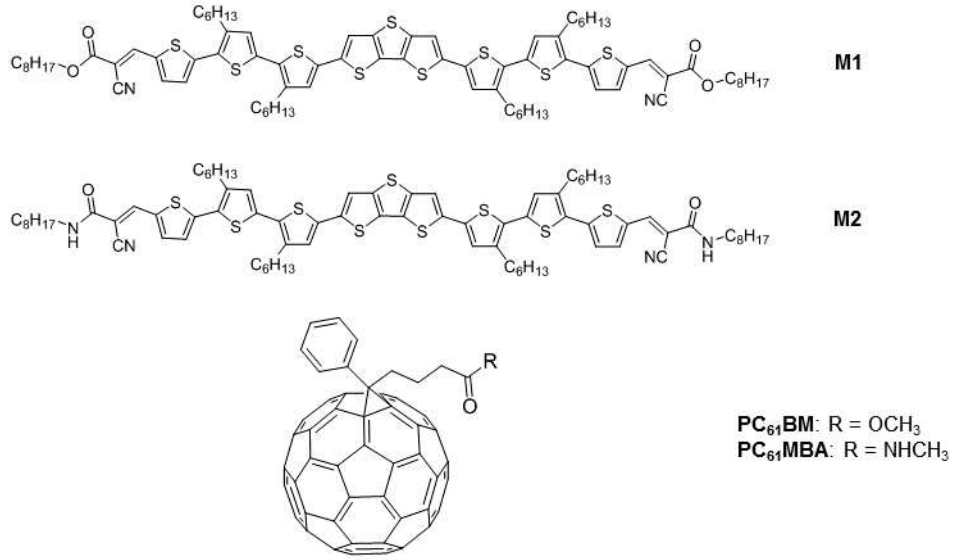

Figure 12: *Chemical structures of M1, M2, $PC_{61}BM$ and $PC_{61}MBA$.*

Like in the work of Bumjoon *et al.*, the ester product presents absorption bands more red-shifted than the ones of the amide derivatives in solution and on thin films. It presents also a lower energy bandgap. AFM revealed that the H-bonding product self-assembles in nanowires, which should be advantageous for solar cells. However, GIWAXS analysis showed the packing of the amide compound is less organized than the one of the ester compound. Moreover it changes when blended with PCBM, whereas the organization of the ester analog domains remains undisturbed. These features impact the device performance: the PCE values are lower for the H-bonded dithienothiophene than those of the esters analogs. At about the same time, *Stupp et al*. published other examples of the influence of H-bonds on OFET and OPV, the diketopyrropyrrole derivatives discussed in the following paragraphs.

All these studies present semiconductors based on different semiconducting segments and H-bonding functionalities. For this reason, in this thesis we have chosen

a defined electroactive segment based on **DPP** and different H-bonding functionalities are being explored. In the next paragraphs, the previous work reported on H-bonded **DPP** derivatives will be described to put in context the work of this thesis.

3. Hydrogen-bonded DPP with unsubstituted lactam rings

a. Structural characterization, crystallization and optical properties

1,4-diketo-3,6-diaryl-pyrrolo–[3,4-c]-pyrrole as synthesized contains two unsubstituted lactams with ability to form hydrogen bonds (Figure 4). In the solid state, there are chains of NH···O intermolecular H-bonds between the NH group of one molecule and the O atom of the neighboring molecule forming linear chains. These H-bonds are necessary to align the transition dipole in a "head-to-tail" mode that results in a bathochromic shift of the absorption band when transitioning from the solution state to the solid state. Besides, the NH···O hydrogen bonds connect the **DPP** molecules to achieve stability similar to those of polymers. The linear chains are parallel to each other and to the plane, while brick wall-pattern π-π stacking is found perpendicular to the plane (Figure 13).[84–86]

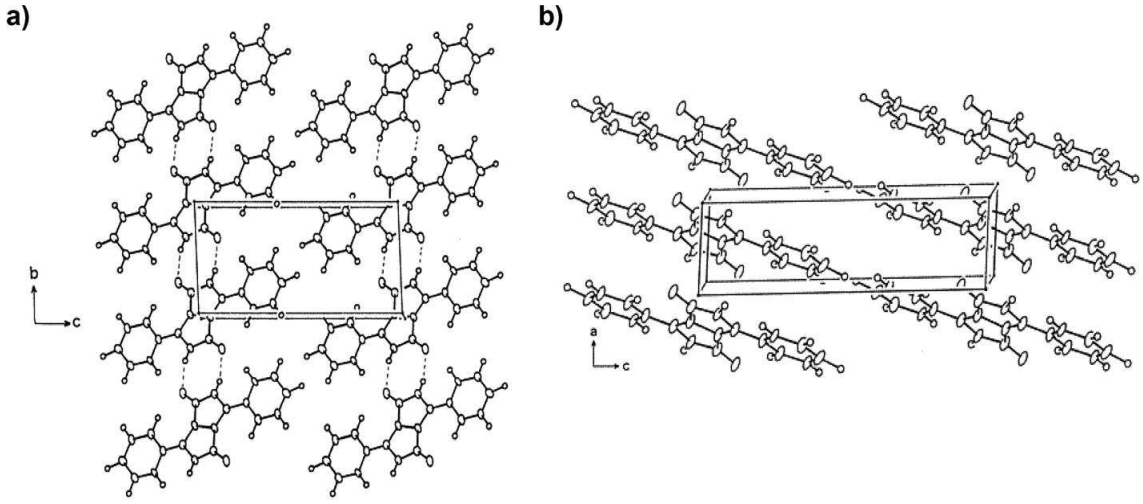

Figure 13. *Crystal structure projection of* ***DPP*** *a) onto the plane (b,c), b) onto the (a,c) plane.*

This same structural behavior is seen in other H-bonded pigments, such as indigo,[87,88] perylene bisimides,[89] quinacridone[90,91] or epindolidione,[90] yet the H-bonding distances were found to be shorter in **DPP**.[92] Even though many authors have claimed that amine and carbonyl groups should be avoided in the molecular structures of semiconductors due to a possible disruption of the conjugation,[93] it has been demonstrated that maximizing the charge transfer integrals through neighboring molecules can enhance the mobility.[92] In this sense, crystal engineering through H-bonding has been one of the main strategies applied in device fabrication.

Early investigations by Mizuguchi[94–101] in the late 80's and early 90's show the crystal and electronic structures of several small H-bonded **DPP** molecules, starting from 1,4-diketo-3,6-diphenyl-pyrrolo-[4,4-c]-pyrrole[94–96] and extending it to the dithioketo,[102] pyridine-containing[103,104] and halogenated analogues.[97] These studies conclude that the intermolecular NH···O H-bonds result in a bathochromic shift in the absorption maxima upon crystallization with respect to solutions (Figure 14), and that the spectral shape in solid state differs substantially from the one in solution mainly depending on the extent of the molecular overlap along the stacking axis.

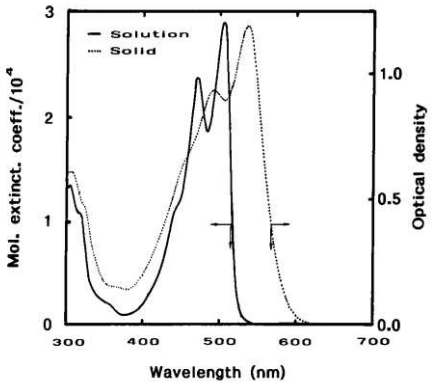

Figure 14: *Absorption spectra of* ***DPP-Ph*** *in dimethyl sulfoxide (DMSO) solution and on evaporated thin film.*

When the molecular overlap is insignificant, the solid state and solution absorption spectra are quite similar and when the molecular overlap increases along the stacking axis, the absorption maximum shows a hypsochromic shift, making the color more yellow.
The authors found that the "head-to-tail" arrangement caused by H-bonding results in bathochromic shifts, while the stack pair or parallel arrangement results in hypsochromic shifts.[84] This correlation between the crystal and electronic structures in **DPP** derivatives can be explained by the exciton coupling model based on the interaction between transition dipoles[105] The same model explains the famous bright red color "Ferrari red" pigment (***p*-ClDPP**) by the formation of the "head-to-tail" arrangement thanks to H-bonding. On the contrary, *m*-substituted derivatives present a yellowish color in (hypsochromic shift) because they stack in pairs that overpower the H-bonding. These initial findings led to study different applications, such as H_2 gas sensors,[104] information storage[98] and photoconductivity.[100]

Still until very recently the supramolecular ordering of H-bonded **DPP** pigments have continued to be studied. Perepichka *et al*,[106] combined scanning tunneling microscopy (STM) and X-ray crystallographic and analyzed how the interactions of heteroatoms in the aromatic substituents of the **DPP** core interplay with H-bonding and how it influences the charge transport properties. The authors studied the supramolecular order of H-bonded difuran, dithiophene and diphenyl **DPP** derivatives in monolayers at the solid-liquid interface and in bulk crystalline solids. This study demonstrated that even though H-bonding is the main and strongest interaction in the

supramolecular assemblies of the **DPP** derivatives described, their structures change radically depending on the nature of the aromatic substituents (furan, phenyl or thiophene). The diphenyl derivative was found to form exclusively H-bonded homoassemblies; the difuran **DPP** preferentially co-assembles with alkanoic acids (used to create the solid-liquid interface), and the dithiophene substituted **DPP** either co-assembles with alkanoic acids or self-assembles in one of two H-bonded polymorphs depending on the conditions.

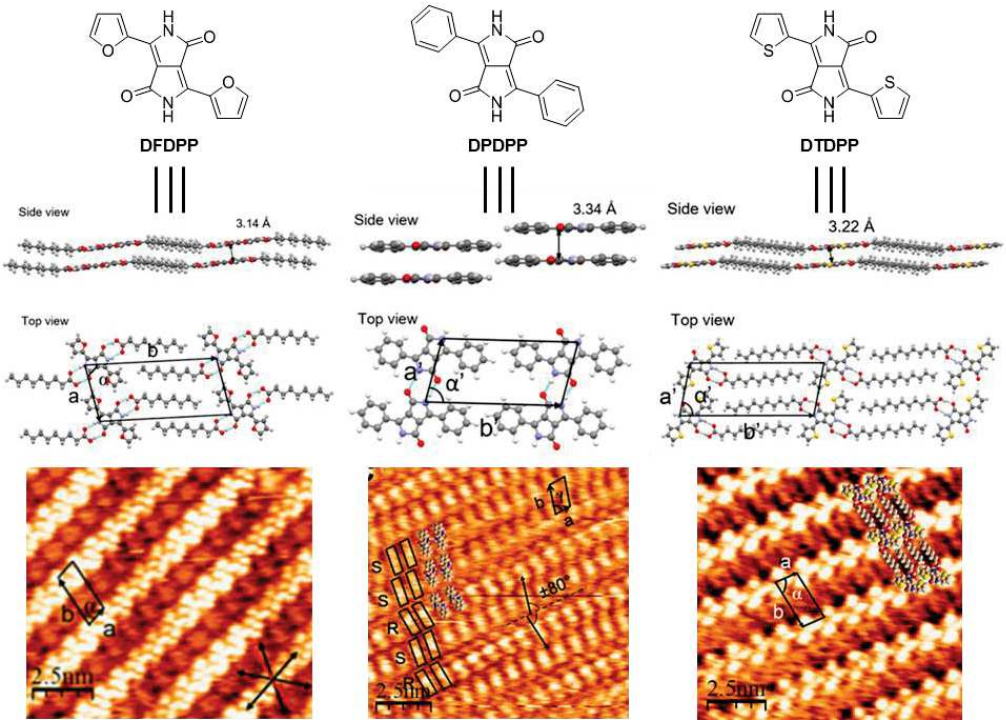

Figure 15: *Chemical structure of **DPP** molecules with several aromatics groups with modelisation and STM images of their self-assembly in monolayer solid-liquid interface.*

Remarkably, one of these two polymorphs shows an out-of-plane (in graphite) twist of the thiophene rings that provides for stronger intermolecular interactions and higher molecular density. This was the first case reported of a planar molecule reorganizing into a less favorable twisted geometry and it could help for example in OFET applications, where the interfacial layer plays a crucial role in the device properties.

b. Vacuum deposited thin films and the use of the latent pigment strategy

In 1997, Iqbal *et* al[107] solubilized **DPP** derivatives by introducing *t*-Boc (*tert*-butoxycarbonyl) protecting groups. The resulting “latent pigments” returns the final dye after thermal cleavage of the *t*-Boc groups, which decomposes into isobutene and CO_2 at approximately 180 ºC (Figure 16).

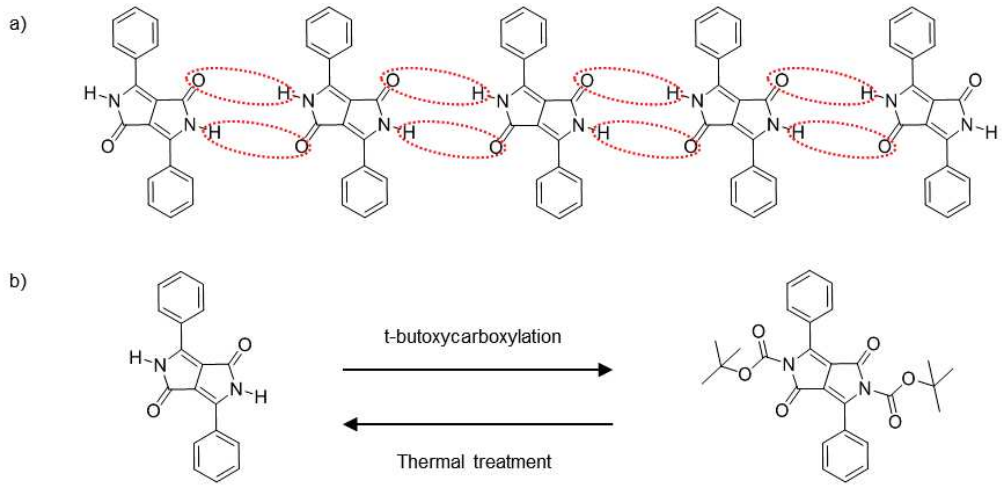

Figure 16: *a) Schematic illustration of the H-bonding network of* ***DPP****. b) Insoluble parent* ***DPP*** *pigment and soluble latent pigment.*

Later, this technique has been widely used for the fabrication of thin films cast from solution because it is easier and cheaper than vacuum deposition techniques, even though several parameters such as removal rate, the nucleation and growth mechanism of the thermally converted derivatives and the role of the volatilized molecules needed to be explored. Several studies report the influence of the solubilizing group removal on the morphology and properties of H-bonded **DPPs**. For instance, Salammal *et al*[108] studied the role of the solubilizing group removal rate on the grain size and crystallinity of **DPP-4T** (Figure 17).

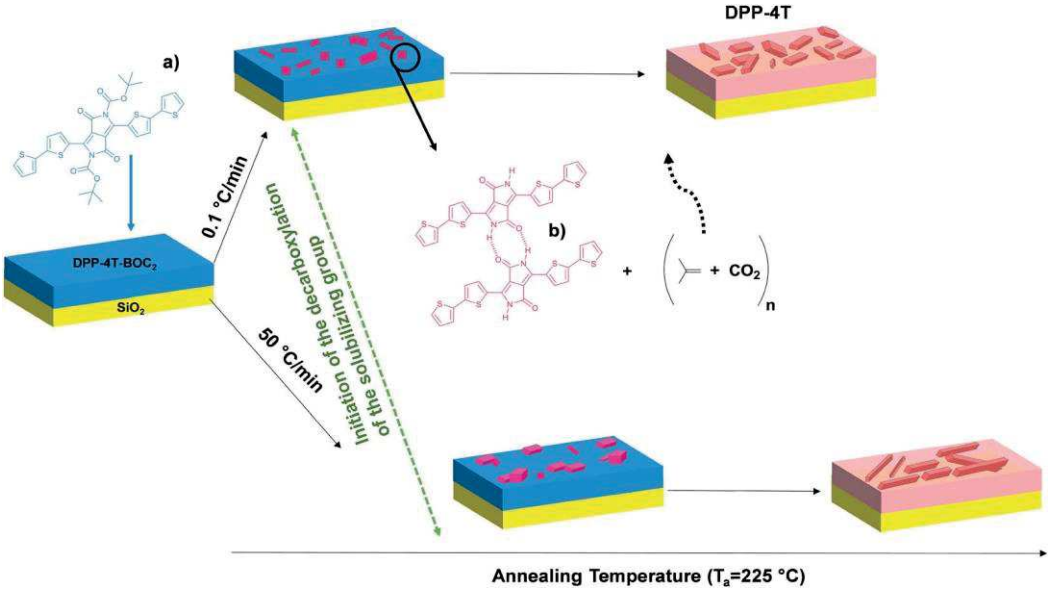

Figure 17: *Schematic representation of the heating rate impact on morphology and final grain size.*

The authors studied the use of different heating rates ranging from 0.1 to 50 ºC/min until reaching 225 ºC. They also investigated isothermal decarboxylation of the **DPP-4T** precursor at different temperatures (Figure 18). The increase of heating rate increased the crystallite size from 344 to 976 nm when the precursor film was heated up to 225 ºC, while improving the crystallinity as well. This result could be explained due the formation of H-bonding between decarboxylated molecules during the removal process. If the heating rate is too low, the *t*-Boc groups not cleaved can hinder the formation of H-bonds (N-H···O) with neighboring molecules, decreasing the crystallite size and crystallinity due to the disruption in growth in one dimension and trapping of *t*-Boc in the network. On the other hand, when the heating rate increases, the volatilized isobutene and CO_2 can escape easily from the network. The growth of crystallites is therefore facilitated by the simultaneous decarboxylation of both *t*-Boc groups that results in the formation of H-bonds. The same thing is observed for the isothermal decarboxylation study when the **DPP-4T** precursor are heated at high temperatures

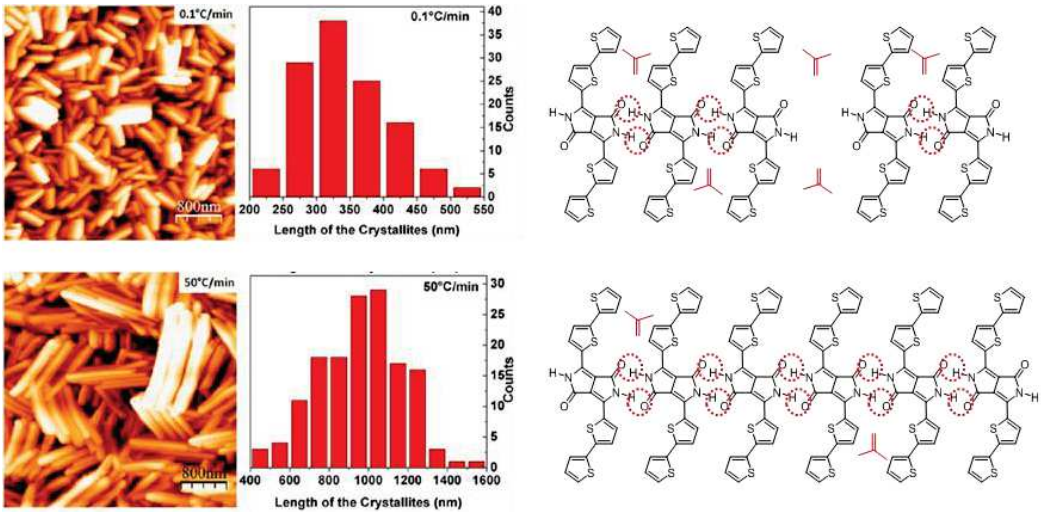

Figure 18: *Schematic representation of the heating rate impact on morphology and final grain size.*

One of the first examples of electronic devices using thermal removal of solubilizing groups was reported by Sakai *et al* in 2008.[91] They used phenyl substituted **DPP** *t*-Boc-protected. This latent pigment is soluble in common organic solvents. OFETs were fabricated by spin coating the latent pigment and by thermally annealing at 180 ºC-200 ºC for 15 minutes to deprotect **DPP** and form H-bonds. The mobility values obtained are in the order of 10^{-6} cm^2 V^{-1} s^{-1}, similar (10^{-5} cm^2 V^{-1} s^{-1}) to the ones obtained by vacuum depositing the same material. The morphology is different when films were spin coated and the H-bonds were thermally regenerated, and when the H-bonded pigments were vacuum deposited. In the first case, the films studied by scanning electron microscopy (SEM) showed a rough and uneven surface with needle-like structures. In the second case, the surface was smooth. The authors demonstrated the simplicity of the preparation method but later, Yamashita *et al*[109]

reported that the mobility values in the work of Sakai could be due to the production of CO_2 and isobutene released during the thermal annealing process, which negatively impacted the morphology of the spin coated film. Yamashita applied the same strategy to larger **DPP** derivatives (Figure 19) for the fabrication of OFETs. His study was the first one finding ambipolar behavior using H-bonded **DPP** molecules and processing the devices from solution.

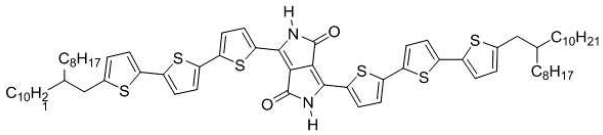

NH BTTDPP 1

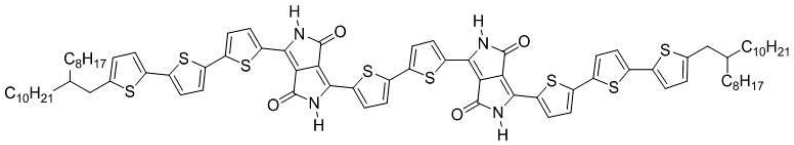

NH BTTDPP 2

Figure 19: *a) Molecular structures of* ***NH BTTDPP1*** *and* ***NH BTTDPP2****.*

With these compounds, OFETs showed ambipolar charge-carrier transfer with field effect mobility values of μ_h of 6.7 x 10^{-3} cm^2 V^{-1} s^{-1} and μ_e of 5.6 x 10^{-3} cm^2 V^{-1} s^{-1}. The optical properties of **NH BTTDPP1** and **NH BTTDPP2** change dramatically. Spectra of solution samples of both compounds initially *Boc*-protected (Figure 20a and 20b, red curves) were compared to spectra of spin coated samples before (blue traces) and after thermal annealing (red traces). A bathochromic shift of 80 nm is observed in the absorption onset of **NH BTTDPP1**, while in **NH BTTDPP2** the absorption onset red-shifts more than 200 nm.

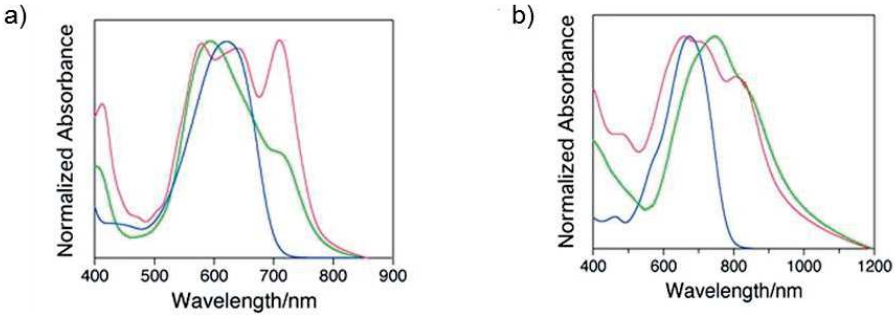

Figure 20: *a) UV-Vis spectra of* ***Boc-protected NH BTTDPP1*** *in solution (blue trace), thin film (green trace), and* ***NH BTTDPP1 after removal of Boc*** *(red trace). b) UV-Vis spectra of* ***Boc-protected NH BTTDPP2*** *in solution (blue trace), thin film (green trace), and* ***NH BTTDPP2 after removal of Boc*** *(red trace).*

For both compounds, a shoulder band at lower energy appears, that dramatically increases after thermal treatment and that is related to the formation of H-bonds. The authors confirm by infrared (IR) measurements the appearance of H-bonds on the thermally treated films. OFET devices were fabricated and field-effect mobility values were measured in devices made with the latent pigments and with H-bonded films. In the first case, hole mobility values in the order of 10^{-6} and 10^{-5} cm^2 V^{-1} s^{-1} were found (similar to the studies of Sakai years before) and that were enhanced by two orders of magnitude after thermal cleavage of the *t*-Boc groups. Interestingly, derivative **NH BTTDPP2** containing two **DPP** moieties in the structure, exhibited well-balanced hole and electron mobilities in the order of 10^{-3} cm^2 V^{-1} s^{-1}. Previously, this group reported a H-bonded **DPP** system containing electron withdrawing $–CF_3$ groups in *p*-position used as n-channel semiconductors with electron mobility values of 2.9×10^{-2} cm^2 V^{-1} s^{-1}.[110] However in this case, the devices were fabricated by vacuum deposition directly from the H-bonded pigment.

Other reports using vacuum deposition techniques of H-bonded **DPPs** present archetypical derivatives (Figure 21a) containing in this case halogen (-Cl and –Br) substituents in the *p*- position of the phenyl rings that decorate the **DPP** core.[92] In this work, the results are complemented with density functional theoretical (DFT) calculations to better understand the charge transport studies. The authors used anodically-grown AlO_x passivated with tetratetracontane ($C_{44}H_{90}$) as a composite low surface-energy dielectric to fabricate OFET devices because they found out in previous works on indigo dyes that low surface-energy dielectrics were crucial to enhance high mobility in H-bonded small molecule devices.[111] The final mobility values were enhanced several orders of magnitude with respect to the initial report by Sakai *et al*,[91] who used phenyl-substituted **DPP** as well. Furthermore, ambipolar behavior was reported for the three hydrogen-bonded **DPP** derivatives shown, being $\mu_h = \mu_e = 0.01$ cm^2 V^{-1} s^{-1} for **DPP-Ph**, μ_h of 0.03 and μ_e of 0.01 for the ***p*-Cl DPP** and μ_h of 0.06 and μ_e of 0.02 for ***p*-Br DPP**. The crystalline structures obtained are very important to understand the differences in mobility values. While in the phenyl derivative, the H-bonded chains are parallel to one another (Figure 21b) and parallel to the plane, which was the same for the *p*-halogenated **DPPs** but the chains were staggered relative to each other making two linear H-bonded chains run along the [001] plane, and other two chains run along the [002] plane, with a tilt with respect to the first chain (Figure 21c).

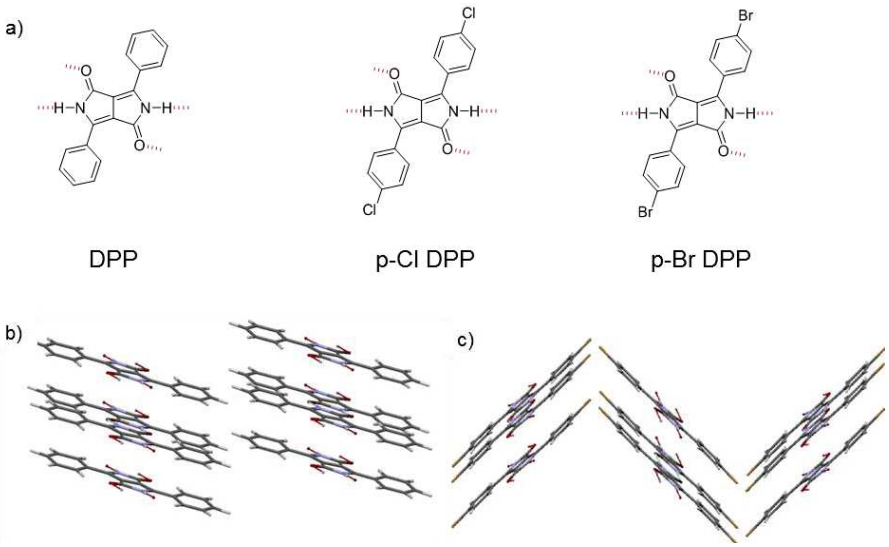

Figure 21: *Molecular structures of a)* ***DPP, p-Cl DPP*** *and* ***p-Br DPP****, b) Crystal structure of* ***PhDPP*** *and c) Crystal structure of* ***p-Cl DPP****.*[92]

The crystal structures were described as pseudo brick-wall π-π stacking. While no discrepancies in charge transport were expected for the three derivatives described, a difference in crystallite size was found. **DPP-Ph** formed crystal grains between 100-200 nm with clearly defined boundaries, ***p*-Cl DPP** had similar crystallites but oblong in shape, and ***p*-Br DPP** had smaller grains making very smooth films and more continuous. The higher mobility values found for ***p*-Br DPP** might be explained according to this morphology.

To demonstrate the strength of this strategy, more sophisticated oligomers have been reported recently, as for example the work of Zhu *et al.*[112] where two **DPP** oligomers with different number of phenyl and thiophene rings were attached to the central **DPP** core, which was functionalized with thermo-labile groups based on 2-methylhexyl-2-oxylcarbonyl. In this case, field effect behavior was only found for the derivative containing thiophene rings (HTBT), including its latent pigment. Other examples as the work of Mula *et al.*[113] showing thiophene-capped **DPP** coupled to triazatruxene (TAT) derivatives (Figure 22) with μ_h of 4.2 x 10^{-4} cm^2 V^{-1} s^{-1}. Interestingly, the charge transport properties were unaffected when blends of **NH-TATDPP** and phenyl [6,6]-Phenyl C_{71} butyric acid methyl ester ($PC_{71}BM$) were studied, emphasizing the robustness of the morphology when **NH-TATDPP** was used as donor material.

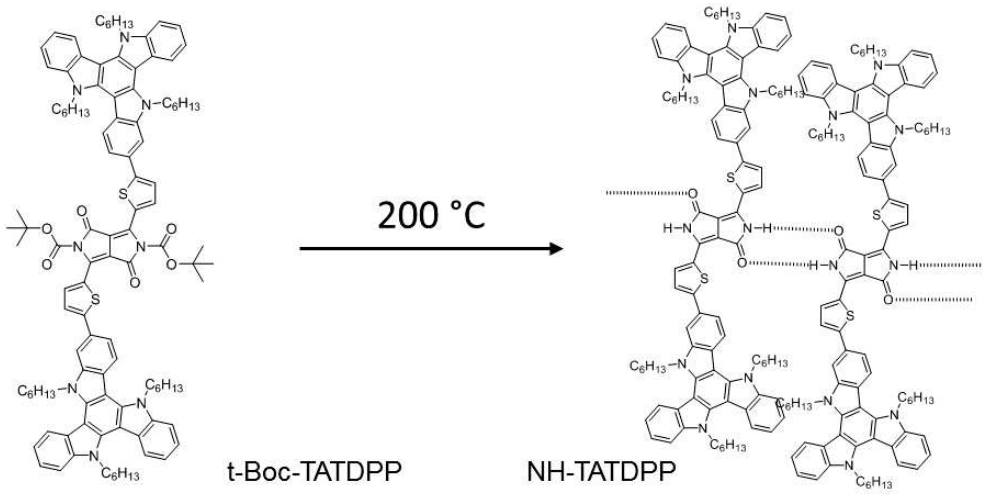

Figure 22: *Synthesis of compound* ***NH-TATDPP****.*

The use of thermocleavable side chains has been applied in semiconductors containing longer solubilizing chains, especially when using polymers. Sun *et al*[114] reported a **DPP**-based polymer containing 2-octyldodecanoyl side chains that can be thermally removed at 200 °C to generate a side chain-free conjugated polymer. X-ray diffraction (XRD) measurements and atomic force microscopy (AFM) images show the thin film progress upon thermal decomposition of the side chains. The as-spun films showed a diffraction peak at 2Θ of 4.40°, which corresponds to a *d*-spacing of 20.1 Å and that was attributed to the inter-lamellar distance. Upon raising the temperature, this peak of the thin film became more intense as a result of the improved molecular ordering by thermal annealing. When reaching 200 °C for 3 hours, this peak disappeared as a result of the total elimination of the side chains, which resulted in the shortening of the interlayer distance. AFM images showed that at 150 °C the films were quite smooth, while at 200 °C for 3 hours, the nanograins initially formed evolved into connected nanofibers with higher roughness and large gaps between domains. The hole mobility values when annealing at 150 °C (μ_h = 0.096 $cm^2 V^{-1} s^{-1}$) were one order of magnitude lower than the mobility of the polymer with solubilizing alkyl chains previously reported.[115] Still at 200 °C, the mobility values (μ_h = 0.078 $cm^2 V^{-1} s^{-1}$) were lower than at 150 °C. The authors concluded that the amorphous nature of the decarboxylated polymer needs to be taken into account.

Other **DPP** polymers with thermocleavable groups can be found in literature. Lee *et al*[116] for example, reported inversion of the dominant polarity in H-bonded **DPP** derivatives upon thermal treatment using low bandgap polymers (**Boc-PTDPP**, figure 23).

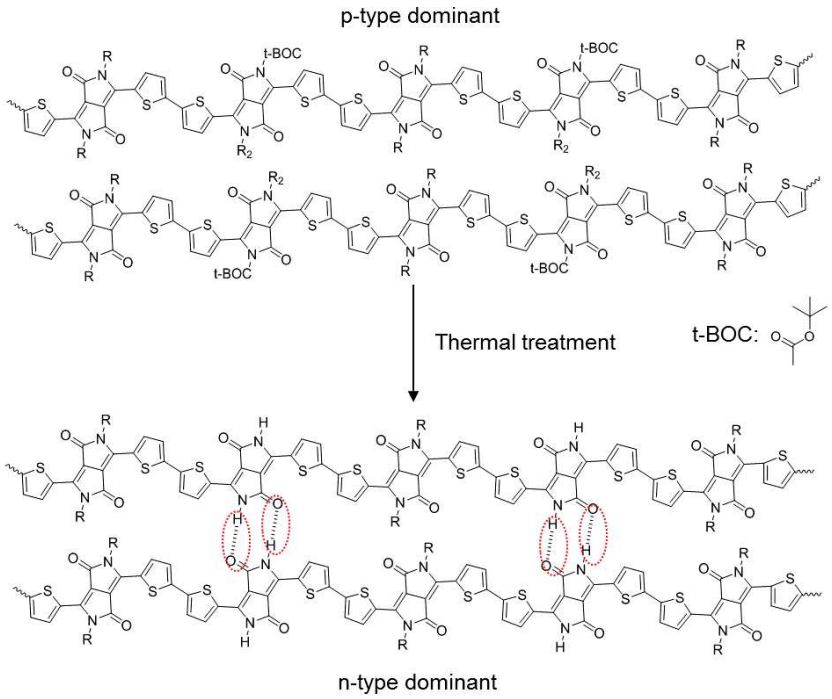

Figure 23: *Thermocleavable polymer based on* ***DPP.***

In this work, OFET devices were fabricated applying a solution-sheared deposition technique, where a volume of the H-bonded **DPP** was placed between two preheated silicon wafers that move relative to each other at a specific rate (Figure 24).

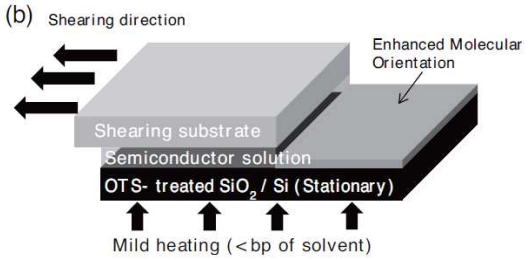

Figure 24: *Schematic illustration of the solution-shearing technique.*

This way, the semiconductor molecules can form highly crystalline and elongated grains along the shearing direction. The authors compared drop cast and solution-sheared films using IR spectroscopy before and after thermal annealing. The C=O stretching signal of the carbamate disappears after thermal treatment with a concomitant appearance of the N-H band as a consequence of the carbamate deprotection. As an indication of H-bonds, the $\nu_{C=O}$ (**DPP** amide) shifted to lower energies. Remarkably, the solution-sheared films showed further shift of the $\nu_{C=O}$ (amide) compared to the drop cast films, probably due to stronger H-bonding in the solid state in these types of films. The ambipolar **Boc-PTDPP** was integrated into transistors and showed p-channel dominant characteristics, resulting in μ_h and μ_e of 1.32 x 10^{-2} cm^2 V^{-1} s^{-1} and 2.3 x 10^{-3} cm^2 V^{-1} s^{-1}, respectively. These values are one order of magnitude higher than the values found in devices made by drop-casting the polymer. After decarboxylation at 200 ºC the dominant polarity of charge carriers

changed from positive to negative in devices fabricated by solution-shearing, reaching μ_e of 4.6 x 10^{-2} cm^2 V^{-1} s^{-1} and decreasing μ_h in one order of magnitude. DFT studies suggest that the LUMO orbitals of the deprotected polymer become much more delocalized than the protected polymer, which is favorable for *n*-channel conduction. Furthermore, the downshift of the HOMO-LUMO levels after thermal treatment could decrease the injection barrier for holes. The authors also suggest that the removal of *t*-Boc groups could act as electron traps and facilitate electron transport.

Even though most of the examples report the fabrication of OFET devices, some reports can be found on the fabrication of bulk heterojunction solar cells (BHJSCs). Brovelli *et al*.[117] used this strategy to optimize the charge separation efficiency at the donor/acceptor interface in an attempt to form interpenetrated phase separated percolation pathways. Proof-of-principle devices consisted of 100 nm blends of *t*-Boc protected **DPP-Ph** and **PCBM** and their performance was followed at different thermal treatment times. While the open circuit voltage (V_{OC}) showed no dependence on increasing the thermal treatment time from 0 to 300 s, the short circuit current (J_{SC}) showed a 30-fold increase (reaching its maximum at 270 s of treatment time), resulting in a 20-fold enhancement of efficiency with respect to the pristine device. The morphology of the devices was followed by AFM and XRD during the thermal treatment. In the initial state, the films were uniform with roughness below 1 nm. After 270 s of thermal treatment, the crystallinity increases and 10-20 nm three-dimensional crystalline domains form. The blends could be stored in air under ambient illumination for up to 6 months, without altering the morphological features. It emphasizes the strength of this strategy to stabilize the nanoarchitecture of the blend. Control experiments were carried out using a **DPP** containing alkyl tails (ethylhexyl) and interestingly, the efficiency values were lower emphasizing the effect of the H-bonding strategy.

*c. Mono-alkylated **DPP** derivatives*

The **DPP** with unsubstituted amides lack solubility and should be processed via vacuum deposition or by the latent pigment technology but the mono-alkylated **DPP** derivatives show very interesting properties while combining solubility and ability to form H-bonds. Patil *et al*.[118] reported monohexyl phenyl **DPP** and monohexyl thiophene **DPP** derivatives (PDPP-MH and TDPP-MH, Figure 25a) and studied their properties by single crystal X-ray analysis and correlated the results to the charge transport properties in both, mono and di-alkylated analogues.

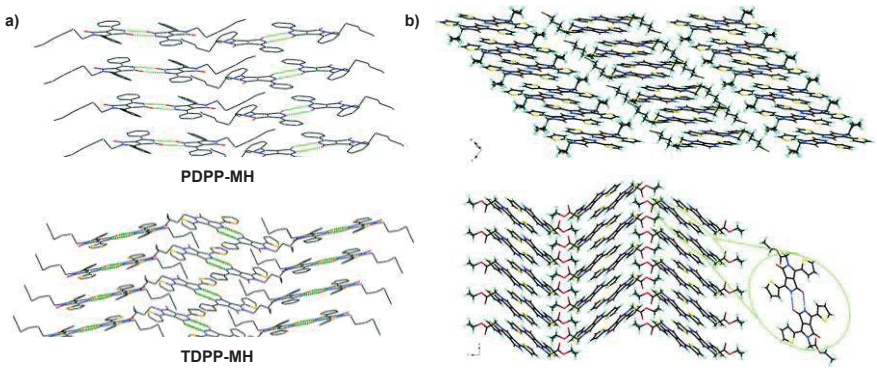

Figure 25: *a) Co-facial packing via H-bonding in* ***PDPP-MH*** *and* ***TDPP-MH****. b) Molecular packing of two of the studied mono-alkylated* ***DPP*** *derivatives, one showing anisotropy of the* π*-stacking along the a axis (top) and another one showing co-facial herringbone arrangement (bottom).*

The di-alkylated analogues show herringbone packing arrangements, but the mono-alkylated derivatives crystallize in a co-facial layered structure thanks to intermolecular H-bonds between the free amide groups. Charge carrier mobility values (p-type) are two orders of magnitude higher for the mono-alkylated derivatives than for the di-alkylated analogues. The authors explain that according to the crystal structures and theoretical calculations, charge transport occurs in two or three directions while it happens in only one direction for the di-alkylated derivatives. Pop and Amabilino showed similar results extending their study to a larger variety of di- and mono-alkylated thiophene-capped **DPPs**.[119] In this case, the authors found out herringbone structures in some of the mono-alkylated **DPP** derivatives. Particularly, the authors found out that the mono-substituted **DPPs** with hexyl and ethyl acetate substituents were less distorted than the other derivatives of the series, causing stronger intermolecular H-bonding that increases the molecular overlap and planarity of the **DPP** cores (Figure 24b). More specifically, the mono-substituted **DPP** with ethyl acetate showed high potential for optimizing the charge transport properties and could be applied in organic electronic devices.

Other examples of mono-alkylated **DPP** derivatives have been reported in literature but most of them have been applied as anion sensors. Indeed, the free amide can bind anions by H-bonding.[120–122]

4. DPP systems with H-bonding groups in different positions: polymers and small molecules

Even though the **DPP** pigment is considered an H-bonded pigment as shown in the previous section, it can only be processed by vacuum deposition or by thermal or acid treatment of a latent pigment. Due to the possibility of functionalization of the **DPP** core, it is possible to introduce different types of H-bonding motifs in soluble derivatives, allowing studying the aggregation in solution as well as device fabrication.

a. Amide-functionalized DPP systems

A common strategy for introducing H-bonds into the molecular structure of **DPP** derivatives is incorporating amide groups at the periphery of the aromatic rings attached to the central **DPP** core. This strategy is usually based on introducing an aldehyde group that can react subsequently with electron-deficient acetamides via Knoevenagel condensation. In this sense, most of the examples found in literature are based on linear molecules, even though some cases of hairpin-shaped **DPP** derivatives are also reported. An example of the latter approach was reported by Stupp *et al*,[123] where solar cells made with a H-bonded small molecule containing *trans*-1,2-diamidocyclohexane and two **DPP** conjugated arms (Figure 26) were fabricated, being the hairpin derivative **DPPHP** the donor material, and **$PC_{71}BM$** the acceptor.

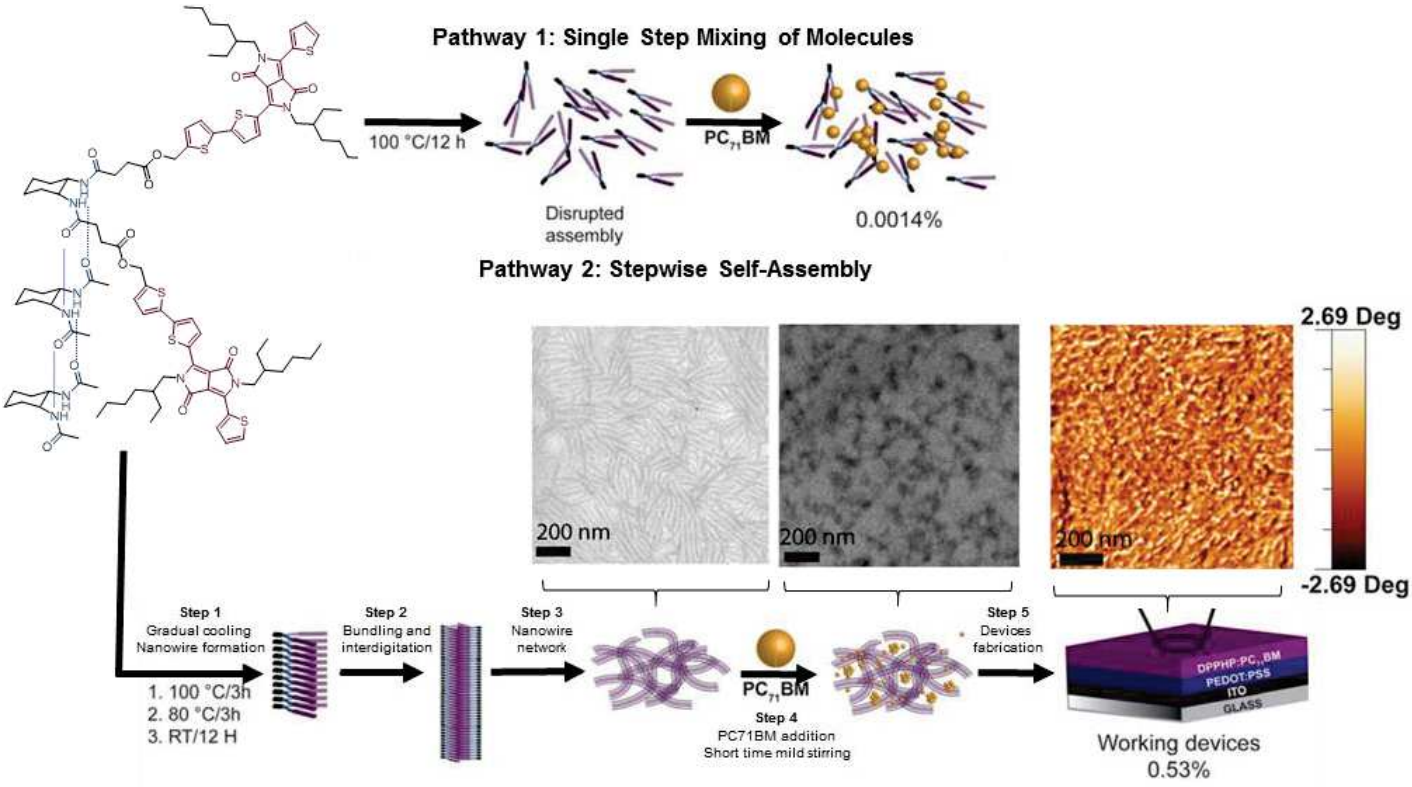

Figure 26: *Schematic representation of the preparation pathways used for device fabrication. Pathway 1 (top) shows the single step self-assembly of* ***DPPPHP*** *and* ***$PC_{71}BM$****. Route 2 (bottom) shows the stepwise self-assembly of* ***DPPHP*** *prior to the addition of* ***$PC_{71}BM$****. Cryo-TEM image of a* ***DPPHP*** *solution in toluene prepared following the stepwise self-assembly pathway. [****DPPHP****] = 7 mg mL^{-1} (****A****). Cryo-TEM image of a* ***DPPHP*****:*****$PC_{71}BM$*** *blend in a 1 : 1 ratio mixed for 30 seconds. [****DPPHP****] = 7 mg ml^{-1} and [****$PC_{71}BM$****] = 27 mg ml^{-1} (****B****). AFM image of the active layer of a device fabricated by the stepwise self-assembly pathway (****C****).*

The authors found that a stepwise self-assembly process was needed to achieve functional devices (Figure 26). When both components were mixed in solution in an attempt to simultaneously assemble them into organized structures, non-working

devices were found (Figure 26, top). On the other hand, a slow cooling process starting from the molecularly dissolved state of the hairpin-shaped derivative (Figure 26, bottom), yielded robust supramolecular wires that were not disrupted when **$PC_{71}BM$** was added, resulting in well-defined heterostructures with improved efficiency.

The self-assembly processes were followed by cryogenic transmission electron microscopy (cryo-TEM) and AFM, observing the presence of nanofibers in solution that were still present after the addition of **$PC_{71}BM$** and visible on the solar cell active layer (Figure 12A, B and C). Despite their proof-of-concept, Stupp *et al*.[124] obtained too low efficiency for the solar cell. Therefore, the same group proposed the use of linear H-bonded **DPPs** (A-Amide) containing terminal amide groups (Figure 27) for the fabrication of BHJSCs. In this case, symmetric and asymmetric H-bonded **DPP** derivatives were studied, finding that the asymmetric derivatives showed improved solubility and more efficient devices. The authors synthesized control molecules containing ester functional groups instead of amides (A-Ester). Both, **A-Amide** and **A-Ester**, showed very similar optoelectronic properties but different morphologies on thin film. While **A-Ester** active layers revealed greater crystallinity and π-π stacking analyzed by grazing incidence X-ray diffraction (GIXD), the active layers of devices made with **A-Amide** presented short fiber-like supramolecular aggregates with much smaller domain sizes and less ordered than the **A-Ester** active layers.

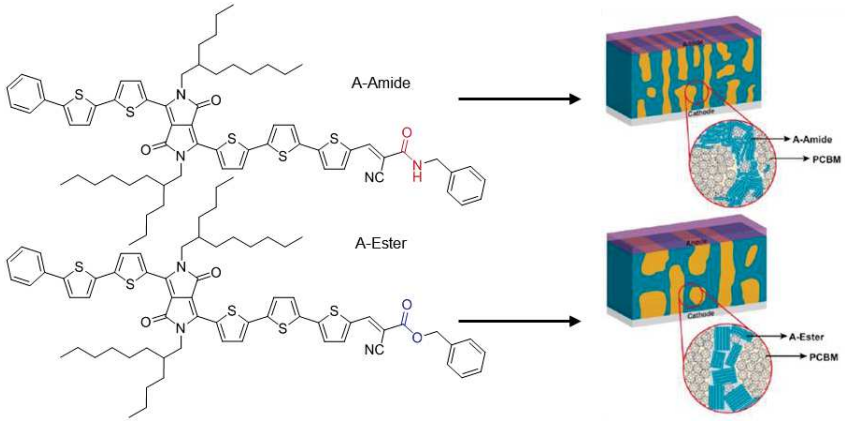

Figure 27: *Structures of **A-Amide** and **A-Ester** and schematic illustration of active layer morphology for **A-Amide** and **A-Ester** devices.*

Interestingly, the devices fabricated in blends with **$PC_{71}BM$** show PCE 50% higher for **A-Amide** than for **A-Ester**. All the results point out that the H-bonds compete with long-range π-π stacking interactions. It results in interconnected and nanoscale smaller donor domains for **A-Amide** *vs* highly crystalline larger domains obtained with **A-Ester**. The first morphology, due to H-bonds, seems to nearly double the device efficiency. The authors showed that with a good compromise between solubility and the formation of the appropriate nanostructures, this strategy of end H-bonding groups could be used to optimize function. Remarkably, other groups reported semiconductors different from **DPP** functionalized with terminal amides. Here, the presence of H-bonding was

detrimental for device performance.[125] However, the devices were prepared with only one solvent and it is possible that poor solubility lower the performance. The terminal amide strategy has been reported by other groups, finding very interesting results and applications. For example, Ghosh *et al*.[126] reported a symmetric **DPP**-based small molecule (**DPP-Amide**) with terminal amide groups (Figure 28a). Figure 28b shows the absorption spectra of **DPP-Amide** in monomeric state in chloroform (as the good solvent, blue curve) and in aggregated state in toluene (purple curve). The spectrum of the aggregates is very different from the spectrum of the monomers, featuring typical bands corresponding to the formation of H- and J-aggregates, a behavior previously observed in other **DPP**[127,128] and H-bonded systems.[129]

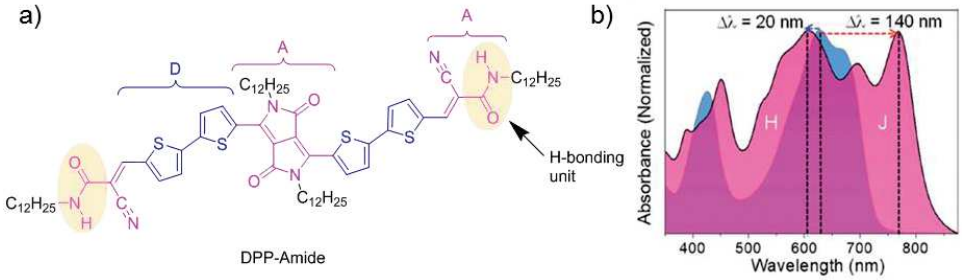

Figure 28: *a) Molecular structure of* ***DPP-Amide****. b) UV-Vis spectra of* ***DPP-Amide*** *in monomeric state and aggregated state.*

A small amount of the self-assembled fibers formed by **DPP-Amide** was incorporated into a polydimtehylsiloxane (PDMS) matrix to fabricate self-standing filter. Thanks to its absorption properties, covering the visible region and being transparent in the NIR region could be employed in anti-counterfeiting, infrared photography and forensic applications. Furthermore, **DPP-Amide** and **$PC_{71}BM$**, were employed to fabricate hybrid gels.[130] These gels afford self-sorted p-n heterojunctions with broad absorption and low bandgap, which was not possible with other hybrid systems especially the ones based on perylene bisimides.[131]

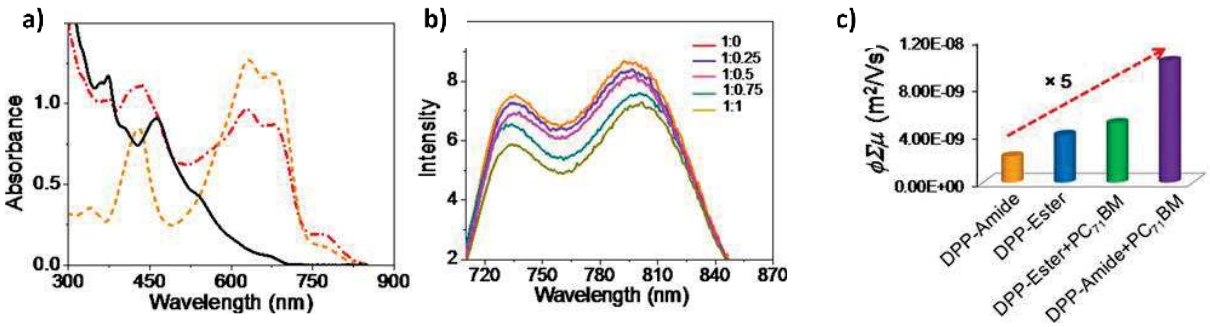

Figure 29*: a) Absorption spectra of* ***DPP-Amide*** *aggregates (orange, dash),* ***$PC_{71}BM$*** *(black, solid) and* ***DPP-Amide*** *:* ***$PC_{71}BM$*** *(1 : 1 wt. ratio) hybrid assembly (red, dash-dot). b) Emission spectra of* ***DPP-Amide*** *in toluene (λ_{ex}=680 nm) with different blend ratio of* ***$PC_{71}BM$****. c) Plot showing increase in photoconductivity of* ***DPP-Amide*** *and* ***DPP-Ester*** *upon addition of* ***$PC_{71}BM$*** *(1 : 1 wt. ratio).*

Further details on these hybrid systems are given in the section dedicated to **DPP** hydrogen-bonded gelators (vide infra). The importance of the self-assembled state by H-bonding was observed by measuring emission quenching upon the addition of **$PC_{71}BM$**. Emission quenching was not detected upon addition of **$PC_{71}BM$** to solutions of **DPP-Amide** or **DPP-Ester** in their molecularly dissolved state (chloroform), indicating the absence of electron transfer processes. The same effect was found in toluene solutions of **DPP-Ester**. In contrast, when different ratios of **$PC_{71}BM$** were added to toluene solutions of **DPP-Amide** (aggregated conditions), attenuation in the emission signal of **DPP-Amide** was observed with increasing weight ratio of **$PC_{71}BM$** (Figure 29b). Such attenuation was not due to ground state charge transfer since the absorption spectrum of the **DPP-Amide**: **$PC_{71}BM$** mixture did not show any additional bands, and was the sum of the spectral features of both components (Figure 29a). These results indicate that the self-assembled structures of **DPP-Amide** are necessary to immobilize **$PC_{71}BM$** aggregates and to facilitate the electron transfer process. Flash-photolysis time resolved microwave conductivity (FP-TRMC) was used to study charge carrier mobility and photovoltaic performance, which can be predicted by plotting transient photoconductivity *vs* different blending ratios of acceptor material. FP-TRMC measurements were performed on assembled (toluene) and disassembled samples (chloroform) of **DPP-Amide** using different ratios of **$PC_{71}BM$**, finding a 5-fold increase in intrinsic conductivity for self-assembled films of **DPP-Amide**:**$PC_{71}BM$** in 1.5:1-1:1.5 ratio (Figure 29c). No enhancement in conductivity was observed in **DPP-Ester**: **$PC_{71}BM$** films.

More recently, the terminal functionalization of **DPP** semiconductors has been used to modulate charge carrier polarity. Ghosh *et al*.,[132] reported three **DPP** derivatives with the same π-conjugated backbone symmetrically functionalized with amide, ester and cyano groups (Figure 30). The authors used FP-TRMC as well to confirm that the n-type charge carrier mobility increased with higher acceptor strength and OFET devices were fabricated to confirm the change of polarity from p- to n-type.

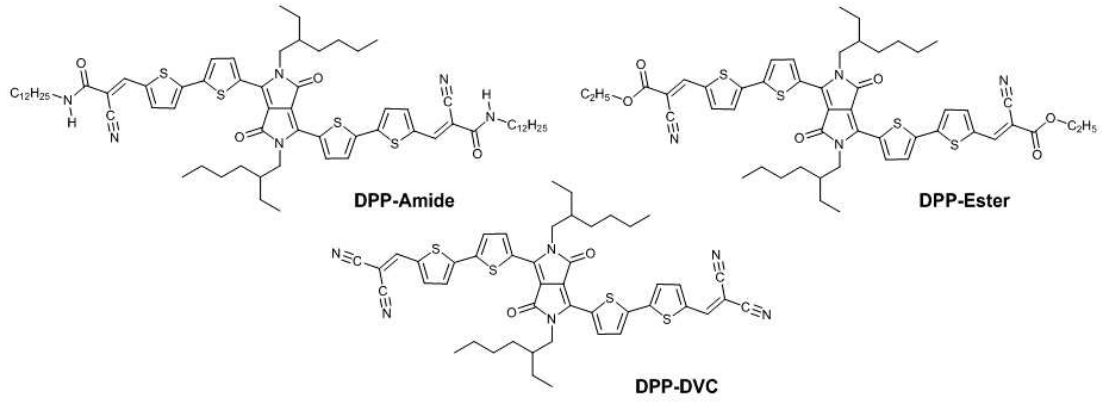

Figure 30: *Structures of the three diphenyl-**DPP** derivatives used to modulate charger carrier polarity.*

The photoconductivity of the three derivatives on thin film was measured, either in their pristine state or mixed with **$PC_{71}BM$**, to analyze the p-type charge mobility. When the amide-functionalized derivative was spin-coated from toluene solutions, the photoconductivity was higher than those casted from chloroform films. This was a clear indication of the importance of the H-bonding formation. Interestingly, in blends with **$PC_{71}BM$** (Figure 31b) the amide-functionalized derivative showed enhanced photoconductivity related to the pristine film. On the other hand, the blends made with the ester-functionalized **DPP** exhibited much lower photoconductivity enhancement with respect to the pristine film and a decrease in photoconductivity in blends made with the dicyano derivative. These results indicate a transition from p-type character of the amide derivative to n-type character in the cyano derivative. Inversely, the three derivatives were blended with poly(3-hexylthiophene) (P3HT) (Figure 31a, b, c, d) to evaluate the n-type character, finding in this case the opposite trend. However, the solvent used in this case was chlorobenzene instead of chloroform, which could yield different supramolecular structures with different electronic properties, especially in the case of the H-bonded derivative. The mobility values, measured in FET devices: μ_h equals 1.3 x 10^{-2} cm^2 V^{-1} s^{-1} for the amide derivative, while μ_e equals 1.5 x 10^{-2} cm^2 V^{-1} s^{-1} for the ester derivative and 1 x 10^{-2} cm^2 V^{-1} s^{-1} for the dicyano **DPP**. With these results the authors offered an alternative strategy to modulate charge transport properties.

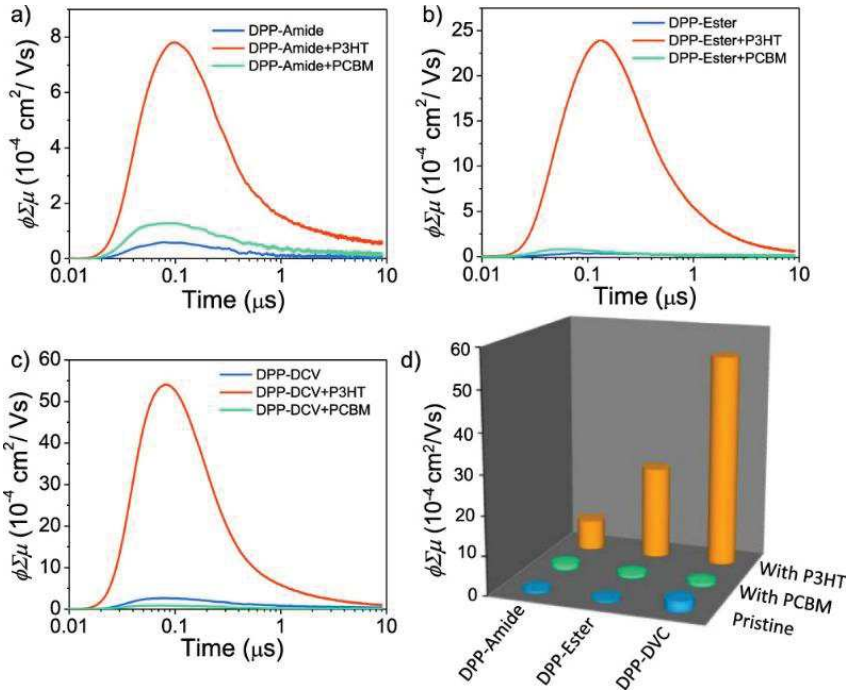

Figure 31: *FP-TRMC transients of a)* ***DPP−amide***, ***DPP− amide:P3HT***, *and* ***DPP−amide:PC71BM***; *b)* ***DPP−ester***, ***DPP− ester:P3HT***, *and* ***DPP−ester:PC71BM***; *and c)* ***DPP−DCV***, ***DPP−DCV:P3HT***, *and* ***DPP−DCV:PC71BM***. *d) Comparison of ϕΣμ values of all the* ***DPP*** *derivatives in the absence and presence of* ***P3HT*** *and* ***PC71BM.***

5. *Complementary H-bonding groups incorporated in DPP derivatives*

Complementary H-bonding between two conjugated species to form heteroaggregates is a great strategy to achieve hierarchical structures, like p-n heterojunctions in the case of semiconductors. In this sense, H-bonding motifs able to form multiple and complementary bonds with other conjugated systems have been incorporated into **DPP** derivatives. Braunschweig *et al*.[133,134] studied systems composed of **DPP** donors with chiral and achiral side chains. These systems can form triple H-bonds with perylene diimide (PDI) acceptors and assemble into superstructures (Figure 32a, b, c).

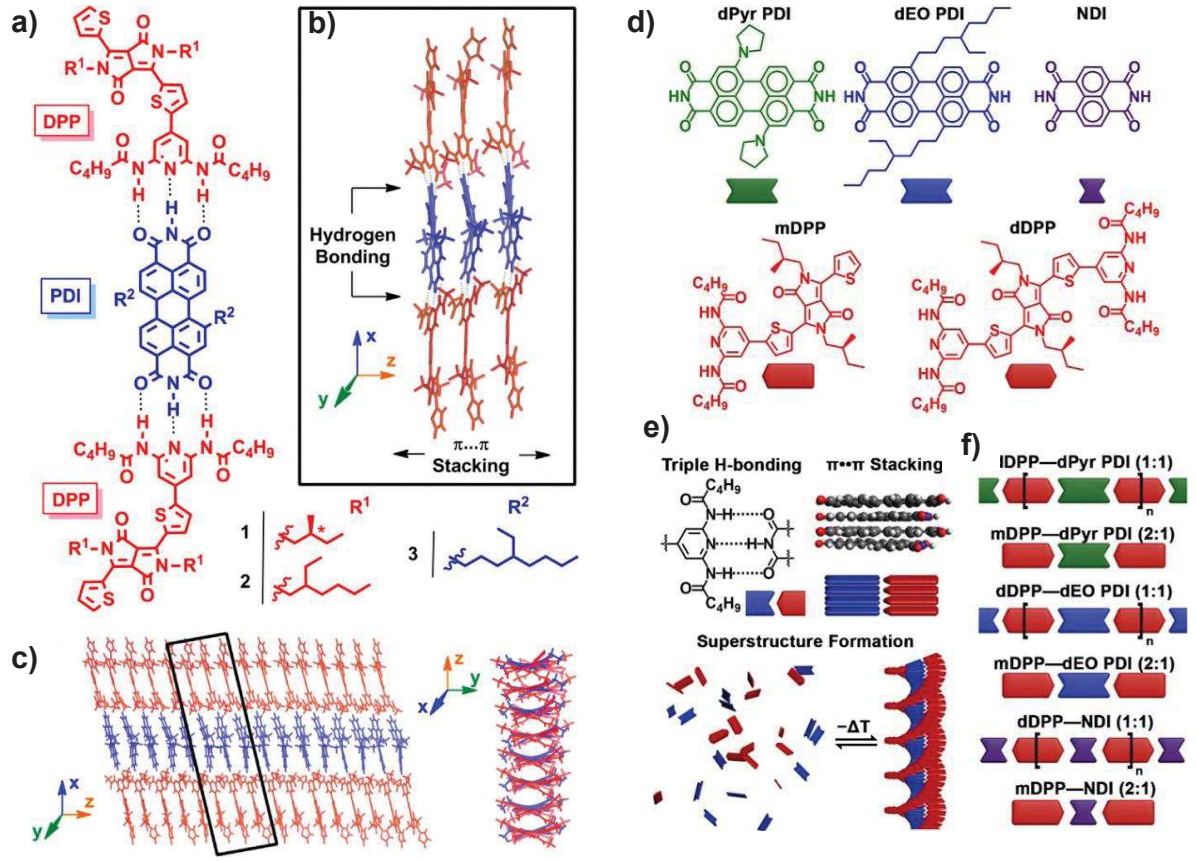

Figure 32: *a)* ***DPP*** *donor (red) and* ***PDI*** *acceptor (blue) molecules 1−3 are capable of* ***b)*** *Heteroaggregation through a combination of H-bonding and π···π stacking, resulting in c) Well-ordered superstructures. d) Library composed of three rylenes and two* ***DPPs****, e) Supramolecular assembly via triple H-bonding and π···π stacking results in* ***DPP****−rylene superstructures, and f) Superstructures vary in the* ***DPP*** *and rylene components and* ***DPP****/rylene stoichiometry.*

When solutions containing both types of molecules are heated and cooled back, achiral **PDIs** bind to disordered **DPP** stacks, which leads to chiral superstructures. Additionally, a model was developed to elucidate the structural cues that induce the transition from a disordered aggregate into a chiral helix. This model allowed the determination of all the thermodynamic parameters. It also establishes that the H-

bonding and the subsequent helix formation are enthalpically favored but entropically disfavored.[133] Recently, this same group has explored six superstructures featuring different geometries, resulting in subtle changes in the solid-state packing of the **DPPs**.[135] They achieved this by combining two **DPPs** and three rylenes (either naphthalene diimides (NDI) or perylene diimides (PDI)) to form six hierarchical superstructures that assemble as a result of orthogonal H-bonding and π···π stacking (Figure 32 d, e, f). The changes in inter-**DPP** stacking that are templated by the neighboring rylenes have a subtle effect on the excited-state dynamics and on the activation of new pathways such as singlet fission (SF). The exclusive benefits of combinatorial supramolecular assembly demonstrated the impact of the structure on advanced light management in the form of SF, affording triplet quantum yields as high as 65% for a correlated pair of triplets and 15% for an uncorrelated pair of triplets.[135] The changes in the molecular structures of the components resulted in various 1D and 2D morphologies, whose long-range order and geometric differences have an influence on the management of light. Further studies of these supramolecular scaffolds will be important to understand the morphology dependence on the photophysics of the supramolecular heterojunctions in order to maximize the junction area to achieve efficient charge separation and transport.[135]

Braunschweig *et al*. have studied how solubilizing side chains, the conjugation length and the type of H-bonding groups affect the homo-assembly of **DPPs** into J-aggregates.[136] These studies were performed by variable temperature (VT) UV-Vis titrations in toluene on multiple thiophene **DPP** derivatives (Figure 33). The presence of diamidopyridine (**DAP**) groups and their ability to form H-bonds improved considerably the driving force of assembly: larger clusters form compared to those without the **DAP** group.

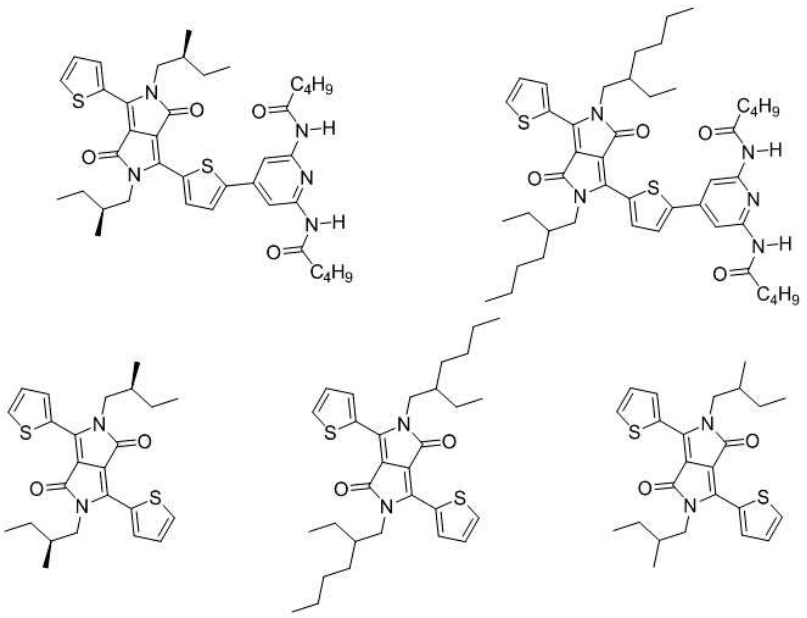

***Figure 33: DPP** derivatives whose aggregation was studied by Braunschweig et al.[137]*

According to their findings, the interplay of π···π stacking, H-bonding, van der Waals forces, solvent, concentration and temperature is responsible for the size, structure, stability and spectroscopic attributes of the resulting superstructures. Moreover, the main discovery in this work was that these molecules assemble into slip-stacked geometries, described as J-aggregates. They also managed to derive two equations for the calculation of the size of aggregated stacks and its average mole fraction.[136] These findings are very important since the structure and properties of supramolecular assemblies are intimately linked, and small changes in the relative orientations of stacks can have great impact on their optoelectronic properties and device performance.[138,139]

6. Other H-bonding motifs present in DPP derivatives

Semicarbazone groups is appended to **DPP** derivatives used as colorimetric chemosensors for fluoride ions.[140] This same group reported another chemosensor for fluoride ions with phenylhydrazone[141] as the H-bonding unit. In these compounds, the H-bonding groups were employed to bind the fluoride ions and the supramolecular structures formed by them were not studied. Reynolds *et al*,[142] have linked **DPP** to triglyme chains (**DPP**$_{amphi}$, Figure 34a) to provide amphiphilic character. It gave solubility and control on the solid state morphology. The self-assembly process of **DPP$_{amphi}$** were studied by UV-Vis spectroscopy (Figure 34c), probing the absorption at different times, the evolution of the absorption bands and the appearance of new bands (750 nm) show the formation of aggregates.

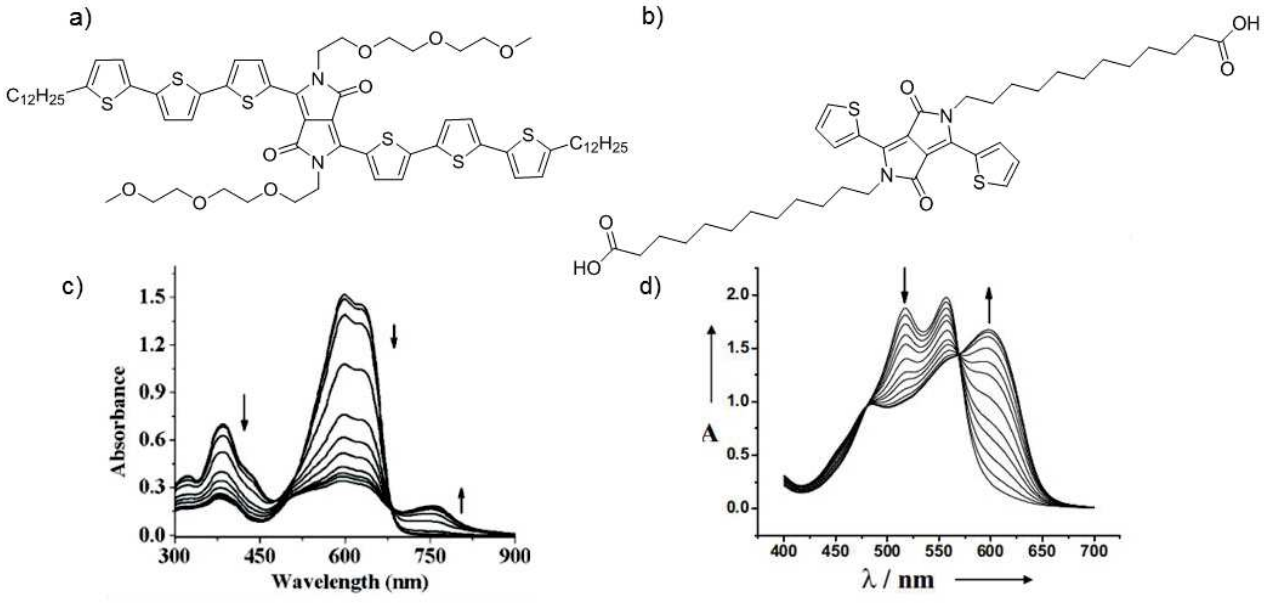

Figure 34: *Molecular structures of a) **DPP$_{amphi}$** and b) **DPP-11a**. Time-dependent absorption spectra of c) **DPP$_{amphi}$** and d) **DPP-11a**.*

The mobility values measured with transistors fabricated with this molecule were not higher than the values reported at the time, but the processing and purification processes were easier due to the solubility. Furthermore, the fill factor (*FF*) values obtained in BHJSCs were higher than the *FF* reported in devices at that time. An example of a bola-amphiphilic **DPP** derivative has also been reported[143] to obtain supramolecular nanofibers by combination of H-bonding and π-π stacking (Figure 34b). Two carboxylic acids were attached to the **DPP** core through a C10 alkyl linker to obtain a bola-amphiphile compound that formed nanofibers in aqueous solution. The self-assembly properties of **DPP-11a** were studied by time dependent UV-Vis spectroscopy in tetrahydrofuran (THF) as a good solvent and water as a bad solvent (Figure 34d). When comparing both molecules, the evolution of the bands and the appearance of aggregate bands (J-aggregate) which are stronger for **DPP-11a** manifest the important role of H-bonds to tune the formation of different morphologies. For **DPP-11a**, THF solutions drop cast on mica showed the formation of nanoparticles, while the aqueous solutions presented the formation of nanofibers.

7. Hydrogen bonds incorporated into DPP-based polymers

H-bonding groups have also been integrated into the structure of semiconducting polymers to enhance charge transport and extend the applications to sensing devices. Zhang *et al*[144] incorporated thymine groups in the side chains of a thiophene-functionalized **DPP** polymer (**PDPP4T-T**) (Figure 35a). Thymine is one of the four nucleobases in DNA and is known to bind Pd(II) and Hg(II).[145] FET devices were fabricated by spin-coating solutions of **DPP4T-T** and controls molecule **PDPP4T-A** (with branched alkyl tails) and **PDPP4T-B** (with branched and linear alkyl tails); the found μ_h values are higher for the polymer containing thymine. This result was accounted by the enhancement of the film crystallinity due to H-bonding. This was demonstrated with grazing incidence wide-angle X-ray scattering (GIWAXS) measurements, which showed improved lamellar stacking than the films made with the control molecules. Furthermore, the FET devices made with the thymine-containing polymer were used as sensors for CO and H_2S. The incorporation of Pd(II) and Hg(II) was achieved through the air-water interface coordination. After the metallic ion coordination, FETs were fabricated and exposed to different gaseous analytes and solvent vapors. The polymer containing Pd(II) could detect CO in concentrations as low as 10 ppb, while devices made with Hg(II) coordinated ions could sense H_2S down to 1 ppb. In this case, the introduction of H-bonding functionalities in semiconducting polymers not only increased the mobility, but also added applications and properties. Urea groups have also been introduced in the pending chains of **DPP** polymers. Zhang *et al*,[146] reported three **DPP**-based polymers containing different ratios of urea groups and branched alkyl chains (Figure 35b). OFETS and BHJSCs were fabricated with these polymers and the control **DPP** polymer without urea units.

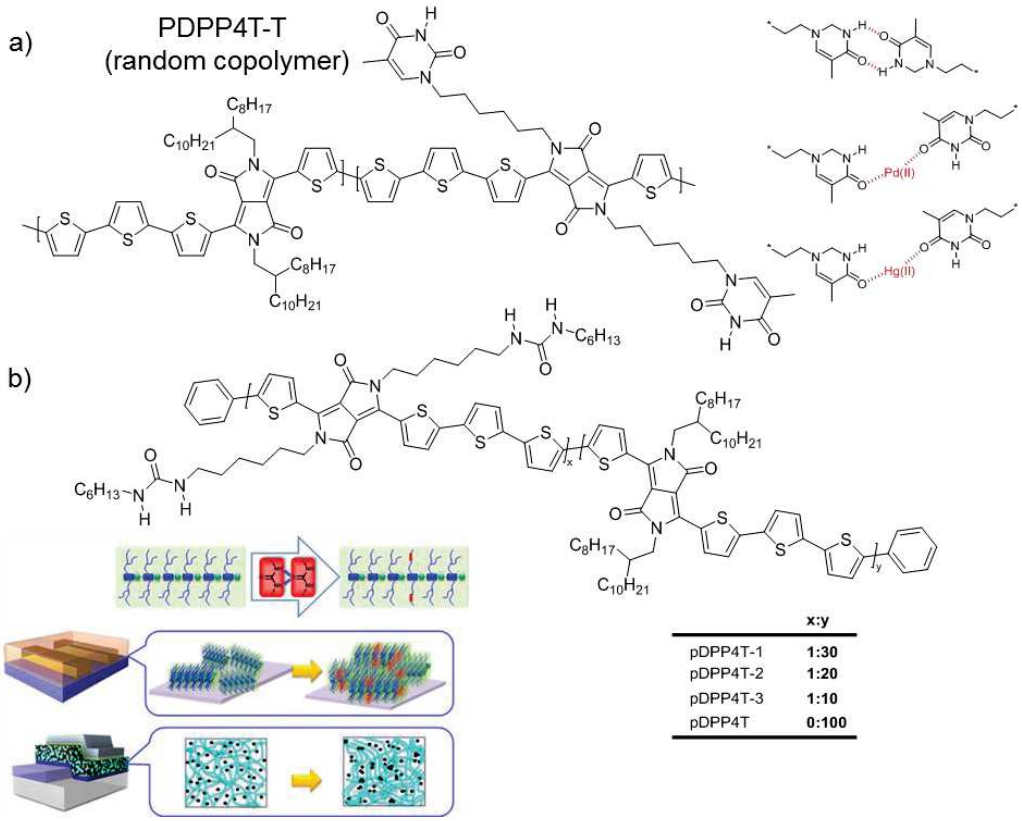

Figure 35: *a) Chemical structure of **PDPP4T-T**; Thymine groups are randomly connected to the conjugated backbone and the illustration of T−T Intermolecular H-bonding and the coordination with Pd(II) and Hg(II). b) Chemical Structures of **pDPP4T-1**, **pDPP4T-2**, **pDPP4T-3**, and **pDPP4T**, and illustration of the design rationale for the incorporation of urea groups in the side chains of conjugated D–A polymers.*

The polymer containing the lowest ratio of urea groups (1:30), showed the highest hole mobility (μ_h = 13.1 cm^2 V^{-1} s^{-1}). The influence of the presence of urea groups in **DPP** polymers was also studied in BHJSCs, finding in this case that the polymer with the highest ratio of urea groups (1:10) presented the best efficiency of all (6.8%), including the control devices made with polymers without urea groups. The high mobility values were attributed to a better lamellar packing order due to H-bonding interactions of the urea groups from the alkyl chains. Regarding the solar cell devices, the presence of urea groups allowed the polymers to self-assembled into nanofibers and direct the ordered aggregation of the acceptor material, resulting in micro-phase separation in the blends were charge separation can be enhanced, compared to the control polymers without urea groups.

The use of H-bonds in **DPP** polymers has also interesting applications in bioelectronics. Du *et al*,[147] reported a **DPP** polymer containing lysine side chains (Figure 36) that promotes neural cell adhesion and growth. This polymer is promising

for applications in bioelectronics because it avoids an additional biological coating step on electrical devices.

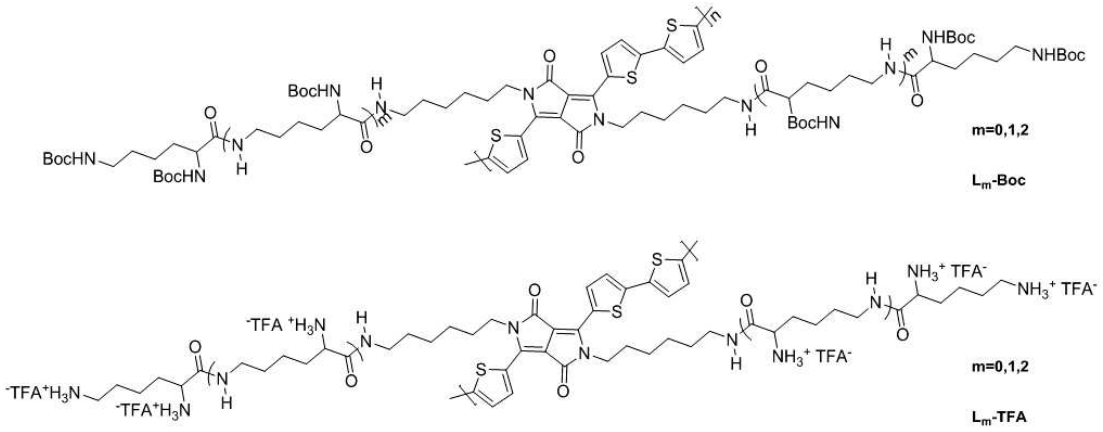

Figure 36: *Chemical structures of* ***DPP*** *polymers containing lysine residues.*

DPP polymers based on **DPP3T** (dithienyl-**DPP**) containing different number of lysine derivatives (Figure 35) were synthesized. However, the H-bonds between lysine resulted in very strong intermolecular aggregation and lack of solubility. The lysine groups were protected with *t*-Boc groups to provide solubility and deprotected subsequently with trifluroacetic acid (TFA) to render protonated lysine units, which increased the surface charge and improved cell adhesion.

IV. Organogels and hydrogels made with hydrogen-bonded DPP derivatives

1. Organogels based on DPP

The preparation of organogels and hydrogels is an attractive strategy for developing complex supramolecular structures. In the recent years, the highly ordered and flexible supramolecular architectures found in gels have been applied in organic electronic devices.[148] Many of these gels are obtained thanks to the presence of noncovalent interactions into the molecular structure of the components. Therefore, the presence of one or multiple H-bonding groups can lead to the formation of gels that in combination with other noncovalent forces, such as π-π stacking result in great flexible semiconducting materials. Among the organo- and hydrogels reported in literature, only a few examples based on H-bonded **DPP** can be found. Thool *et al*.[149] reported in 2016 the ability of small H-bonded **DPP** molecules to form organogels. They designed a **DPP** small molecule containing two phenyl rings at the 3- and 6-positions of the **DPP** core (Figure 37). It can self-assemble by different interactions: Van der Waals interactions with saturated carbon chains, π-π stacking of the aromatic rings and H-bonds groups between peripheral amides. This compounds form gels in different solvents in short times at 0.5 wt % concentration. It was shown by the inverted test tube, no complementary rheology studies were shown. The self-assembly process was followed with UV-Vis spectroscopy and electron microscopy (AFM and HR-TEM).

The thin film and gel spectra show red-shifted absorption band and the presence of J-aggregates originated by H-bonding interactions. Compared with the dilute solutions, the gel spectrum onset presents a red-shift of more than 100 nm. It enlarges the coverage of the solar spectrum. Rod-shaped assemblies with high aspect ratio were found in spin-coated films made with the organogel, which are desirable structures in organic electronics. Organic solar cells were prepared with a conjugated polymer (PTB7)[150] as the donor molecule, **$PC_{71}BM$** as the acceptor and a small amount of the H-bonded **DPP-NCO** derivative as an additive, either in the neat or gel state. Remarkably, the efficiency increases from 6.37% in devices without additive to 7.23% when **DPP-NCO** is added in the neat state, and to 7.85% it is added in the gel state. According to the authors, the enhancement in efficiency is due to the formation of a nanorods network in the blend's active layer that decreases the series resistance and improves the *FF*.

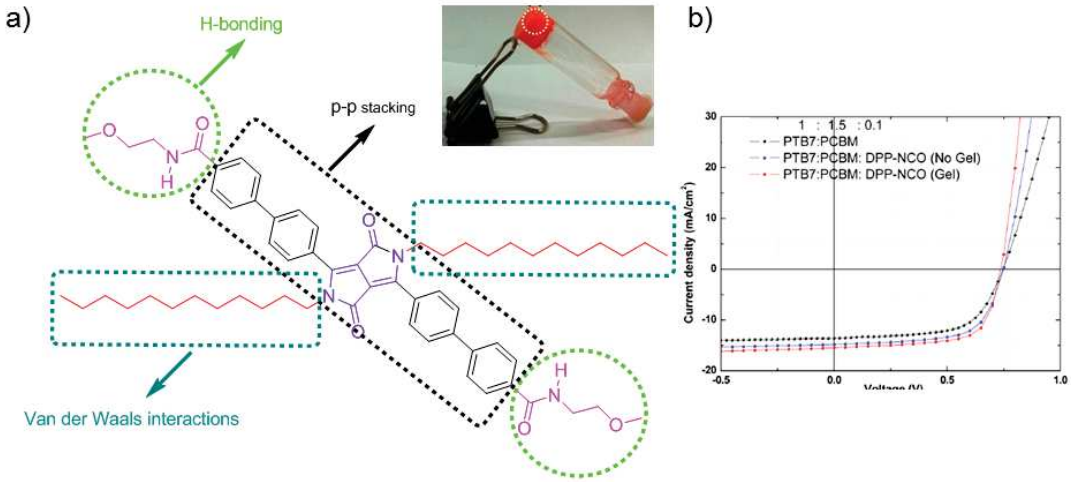

Figure 37: *a) Molecular structure of* ***DPP-NCO****. b) J-V curves of the devices fabricated with* ***PTBT7:$PC_{71}BM$:DPP-NCO*** *in 1:1.5:0.1 ratio.*

Ghosh *et al*.[126] reported a new **DPP**-based small molecule (**DPP-Amide**) with terminal H-bonding groups which formed a black colored gel in toluene (Figure 38).

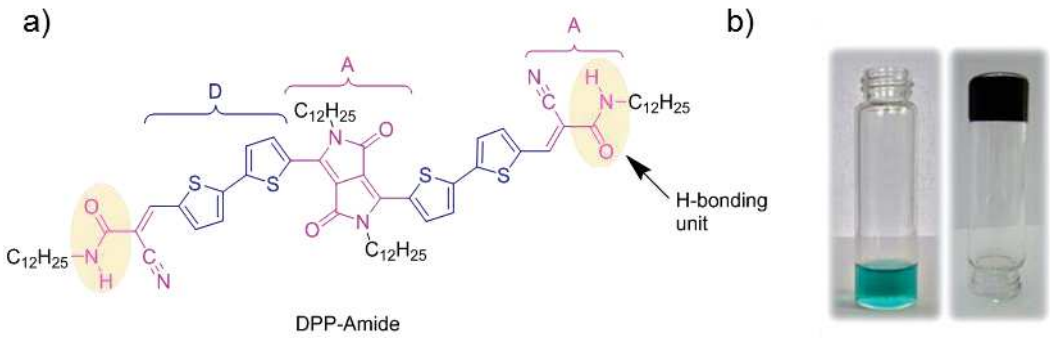

Figure 38: *a) Molecular structure of* ***DPP-Amide****. b) Gel formation of* ***DPP-Amide*** *in toluene.*

The optical properties of **DPP-Amide** in the aggregated state has been described in the previous section. It forms of H- and J-type aggregates, very important for the desired applications. **DPP-Amide** forms gels in toluene at 0.15 wt% concentration. SEM images of the xerogel show a network of nanofibers bundled in large fibers with diameters between 400 and 500 nm.

DPP organogels can combine both H-bonding and polymerizable function. It offer the possibility to stabilize the self-assembly by crosslinks. Rondeu-Gagné *et al*.[151] reported the design of a **DPP** gelator having amide and diacetylene moieties, which could form organogels in several solvents. Three different gelators were synthesized (Figure 39), one containing H-bonding groups (G1), another one having diacetylene moieties to rigidify the network through photopolymerization (G2) and **G3** containing both groups.

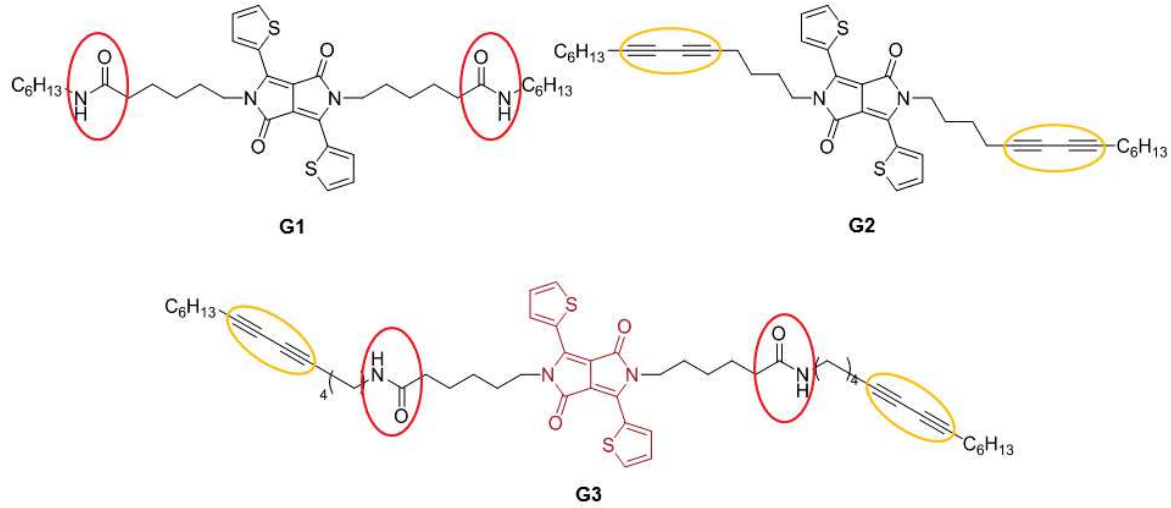

Figure 39: *a) Molecular structures of gelators **G1**, **G2** and **G3**.*

Interestingly, only **G3** containing amide and diacetylene moieties resulted to form robust gels in aromatic solvents. Upon UV irradiation (Figure 40) the xerogel of **G3** underwent a topochemical polymerization to form polydiacetylene, resulting in a crosslinked network maintaining the initial fibrous morphology of the gels made by **G3**. In this case, the authors found out that the H-bond units were critical to obtain the necessary structure for the diyne moieties to polymerize. This strategy is a way to achieve easy and efficient crosslinking without the use of a catalyst or photoinitiators, which is very important for the processing of π-conjugated materials in thin film devices.

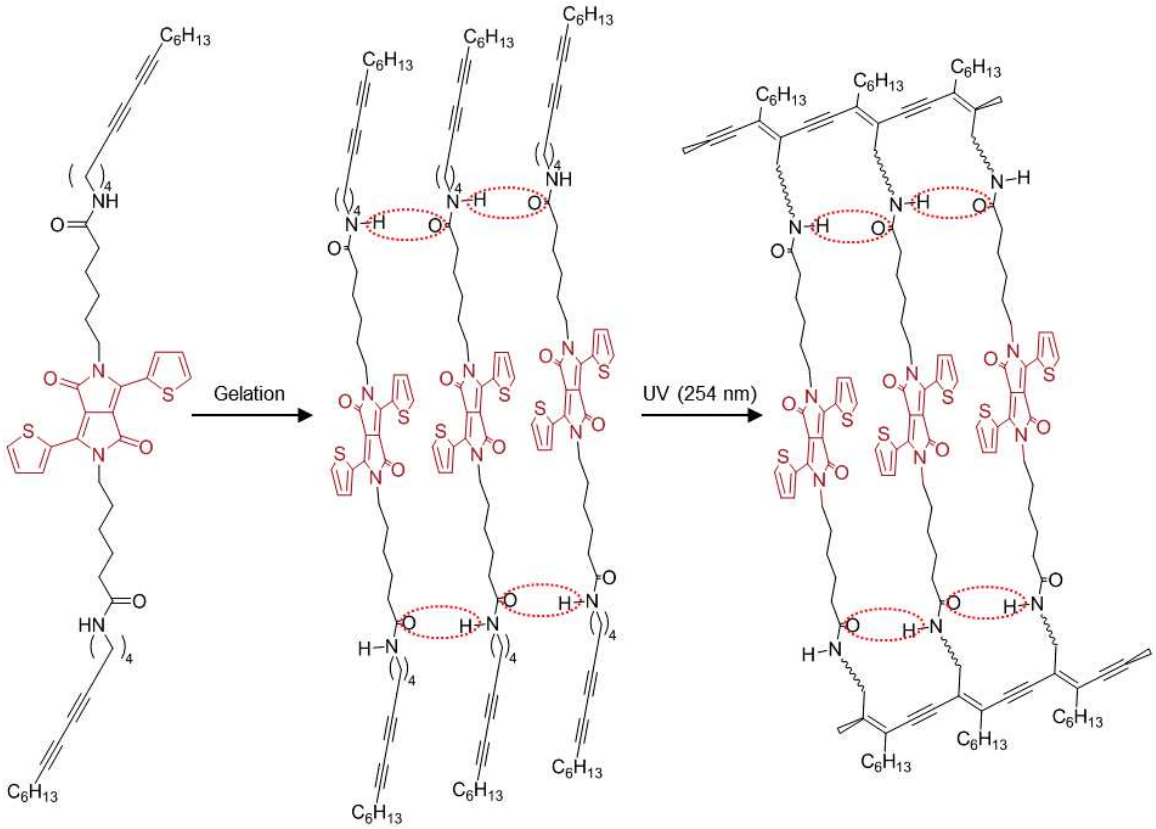

Figure 40: *Gelation and cross-linking mechanism.*

2. Hydrogels based on DPP

Draper *et al*.[152] reported the first hydrogel formed by a **DPP**-based gelator (DPP-1) for which gelation was triggered by pH decrease (Figure 41). **DPP-1** contains two L-phenylalanine aminoacids pending from the lactam nitrogen. The carboxylic acids of the phenylalanines solubilize **DPP-1** at high pH and drive self-assembly upon protonation. Gels were prepared by dissolving **DPP-1** in an aqueous 0.1 M NaOH solution reaching pH = 8. The decrease of pH (pH = 3.3) was triggered by adding glucono-δ-lactone (GdL), resulting in slow hydrolysis and the formation of a gel (Figure 38). Rheology analysis showed the typical behavior of a gel, starting at pH = 7.3 and 8 minutes after GdL was added. **DPP-1** was co-assembled with a perylene-based n-type LMWG in an attempt to achieve a p-n heterojunction through self-sorting of both gelators. Rheology, pHmetry and NMR studies show that the two gelators assemble at different times, and the UV-Vis absorption spectrum of the co-assembled system differs from the spectra of the individual xerogel was lower than the current of the n-type xerogel alone, probably due to inappropriate band-gap overlap between both components and possible recombination originated from intimately mixed gelator fibers. Nonetheless, a different n-type gelator with appropriate energy levels could be combined with **DPP-1**, resulting in conductive systems processed from water, a cheaper and more environmentally friendly solvent.

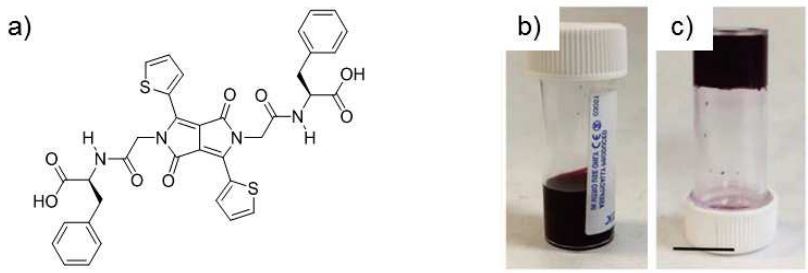

Figure 41: *a) Molecular structure of* ***DPP-1****. b) Photograph of a solution of* ***DPP-1at*** *pH 8 and a concentration of 5 mg mL^{-1}. c) Photograph of a gel of* ***DPP-1*** *at pH 3.3.*

V. References

[1] N. S. Lewis, *MRS Bull.* **2007**, *32*, 808–820.
[2] N. S. Lewis, *Science* **2007**, *315*, 798–801.
[3] J. S. Blakemore, *J. Appl. Phys.* **1982**, *53*, R123–R181.
[4] X. Fang, Y. Bando, C. Ye, D. Golberg, *Chem. Commun.* **2007**, 3048.
[5] E. Schlam, *Proc. IEEE* **1973**, *61*, 894–901.
[6] S. Brittman, Y. Yoo, N. P. Dasgupta, S. Kim, B. Kim, P. Yang, *Nano Lett.* **2014**, *14*, 4665–4670.
[7] E. M. C. Fortunato, P. M. C. Barquinha, A. C. M. B. G. Pimentel, A. M. F. Gonçalves, A. J. S. Marques, L. M. N. Pereira, R. F. P. Martins, *Adv. Mater.* **2005**, *17*, 590–594.
[8] R. L. Hoffman, B. J. Norris, J. F. Wager, *Appl. Phys. Lett.* **2003**, *82*, 733–735.
[9] V. Coropceanu, J. Cornil, D. A. da Silva Filho, Y. Olivier, R. Silbey, J.-L. Brédas, *Chem. Rev.* **2007**, *107*, 926–952.
[10] S. Günes, H. Neugebauer, N. S. Sariciftci, *Chem. Rev.* **2007**, *107*, 1324–1338.
[11] A. C. Grimsdale, K. Leok Chan, R. E. Martin, P. G. Jokisz, A. B. Holmes, *Chem. Rev.* **2009**, *109*, 897–1091.
[12] **N.d.**
[13] C. K. Chiang, C. R. Fincher, Y. W. Park, A. J. Heeger, H. Shirakawa, E. J. Louis, S. C. Gau, A. G. MacDiarmid, *Phys. Rev. Lett.* **1977**, *39*, 1098–1101.
[14] L. Dou, Y. Liu, Z. Hong, G. Li, Y. Yang, *Chem. Rev.* **2015**, *115*, 12633–12665.
[15] L. Lu, T. Zheng, Q. Wu, A. M. Schneider, D. Zhao, L. Yu, *Chem. Rev.* **2015**, *115*, 12666–12731.
[16] W. Tang, Y. Huang, L. Han, R. Liu, Y. Su, X. Guo, F. Yan, *J. Mater. Chem. C* **2019**, *7*, 790–808.
[17] A. P. Kulkarni, C. J. Tonzola, A. Babel, S. A. Jenekhe, *Chem. Mater.* **2004**, *16*, 4556–4573.
[18] A. Mishra, P. Bäuerle, *Angew. Chem. Int. Ed.* **2012**, *51*, 2020–2067.
[19] M. Mas-Torrent, C. Rovira, *Chem. Soc. Rev.* **2008**, *37*, 827.
[20] A. Mishra, P. Bäuerle, *Angew. Chem. Int. Ed.* **2012**, *51*, 2020–2067.
[21] P. K. Watkins, A. B. Walker, G. L. B. Verschoor, *Nano Lett.* **2005**, *5*, 1814–1818.
[22] F. C. Krebs, *Sol. Energy Mater. Sol. Cells* **2009**, *93*, 394–412.
[23] M. Choe, B. H. Lee, G. Jo, J. Park, W. Park, S. Lee, W.-K. Hong, M.-J. Seong, Y. H. Kahng, K. Lee, *Org. Electron.* **2010**, *11*, 1864–1869.
[24] N. Stingelin, *Polym. Int.* **2012**, *61*, 866–873.

[25] E. Verploegen, R. Mondal, C. J. Bettinger, S. Sok, M. F. Toney, Z. Bao, *Adv. Funct. Mater.* **2010**, *20*, 3519–3529.
[26] J. C. Conboy, E. J. C. Olson, D. M. Adams, J. Kerimo, A. Zaban, B. A. Gregg, P. F. Barbara, *J. Phys. Chem. B* **1998**, *102*, 4516–4525.
[27] T. Ghosh, J. Panicker, V. Nair, *Polymers* **2017**, *9*, 112.
[28] I. D. Tevis, W.-W. Tsai, L. C. Palmer, T. Aytun, S. I. Stupp, *ACS Nano* **2012**, *6*, 2032–2040.
[29] M. J. Sung, A. Luzio, W.-T. Park, R. Kim, E. Gann, F. Maddalena, G. Pace, Y. Xu, D. Natali, C. de Falco, et al., *Adv. Funct. Mater.* **2016**, *26*, 4984–4997.
[30] H. Sirringhaus, *Adv. Mater.* **2014**, *26*, 1319–1335.
[31] C. Wang, H. Nakamura, H. Sugino, K. Takimiya, *J. Mater. Chem. C* **2018**, *6*, 3604–3612.
[32] H. Lee, D. Lee, D. H. Sin, S. W. Kim, M. S. Jeong, K. Cho, *NPG Asia Mater.* **2018**, *10*, 469–481.
[33] J. R. Tumbleston, B. A. Collins, L. Yang, A. C. Stuart, E. Gann, W. Ma, W. You, H. Ade, *Nat. Photonics* **2014**, *8*, 385–391.
[34] O. A. Ibraikulov, C. Ngov, P. Chávez, I. Bulut, B. Heinrich, O. Boyron, K. L. Gerasimov, D. A. Ivanov, S. Swaraj, S. Méry, et al., *J. Mater. Chem. A* **2018**, *6*, 12038–12045.
[35] X. Zhang, L. J. Richter, D. M. DeLongchamp, R. J. Kline, M. R. Hammond, I. McCulloch, M. Heeney, R. S. Ashraf, J. N. Smith, T. D. Anthopoulos, et al., *J. Am. Chem. Soc.* **2011**, *133*, 15073–15084.
[36] S. Subramaniyan, H. Xin, F. S. Kim, S. Shoaee, J. R. Durrant, S. A. Jenekhe, *Adv. Energy Mater.* **2011**, *1*, 854–860.
[37] I. Osaka, T. Kakara, N. Takemura, T. Koganezawa, K. Takimiya, *J. Am. Chem. Soc.* **2013**, *135*, 8834–8837.
[38] I. Osaka, M. Saito, T. Koganezawa, K. Takimiya, *Adv. Mater.* **2014**, *26*, 331–338.
[39] R. Rieger, D. Beckmann, A. Mavrinskiy, M. Kastler, K. Müllen, *Chem. Mater.* **2010**, *22*, 5314–5318.
[40] M. S. Chen, J. R. Niskala, D. A. Unruh, C. K. Chu, O. P. Lee, J. M. J. Fréchet, *Chem. Mater.* **2013**, *25*, 4088–4096.
[41] L. Yang, S. Zhang, C. He, J. Zhang, Y. Yang, J. Zhu, Y. Cui, W. Zhao, H. Zhang, Y. Zhang, et al., *Chem. Mater.* **2018**, *30*, 2129–2134.
[42] S. Guo, E. M. Herzig, A. Naumann, G. Tainter, J. Perlich, P. Müller-Buschbaum, *J. Phys. Chem. B* **2014**, *118*, 344–350.
[43] T. Ghosh, A. Gopal, S. Nagasawa, N. Mohan, A. Saeki, V. C. Nair, *ACS Appl. Mater. Interfaces* **2016**, *8*, 25396–25404.
[44] D. G. Farnum, G. Mehta, G. G. I. Moore, F. P. Siegal, *Tetrahedron Lett.* **1974**, *15*, 2549–2552.
[45] E. D. Głowacki, H. Coskun, M. A. Blood-Forsythe, U. Monkowius, L. Leonat, M. Grzybowski, D. Gryko, M. S. White, A. Aspuru-Guzik, N. S. Sariciftci, *Org. Electron.* **2014**, *15*, 3521–3528.
[46] H. Bürckstümmer, A. Weissenstein, D. Bialas, F. Würthner, *J. Org. Chem.* **2011**, *76*, 2426–2432.
[47] M. Kaur, D. H. Choi, *Chem. Soc. Rev.* **2015**, *44*, 58–77.
[48] H. Ftouni, F. Bolze, H. de Rocquigny, J.-F. Nicoud, *Bioconjug. Chem.* **2013**, *24*, 942–950.
[49] X. Yang, L. Xie, R. Ning, X. Gong, Z. Liu, Y. Li, L. Zheng, G. Zhang, B. Gao, Y. Cui, et al., *Sens. Actuators B Chem.* **2015**, *210*, 784–794.

[50] X. Yang, L. Zheng, L. Xie, Z. Liu, Y. Li, R. Ning, G. Zhang, X. Gong, B. Gao, C. Liu, et al., *Sens. Actuators B Chem.* **2015**, *207*, 9–24.
[51] M. Stolte, S.-L. Suraru, P. Diemer, T. He, C. Burschka, U. Zschieschang, H. Klauk, F. Würthner, *Adv. Funct. Mater.* **2016**, *26*, 7415–7422.
[52] J. C. Bijleveld, A. P. Zoombelt, S. G. J. Mathijssen, M. M. Wienk, M. Turbiez, D. M. de Leeuw, R. A. J. Janssen, *J. Am. Chem. Soc.* **2009**, *131*, 16616–16617.
[53] W. Li, K. H. Hendriks, M. M. Wienk, R. A. J. Janssen, *Acc. Chem. Res.* **2016**, *49*, 78–85.
[54] C. J. H. Morton, R. Gilmour, D. M. Smith, P. Lightfoot, A. M. Z. Slawin, E. J. MacLean, *Tetrahedron* **2002**, *58*, 5547–5565.
[55] D. Feng, G. Barton, C. N. Scott, *Org. Lett.* **2019**, *21*, 1973–1978.
[56] A. Iqbal, M. Jost, R. Kirchmayr, J. Pfenninger, A. Rochat, O. Wallquist, *Bull. Sociétés Chim. Belg.* **1988**, *97*, 615–644.
[57] M. Grzybowski, E. Glodkowska-Mrowka, G. Clermont, M. Blanchard-Desce, D. T. Gryko, *Chem. Heterocycl. Compd.* **2017**, *53*, 72–77.
[58] C. B. Nielsen, M. Turbiez, I. McCulloch, *Adv. Mater.* **2013**, *25*, 1859–1880.
[59] M. Kaur, D. Hoon Choi, *Chem. Soc. Rev.* **2015**, *44*, 58–77.
[60] A. Chiminazzo, G. Borsato, A. Favero, C. Fabbro, C. E. McKenna, L. G. Dalle Carbonare, M. T. Valenti, F. Fabris, A. Scarso, *Chem. – Eur. J.* **2019**, *25*, 3617–3626.
[61] W. Hong, B. Sun, H. Aziz, W.-T. Park, Y.-Y. Noh, Y. Li, *Chem. Commun.* **2012**, *48*, 8413–8415.
[62] B. P. Karsten, J. C. Bijleveld, R. A. J. Janssen, *Macromol. Rapid Commun.* **2010**, *31*, 1554–1559.
[63] H. Bürckstümmer, A. Weissenstein, D. Bialas, F. Würthner, *J. Org. Chem.* **2011**, *76*, 2426–2432.
[64] "Effects of Block Length in Copolymers Based on Regioregular Oligothiophenes Linked With Electron-Accepting Units - Zhang - 2012 - Macromolecular Rapid Communications - Wiley Online Library," can be found under https://onlinelibrary-wiley-com.scd-rproxy.u-strasbg.fr/doi/full/10.1002/marc.201100827, **n.d.**
[65] X. Hu, L. Zuo, W. Fu, T. T. Larsen-Olsen, M. Helgesen, E. Bundgaard, O. Hagemann, M. Shi, F. C. Krebs, H. Chen, *J. Mater. Chem.* **2012**, *22*, 15710–15716.
[66] A. Jain, S. J. George, *Mater. Today* **2015**, *18*, 206–214.
[67] F. Würthner, K. Meerholz, *Chem. - Eur. J.* **2010**, *16*, 9366–9373.
[68] Ronald. Breslow, L. E. Overman, *J. Am. Chem. Soc.* **1970**, *92*, 1075–1077.
[69] C. J. Pedersen, *J. Am. Chem. Soc.* **1967**, *89*, 7017–7036.
[70] I. Tabushi, N. Shimizu, T. Sugimoto, M. Shiozuka, K. Yamamura, *J. Am. Chem. Soc.* **1977**, *99*, 7100–7102.
[71] A. Ruiz-Carretero, Y. Atoini, T. Han, A. Operamolla, S. Ippolito, C. Valentini, S. Carrara, S. Sinn, E. A. Prasetyanto, T. Heiser, et al., *J. Mater. Chem. A* **2019**, *7*, 16777–16784.
[72] E. D. Głowacki, M. Irimia-Vladu, S. Bauer, N. S. Sariciftci, *J. Mater. Chem. B* **2013**, *1*, 3742.
[73] E. D. Głowacki, M. Irimia-Vladu, M. Kaltenbrunner, J. Gsiorowski, M. S. White, U. Monkowius, G. Romanazzi, G. P. Suranna, P. Mastrorilli, T. Sekitani, et al., *Adv. Mater.* **2013**, *25*, 1563–1569.
[74] S. Mula, T. Han, T. Heiser, P. Lévêque, N. Leclerc, A. P. Srivastava, A. Ruiz-Carretero, G. Ulrich, *Chem. – Eur. J.* **n.d.**, *0*, DOI 10.1002/chem.201900689.

[75] Z. Xiao, T. Duan, H. Chen, K. Sun, S. Lu, *Sol. Energy Mater. Sol. Cells* **2018**, *182*, 1–13.
[76] C.-H. Huang, N. D. McClenaghan, A. Kuhn, J. W. Hofstraat, D. M. Bassani, *Org. Lett.* **2005**, *7*, 3409–3412.
[77] W.-W. Tsai, I. D. Tevis, A. S. Tayi, H. Cui, S. I. Stupp, *J. Phys. Chem. B* **2010**, *114*, 14778–14786.
[78] H. Ouchi, X. Lin, T. Kizaki, D. D. Prabhu, F. Silly, T. Kajitani, T. Fukushima, K. Nakayama, S. Yagai, *Chem Commun* **2016**, *52*, 7874–7877.
[79] F. Würthner, Z. Chen, F. J. M. Hoeben, P. Osswald, C.-C. You, P. Jonkheijm, J. v. Herrikhuyzen, A. P. H. J. Schenning, P. P. A. M. van der Schoot, E. W. Meijer, et al., *J. Am. Chem. Soc.* **2004**, *126*, 10611–10618.
[80] M. Palma, J. Levin, O. Debever, Y. Geerts, M. Lehmann, P. Samorì, *Soft Matter* **2008**, *4*, 303–310.
[81] K.-H. Kim, H. Yu, H. Kang, D. J. Kang, C.-H. Cho, H.-H. Cho, J. H. Oh, B. J. Kim, *J. Mater. Chem. A* **2013**, *1*, 14538.
[82] B. M. Schulze, N. T. Shewmon, J. Zhang, D. L. Watkins, J. P. Mudrick, W. Cao, R. Bou Zerdan, A. J. Quartararo, I. Ghiviriga, J. Xue, et al., *J Mater Chem A* **2014**, *2*, 1541–1549.
[83] Z. Xiao, K. Sun, J. Subbiah, S. Ji, D. J. Jones, W. W. H. Wong, *Sci. Rep.* **2015**, *4*, 5701.
[84] J. Mizuguchi, *J Phys Chem A* **2000**, *104*, 1817–1821.
[85] Z. Hao, A. Iqbal, *Chem. Soc. Rev.* **1997**, *26*, 203–213.
[86] G. R. Desiraju, *J. Mol. Struct.* **2003**, *656*, 5–15.
[87] M. Irimia-Vladu, E. D. Głowacki, P. A. Troshin, G. Schwabegger, L. Leonat, D. K. Susarova, O. Krystal, M. Ullah, Y. Kanbur, M. A. Bodea, et al., *Adv. Mater.* **2012**, *24*, 375–380.
[88] E. D. G\lowacki, G. Voss, L. Leonat, M. Irimia-Vladu, S. Bauer, N. S. Sariciftci, *Isr. J. Chem.* **2012**, *52*, 540–551.
[89] D. Basak, D. S. Pal, T. Sakurai, S. Yoneda, S. Seki, S. Ghosh, *Phys. Chem. Chem. Phys.* **2017**, *19*, 31024–31029.
[90] E. D. Głowacki, M. Irimia-Vladu, M. Kaltenbrunner, J. Gsiorowski, M. S. White, U. Monkowius, G. Romanazzi, G. P. Suranna, P. Mastrorilli, T. Sekitani, et al., *Adv. Mater.* **2013**, *25*, 1563–1569.
[91] H. Yanagisawa, J. Mizuguchi, S. Aramaki, Y. Sakai, *Jpn. J. Appl. Phys.* **2008**, *47*, 4728.
[92] E. D. Głowacki, H. Coskun, M. A. Blood-Forsythe, U. Monkowius, L. Leonat, M. Grzybowski, D. Gryko, M. S. White, A. Aspuru-Guzik, N. S. Sariciftci, *Org. Electron.* **2014**, *15*, 3521–3528.
[93] A. Facchetti, *Chem. Mater.* **2011**, *23*, 733–758.
[94] J. Mizuguchi, G. Wooden, *Berichte Bunsenges. Für Phys. Chem.* **1991**, *95*, 1264–1274.
[95] J. Mizuguchi, G. Rihs, *Berichte Bunsenges. Für Phys. Chem.* **1992**, *96*, 597–606.
[96] J. Mizuguchi, A. Grubenmann, G. Wooden, G. Rihs, *Acta Crystallogr. B* **1992**, *48*, 696–700.
[97] J. Mizuguchi, A. Grubenmann, G. Rihs, *Acta Crystallogr. B* **1993**, *49*, 1056–1060.
[98] J. Mizuguchi, G. Giller, E. Baeriswyl, *J. Appl. Phys.* **1994**, *75*, 514–518.
[99] J. Mizuguchi, A. Grubenmann, G. Wooden, G. Rihs, *Acta Crystallogr. B* **1992**, *48*, 696–700.
[100] J. Mizuguchi, *J. Appl. Phys.* **1989**, *66*, 3111–3113.

[101] J. Mizuguchi, S. Homma, *J. Appl. Phys.* **1989**, *66*, 3104–3110.
[102] J. Mizuguchi, A. C. Rochat, G. Rihs, *Berichte Bunsenges. Für Phys. Chem.* **1992**, *96*, 607–619.
[103] J. Mizuguchi, *Berichte Bunsenges. Für Phys. Chem.* **1993**, *97*, 684–693.
[104] J. Mizuguchi, T. Imoda, H. Takahashi, H. Yamakami, *Dyes Pigments* **2006**, *68*, 47–52.
[105] M. Kasha, H. R. Rawls, M. Ashraf El-Bayoumi, *Pure Appl. Chem.* **1965**, *11*, 371–392.
[106] C. Fu, P. J. Beldon, D. F. Perepichka, *Chem. Mater.* **2017**, *29*, 2979–2987.
[107] J. S. Zambounis, Z. Hao, A. Iqbal, *Nature* **1997**, *388*, 131.
[108] S. T. Salammal, J.-Y. Balandier, S. Kumar, E. Goormaghtigh, Y. H. Geerts, *Cryst. Growth Des.* **2014**, *14*, 339–349.
[109] Y. Suna, J. Nishida, Y. Fujisaki, Y. Yamashita, *Org. Lett.* **2012**, *14*, 3356–3359.
[110] SunaYuki, NishidaJun-ichi, FujisakiYoshihide, YamashitaYoshiro, *Chem. Lett.* **2011**, DOI 10.1246/cl.2011.822.
[111] E. Daniel Głowacki, M. Irimia-Vladu, S. Bauer, N. Serdar Sariciftci, *J. Mater. Chem. B* **2013**, *1*, 3742–3753.
[112] K. Yang, L. Xiang, Y. F. Huang, R. S. Bhatta, J. Liu, M. Tsige, C. L. Wang, S. Cheng, Y. Zhu, *Polymer* **2019**, 238–245.
[113] S. Mula, T. Han, T. Heiser, P. Lévêque, N. Leclerc, A. P. Srivastava, A. Ruiz-Carretero, G. Ulrich, *Chem. – Eur. J.* **n.d.**, *0*, DOI 10.1002/chem.201900689.
[114] B. Sun, W. Hong, H. Aziz, Y. Li, *J. Mater. Chem.* **2012**, *22*, 18950–18955.
[115] Y. Li, P. Sonar, S. P. Singh, M. S. Soh, M. van Meurs, J. Tan, *J. Am. Chem. Soc.* **2011**, *133*, 2198–2204.
[116] J. Lee, A.-R. Han, J. Hong, J. H. Seo, J. H. Oh, C. Yang, *Adv. Funct. Mater.* **2012**, *22*, 4128–4138.
[117] F. Bruni, M. Sassi, M. Campione, U. Giovanella, R. Ruffo, S. Luzzati, F. Meinardi, L. Beverina, S. Brovelli, *Adv. Funct. Mater.* **2014**, *24*, 7410–7419.
[118] J. Dhar, D. Prasad Karothu, S. Patil, *Chem. Commun.* **2015**, *51*, 97–100.
[119] F. Pop, W. Lewis, D. B. Amabilino, *CrystEngComm* **2016**, *18*, 8933–8943.
[120] Y.-J. Zhang, X. Wang, Y. Zhou, C.-K. Wang, *Chem. Phys. Lett.* **2016**, *658*, 125–129.
[121] C. Yang, M. Zheng, Y. Li, B. Zhang, J. Li, L. Bu, W. Liu, M. Sun, H. Zhang, Y. Tao, et al., *J. Mater. Chem. A* **2013**, *1*, 5172–5178.
[122] K. Nie, B. Dong, H. Shi, Z. Liu, B. Liang, *Sens. Actuators B Chem.* **2017**, *244*, 849–853.
[123] A. Ruiz-Carretero, T. Aytun, C. J. Bruns, C. J. Newcomb, W.-W. Tsai, S. I. Stupp, *J. Mater. Chem. A* **2013**, *1*, 11674.
[124] T. Aytun, L. Barreda, A. Ruiz-Carretero, J. A. Lehrman, S. I. Stupp, *Chem. Mater.* **2015**, *27*, 1201–1209.
[125] Z. Xiao, K. Sun, J. Subbiah, S. Ji, D. J. Jones, W. W. H. Wong, *Sci. Rep.* **2014**, *4*, DOI 10.1038/srep05701.
[126] S. Ghosh, S. Cherumukkil, C. H. Suresh, A. Ajayaghosh, *Adv. Mater.* **2017**, *29*, 1703783.
[127] M. Kirkus, L. Wang, S. Mothy, D. Beljonne, J. Cornil, R. A. J. Janssen, S. C. J. Meskers, *J. Phys. Chem. A* **2012**, *116*, 7927–7936.
[128] M. Más-Montoya, R. A. J. Janssen, *Adv. Funct. Mater.* **2017**, *27*, DOI 10.1002/adfm.201605779.
[129] W.-W. Tsai, I. D. Tevis, A. S. Tayi, H. Cui, S. I. Stupp, *J. Phys. Chem. B* **2010**, *114*, 14778–14786.

[130] S. Ghosh, S. Das, A. Saeki, V. K. Praveen, S. Seki, A. Ajayaghosh, *ChemNanoMat* **2018**, *4*, 831–836.
[131] A. Mishra, P. Bäuerle, *Angew. Chem. Int. Ed.* **2012**, *51*, 2020–2067.
[132] S. Ghosh, R. Raveendran, A. Saeki, S. Seki, M. Namboothiry, A. Ajayaghosh, *ACS Appl. Mater. Interfaces* **2019**, *11*, 1088–1095.
[133] S. Rieth, Z. Li, C. E. Hinkle, C. X. Guzman, J. J. Lee, S. I. Nehme, A. B. Braunschweig, *J. Phys. Chem. C* **2013**, *117*, 11347–11356.
[134] D. Ley, C. X. Guzman, K. H. Adolfsson, A. M. Scott, A. B. Braunschweig, *J. Am. Chem. Soc.* **2014**, *136*, 7809–7812.
[135] A. M. Levine, C. Schierl, B. S. Basel, M. Ahmed, B. A. Camargo, D. M. Guldi, A. B. Braunschweig, *J. Phys. Chem. C* **2019**, *123*, 1587–1595.
[136] Y. Zhou, C. X. Guzman, L. C. Helguero-Kelley, C. Liu, S. R. Peurifoy, B. Captain, A. B. Braunschweig, *J. Phys. Org. Chem.* **2016**, *29*, 689–699.
[137] Y. Zhou, C. X. Guzman, L. C. Helguero-Kelley, C. Liu, S. R. Peurifoy, B. Captain, A. B. Braunschweig, *J. Phys. Org. Chem.* **2016**, *29*, 689–699.
[138] E. H. A. Beckers, S. C. J. Meskers, A. P. H. J. Schenning, Z. Chen, F. Würthner, P. Marsal, D. Beljonne, J. Cornil, R. A. J. Janssen, *J. Am. Chem. Soc.* **2006**, *128*, 649–657.
[139] R. F. Fink, J. Seibt, V. Engel, M. Renz, M. Kaupp, S. Lochbrunner, H.-M. Zhao, J. Pfister, F. Würthner, B. Engels, *J. Am. Chem. Soc.* **2008**, *130*, 12858–12859.
[140] X. Yang, L. Zheng, L. Xie, Z. Liu, Y. Li, R. Ning, G. Zhang, X. Gong, B. Gao, C. Liu, et al., *Sens. Actuators B Chem.* **2015**, *207*, 9–24.
[141] X. Yang, L. Xie, R. Ning, X. Gong, Z. Liu, Y. Li, L. Zheng, G. Zhang, B. Gao, Y. Cui, et al., *Sens. Actuators B Chem.* **2015**, *210*, 784–794.
[142] J. Mei, K. R. Graham, R. Stalder, S. P. Tiwari, H. Cheun, J. Shim, M. Yoshio, C. Nuckolls, B. Kippelen, R. K. Castellano, et al., *Chem. Mater.* **2011**, *23*, 2285–2288.
[143] B. Song, H. Wei, Z. Wang, X. Zhang, M. Smet, W. Dehaen, *Adv. Mater.* **2007**, *19*, 416–420.
[144] Y. Yang, Z. Liu, L. Chen, J. Yao, G. Lin, X. Zhang, G. Zhang, D. Zhang, *Chem. Mater.* **2019**, *31*, 1800–1807.
[145] J. Šebera, J. Burda, M. Straka, A. Ono, C. Kojima, Y. Tanaka, V. Sychrovský, *Chem. – Eur. J.* **2013**, *19*, 9884–9894.
[146] J. Yao, C. Yu, Z. Liu, H. Luo, Y. Yang, G. Zhang, D. Zhang, *J. Am. Chem. Soc.* **2016**, *138*, 173–185.
[147] W. Du, D. Ohayon, C. Combe, L. Mottier, I. P. Maria, R. S. Ashraf, H. Fiumelli, S. Inal, I. McCulloch, *Chem. Mater.* **2018**, *30*, 6164–6172.
[148] S. S. Babu, S. Prasanthkumar, A. Ajayaghosh, *Angew. Chem. Int. Ed.* **2012**, *51*, 1766–1776.
[149] G. S. Thool, K. Narayanaswamy, A. Venkateswararao, S. Naqvi, V. Gupta, S. Chand, V. Vivekananthan, R. R. Koner, V. Krishnan, S. P. Singh, *Langmuir* **2016**, *32*, 4346–4351.
[150] J. Razzell-Hollis, J. Wade, W. C. Tsoi, Y. Soon, J. Durrant, J.-S. Kim, *J. Mater. Chem. A* **2014**, *2*, 20189–20195.
[151] A. Nyayachavadi, G. T. Mason, M. Nazir Tahir, M. U. Ocheje, S. Rondeau-Gagné, *Langmuir* **2018**, *34*, 12126–12136.
[152] E. R. Draper, B. Dietrich, D. J. Adams, *Chem Commun* **2017**, *53*, 1864–1867.

Chapter 2: Semicarbazone functionalized thiophene-capped diketopyrrolopyrole derivatives. Peripheral functionalization

Summary

Two **DPP** molecules were synthesized with ethylhexyl branches on both lactams. A phenyl semicarbazone structure was attached on one of the two peripheral thiophene rings. Both molecules differ by the presence or not of a bromine atom on the other thiophene of the main core. Some steps of the syntheses were optimized by changing parameters such as the base used, the time and temperature of the reaction. Sub-products were isolated and identified by ^{1}H-NMR and information found in the literature. Some of these sub-products were even used to form **DPP** gelators that will be presented in chapter 4.

The self-assembling properties were studied by UV-visible spectroscopy and Fourier Transform Infrared (FT-IR) spectroscopy in solution and thin films. The solutions were prepared at a fixed concentration (2.5 mg.mL^{-1}) in chloroform, chlorobenzene, toluene and ethyl acetate. The thin films were prepared by spin coating of these solutions. Signals characteristic of J-type aggregates were observed at different intensities depending on the nature of the solvent. FT-IR spectra of solids and solutions showed that H-bonds form under certain conditions. UV-Vis experiments with addition of MeOH, a solvent competing with H-bonding, proved that H-bonds are involved in the formation of the J-aggregates. The progressive addition of MeOH resulted in spectra similar to the ones in chloroform samples. The same effect was also observed when samples were diluted or temperature increased.

Morphology was investigated by SEM microscopy on spin coated thin films. The micrographs revealed the formation of different structures depending on the molecules and on the solvent. Thin films were also prepared from solution containing methanol. In this case, the well-defined structures seen in the previous spin coated samples are no longer observed. This clearly shows the self-assembly of the **DPP** molecules are dependent on H-bonding interactions. Further studies will need to be pursued to see which kind of structure obtained is the best fitted for electronic devices.

Gelation was tested using a heating and cooling process as previously done for the self-assembly studies. Gel-like materials were obtained in cyclohexane, *trans*-decalin and ethyl acetate. SEM images of spin coated samples revealed these compounds form fibers or ribbons with several micrometer lengths. However, these products could not be used for further studies since they underwent a macroscopic phase separation at room temperature. Their dissolution at high temperature in solvent is not complete, because they do not dissociate below the boiling point of the solvent.

The energy levels were determined using cyclic voltammetry. The HOMO energy levels go from -5.26 eV to -5.18 eV, whereas the LUMO energy levels go from -3.5 eV to -3. 43 eV. These values make these **DPP** molecules suitable candidates for making devices such as solar cells or transistors**.**

I. Introduction

In this chapter, we have explored the incorporation of hydrogen-bonding units into the peripheral thiophene rings of the semiconducting **DPP** segment (Figure 1). As previously explained, a library of hydrogen-bonded **DPP** derivatives was designed, and in this case, derivatives capable of forming two hydrogen bonds within the same functional group are studied (Figure 1). Two solubilizing groups have been added, namely ethylhexyl and butyloctyl to study solubility effects on the aggregation properties. Semicarbazone groups provide two hydrogen-bonding sites and can be attached to the semiconducting core by reacting a carbonyl group and a semicarbazide derivative. In this part of the thesis, we designed a family of **DPP** derivatives containing 4-phenylsemicarbazone attached to the periphery of the molecule. Only one semicarbazone group was incorporated into the **DPP** structure to avoid solubility issues. The other thiophene ring was functionalized in one of the derivatives with a bromine atom (Figure 1) to study its possible influence in the optical and self-assembly properties. Furthermore, the incorporation of a halogen atom was envisioned for possible further functionalization. In this case, solubilizing alkyl tails were introduced in the nitrogen of the lactam rings, synthesizing ethylhexyl containing **DPP** derivatives (Figure 1).

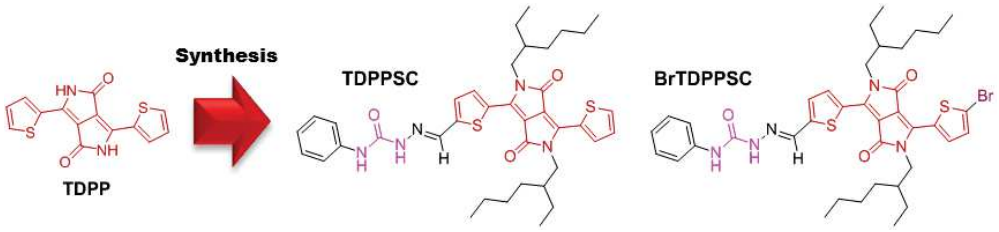

Figure 1: *Chemical structure of the targeted semicarbazone **DPP** derivatives*

The semicarbazone function has been used mainly in biology as biomarkers[1], fluorescence detection[2], and the development of drugs[3,4]. They are very versatile ligands in coordination chemistry, especially in the formation of heterodinuclear complexes of palladium and ruthenium[5].

It is in the field of optical sensing where derivatives combine semicarbazones and **DPP**.[6] In this case, phenyl-capped **DPP** derivatives containing two semicarbazone or thiosemicarbazone (Figure 2a) were used as fluoride ion sensors (Figure 2b). These molecules revealed to be highly specific toward fluoride anion compared to other anions. The bonding between F^- ions and the **DPP** sensors generated a bathochromic shift in UV-visible absorption spectra and a quenching of fluorescence (Figure 1b). The spectral changes were due to the deprotonation of the urea or thiourea structures by the F^- ions. Even though the optical properties of this systems are used to achieve the sensing properties, the self-assembly and supramolecular structures were not studied.

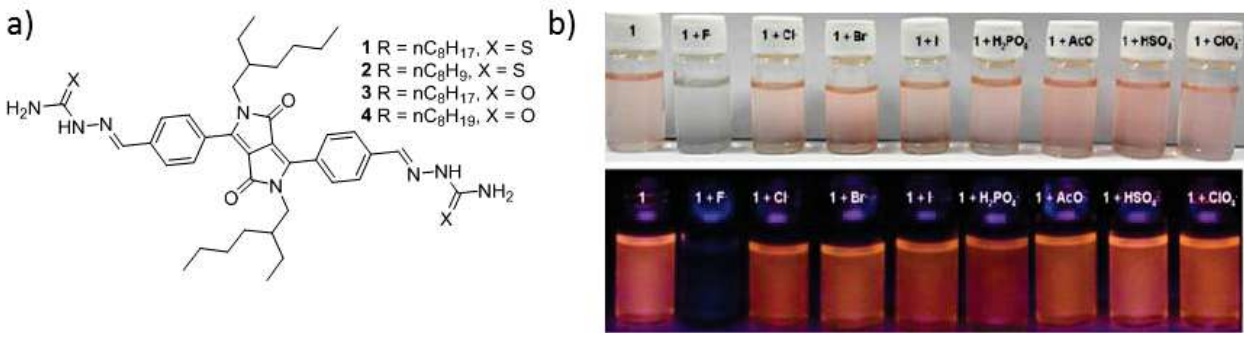

Figure 2: *a) chemical structure of the **DPP** chemosensor; b) Color change upon addition of fluoride anioin ions in comparison to other anionic species.*

II. Synthesis

The synthesis of the **DPP** core (1) was made following a protocol previously reported[7] involving a condensation between 2-thiophenecarbonitrile and diethylsuccinate (Scheme 1). Derivative **1** was obtained with a yield of 82% and was further alkylated using two ethylhexyl bromide equivalents to obtain derivative **2** in 18% yield (Scheme 1).

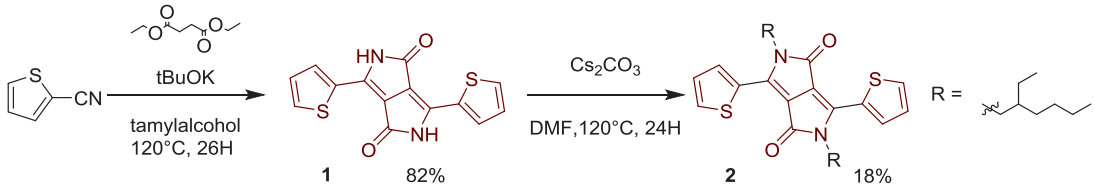

Scheme 1*: Synthesis of the **DPP** core (1) and the N,N alkylated **DPP** (2).*

Derivative **2** was asymmetrically brominated with N-bromosuccinimide (NBS) to get compound **3** in 60% yield (Scheme 2), or formylated via a Vilsmeier-Haack reaction to yield the mono-aldehyde derivative **4a** in 12% yield (Scheme 2).

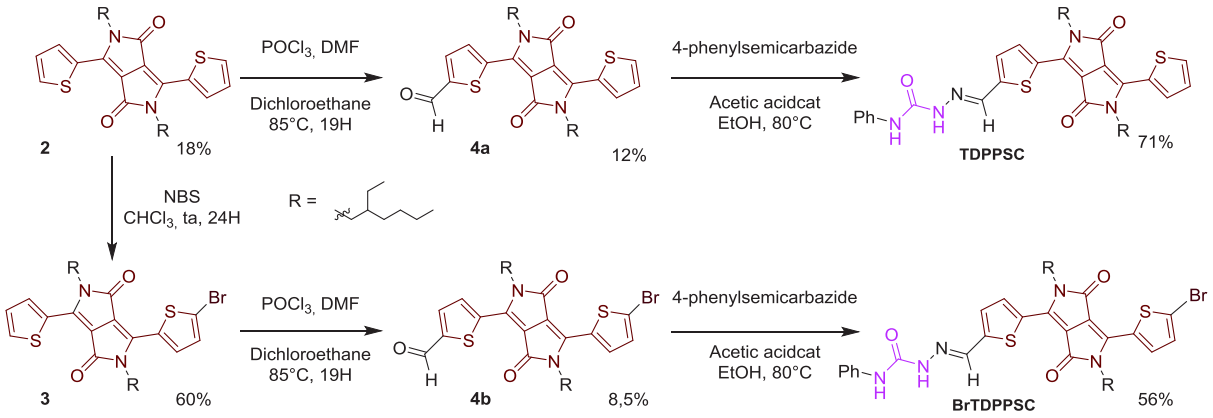

Scheme 2: *Synthetic steps towards **TDPPSC** and **BrTDPPSC.***

The final product **TPPSC** was formed by a condensation reaction between **4a** and 4-phenylsemicarbazide using ethanol as solvent and acetic acid in catalytic amount. T**DPPSC** was finally obtained in 71% yield. The brominated analogue **BrTDPPSC** (Scheme 2) was also synthesized, by the same condensation protocol with the aldehyde **4b**, obtained by formylation of the monobrominated **DPP 3** in 8.5% yield. The yield of the final condensation was 56%.

Two steps of this synthesis proved challenging: the alkylation and the formylation. We optimized them to improve their low yields. Table 1 shows the different conditions tested for the alkylation reaction. The nature of the base impacts the yield (entries 1 and 2, table 1): in the same conditions of stoichiometry and temperature, the yield is only 17% after 18 h with potassium carbonate (K_2CO_3), and 29% after 5 hours with cesium carbonate ($CsCO_3$). The same yield was obtained when increasing the equivalents of alkylating agent to 4 equivalents and using $CsCO_3$ as the base (entry 3, table 1). The yield could not be further increased when the reaction time was prolonged (entry 4, table 1). In all these reactions, N,N-dimethylformamide (DMF) was used as the solvent since good solubility was obtained. However, in later reports **DPP** was alkylated[8] efficiently in acetonitrile and by microwave irradiation.

Table 1: *Alkylation reaction conditions.*

	Eq. of 2-ethylhexyl bromide	Base (eq.)	Time (h)	Temperature (°C)	Yield (%)
1	2.5	Cs_2CO_3, 2.5	18	120	17
2	2.5	K_2CO_3, 2.5	5	120	29
3	4	Cs_2CO_3, 4	5	120	28
4	2.5	Cs_2CO_3, 2.5	72	20	27

The alkylation step yielded several sub-products. We successfully isolated them. The first one is the N,O-alkylated isomer of **2** (Scheme 2) [9] (Figure 3b). Both isomers can be distinguished by the naked eye because of their different color and physical aspect: **2** is a dark red solid, whereas the N,O-alkylated analogue (Figure 3b) is a viscous dark purple oil. The isolation of both compounds is rather challenging by column chromatography since they have very similar retardation factors (Rf), which requires several columns to isolate them. They can be perfectly distinguished by ^{1}H-NMR by the signals of the methylene (-CH_2-) directly attached to the lactam nitrogen and the signals of the thiophenes rings (Figure 3a and 3b). Regarding the N,N alkylated **DPP**, the presence of three doublets, each one integrating for two protons in the aromatic region, and a multiplet integrating for four protons at 4 ppm were observed. For the N,O-alkylated isomer, the ^{1}H-NMR spectra show a new signal at 4.5 ppm integrating for two protons corresponding to the -CH_2- and five signals in the aromatic region. These signals confirm the formation of the N,O-alkylated isomer according to previous synthesis mentioned in the literature[9].

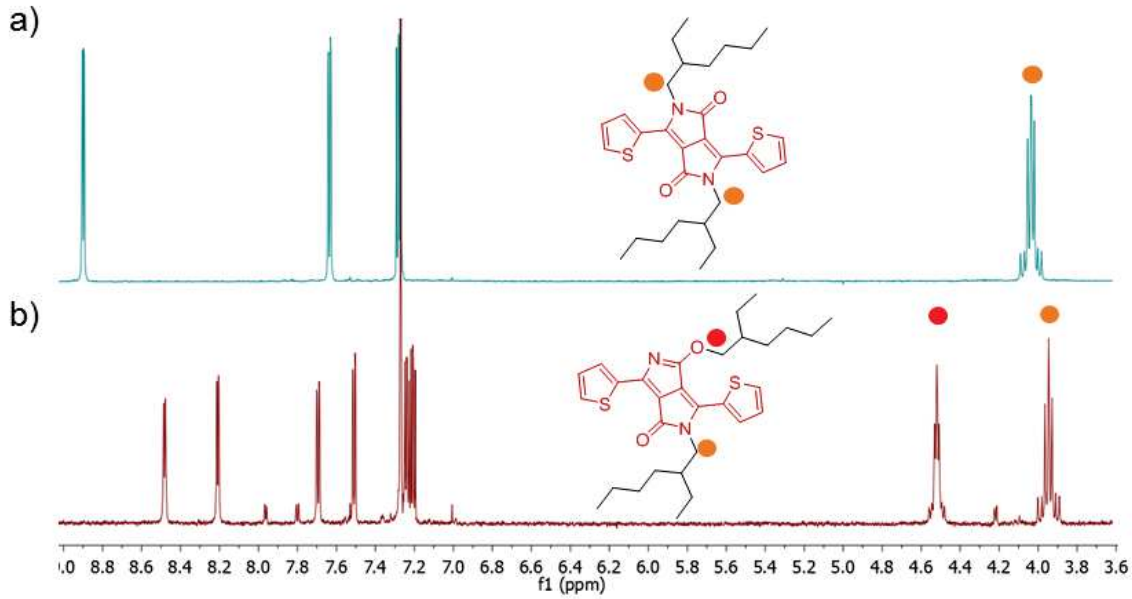

Figure 3: *^{1}H NMR spectra of a) N,N-alkylated **DPP** and b) N,O-alkylated **DPP.***

Previous work in the literature[10] mentions another subproduct: the isomer where both oxygen atoms of the **DPP** carbonyls are alkylated. Nevertheless, we never found this product in any of our reaction conditions. Other sub-products were isolated: the mono N- and O-alkylated **DPP** derivatives (Figure 4a and 4b). Like for the bis-alkylated isomers, these two compounds have different physical aspect and color, and ^{1}H NMR spectrum (Figure 4a and 4b).

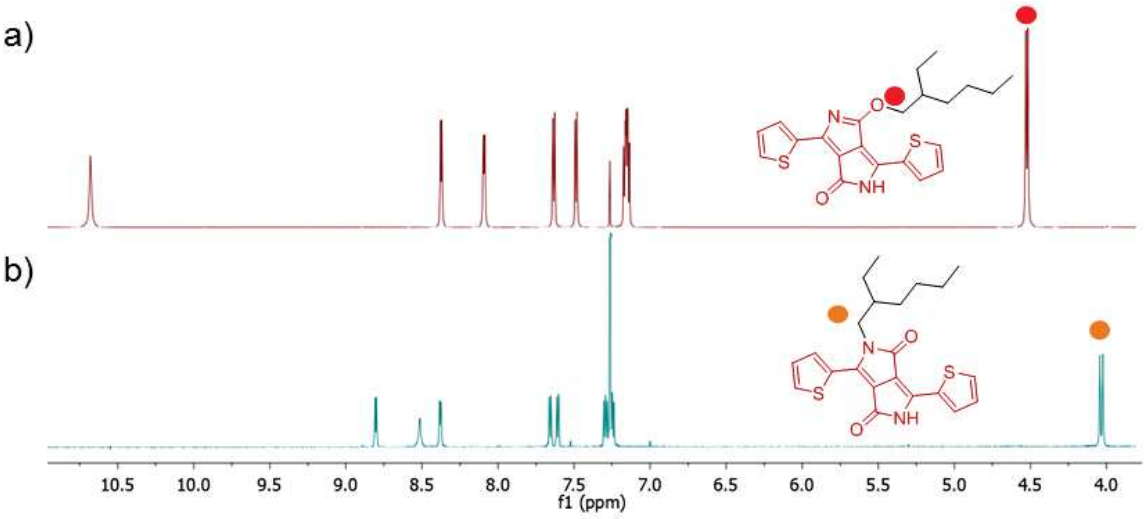

Figure 4: *Chemical structure and ^{1}H NMR spectra of a) the N-monoalylated **DPP** and b) the O-monoalkylated **DPP.***

Their separation is also challenging since they have identical Rf on thin layer chromatography (TLC). The formation of mono N-alkylated **DPP** has been reported in previous works[11–13], but to the best of our knowledge there is no mention up to date on the formation of the mono O-alkylated isomer. All the sub-products obtained were

analyzed and further used to synthesize other compounds that will be studied in the following chapters.

The formylation reaction was also optimized and the results are shown in table 2. The first reaction performed was a classical Vilsmeier-Haack formylation: the Vilsmeier reagent is prepared from phosphoryl (V) chloride ($POCl_3$) and DMF, added to a solution of N,N-alkylated **DPP** in dichloroethane and stirred overnight at 85°C. The desired product was obtained in only 17 % yield, probably due to the electron-poor character of the starting material: other **DPP** systems found in literature[14], have more thiophene rings in the electroactive segment, resulting in higher yields. Alternative conditions were tried to obtain a higher amount of product **3**. They are summed up in table 2.

Table 2: *Formylation reaction conditions.*

Entry	Reactants (eq)	Solvent (ml)	T (°C)	Time (h)	Yield (%)
1	$POCl_3$ (20) DMF (20)	Dichloroethane (V= 15ml)	85	19	17%
2	LDA (0.5) N-formylpiperidine (0.5)	THF (V= 25ml)	0	2.5	-
3	LDA (1) DMF (1.2)	THF (V=80 ml)	0	1	9%
4	LDA (1) DMF (1.2)	THF (V=40 ml)	0	1	27%

An attempt was made using lithium diisopropylamide (LDA) and N-formylpiperidine instead of the Vilsmeier reagent (entry 2). The protocol was inspired by a previous work using these reagents to make the bis-aldehyde **DPP**[15] derivative (Scheme 7). Derivative **2** was reacted at -20 °C with LDA in anhydrous THF. The metallated compound is reacted at 0 °C with N-formylpiperidine. In these conditions, the desired compound was not obtained, neither the bis-aldehyde derivative, which this protocol was originally established for. The best yields were obtained when N-formylpiperidine was replaced by anhydrous DMF[16] (entry 3) and **2** was reacted with LDA at -80 °C. The desired product was obtained in 27 % yield.

In these conditions, side-products were obtained (Figure 5). We identified and isolated two of them. The first one is the bis-aldehyde **DPP** product identified by ^{1}H-NMR (Figure 5b), with two doublets in the aromatic region and a singlet at 10 ppm integrating for the aldehyde protons. This result was very interesting since it resulted in the only synthetic protocol able to render the bis-aldehyde derivative in thiophene-capped **DPPs**. The second sub-product was an alcohol derivative (Figure 5c), obtained when the reaction was quenched with water. This sub-product is formed when the mixture is washed with a saturated solution of NaCl, but it is no longer formed when it is washed with a hydrochloric acid solution.

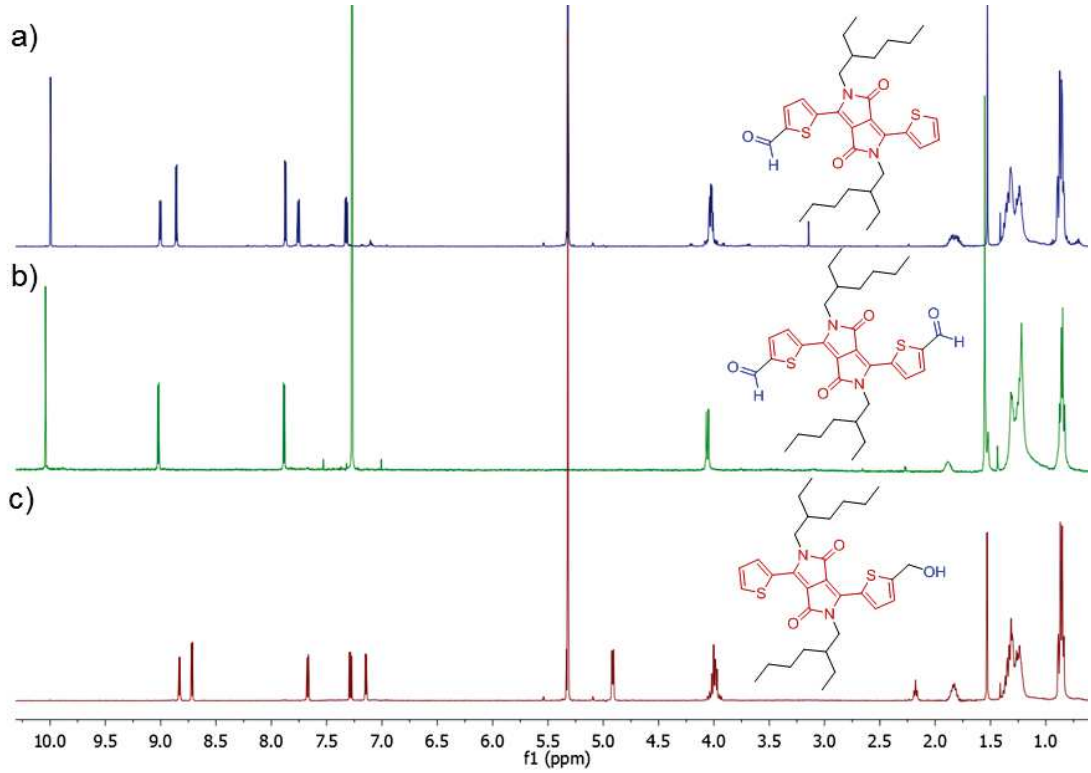

Figure 5: *Chemical structure and ^{1}H NMR spectra of (a) mono-aldehyde **DPP**, (b) the bis-aldehyde **DPP** and (c) mono-alcohol **DPP**.*

III. Self-assembly studies using UV-Vis and Fourier Transform Infrared (FTIR) spectroscopy

The self-assembly of **TDPPSC** and **BrTDPPSC** derivatives was followed in solution and on thin film by UV-vis spectroscopy (Figure 6). We studied the solutions in various solvents: chloroform ($CHCl_3$), toluene, chlorobenzene and ethyl acetate. Prior to experiments, **TDPPSC** and **BrTDPPSC** were dissolved, warmed up to a temperature close to the boiling point of the solvent and then cooled down to room temperature. Chloroform was used as a good solvent: in this solvent **TDPPSC** and **BrTDPPSC** showed no aggregate signals at the concentration studied (c = 2.5 mg/mL) (Figure 6, green curve). The absorption spectra are characteristic of isolated molecules with broad absorption bands ranging from 450 to 650 nm in the visible region with maxima (λ_{max}) at 552 and 584 nm and at 557 and 594 nm for **TDPPSC** and **BrTDPPSC**, respectively. The vibronic structure of the absorption bands is typical of **DPP** derivatives, but in this case they are red-shifted compared to analogue molecules without semicarbazone groups, which are electron-withdrawing. The signals at higher energy are usually attributed to internal C-C interactions of the carbons rings.

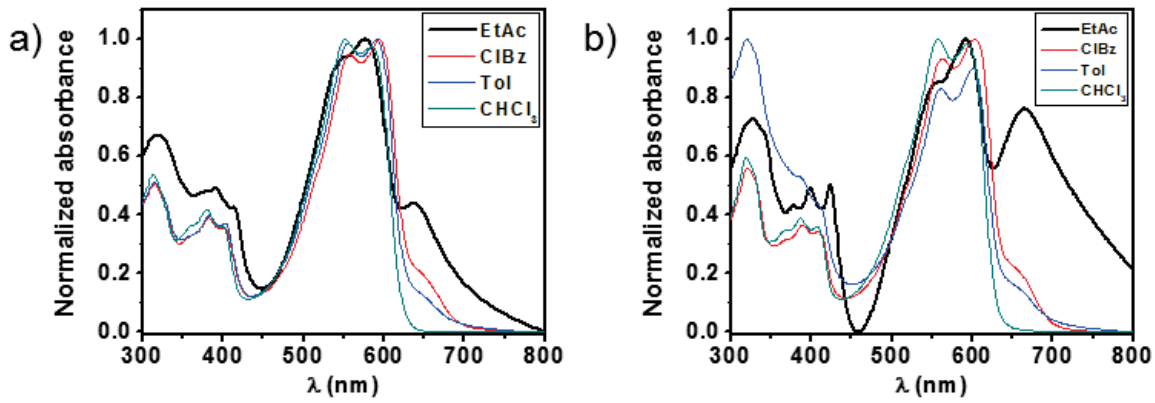

Figure 6: *UV-Vis absorption spectra of (a)* ***TDPPSC*** *and (b)* ***BrTDPPSC*** *in solution in different solvents (c = 2.5 mg/mL).*

The formation of hydrogen bonds was also confirmed by Fourier transform infrared spectroscopy (FTIR) in solution. The C=O stretching band of the semicarbazone shifted from 1681 cm^{-1} in the solid state to 1696 cm^{-1} in solution (Figure 7a), confirming the carbonyl group is not H-bonded. Other spectral changes in this area concern the C=O stretching band of the **DPP** core that shifts from 1667 cm^{-1} in the solid to 1661 cm^{-1} in chloroform, which confirms that the presence of H-bonds influence the packing of the aromatic cores. The samples in solid state show one signal in the -NH stretching region, at 3381 cm^{-1} for **TDPPSC** and at 3380 cm^{-1} for **BrTDPPSC**, attributed to H-bonded semicarbazones. However, the sample in deuterated chloroform shows two bands corresponding to free -NH. Regarding solutions of **TDPPSC** or **BrTDPPSC** in ethyl acetate, the same single -NH stretching band located around 3380 cm^{-1} in solid state can be observed, confirming the formation of hydrogen-bonding (Figure 7b).

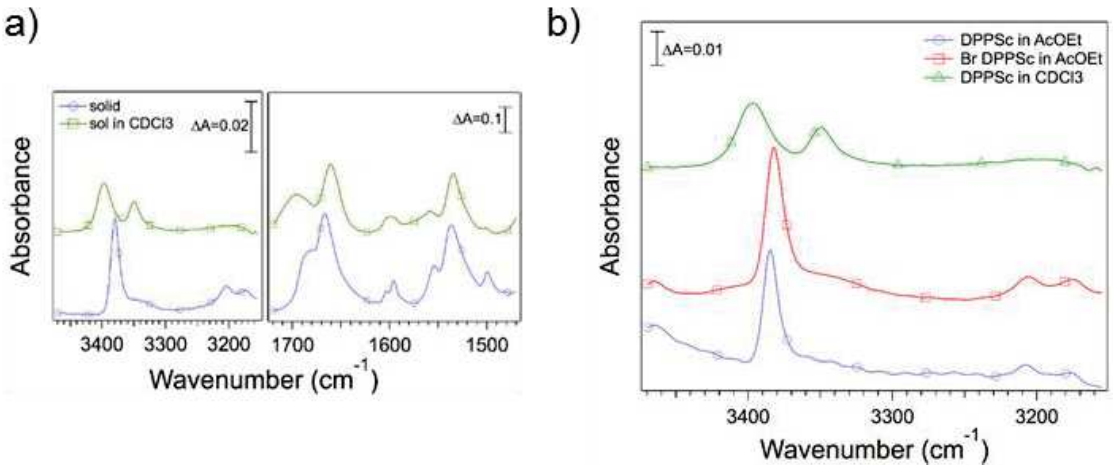

Figure 7: *Comparison of FTIR spectra between (a)* ***TDPPSC*** *in chloroform and in solid state.(b)* ***TDPPSC*** *in chloroform and* ***TDPPSC*** *and* ***BrTDPPSC*** *in ethyl acetate.*

The optical energy band gaps (E_g^{opt}) were also calculated from the chloroform solutions. The values determined from the onsets of absorption at low energy are 1.96 eV and 1.90 eV for **TDPPSC** and **BrTDPPSC**, respectively. These values are consistent with the electrochemical band gaps measured by cyclic voltammetry (Figure 6 and table 3).

In chlorobenzene or toluene, the absorption spectra showed a red-shift of the main absorption bands for both, **TDPPSC** and **BrTDPPSC**. Moreover, new bands corresponding to J-aggregate signals appeared at 630 nm and 665 nm for both derivatives in chlorobenzene and toluene (Figure 6 red and blue curves). These signals arise from π-stacking with certain tilt angle in respect with the stacking direction.[17] In many examples this packing is driven by hydrogen-bonding[18–22]. Therefore, it is possible to tune the optoelectronic properties by controlling the packing of the monomer units. Solutions prepared with ethyl acetate revealed a major change in the vibronic structure with a strong intensity of the J-aggregate absorption band, especially for **BrTDPPSC** (Figure 6, black curve), reaching in this case the near infrared (NIR) region.

When the samples were heated (100 °C for toluene and chlorobenzene solutions, 60 °C for ethyl acetate and chloroform solutions), the intensity of the J-aggregate signals decreased until they completely disappeared, showing similar spectra to the ones in chloroform at room temperature (Figure 8). When the solutions are heated, the vibronic peak experiences a hypsochromic shift and the ratio of the intensity of 0-0 and 0-1 varies (Figure 8). According to previous studies[23,24], this effect was also observed on **DPP** derivatives without hydrogen bonds in solid state, which could be, related the formation of two different aggregates when the strength of the intermolecular excitonic coupling and the electron-vibrational coupling are similar.

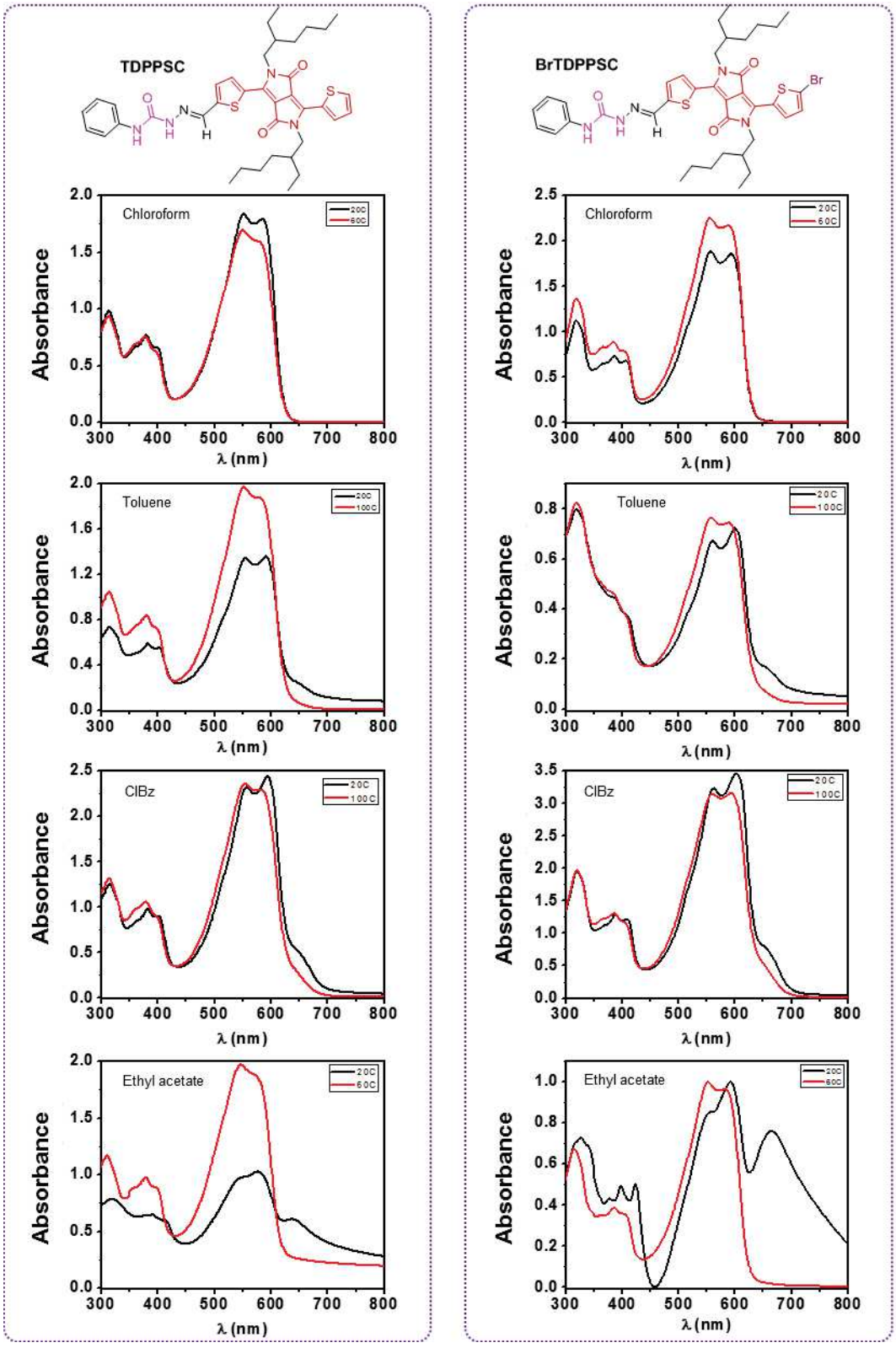

Figure 8: *Comparison of the UV absorption spectra of* ***TDPPSC*** *and* ***BrTDPPSC*** *solutions at room temperature and elevated temperature (60°C or 100°C depending on the solvent; c = 2.5 mg/mL).*

The distinction between H- and J-aggregates could be made by decreasing (H-) or increasing (J-) ratio of the two vibronic peak intensities of the main **DPP** absorption

band[25,26]. For both solvents, the 0-0/0-1 vibronic peak ratio is below 1 at 100°C, whereas at room temperature it is above 1. This indicates that at high temperature, π-π stacking is preserved forming H-aggregates (stacks) without H-bonding. At room temperature, hydrogen bonding is predominant leading to a head-to-tail self-assembly of the **DPP** molecules, which is characteristic of J-aggregates. The presence of such aggregate bands is interesting especially since previous work reported they improve device performance in organic solar cells[27] and increase exciton transport[28].The intensity of the J-aggregates bands decreased also upon diluting the solution (Figure 9).

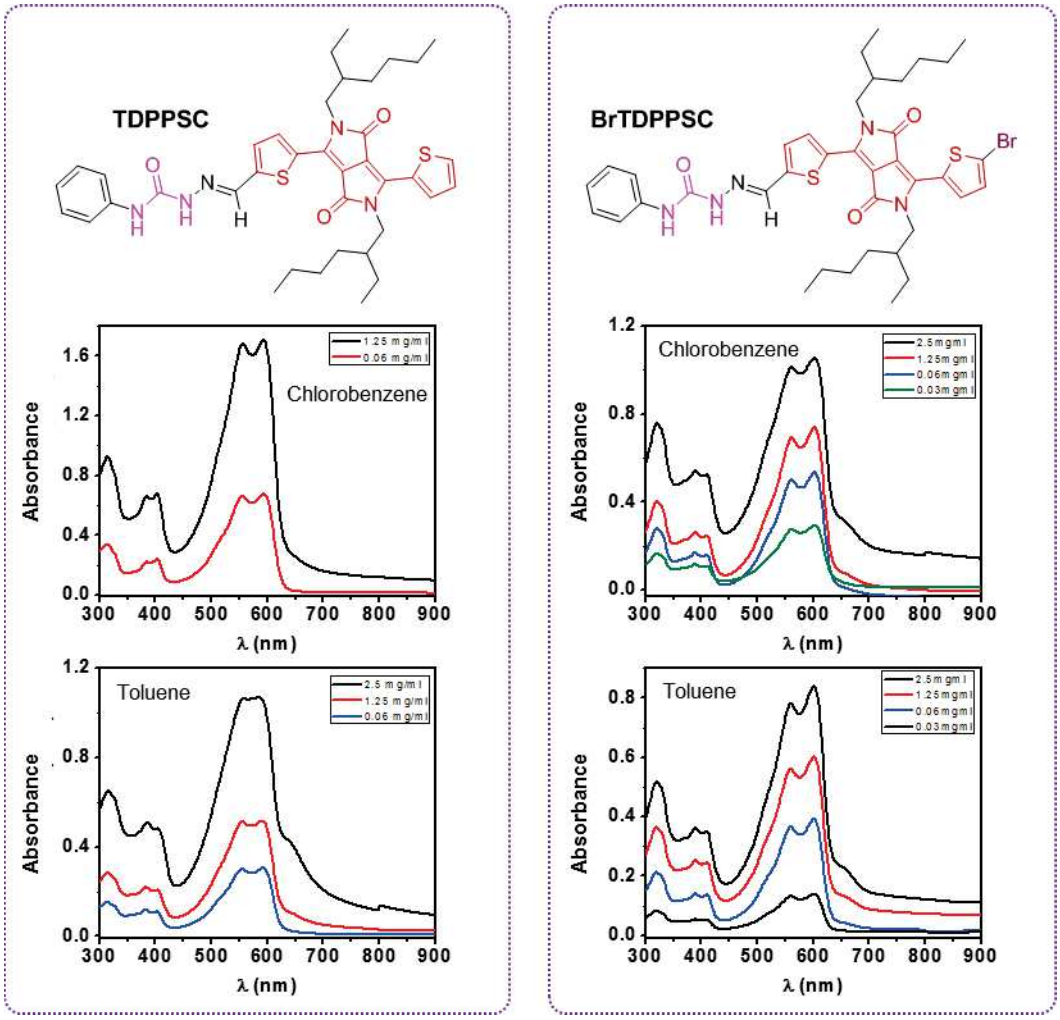

Figure 9: *UV absorption spectra of* ***TDPPSC*** *and* ***BrTDPPSC*** *with concentration variation in chlorobenzene and in toluene.*

In order to prove the influence of hydrogen bonds in the J-aggregate formation, solutions of **TDPPSC** and **BrTDPPSC** were prepared in every solvent used previously, and small amounts of methanol (H-bonding competing) were added progressively (Figure 10). 4% and 6% volume of methanol was required to entirely vanish the J-aggregate signals for **TDPPSC** in chlorobenzene and toluene, respectively, resulting in spectra similar to the one in chloroform at room temperature. Regarding **BrTDPPSC**,

4% of methanol was needed to disrupt entirely the H-bonds in both solvents (Figure 10). The samples in ethyl acetate needed larger amounts of methanol to disrupt entirely the hydrogen bonds, especially for **BrDPPSC** (Figure 10).

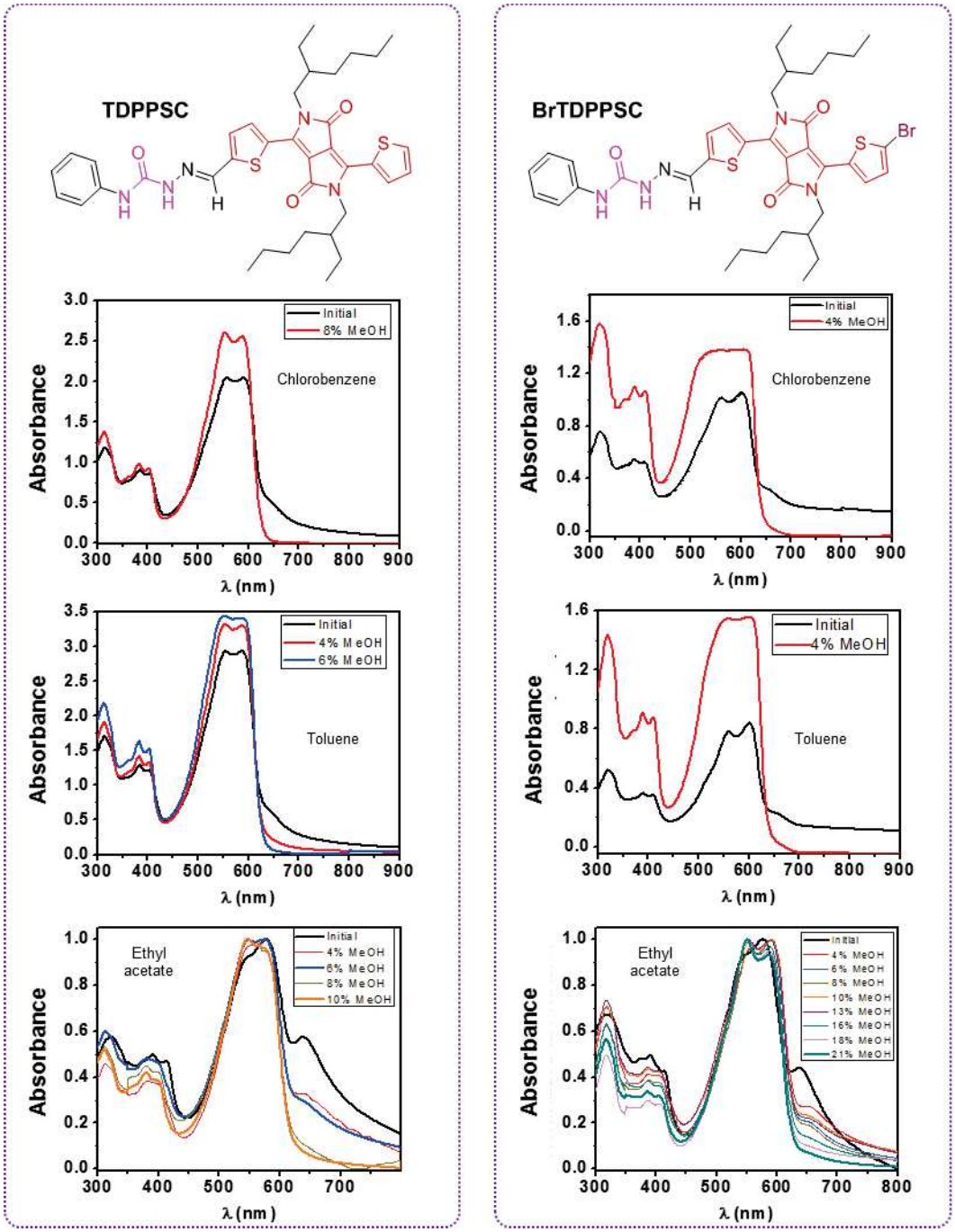

Figure 10: *UV absorption spectra of* ***TDPPSC*** *and* ***BrDPPSC*** *upon addition of methanol (c = 2.5 mg/mL).*

Samples of **TDPPSC** and **BrTDPPSC** were spin coated from the solutions in different solvents, and the spectra of the deposited samples were recorded (Figure 11).

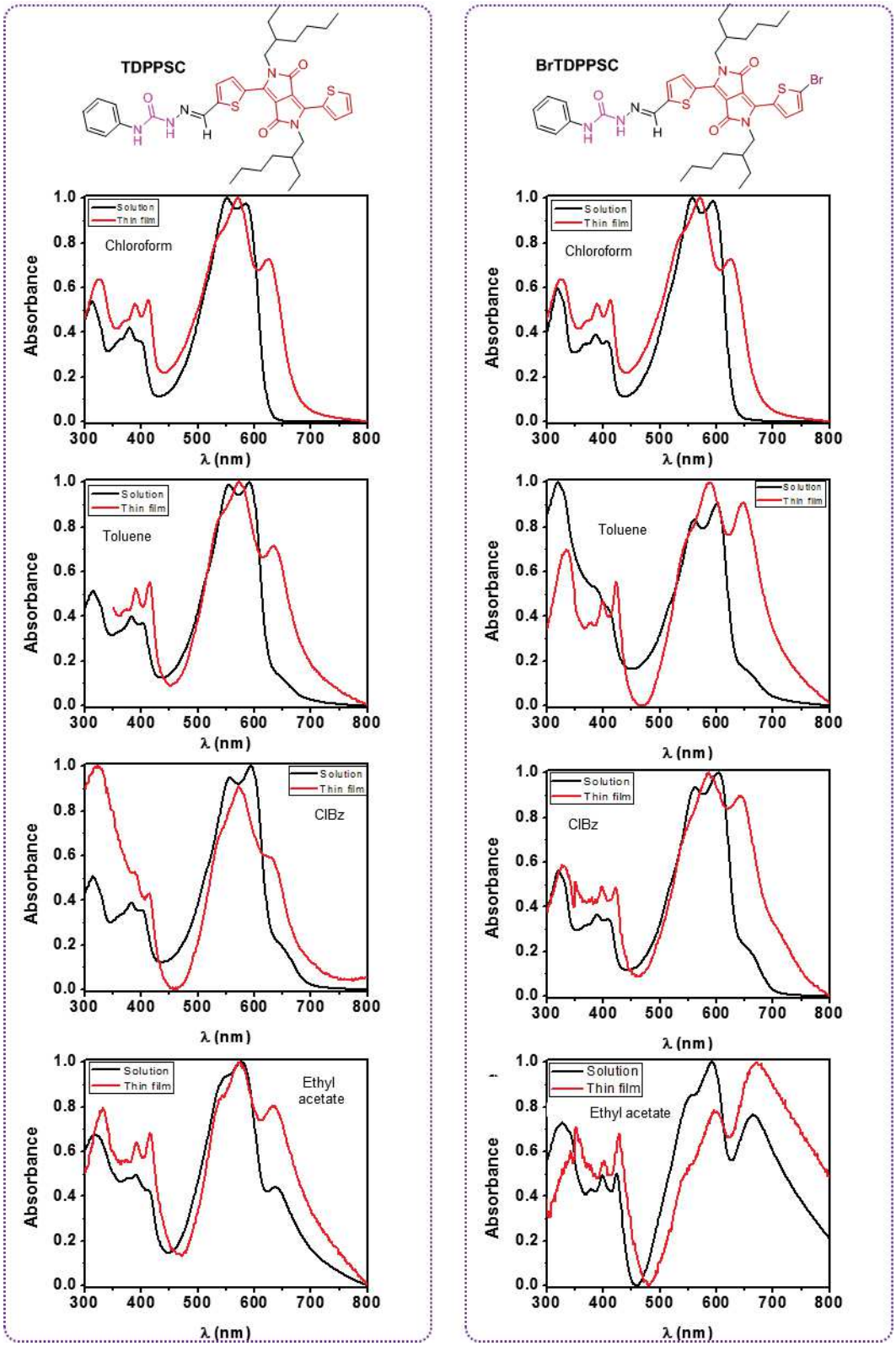

***Figure 11**: UV-vis spectra of both, **TDPPSC** and **BrTDPPSC** spin coated samples (c = 2.5 mg/mL).*

The spectra of the films are different form those of the solutions: a bathochromic shift was observed due to stronger intermolecular interactions in solid state; J-aggregate bands were more intense than in solution. The thin films absorption spectra of **TDPPSC** were very similar to the spectra in ethyl acetate solution (Figure 6) with increasing intensity of the J-type aggregate. The spectra of **BrTDPPSC** on thin film also revealed absorption bands similar to the ethyl acetate solution (Figure 10). For the thin film in the latter solvent, the absorption was red-shifted, with the J-aggregate band more intense indicating that hydrogen bonding is predominant (Figure 11)

IV. Electrochemical measurements. Energy levels calculation.

In order to determine whether **TDPPSC** and **BrTDPPSC** are suitable candidates for electronic devices, the energy levels were determined by cyclic voltammetry (Table 3). The highest occupied molecular orbital (HOMO) was determined by calculation using the following formula :

E_{HOMO}= -4.8+(0.49-E_{ox})

E_{ox} was determined from the onset of the oxidation wave of the cyclovoltammogram and 4.8 is the energy level of ferrocene/ ferrocenium (Fc/Fc^{+}) redox couple used as an external standard under the vacuum. The lowest unoccupied molecular orbital (LUMO) was also calculated with the following formula:

E_{LUMO}= -4.8+(0.49-E_{red})

E_{red} was determined from the onset of the reduction wave of the cyclovoltamogram. The energy band gap (Eg CV) is the difference between E_{HOMO} and E_{LUMO} .The HOMO energy levels found were -5.18 eV for **TDPPSC** and -5.26 eV for **BrTDPPSC**, whereas the LUMO energy levels were -3.43 eV for **TDPPSC** and -3.5 eV for **BrTDPPSC**. The corresponding energy band gaps are1.75 eV for both compounds (Table 3). The optical energy band gaps were also determined from the onsets of the absorption curves for both solution (Table 3) and thin film (Table 4) samples. The optical band gaps range from 1.69–1.96 eV for **TDPPSC** and from 1.72 to 1.90 eV for **BrTDPPSC**. These values are in good agreement with the electrochemical band gaps. These values make these semicarbazone **TDPPSC** suitable candidates for making OPVs or OFETs devices.

***Table 3**: Optoelectronic properties of solution samples.*

	Solvent	λmax abs sol (nm)	E sol opt (eV)	E HOMO (eV)	E LUMO (eV)	Eg CV (eV)
TDPSSC	Chloroform	504 (S), 552, 584	1.96	-5.18	-3.43	1.75
	Chlorobenzene	510 (S), 556, 595, 660	1.77			
	Toluene	505 (S), 555, 591, 654	1.74			
	Ethyl acetate	546,577,638	1.69			
BrTDPPSC	Chloroform	510 (S), 557, 594	1.90	-5.26	-3.5	1.76
	Chlorobenzene	510 (S), 562, 602,663	1.74			
	Toluene	509 (S), 561, 601, 667	1.72			
	Ethyl acetate	555, 593, 665	<1.5			

***Table 4**: Optoelectronic properties of spin coated samples.*

	Solvent	λmax abs film (nm)	E film opt (eV)
TDPSSC	Chloroform	533, 571, 624	1.77
	Chlorobenzene	535, 572, 633	1.67
	Toluene	535, 572, 634	1.65
	Ethyl acetate	539, 576, 633	1.50
BrTDPPSC	Chloroform	534, 570? 625	1.73
	Chlorobenzene	545, 587, 643	1.50
	Toluene	545, 587, 647	1.50
	Ethyl acetate	541, 597, 672	<1.5

V. Morphology studies using scanning electron microscopy (SEM)

In order to determine the morphology of **TDPPSC** and **BrTDPPSC** formed in the solutions examined previously, spin coated samples were prepared and analyzed by scanning electron microscopy (SEM) (Figure 12). Each sample observed showed different structures. When coated from solutions in chloroform **TDPPSC** and **BrTDPPSC** did not form any well-defined structure, which correlates to the fact that they are dissociated and not aggregated in this solvent. For all the other solvents, the micrographs show high aspect ratio aggregates. When casted from chlorobenzene solution, **DPPSC** molecules tended to form nanoribbons, whereas its brominated analog formed curved fibers. Spin coated samples of **TDPPSC** made with toluene solutions revealed the presence of nanotape structures. Regarding **BrTDPPSC** samples, entangled nanofibers were observed. Both molecules formed nanoribbon

structures on spin coated sample made with ethyl acetate solutions. From ethyl acetate, the compounds form thicker and longer fibers.

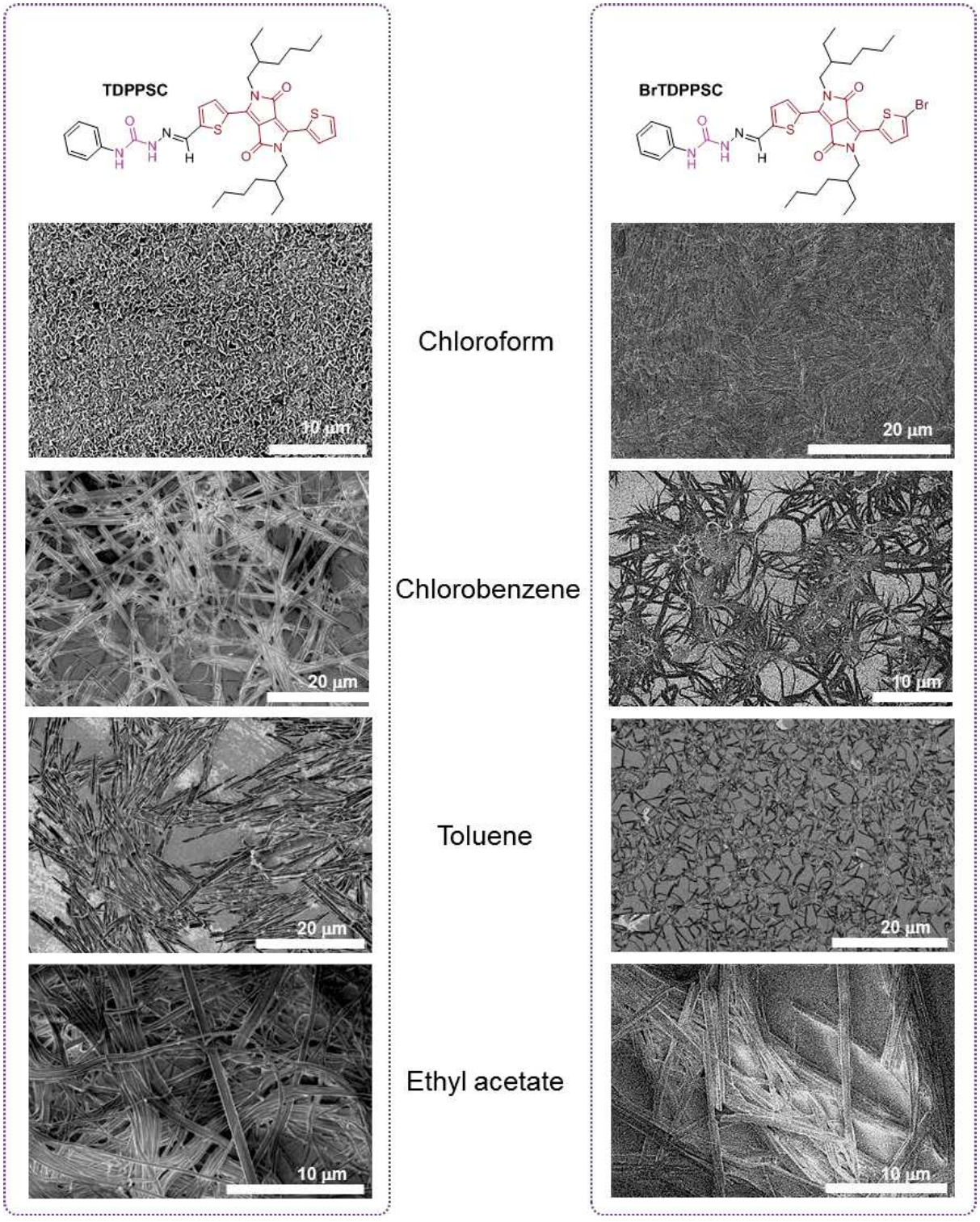

***Figure 12**: SEM images of thin films made by spin coating solutions at 2000 rpm of **TDPPSC** and **BrTDPPSC** in chloroform, chlorobenzene, toluene and ethyl acetate [**TDPPSC**]=[**BrTDPPSC**] = 2.5 mg/mL.*

Spin coated samples were also prepared using solutions in which small amounts of methanol were added (Figure 13). In all cases, most of the structures previously shown were disrupted to a large extent. Especially, the structures observe without methanol do not reform after evaporation of the solvent and methanol, or after evaporation of chloroform. It suggests that the observed structures exist in the cast solution and do not result from a mere drying effect.

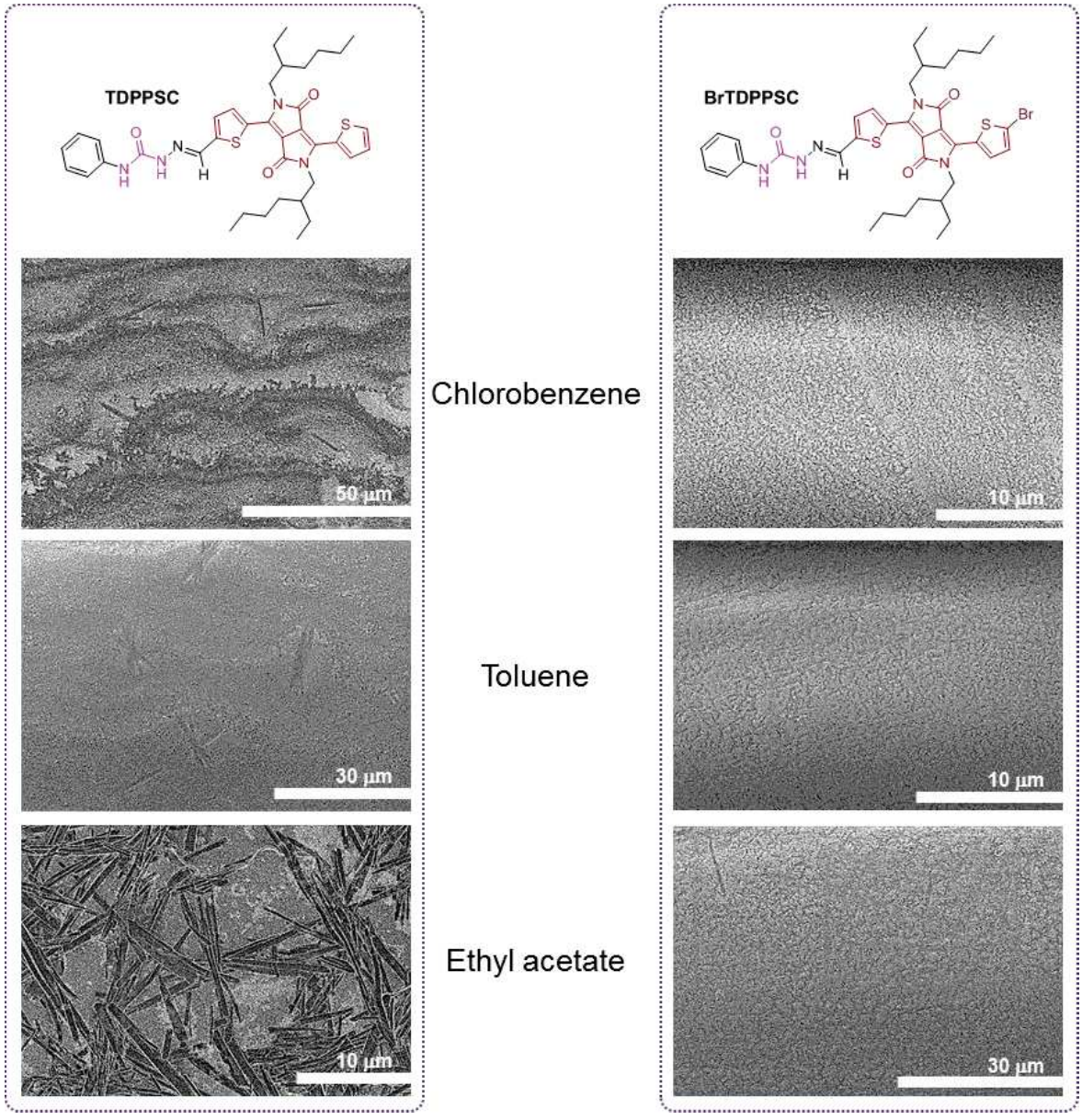

Figure 13: *SEM images of thin films made by spin coating solutions of* ***TDPPSC*** *and* ***BrTDPPSC*** *in chlorobenzene toluene and ethyl acetate after the addition of methanol. [**TDPPSC**] = [**BrTDPPSC**] = 2.5 mg/mL.*

This morphology study reveals the self-assembly of these **DPP** molecules are influenced by the nature of the organic solvent used, but also their structure since they

differ when a bromine atom is added. The exposure to methanol disrupts the aggregates, and complete the confirmation made by the UV and FT-IR spectroscopy analysis of the role of hydrogen bonding.

VI. Gel-like materials formation

After heating and cooling **BrTDPPSC** in ethyl acetate, the mixture formed a gel-like material for which absorption spectra revealed the formation of H- and J- type aggregates. Such phenomenon has already been previously reported in works made with hydrogen-bonded organogelators containing oligophiophenes and **DPP**[29–31]. Other gel-like materials were also obtained in cyclohexane and in *trans*-decalin, where nanofiber and nanoribbon structures could be observed on spin coated samples by SEM microscopy (Figure 14).

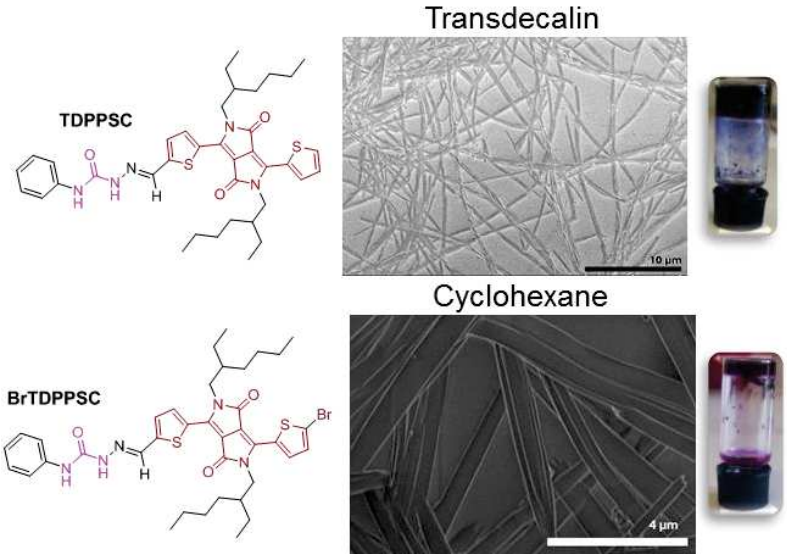

Figure 14: *Gel-like material formed by* ***TDPPSC*** *and* ***BrTDPPSC*** *in trans-decalin and cyclohexane respectively.*

Unfortunately, these gel-like materials were unstable since they instantly underwent a macroscopic phase separation at room temperature, with the solid at the bottom and the liquid phase above. Furthermore, solubility issues were encountered since the products did not dissolved entirely when the solutions prepared where heated up. Another issue encountered was the thermal stability of the **DPP** molecules. Thermogravimetric analysis (TGA) was performed (Figure 14) on **DPPSC** and **BrTDPPSC**, with a temperature range between 25 and 700 °C and a temperature rate of 10 °C per minute. In both cases, the molecules started to degrade at 140 °C, which could be detrimental when solvents with high ebullition point such as *trans*-decalin are used for self-assembly studies.

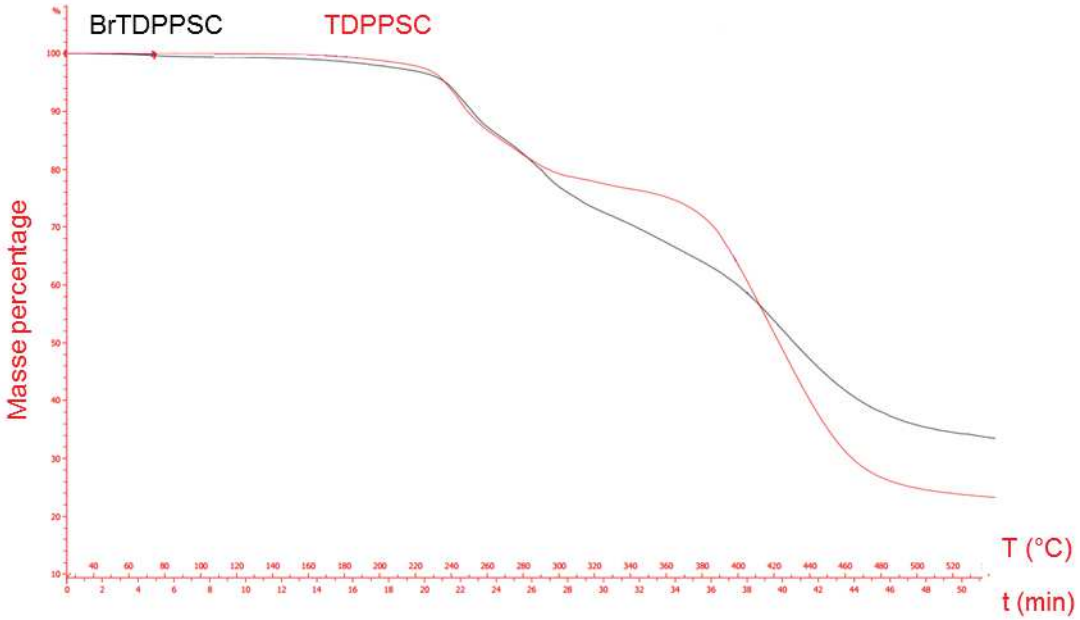

Figure 15: *Thermogravimetic analysis of* ***TDPPSC*** *and* ***BrTDPPSC****.*

VII. Conclusion and perspective

In summary, two **DPP** derivatives containing semicarbazone moieties have been synthesized and their optical and self-assembly properties have been studied. The formation of hydrogen bonds resulted in the appearance of J-aggregates reaching the near infrared region. These aggregates are influenced by the nature of solvents, the concentrations, and temperature variations. The appearance of such aggregate band is particularly interesting since it has been reported to be beneficial for the development organic electric devices.

Thin films were studied by scanning electron microscopy (SEM), different structures in all solvents were found. This will be particularly interesting to study the influence of different morphologies in device performance and to study charge transport using different structures.

Studies are currently devoted to examine charge transport and device performance at different aggregation states. The energy levels were calculated using cyclic voltammetry, finding HOMO values between -5.2 to -5.52 eV and LUMO values between -3.26 to -3.58 eV, which are very appropriate values for device fabrication.

The compounds have been tested in transistors. However, no current was detected due to processing issues. As shown by SEM images of the organic devices, the aggregates were too short to connect the electrodes (Figure 16), thus preventing current circulation. Thin films made by drop casting were therefore prepared and observed by SEM microscopy (Figure 16).

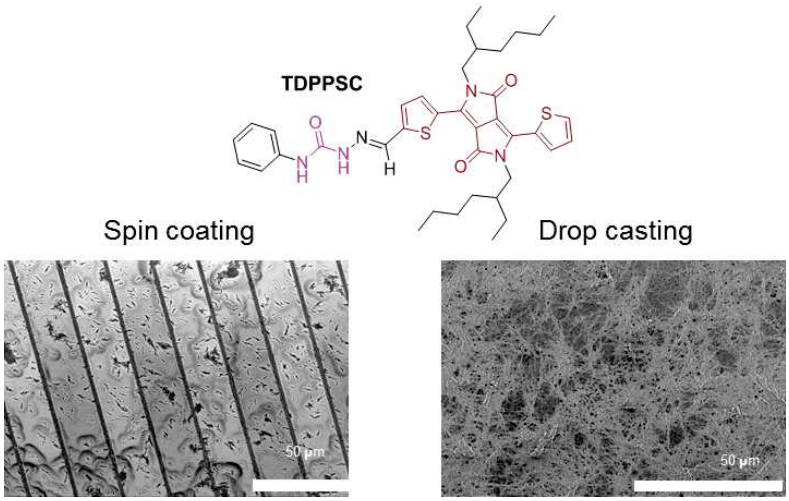

Figure 16: *Comparison between spin coating and drop casting deposition technic made with* ***TDPPSC*** *solutions in chlorobenzene.*

The images showed a network of fibers with lengths superior to 100 µm, which is long enough for connecting the electrodes of the transistor devices. We compared warm and cold drop casting of a semicarbazone **DPP** with butyl octyl branches (Figure 17). This molecule was synthesized using the same procedure as for its analogs with ethyl hexyl carbon chains and should provide more solubility.

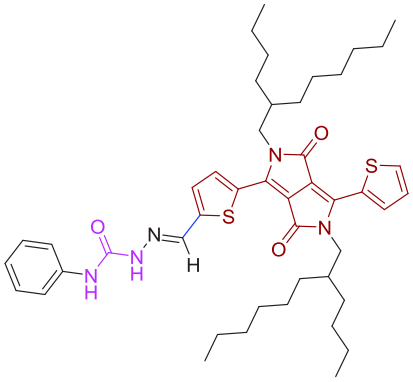

Figure 17: *Chemical structure of semicarbazone* ***DPP*** *with butyl octyl branches*

Once synthesized and analyzed, the molecule was diluted in solvents used for the previous compounds at the same concentration. The solutions were then heated up to boiling points until the **DPP** totally dissolved, and were instantly deposited on glass support (warm drop casting). The film was dried for 5 minutes and analyzed by SEM microscopy (Figure 18).

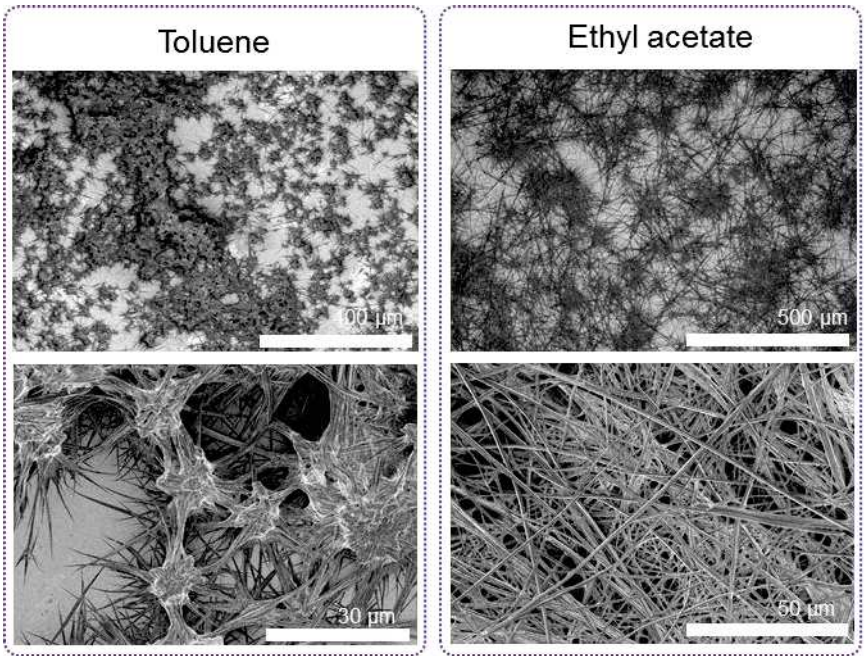

Figure 18: *Comparison between drop cast samples made with ethyl acetate and toluene solution samples; C = 5 mg/mL.*

The images revealed the formation of a network of tapes interconnected by knots in which the bands are overlapped and entangled. A major difference observed when comparing the samples was the length and shape of the structures formed. The solution samples made with toluene formed nanobands with an averages width of 20 nm with pointy extremities. Regarding the samples made in ethyl acetate, the SEM images showed the presence of bands with length reaching several hundreds of micrometers, which could therefore cover the electrodes of the transistor devices. The samples made with ethyl acetate would therefore be a perfect candidate for making organic devices despite the fact a lot of process work will be needed in order to improve the results. Since the derivatives with butyloctyl akyl tails are more soluble and seem to form better quality films, the next studies on this family will be focused on such alkyl side chains. UV absorption spectra were measured at ambient temperature with the same solvent than for the ethyl hexyl analogs. Other solvents such as cyclohexane and *trans*-decalin were also tested. The aggregate signals are less intense than for the ethyl hexyl analogue. This behavior is because the butyloctyl alkyl tails make the molecule more soluble. The signals are considerably decreased in ethyl acetate; it is in only in solvents such as cyclohexane and *trans*-decalin that they remain significative.

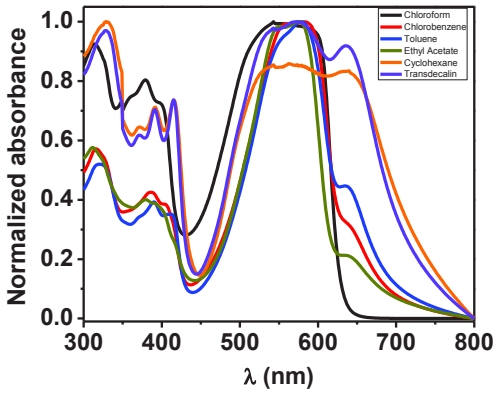

Figure 19: *UV absorption spectra in all solvents at room temperature. (c= 2.5 mg/mL and 1.25 mg/mL in chloroform).*

Due to the large amount of parameters that can be tested (concentration, solvents and temperature), faster screening methods to measure charge transport are very convenient. For this purpose, dielectric loss microwave spectroscopy measurements are being performed in collaboration with the group of Prof. Shu Seki from the University of Kyoto. They have pioneered contactless techniques based on microwave conductivity, where multiple conditions can be tested without the need of fabricating entire devices. A technique named flash-photolysis time-resolved microwave conductivity (FP-TRMC) has been applied to measure photoconductivity as $\Phi\Sigma\mu$ were Φ is the charge carrier generation quantum yield and $\Sigma\mu$ is the sum of charge carrier mobilities, meaning the sum of electron and hole mobilities. Drop cast samples in different conditions have been measured and the results will be discussed in the next chapters.

References

[1] J. B. Ubbink, W. J. Serfontein, L. S. De Villiers, *J. Chromatogr. B. Biomed. Sci. App.* **1985**, *342*, 277–284.
[2] M. Cigáň, J. Gašpar, K. Gáplovská, J. Holekšiová, K. Jakusová, J. Donovalová, V. Garaj, H. Stankovičová, *New J. Chem.* **2016**, *40*, 8946–8953.
[3] D. Palanimuthu, Z. Wu, P. J. Jansson, N. Braidy, P. V. Bernhardt, D. R. Richardson, D. S. Kalinowski, *Dalton Trans.* **2018**, *47*, 7190–7205.
[4] D. C. Greenbaum, Z. Mackey, E. Hansell, P. Doyle, J. Gut, C. R. Caffrey, J. Lehrman, P. J. Rosenthal, J. H. McKerrow, K. Chibale, *J. Med. Chem.* **2004**, *47*, 3212–3219.
[5] S. Datta, D. Kumar Seth, S. Halder, W. S. Sheldrick, H. Mayer-Figge, M. G. B. Drew, S. Bhattacharya, *RSC Adv.* **2012**, *2*, 5254.
[6] X. Yang, L. Zheng, L. Xie, Z. Liu, Y. Li, R. Ning, G. Zhang, X. Gong, B. Gao, C. Liu, et al., *Sens. Actuators B Chem.* **2015**, *207*, 9–24.
[7] A. Iqbal, M. Jost, R. Kirchmayr, J. Pfenninger, A. Rochat, O. Wallquist, *Bull. Sociétés Chim. Belg.* **2010**, *97*, 615–644.
[8] F. Pop, J. Humphreys, J. Schwarz, L. Brown, A. van den Berg, D. B. Amabilino, *New J. Chem.* **2019**, *43*, 5783–5790.

[9] G. Qian, J. Qi, J. A. Davey, J. S. Wright, Z. Y. Wang, *Chem. Mater.* **2012**, *24*, 2364–2372.
[10] Š. Frebort, Z. Eliáš, A. Lyčka, S. Luňák, J. Vyňuchal, L. Kubáč, R. Hrdina, L. Burgert, *Tetrahedron Lett.* **2011**, *52*, 5769–5773.
[11] M. V. R. Raju, H.-C. Lin, *Org. Lett.* **2013**, *15*, 1274–1277.
[12] X. A. Jeanbourquin, A. Rahmanudin, A. Gasperini, E. Ripaud, X. Yu, M. Johnson, N. Guijarro, K. Sivula, *J. Mater. Chem. A* **2017**, *5*, 10526–10536.
[13] A. Rahmanudin, X. A. Jeanbourquin, S. Hänni, A. Sekar, E. Ripaud, L. Yao, K. Sivula, *J. Mater. Chem. A* **2017**, *5*, 17517–17524.
[14] K.-H. Kim, H. Yu, H. Kang, D. J. Kang, C.-H. Cho, H.-H. Cho, J. H. Oh, B. J. Kim, *J. Mater. Chem. A* **2013**, *1*, 14538.
[15] W. Hong, B. Sun, H. Aziz, W.-T. Park, Y.-Y. Noh, Y. Li, *Chem. Commun.* **2012**, *48*, 8413.
[16] B. P. Karsten, J. C. Bijleveld, R. A. J. Janssen, *Macromol. Rapid Commun.* **2010**, *31*, 1554–1559.
[17] A. S. Davidov, **1971**.
[18] H. Kar, D. W. Gehrig, N. K. Allampally, G. Fernández, F. Laquai, S. Ghosh, *Chem. Sci.* **2016**, *7*, 1115–1120.
[19] F. Würthner, T. E. Kaiser, C. R. Saha-Möller, *Angew. Chem. Int. Ed.* **2011**, *50*, 3376–3410.
[20] A. Das, S. Ghosh, *Chem. Commun.* **2016**, *52*, 6860–6872.
[21] F. Würthner, C. Thalacker, A. Sautter, *Adv. Mater.* **1999**, *11*, 754–758.
[22] D. González-Rodríguez, A. P. H. J. Schenning, *Chem. Mater.* **2011**, *23*, 310–325.
[23] M. Kirkus, L. Wang, S. Mothy, D. Beljonne, J. Cornil, R. A. J. Janssen, S. C. J. Meskers, *J. Phys. Chem. A* **2012**, *116*, 7927–7936.
[24] M. Más-Montoya, R. A. J. Janssen, *Adv. Funct. Mater.* **2017**, *27*, 1605779.
[25] N. J. Hestand, F. C. Spano, *Chem. Rev.* **2018**, *118*, 7069–7163.
[26] F. C. Spano, *Acc. Chem. Res.* **2010**, *43*, 429–439.
[27] M. Más-Montoya, R. A. J. Janssen, *Adv. Funct. Mater.* **2017**, *27*, 1605779.
[28] F. Würthner, T. E. Kaiser, C. R. Saha-Möller, *Angew. Chem.* **2011**, *123*, 3436–3473.
[29] S. Ghosh, S. Cherumukkil, C. H. Suresh, A. Ajayaghosh, *Adv. Mater.* **2017**, *29*, 1703783.
[30] W.-W. Tsai, I. D. Tevis, A. S. Tayi, H. Cui, S. I. Stupp, *J. Phys. Chem. B* **2010**, *114*, 14778–14786.
[31] A. Ruiz-Carretero, T. Aytun, C. J. Bruns, C. J. Newcomb, W.-W. Tsai, S. I. Stupp, *J. Mater. Chem. A* **2013**, *1*, 11674.

Experimental

Materials and methods

All reagents and solvents were obtained from commercial suppliers and purified or dried according to standard procedures. Column chromatography was performed on silica gel (VWR Silica 60, particle size 0.040–0.063 mm). Solvents for spectroscopic studies were of spectroscopic grade and used as received.

Measurements and Characterization

Elemental analysis was performed on a Thermofischer Scientific Flash 2000. Matrix-assisted laser desorption/ionisation-time of filght (MALDI) was performed in a Bruker Daltonics. ^{1}H and 13C spectra were recorded in $CDCl_3$ on a Bruker Avance 400 MHz spectrometer and/or Bruker Avance III HD 500 MHz spectrometer. UV–vis measurements were performed in a conventional quartz cell (light pass 1 mm) on a Cary 5000 UV-Vis-NIR spectrophotometer. For cyclic voltammetry, a standard commercial electrochemical analyzer (BioLogic VSP potentiostat) with a three electrode single-compartment cell was used. CH_2Cl_2 (HPLC grade) was dried over calcium hydride under argon and degassed before use. The supporting electrolyte used was tetrabutylammonium hexafluorophosphate ($TBAPF_6$, 0.1 M). The measurements were carried out in CH_2Cl_2 at a concentration of 1 mM with ferrocene (Fc) as an internal standard for the calibration of the potential (scan speed: 100 mV s−1). Ag/AgCl, a Pt disc, and a Pt wire were used as reference, working, and auxiliary electrodes, respectively. SEM images were taken with a Hitachi SU8010 microscope. FTIR spectra were recorded with a Vertex 70 from Bruker Optics, equipped with MCT detector and a black-body source. The spectra of the solids were measured by ATR on diamond. The solutions were studied in cells from Specac with KBr windows. The spin coated samples were prepared using a Spin 150 spin coater at 2000 rpm using 80 □l of solution on glass slides or silicon wafers.

Synthesis

The initial ethylhexyl alkylated and the monobrominated **DPP** starting materials were synthesized according to a reported literature procedure.

<u>Compound 1 (TDPP):</u> 3,6-di(thiophen-2-yl)-2,5-dihydropyrrolo[3,4-c]pyrrole-1,4-dione

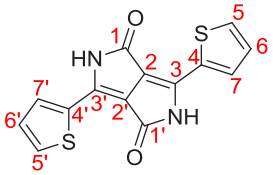

A solution of 2-thiophenecarbonitrile (10.4 g, 95 mmol) and potassium tert-butoxyde (12.3 g, 109 mmol) was stirred under argon in *tert*-amyl alcohol (200 ml) at 120°C. Diethyl succinate (8.25 g, 47 mmol) was added dropwise. The solution was stirred at 120 °C overnight, and cooled down to room temperature. The mixture was neutralized

with 5 ml of concentrated acetic acid while being vigorously stirred for two hours at ambient temperature. The crude was filtered, washed several times with MeOH and dried to afford **TDPP** as a dark red solid (11.6 g, 82 %).

^{1}H-NMR (400 MHz, DMSO) δ [ppm]: 8.22 (d, *J* = 3.42 Hz, 2H, H_5 and $H_{5'}$); 7.88 (d, *J* = 4.76 Hz, 2H, H_7 and $H_{7'}$); 7.26 (t, *J* = 4.2 Hz, 2H, H_6 and $H_{6'}$)

^{13}C NMR (126 MHz, DMSO) δ [ppm]: 174.16 (C_7 and $C_{7'}$), 148.68 (C_2 and $C_{2'}$), 133.41 (C_3 and $C_{3'}$), 130.52 (C_6 and $C_{6'}$), 130.18 (C_4 and $C_{4'}$), 128.33 (C_5 and $C_{5'}$), 110.41 (C_1 and $C_{1'}$).

HRMS (ESI+) m/z: 301.0095; calcd for $C_{14}H_9N_2O_2S_2$ (MH+): 301.0100

<u>Compound 2</u>: 2,5-bis(2-ethylhexyl)-3,6-di(thiophen-2-yl)-2,5-dihydropyrrolo[3,4-c]pyrrole-1,4-dione

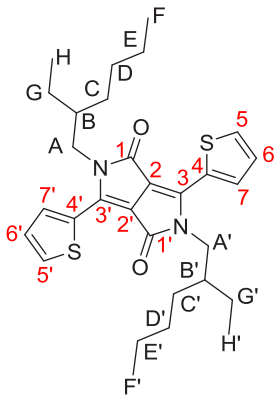

A solution of **TDPP** (10 g, 33,6 mmol) in anhydrous DMF (150 ml) was stirred under argon at 120°C. Cs_2CO_3 (27 g, 83 mmol) was added progressively. The mixture was stirred for 1 h at 120° C. 2-ethylhexyl bromide (16.22 g, 84 mmol) was added dropwise and the solution was stirred overnight at 120°C. After cooling at room temperature, it was mixed with distilled water (600ml) and the mixture was extracted with DCM. The organic phase was dried ($MgSO_4$) and the solvent was removed under vacuum. The crude was purified by column chromatography (DCM/cyclohexane: 50/50) to afford **compound 2** as a dark red solid (3,1 g, 17%).

Improved protocol:

TDPP (1 g, 3.3 mmol) was dissolved in anhydrous DMF (10 ml) under argon.2-ethylhexyl bromide (2.56 g, 8.3 mmol) then Cs_2CO_3 (2.72 g, 8.3 mmol) were added and the solution was stirred for 72 h at room temperature. The solvent was removed under vacuum and the residue was dissolved in chloroform, washed with distilled water and dried with $MgSO_4$. The solvent was removed under vacuum and the crude was purified by column chromatography (cyclohexane/THF: 60/40) to afford **compound 2** as a dark red solid (471 mg, 27%).

^{1}H-NMR (400 MHz, CD_2Cl_2) δ [ppm]: 8.85 (dd, *J* = 4, 1.1 Hz, 2H, H_5 and $H_{5'}$); 7.67 (dd, *J* = 5.1, 1.1 Hz, 2H, H_7 and $H_{7'}$); 7.26 (dd, *J* = 5.1, 4 Hz, 2H, H_6 and $H_{6'}$), 4 (m, 2H, H_A

and $H_{A'}$), 1.83 (m, 2H, H_B and $H_{B'}$), 1.31 (m, 16H, H_C, $H_{C'}$, H_D, $H_{D'}$, H_E, $H_{E'}$, H_G and $H_{G'}$), 0.87 (m, 12H, H_F, $H_{F'}$, H_H and H_H).

^{13}C NMR (101 MHz, CDCl3) δ 161.53 (C_1 and $C_{1'}$), 140.23 (C_3 and $C_{3'}$), 135.28 (C_4 and $C_{4'}$), 130.46 (C_5 and $C_{5'}$), 129.77 (C_6 and $C_{6'}$), 128.31 (C_7 and $C_{7'}$), 107.77 (C_2 and $C_{2'}$), 45.74 (C_A and $C_{A'}$), 39.00 (C_B and $C_{B'}$), 30.15 (C_C and $C_{C'}$), 28.29 (C_D and $C_{D'}$), 23.49 (C_G and $C_{G'}$), 23.01 (C_E and $C_{E'}$), 13.99 (C_F and $C_{F'}$), 10.43 (C_H and $C_{H'}$).

HRMS (ESI+) m/z: 525.2573; calcd for $C_{30}H_{41}N_2O_2S_2$ (MH+): 525.2604

Elemental analysis. Found : C 68.80; H, 7.87; N, 5.09. Calculated : C, 68.60; H, 7.68; N, 5.34.

<u>Compound 3</u>: 3-(5-bromothiophen-2-yl)-2,5-bis(2-ethylhexyl)-6-(thiophen-2-yl)-2,5dihydropyrrolo[3,4-c]pyrrole-1,4-dione

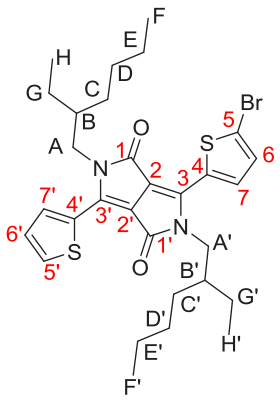

A solution of alkylated **DPP 7** (3 g, 5,7 mmoles) was stirred under argon in chloroform (200 ml) at 0°C. A solution N-Bromosuccinimide (0,516 g, 2,84 mmoles) in chloroform (150 ml) was added very slowly. The mixture was stirred overnight at ambient temperature. The reaction was quenched with water and the organic phase was dried with $MgSO_4$, filtered and concentrated under vacuum. The product was purified by column chromatography (DCM/cyclohexane: 50/50) to afford **compound 3** as a dark purple solid (0,98 g, 57 %).

^{1}H NMR (400 MHz, CD_2Cl_2) δ [ppm]: 8.86 (dd, *J* = 3.9, 1.2 Hz, 1H, $H_{5'}$), 8.60 (d, *J* = 4.2 Hz, 1H, H_7), 7.69 (dd, J = 5.0, 1.2 Hz, 1H, $H_{7'}$), 7.29 (dd, *J* = 5.0, 3.9 Hz, 1H, $H_{6'}$), 7.26 (d, *J* = 4.2 Hz, 1H, H_6), 4.07 – 3.83 (m, 4H, H_A and $H_{A'}$), 1.94 – 1.72 (m, 2H, H_B and $H_{B'}$), 1.44 – 1.13 (m, 16H, H_C, $H_{C'}$, H_D, $H_{D'}$, H_E, $H_{E'}$, H_G and $H_{G'}$), 0.97 – 0.76 (m, 12H, H_F, $H_{F'}$, H_H and H_H).

^{13}C-NMR (100 MHz, $CDCl_3$) δ [ppm]: 161.85 (C_1 and $C_{1'}$), 141.09 ($C_{3'}$) 139.14 (C_3), 135.74 (C_7), 135.28($C_{7'}$), 131.58 (C_3 and $C_{3'}$), 131.46 (C_4), 131.03 ($C_{4'}$), 129.94 (C_6), 128.68 ($C_{6'}$), 118.82 (C_5), 108.36 ($C_{2'}$), 107.99 (C_2), 46.19 (C_A and $C_{A'}$), 39.39 (C_B and $C_{B'}$), 33.22 (C_C and $C_{C'}$), 30.25 (C_D and $C_{D'}$), 28.40 (C_G and $C_{G'}$), 23.66, 23.14 (C_E and $C_{E'}$), 14.13 (C_F and $C_{F'}$), 10.56 (C_H and $C_{H'}$).

HRMS (ESI+) m/z: 603.1717; calcd for $C_{30}H_{40}BrN_2O_2S_2$ (MH+): 603.1709

<u>Compound 4a</u>: 5-(2,5-bis(2-ethylhexyl)-3,6-dioxo-4-(thiophen-2-yl)-2,3,5,6-tetrahydropyrrolo[3,4-c]pyrrol-1-yl)thiophene-2-carbaldehyde

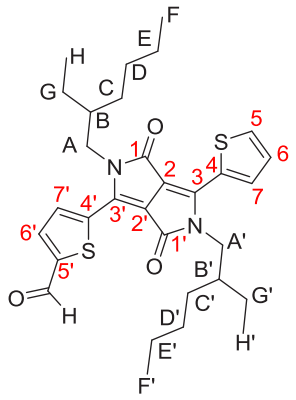

A solution of **DPP** alkylated with ethylhexyl (1.2 g, 2.3 mmol) in dichloroethane (20ml) was stirred at 80 °C. Meanwhile in a separate vial, the Vilsmeier-Haack reagent was prepared by adding $POCl_3$ (3.2 ml, 34 mmol) to DMF (2,7 ml, 35 mmol) at 80 °C. The mixture turned instantly dark orange and was immediately added to the **DPP** solution. The reaction was stirred at 80 °C overnight and was cooled down to room temperature. Aqueous saturated $NaHCO_3$ solution was added and the crude was extracted with dichloromethane. The organic phase was dried with $MgSO_4$ and filtered. After the solvent was removed under vacuum, the crude was purified by column chromatography (DCM/heptane 80/20) to afford **compound 4a** as a purple solid (147 mg, 12 %).

1H NMR (400 MHz, CD_2Cl_2) δ [ppm]: 9.98 (s, 1H, CHO), 9.01 (dd, J = 3.9, 1.2 Hz, 1H, H_5), 8.87 (d, J = 4.2 Hz, 1H, $H_{6'}$), 7.85 (d, J = 4.2 Hz, 1H, $H_{7'}$), 7.75 (dd, J = 5.0, 1.2 Hz, 1H, H_7), 7.31 (dd, J = 5.0, 3.9 Hz, 1H, H_6), 4.00 (s, 4H, H_A and $H_{A'}$), 1.82 (m, 2H, H_B and $H_{B'}$), 1.32 (m, 16H, H_C, $H_{C'}$, H_D, $H_{D'}$, H_E, $H_{E'}$, H_G and $H_{G'}$), 0.85 (s, 12H, H_F, $H_{F'}$, H_H and $H_{H'}$).

^{13}C-NMR (100 MHz, $CDCl_3$) δ [ppm]: 182.88 (CHO), 161.28 (C_1 and $C_{1'}$), 145.84 ($C_{5'}$), 141.55 (C_3 and $C_{3'}$), 138.5 (C_4 and $C_{4'}$), 136.15 (C_5), 135.65 ($C_{7'}$), 134.26 ($C_{6'}$), 131.78 (C_7), 129.32 (C_6), 128.23, 120.59, 110.84 (C_2), 108.33 ($C_{2'}$), 46.19 (C_A and $C_{A'}$), 39.39 (C_B and $C_{B'}$), 33.22 (C_C and $C_{C'}$), 30.25 (C_D and $C_{D'}$), 28.40 (C_G and $C_{G'}$), 23.66, 23.14 (C_E and $C_{E'}$), 14.13 (C_F and $C_{F'}$), 10.56 (C_H and $C_{H'}$).

HRMS (ESI+) m/z: 301.0095; calcd for $C_{14}H_9N_2O_2S_2$ (MH+): 301.0100

<u>Compound 4b</u>: 5-(4-(5-bromothiophen-2-yl)-2,5-bis(2-ethylhexyl)-3,6-dioxo-2,3,5,6-tetrahydropyrrolo[3,4-c]pyrrol-1-yl)thiophene-2-carbaldehyde

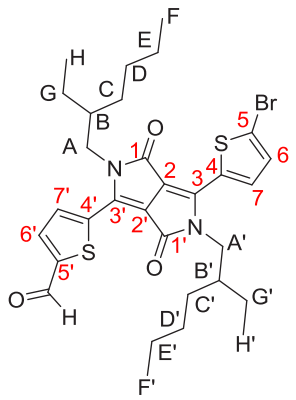

DPPBr (370 mg, 0.6 mmol) was placed in a flask and dissolved in DCM (25 ml). The solution was stirred at 80 °C. Meanwhile in a small vial, the Vilsmeier-Haack reagent was prepared by adding $POCl_3$ (1.2 ml, 12.6 mmol) to DMF (0.98 ml, 12.6 mmol) at 80°C. The mixture turned instantly dark red and immediately was added into the DPPBr solution. The reaction was stirred at 80 °C overnight and was cooled down to room temperature. Aqueous $NaHCO_3$ (saturated) was added and the crude was extracted with dichloromethane. The organic phase was dried ($MgSO_4$) and the solvent removed under vacuum. The crude was purified by column chromatography (DCM/heptane : 80/20) to afford **compound 4b** as a purple solid (33 mg, 8.5 %).

1H NMR (400 MHz, CD_2Cl_2) δ [ppm]: δ 10.00 (s, 1H, CHO), 8.86 (d, J = 4.2 Hz, 1H, $H_{6'}$), 8.76 (d, J = 4.2 Hz, 1H, $H_{7'}$), 7.87 (d, J = 4.2 Hz, 1H, H_7), 7.29 (d, J = 4.2 Hz, 1H, H_6), 4.04 (m, 4H, H_A and $H_{A'}$), 1.81 (m, J = 5.9 Hz, 2H, H_B and $H_{B'}$), 1.31 (m, 16H, H_C, $H_{C'}$, H_D,$H_{D'}$, H_E, $H_{E'}$, H_G and $H_{G'}$), 0.87 (s, 16H, s, 12H, H_F, $H_{F'}$, H_H and $H_{H'}$).

^{13}C-NMR (100 MHz, CD_2Cl_2) δ [ppm]: 182.88 (CHO), 161.68 (C_1 and $C_{1'}$), 141.09 (C_3 and $C_{3'}$), 139.14 (C_4 and $C_{4'}$), 135.74 (C_7), 131.58 ($C_{7'}$), 131.03 (C_6), 129.94 ($C_{6'}$), 128.68 ($C_{5'}$), 118.82 (C_5), 110.84 (C_2), 108.33 ($C_{2'}$), 46.19 (C_A and $C_{A'}$), 39.39 (C_B and $C_{B'}$), 33.22 (C_C and $C_{C'}$), 30.25 (C_D and $C_{D'}$), 28.40 (C_G and $C_{G'}$), 23.24 (C_E and $C_{E'}$), 14.21 (C_F and $C_{F'}$), 10.68 (C_H and $C_{H'}$).

TDPPSC: (E)-2-((5-(2,5-bis(2-ethylhexyl)-3,6-dioxo-4-(thiophen-2-yl)-2,3,5,6-tetrahydropyrrolo[3,4-c]pyrrol-1-yl)thiophen-2-yl)methylene)-N-phenylhydrazine-1-carboxamide

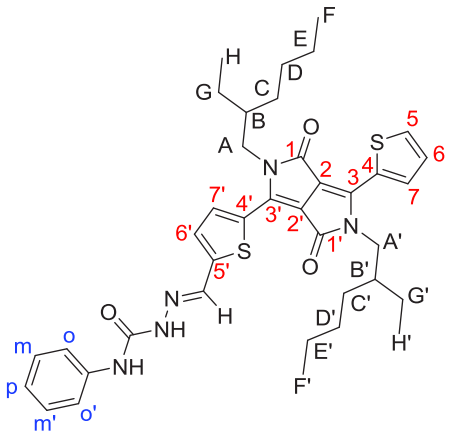

A solution of DPPCHO (147 mg, 0.26 mmol) and 4-phenylsemicarbazide (84.2 mg, 0.53 mmol) in EtOH (20 ml) and DCM (2 ml) was stirred at 80 °C and 4 drops of concentrated acetic acid were added. The mixture was stirred at 80 °C overnight and cooled down to room temperature. The solvent was removed under vacuum and the crude was purified by column chromatography (99% dichloromethane: 1% methanol) to afford **TDPPSC** as a purple solid (130.4 mg, 71 %).

^{1}H-NMR (400 MHz, $CDCl_3$) δ [ppm]: 9.29 (s, 1H, H_A), 8.98 (d, J= 3.9 Hz, 1H, H_5), 8.96 (d, J= 4.1 Hz, 1H, $H_{7'}$) 8.06 (s, 1H, NH), 8.01 (s, 1H, NH), 7.69 (dd, J= 5, 1.2 Hz, 1H, H_7), 7.57 (d, J = 7.6 Hz, 2H, H_O), 7.44-7.34 (t, 3H, Hm and $H_{6'}$), 7.32 (m, 1H, H_6), 7.16 (t, *J*= 7.5 Hz, 1H, H_p), 4.09 (m, 4H, H_A and $H_{A'}$), 1.93 (m, 2H, H_B and $H_{B'}$), 1.34 (m, 16H, H_C, $H_{C'}$, H_D,$H_{D'}$, H_E, $H_{E'}$, H_G and $H_{G'}$), 0.90 (s, 12H, H_F, $H_{F'}$, H_H and $H_{H'}$).

^{13}C NMR (126 MHz, $CDCl_3$) δ [ppm]: 161.90 (C_1 and $C_{1'}$), 152.83 (NHCONH), 142.71 ($C_{5'}$), 141.30 (C_3 and $C_{3'}$), 139.34 (C_4), 137.66 ($C_{4'}$), 135.99 (C_5), 135.80 ($C_{7'}$), 135.17 ($C_{6'}$), 131.24, 131.22 (C_7), 130.26 (CH=N-), 129.86 (C_{arom}-NH-CO-NH-), 129.26 (C_m and $C_{m'}$), 128.72 (C_6), 124.04 (C_p), 119.86 (C_o and $C_{o'}$), 109.42 (C_2), 108.29 ($C_{2'}$), 46.12 (C_A and $C_{A'}$), 39.42 (C_B and $C_{B'}$), 30.42 (C_C and $C_{C'}$), 29.85 (C_D and $C_{D'}$), 28.43 (C_G and $C_{G'}$), 23.21 (C_E and $C_{E'}$), 14.15 (C_F and $C_{F'}$), 10.71 (C_H and $C_{H'}$).

MS (MALDI+) m/z: 686.3200; calcd for $C_{38}H_{48}BrN_5O_2S_2$ (MH+): 685.3200

Elemental analysis. Obtained: C, 66.59; H, 6.91; N, 10.22. Calculated: C, 66.10; H, 6.92; N, 10.25.

<u>BrTDPPSC:</u> (E)-2-((5-(4-(5-bromothiophen-2-yl)-2,5-bis(2-ethylhexyl)-3,6-dioxo-2,3,5,6-tetrahydropyrrolo[3,4-c]pyrrol-1-yl)thiophen-2-yl)methylene)-N-phenylhydrazine-1-carboxamide

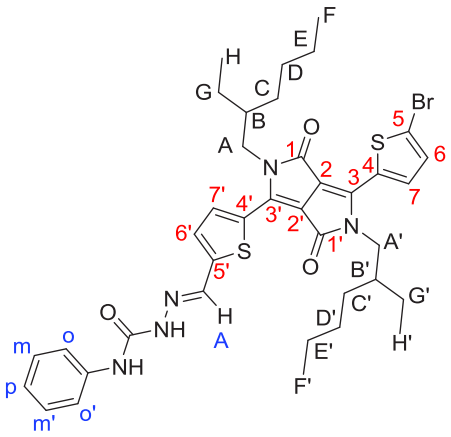

A solution of BrDPPCHO (106 mg, 0.17 mmol) and 4-phenylsemicarbazide (51.6 mg, 0,33 mmol) in EtOH (20 ml) and DCM (2 ml) was stirred at 80°C and 4 drops of concentrated acetic acid were added. The mixture was stirred at 80°C overnight and cooled down to room temperature. The solvent was removed under vacuum and the crude was purified by column chromatography (MeOH/DCM 1/99) to afford **BrTDPPSC** as a purple solid (69.7 mg, 56 %).

^{1}H-NMR (400 MHz, $CDCl_3$) δ [ppm]: 8.94 (d, J = 4.1 Hz, 1H, $H_{7'}$), 8.71(s, 1H, H_A), 8.71 (d, J = 4.2 Hz, 1H, H_7), 7.54 (d, J = 7.6 Hz, 2H, H_O), 8.06 (s, 1H, NH), 8.01 (s, 1H, NH), 7.37 (m, 3H, H_m and $H_{6'}$), 7.25 (d, J = 4.2 Hz, 1H, H_6), 7.14 (t, J= 7.2 Hz, 1H, H_p), 4.02 (m, 4H, H_A and $H_{A'}$), 1.89 (m, 2H, C_B and $C_{B'}$), 1.45 – 1.15 (m, 16H, H_C, $H_{C'}$, H_D,$H_{D'}$, H_E, $H_{E'}$, H_G and $H_{G'}$), 0.91 (s, 12H, H_F, $H_{F'}$, H_H and $H_{H'}$).

^{13}C-NMR (100 MHz, $CDCl_3$) δ [ppm]: 161.51 (C_1 and $C_{1'}$), 152.44 (NHCONH), 142.77 (C_3 and $C_{3'}$), 139.69 (C_4), 139.61 ($C_{4'}$), 137.47, 135.89 (C_5), 135.69 (C_5), 134.84 (CH=N-), 131.55 (C_6), 131.11 ($C_{6'}$), 130.99 (C_7), 130.15 ($C_{7'}$), 129.11 (C_m and $C_{m'}$), 123.91 (C_p), 119.69 (C_o and $C_{o'}$), 109.30 (C_2), 108.41 ($C_{2'}$),46.01 (C_A and $C_{A'}$), 39.13 (C_B and $C_{B'}$), 30.27, 30.17 (C_C and $C_{C'}$), 29.71 (C_D and $C_{D'}$), 28.31 (C_G and $C_{G'}$), 28.27 (C_E and $C_{E'}$), 23.04 (C_E and $C_{E'}$), 14.03 (C_F and $C_{F'}$), 10.63, 10.46 (C_H and $C_{H'}$).

MS (MALDI+) m/z: 763.2410; calcd for $C_{38}H_{47}BrN_5O_2S_2$ (MH+): 763.2200

Chapter 3: Amide-functionalized thiophene-capped diketopyrrolopyrole derivatives. Electroactive core functionalization

Summary

This chapter focuses on the study of two bisamide **DPP** compounds. Both were synthesized by alkylating the lactams of the main core by chains containing an amide. One of the compounds has chiral branched amide side chains. The other molecule has a linear amide chain and is not chiral.

Compared to the semicarbazone **DPP** in the previous chapter, UV-visible spectra of solutions and thin films, revealed more intense J-type aggregate signals. These J-aggregates could be related to the formation of H-bonds according to FT-IR spectra and experiments with addition of MeOH. The stability of the self-assembly with dilution and temperature was also probed. Circular dichroism spectra showed a strong Cotton effect for the chiral **DPP**.

The morphology of the aggregates was studied by TEM microscopy. The chiral and achiral derivatives form different kinds of nanostructures. These results indicate an influence of chirality in the self-assembly and optoelectronic properties.

The photoconductivity was measured by flash-photolysis time-resolved microwave conductivity (FP-TRMC). This technique yields the sum of hole and electron mobility. The highest photoconductivity was obtained for the achiral bisamide **DPP**. The semicarbazone **DPPs** have lower mobilities as well as faster charge carrier recombination. This would suggest that the distance between the H-bonding groups plays a significant role: too short a distance seems detrimental. The presence of chiral center next to amide function also affects photoconductivity.

I. Introduction

As we have shown in chapter 1, supramolecular chemistry can lead to the formation of highly organized semiconducting structures.[1] Especially, directional noncovalent interactions, such as hydrogen bonds, can be introduced in the semiconducting segments and guide the self-assembly toward different supramolecular structures with different optoelectronic properties.[2–4] These properties can be also impacted by chirality.[5,6] Regarding supramolecular materials, chirality is amplified by transferring molecular chirality to the supramolecular structure formed, finding emerging properties arising from such effect.

Supramolecular chirality has been explored in organic semiconductors using **π-π** stacking and hydrogen-bonding mainly.[5,7–9] Different chiral **DPP** derivatives have been studied: with chiral alkyl tails, usually 2-ethylhexyl tails[10–13] pending from the lactam rings, with **DPP** attached to helicene molecules,[14] and with chiral groups attached to the **DPP** scaffold.[15] In these examples the chiral groups do not form H-bonds. Regarding chiral H-bonded **DPP** derivatives, examples by Brauchsweig[16–20] have been reported where **DPPs** with chiral side chains were attached to a diaminopyridine (DAP) H-bonding motif to study supramolecular donor-acceptor systems.

In this chapter, we study and compare two H-bonded **DPP** small molecule derivatives: one chiral, and one achiral, which are illustrated in the following figure.

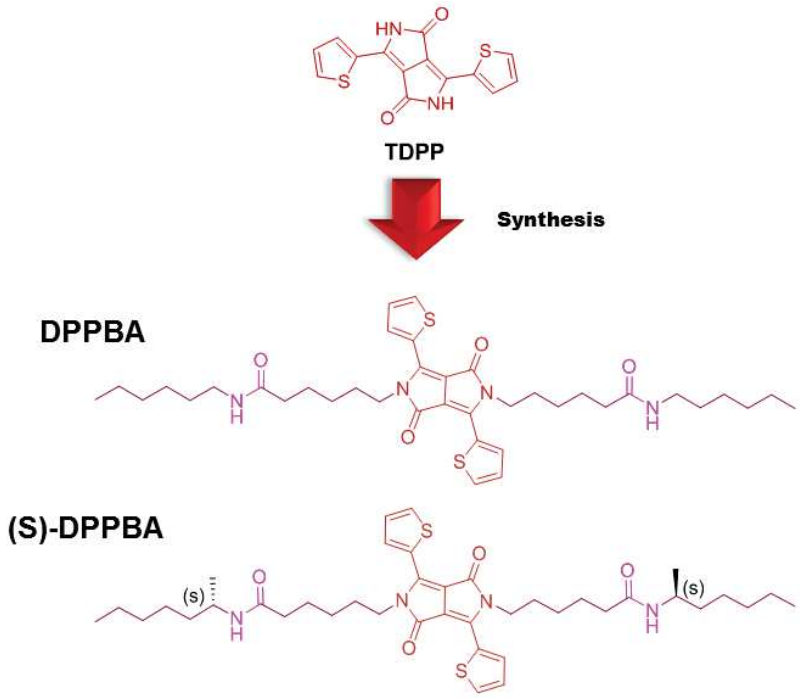

Figure 1: *Chemical structure of the targeted bisamide **DPP** derivatives*

In these derivatives the H-bonding group is an amide. The chiral derivative (**(S)-DPPBA) is** composed of branched amides side chains with one chiral center. The

achiral derivative is the linear analogue. A combination of variable temperature UV-Vis, infrared and circular dichroism spectroscopy together with microscopy techniques are used to understand the different types of aggregates found in solution and on thin film. The impact of H-bonding and chirality on the charge transport properties were studied by flash-photolysis time-resolved microwave conductivity (FP-TRMC), indicating the positive role of H-bonding on electric conductivity.

II. Synthesis

To obtain the **DPP** bisamide derivatives, the amide arms were first synthesized by ring opening of Ɛ-caprolactone (Scheme 1). Hexylamine or 2-(S)-aminoheptane were reacted with Ɛ-caprolactone to give the intermediates **1** and **1'** with respective yields of 68 % and 61 %. These intermediate were mesylated (NEt_3/THF) to form **2** and **2'** with yields of 77 % and 88 %, respectively. **DPP** was N-alkylated with **2** and **2'** to obtain the final achiral and (S)-**DPP** bisamide compounds with respective yields of 9 and 8 %.

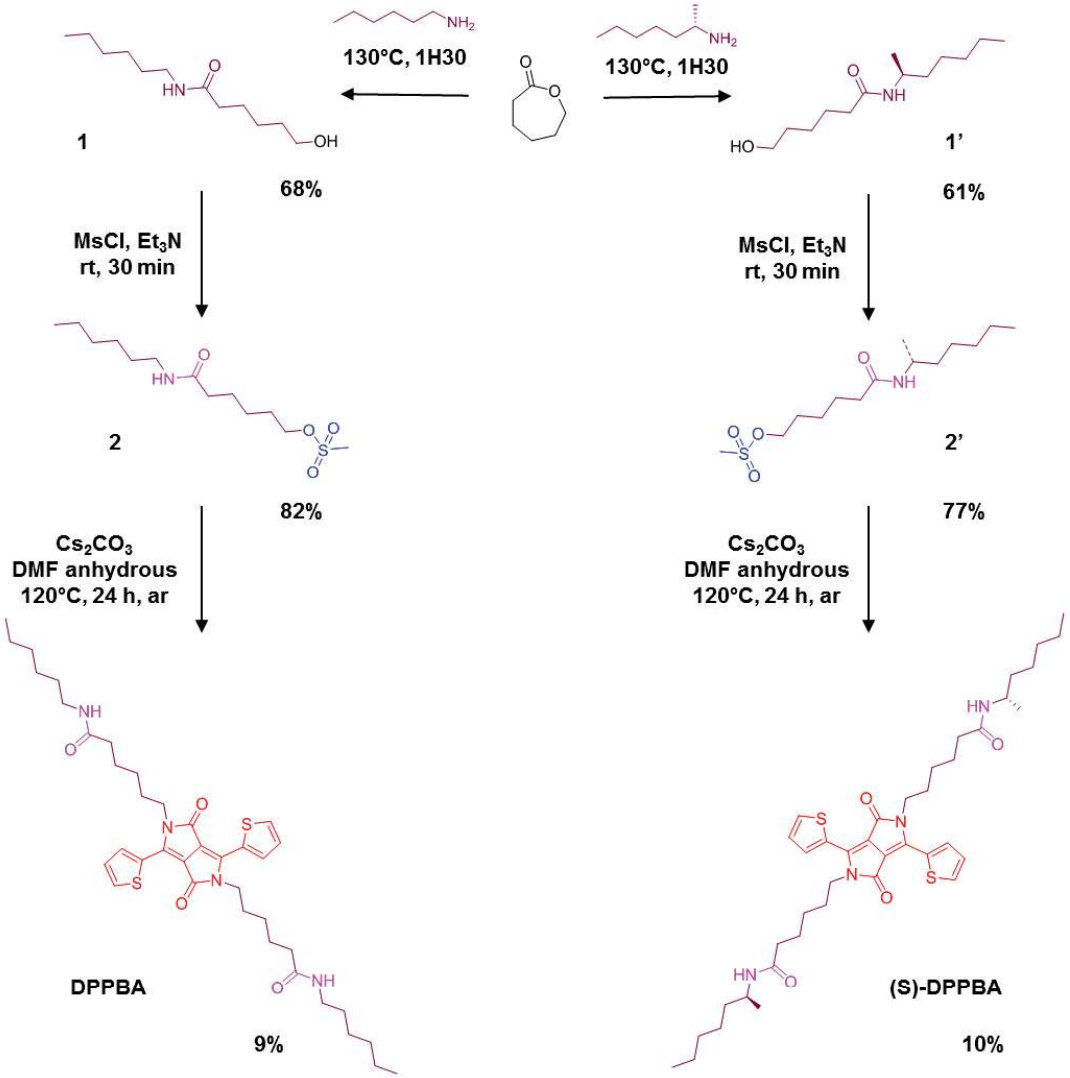

Scheme 1: *Synthesis of the* ***(S)-DPPBA*** *and the achiral* ***DPPBA.***

In the N-alkylation step, the reaction conditions were the same as for the alkylation with ethylhexyl or butyloctyl chains. The yields were, however, much lower and the isolation of the final products was more challenging, needing several chromatography columns. Thin layer chromatography (TLC) analysis revealed the formation of sub-products with R_f very close to each other and to the final **DDP** compounds. Several attempts were conducted to separate them. Like for the semicarbazone derivatives, the two mono N- and O-alkylated isomers were found and isolated. ^{1}H-NMR analysis revealed similar aromatic signals very close to those of the N- and O-monoalkylated **DPP** with either ethylhexyl or butyloctyl chains (Figure 2).

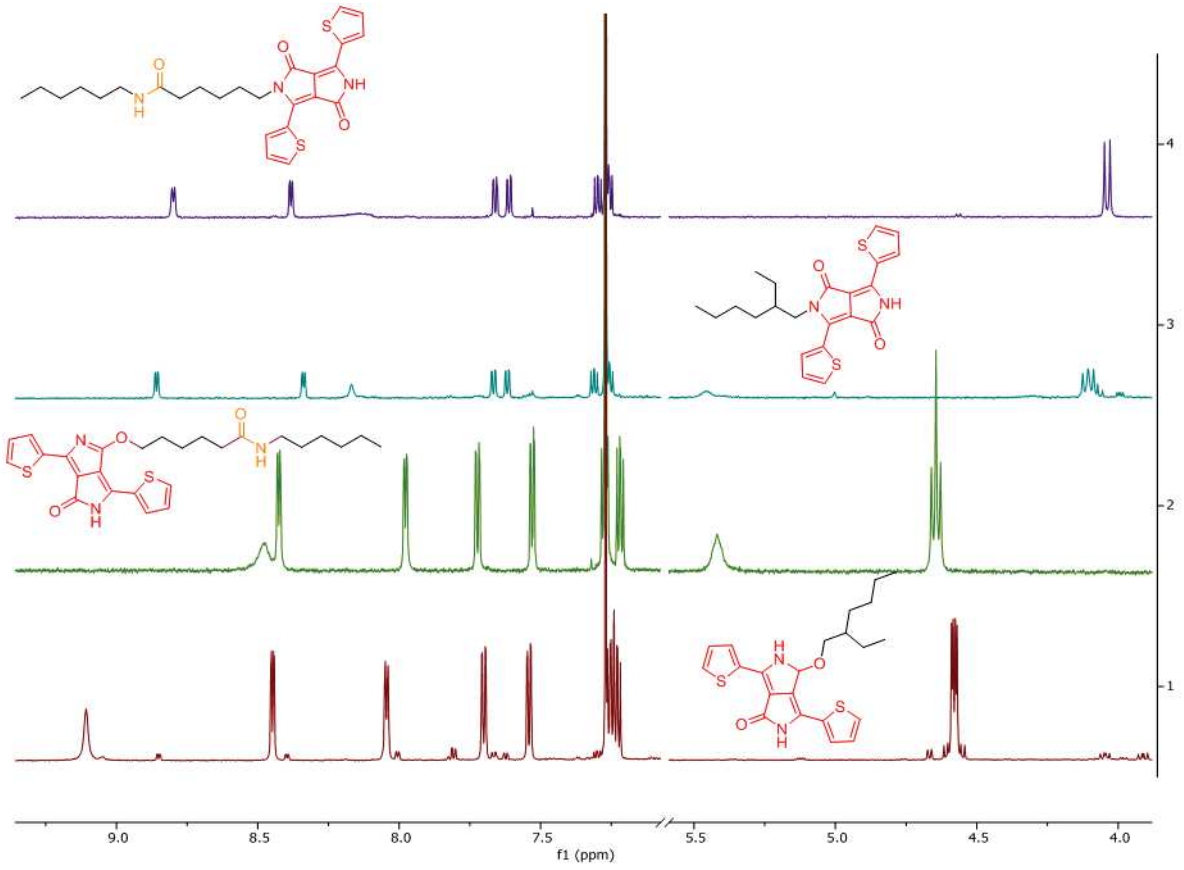

Figure 2: *Comparison of ^{1}H-NMR spectra between **DPPBisamide**, N- or O-monoalkylated **DPP** sub-products and N- or O-monoalkylated **DPP** with butyloctyl chains.*

III. Self-assembly studies: UV-Vis spectroscopy, FTIR and circular dichroism (CD)

UV-Vis, FTIR and circular dichroism (CD) spectroscopy analysis were performed in solution and in the solid state to shed light into the self-assembly processes of the bisamide derivatives. Chloroform was used as a good solvent as in the case of the semicarbazone derivatives described in chapter 2. Broad absorption bands ranging from 415 to 600 nm were found for 5 mg/mL solutions at 20 ^{0}C (Figure

3a). However, for **(S)-DPPBA** an additional absorption band appears at lower energy. This signal is related to the formation of H-bonds since it disappears upon the addition of methanol, an H-bonding competing solvent (Figure 3b). Like for other H-bonded **DPP** derivatives, including the semicarbazone-containing **DPPs**, this band could be attributed to the formation of J-type aggregates.[21–24] This band was not observed for **DPPBA** in chloroform, even upon saturation conditions (figure 3a). A total amount of 4% of methanol was added to the **(S)-DPPBA** in $CHCl_3$ solution until the aggregate signal disappeared (Figure 3b). FTIR spectra of chloroform solutions were measured to prove the existence of hydrogen bonds in the bisamide derivatives (Figure 3c and 3d). At 27 °C, the spectrum of **DPPBA** showed only one band at 3450 cm^{-1} in the NH stretching area, which is characteristic of the NH stretching mode (amide A) of free amide groups.

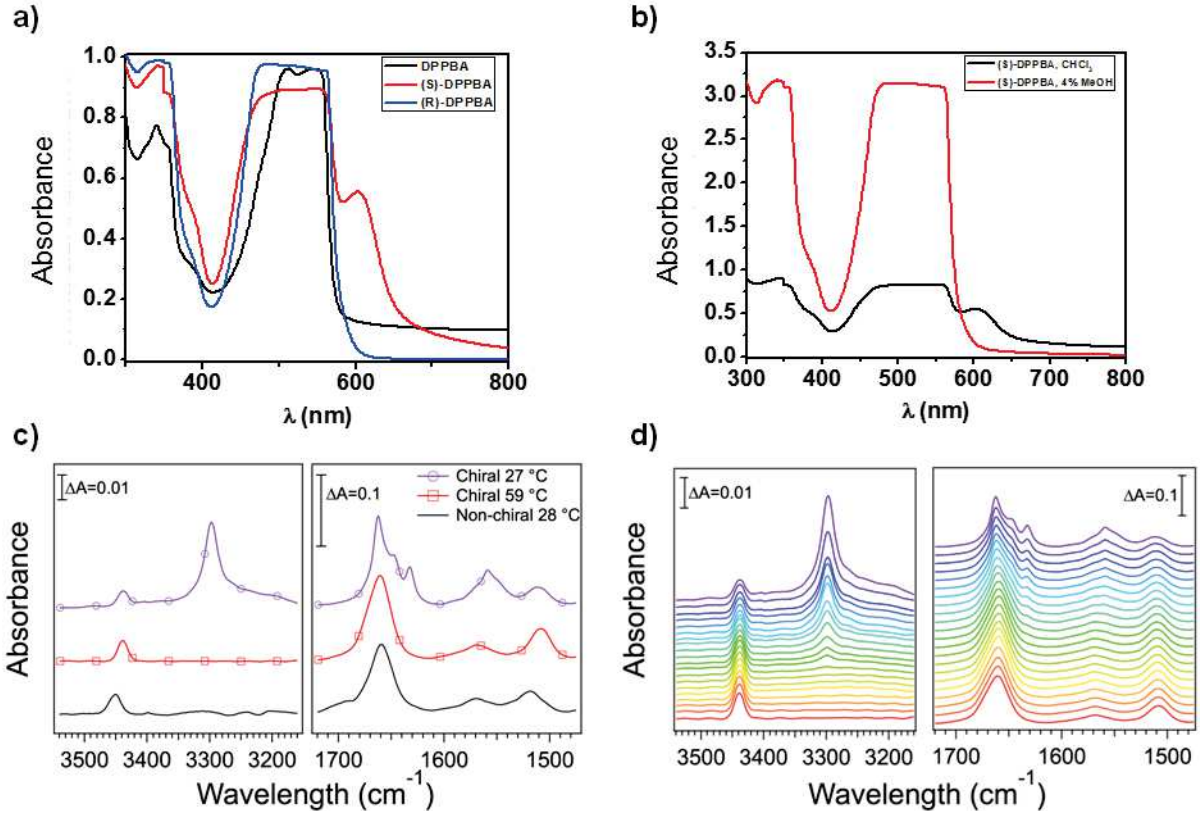

Figure 3: *(a) Normalized UV-Vis spectra of **DPPBA**, **(S)-DPPBA** and **(R)-DPPBA** in chloroform at room temperature. (c = 5 mg/mL). (b) UV-Vis of **(S)-DPPBA** in chloroform and upon the addition of 4% volume of methanol. (c) Variable temperature FTIR spectra for **DPPBA** and **(S)-DPPBA** in $CDCl_3$. (c = 5 mg/mL). (d) Variable temperature FTIR of **(S)-DPPBA** from 27 °C to 59 °C with 1 °C steps.*

This result points out that **DPPBA** is not H-bonded in chloroform at this concentration. The amide I mode is found at 1659 cm^{-1}, which also corresponds to free amide groups (note: this peak also overlaps with the CO of the core). When increasing the temperature to 59 °C the spectra of **DPPBA** did not show significant evolution. On the

other hand, **(S)-DPPBA** showed two bands at 3439 cm^{-1} and 3297 cm^{-1} in the NH stretching area. The first band can be attributed to the free amide, analogously to the band at 3450 cm^{-1} for **DPPBA**; the second band corresponds to H-bonded amide groups. Hence, part of **(S)-DPPBA** is H-bonded and part of it is free. In the region between 1600 cm^{-1} and 1700 cm^{-1}, **(S)-DPPBA** shows three peaks at 1632 cm^{-1}, 1648 cm^{-1} and 1663 cm^{-1}. The peak at 1632 cm^{-1} corresponds to amide groups engaged in strong H-bonds[25], while the peak at 1648 cm^{-1} corresponds to weaker bonds. The peak at 1663 cm^{-1} matches with the peak for free amide observed for **DPPBA**. When the temperature increases, the peaks corresponding to H-bonded amides gradually decreases and fully disappear at 59 °C. At 59 °C and above, the spectrum of **(S)-DPPBA** matches the one of **DPPBA** at room temperature.

The optical properties were measured in different solvents: toluene, chlorobenzene, cyclohexane and ethyl acetate. In these solvents, the J-aggregate band is higher than in chloroform for both, **DPPBA** and **(S)-DPPBA** (Figure 4a and b). For both derivatives, an H-aggregate signal appears at approximately 480 nm in several solvents, and is particularly intense in chlorobenzene, toluene and cyclohexane. In the case of **(S)-DPPBA**, the J-aggregate signal (**λ** = 600 nm) is the predominant one in solvents like toluene and cyclohexane, showing the strong formation of H-bonds in these conditions. Thanks to the formation of J-aggregates it is possible to cover a larger zone of the spectrum and to tune the energy band gap. This is very interesting since the optoelectronic properties can be modified by varying the aggregation state and not by modifying the molecule. Furthermore, this strategy allows us, with very simple semiconducting segments, to control the properties through aggregation.

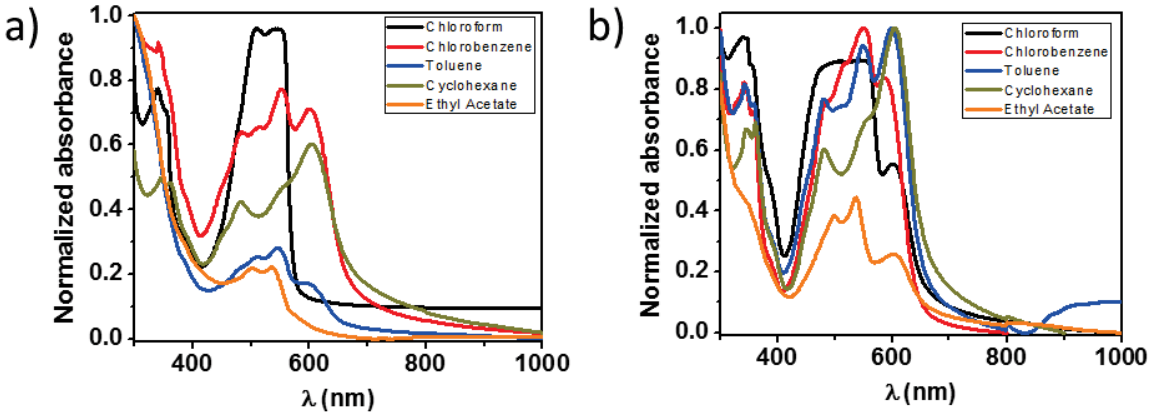

Figure 4: *UV-Vis spectra of (a)* ***DPPBA*** *and (b)* ***(S)-DPPBA*** *in different solvents. (c = 5 mg/mL).*

Dilution series and variable temperature measurements were performed to explore further the aggregation process. The J-aggregate bands were observed upon diluting, still appearing at low concentrations in solvents that promote the formation of strong H-bonds (Figure 5a and b). When the temperature increases, even to the boiling point,

the J-aggregate signal is still present, emphasizing the formation of aggregates even at high temperature (Figure 5). This trend was also observed for both derivatives, but the bands assigned to aggregates disappeared at lower temperatures and higher concentrations for the achiral derivative: the chiral derivatives forms more stable aggregates than the achiral one.

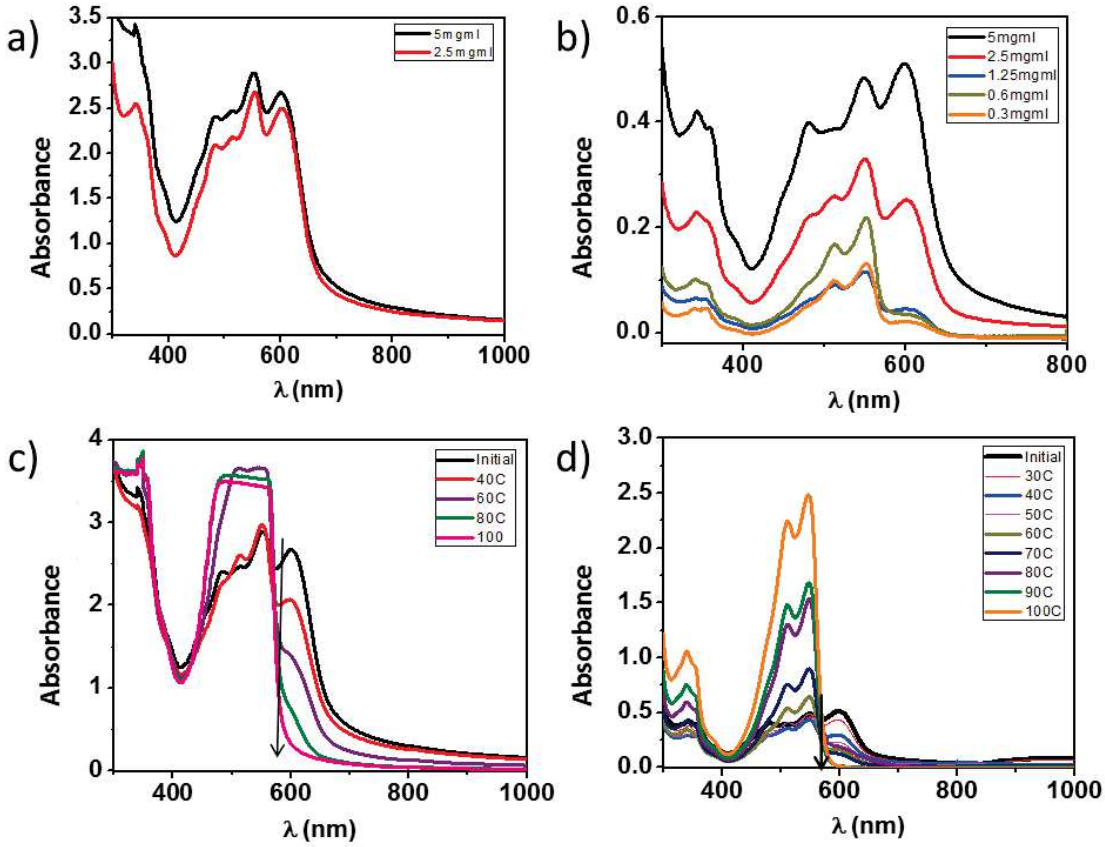

Figure 5: *a) Dilution series for a)* ***DPPBA*** *in chlorobenzene and b)* ***(S)-DPPBA*** *in chlorobenzene. Variable temperature UV-Vis for c)* ***DPPBA*** *in chlorobenzene and d)* ***(S)-DPPBA*** *in toluene.*

Circular dichroism (CD) spectra were measured in several solvents and showed signals with strong Cotton effect. Figure 6a shows variable temperature CD spectra in chlorobenzene, where strong signals are found at low temperature at the J-aggregate wavelength. This signal can be observed up to 60 ºC, as evidenced as well in the melting curve showed in figure 6b. On the other hand, the achiral derivative did not show Cotton effect in any of the conditions studied (Figure 6c).

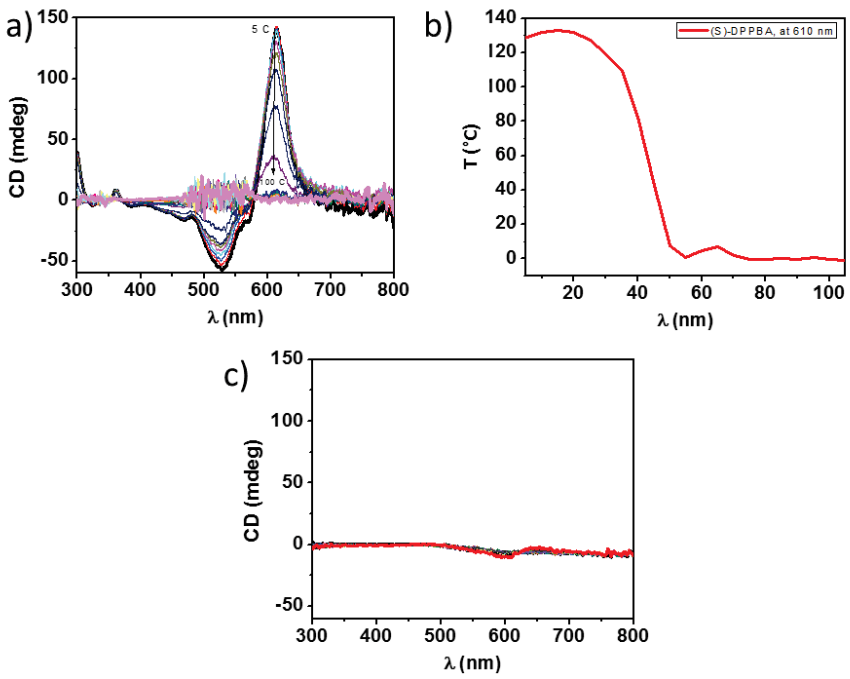

Figure 6: *a) Variable temperature CD spectra in chlorobenzene solution for **(S)-TDPPBA**. b) Variable temperature CD signal followed at 610 nm for **(S)-TDPPBA**. c) Variable temperature CD spectra in chlorobenzene solution for **TDPPBA** (c = 5 mg/mL).*

Due to the interesting differences found between the achiral and chiral **DPP** derivatives, we decided to synthesize also the (R)-enantiomer. The **(R)-DPPBA** derivative has been synthesized and characterized by Ricardo Avila, PhD student of our group, but we would like to show some preliminary results obtained with this molecule. Interestingly, we observed that this molecule was more soluble than the (S)-enantiomer and showed lower J-aggregate bands in UV-Vis and CD signals (Figure 7a and 7b). Nevertheless, the complete study of this molecule still needs to be finished and will not be presented in detail in this thesis.

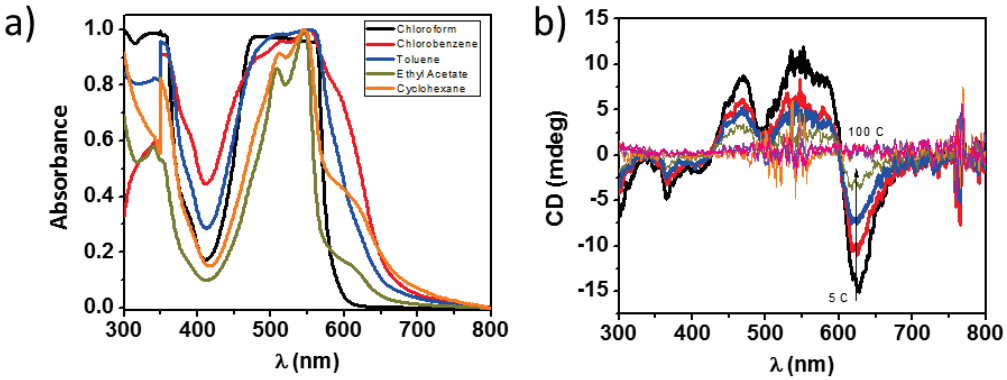

Figure 7: *a) UV-Vis spectra of **(R)-DPPBA** in several solvents at room temperature. b) Variable temperature CD spectra of **(R)-DPPBA** in chlorobenzene. (c = 5 mg/mL).*

IV. Morphology

We studied the morphology of **DPPBA** and **(S)-DPPBA** solutions in all the solvents previously used for UV-visible and CD spectroscopy. Droplets of the solution were deposited on carbon coated grids and blotted and observed under transmission electron microscopy (TEM).

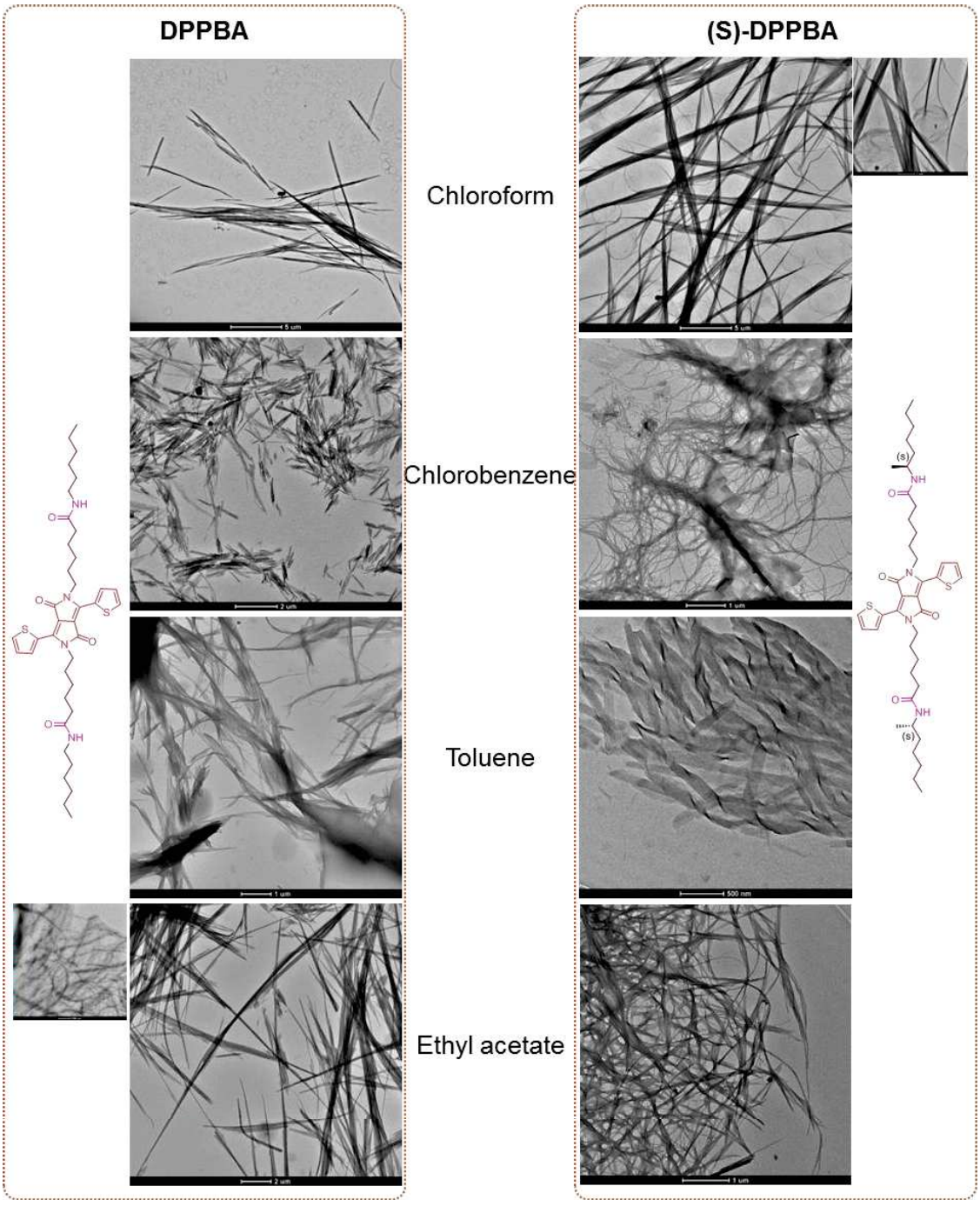

Figure 8: *TEM images of* ***DPPBA*** *and* ***(S)-DPPBA*** *in chloroform, chlorobenzene, toluene and ethyl acetate.*

Samples made from chloroform solution of **DPPBA** showed rare fibers with an average length of 10 µm. Since no aggregate and no H-bonds are visible in UV and FTIR these few structure may come from evaporation during the sample preparation. **(S)-DPPBA** in the same solvent, forms much more objects. The fibers tend to aggregate and form bundles of width from 100 to 400 nm. In chlorobenzene, smaller structures, with an average length of 2 µm are seen for **DPPBA**. The fibers pool into bundles with width of several hundreds of nanometers. In the same solvent, **(S)-DPPBA** forms fibers with much higher factor ratio: thinner and longer. Samples made from solution of ethyl acetate revealed the formation of fibers which are either strait or curved. These fibers are overlapping one from each other to form thicker fibers. For the chiral compound, helical structures were also observed. Toluene samples of TDPPBA revealed the presence of fibers either entangled or overlapped whereas those of (S)-TDPPBA reveal the formation of helical tapes. These structures tend to regroup into large twisted ribbons of several hundreds of nanometers widths.

Samples were prepared the same way from solutions in cyclohexane and *trans*-decalin and analyzed by TEM. Regarding Cyclohexane samples, a mixture of ribbons and twisted fibers was observed for **DPPBA.** For **(S)-DPPBA**, the presence of twisted fibers was mostly noticed. These fibrillary structures tend to entangle themselves into thicker fibers. Major differences were observed *trans*-decalin in terms of size and shape. TEM images of **DPPBA** samples showed to presence of small tapes structures while **(S)-DPPBA** formed twisted and entangled fibers.

The overall trend, the chiral compound forms longer and thinner aggregates than the achiral compound. Moreover the chiral compound may form helical structures.

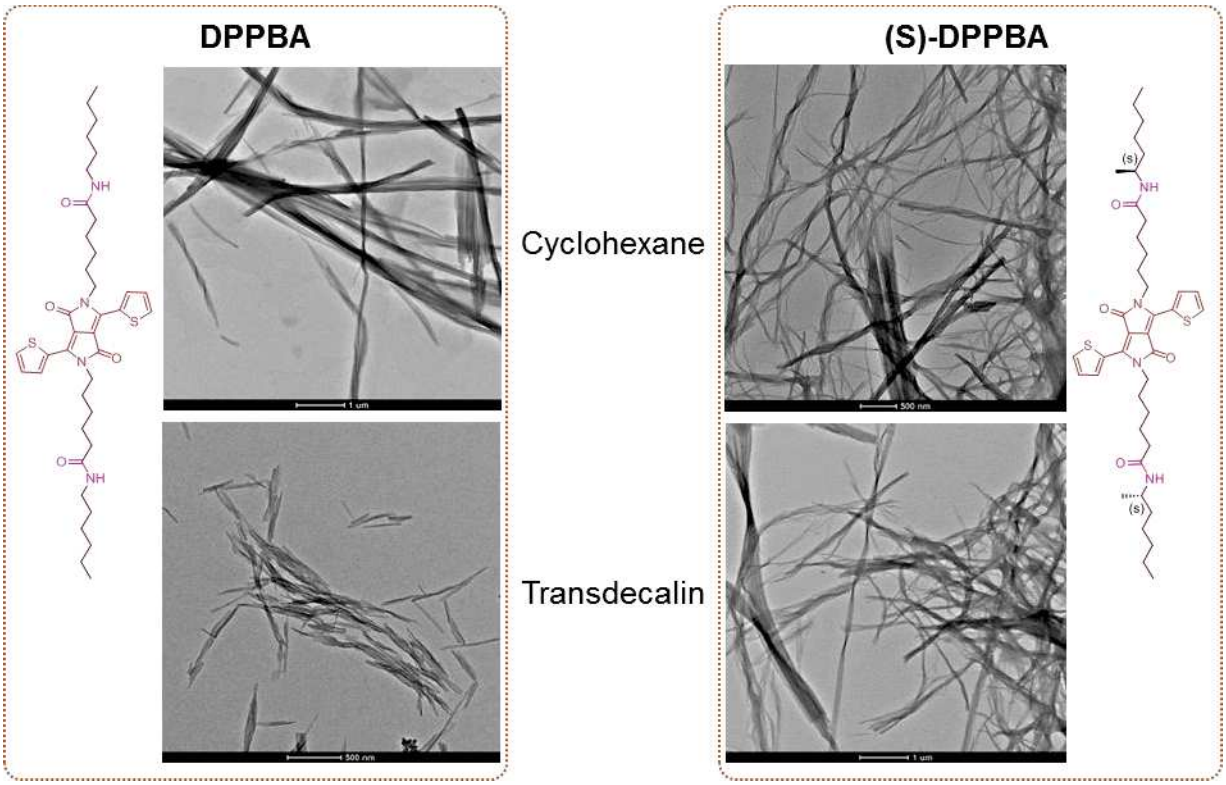

Figure 9: *TEM images of* ***DPPBA*** *and* ***(S)-DPPBA*** *in cyclohexane and trans-decalin.*

V. Photoconductivity measurements

The implementation of new semiconductors in organic electronic devices is a time consuming process. Many devices must be fabricated to test every condition of concentration, solvent, and process. Regarding non-conventional semiconductors, the optimization process is even more tedious. As mentioned in the introduction chapter, this is the case for H-bonded semiconductors. Even though some examples report the benefit of H-bonds for the efficiency of the final organic electronic devices, the published works are scarce and do not find consensus.[26] This is mainly due to the urge for achieving record efficiencies, which hampers research focused on solving fundamental issues. Therefore, alternative measuring techniques that give faster information are very beneficial to study new semiconducting systems. This is the case of noncontact techniques based on microwave dielectric loss spectroscopy, such as flash-photolysis time-resolved microwave conductivity (FP-TRMC).[27–29] FP-TRMC is an electrodeless technique that measures photoconductivity as the sum of electron and hole mobilities. In the world, only a few experts master this technique. We collaborate with one of them, Prof. Seki, to study the influence of H-bonding in organic semiconductors, screening multiple conditions without fabricating more sophisticated devices. By screening different parameters, we will identify the most efficient H-bonding functionalities to be applied in a final device. Our preliminary results provide important information on our H-bonded systems. The photoconductivity behaviour of **DPPBA**, **(S)-DPPBA** and **(R)-DPPBA** have been measured by FP-TRMC, using a 355 nm laser as the excitation source. FP-TRMC provides a measurement of photoconductivity as $\Phi\Sigma\mu$ were Φ is the charge carrier generation quantum yield and $\Sigma\mu$ is the sum of charge carrier mobilities, meaning the sum of electron and hole mobilities. Thin films of the three derivatives were prepared by drop casting chloroform solutions on quartz substrates (Figure 10) and they were analysed before and after exposure to different solvent vapours.

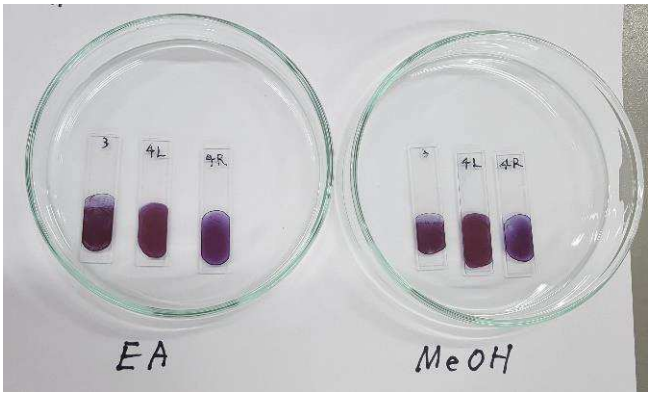

Figure 10: *Sample preparation for the **DPP** bisamide derivatives. All the films are drop cast from chloroform (c = 5 mg/mL) to be subsequently exposed to ethyl acetate and methanol.*

Two samples of each bisamide were prepared. One of them was exposed to ethyl acetate and another one to methanol: the first promotes aggregation, the second disrupts H-bonds. The kinetic traces of conductivity transients observed are shown on figure 11 and the initial photoconductivity values are shown in table 1. The following graphs in figure 11 shows the value of photoconductivity $\phi\Sigma\mu$ obtained after irradiation (time = 0 s) and its evolution with time. The photoconductivity $\phi\Sigma\mu$ of **DPPBA** is slightly larger than those of **(S)-** and **(R)-DPPBA**. Nevertheless, $\phi\Sigma\mu$ depends on the yield of photogeneration yield ϕ, which can be different depending on the amount of sample deposited on the substrates. The decay kinetics of photoconductivity for **DPPBA** shows that the free charge carriers are stable up to 10 µs. The recombination of charge carriers is slower for **DPPBA** than for **(S)-** and **(R)-DPPBA**, with a lifetime of one order of magnitude higher: it seems that the lower solubility of the chiral **DPP**s and the presence of the methyl group next to the amide group are detrimental for the charge carrier pathways.

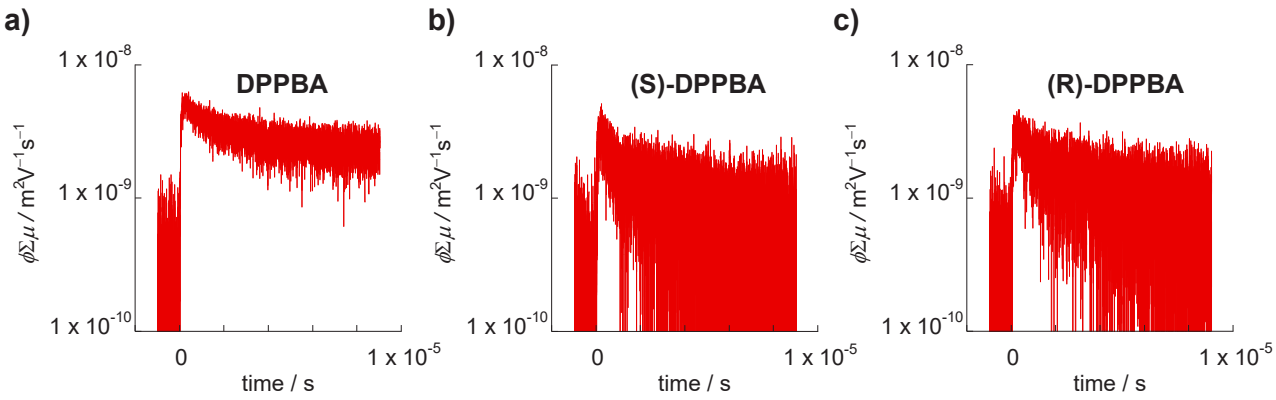

Figure 11: *Kinetic traces of conductivity transients observed for drop cast films of a)* ***DPPBA****. b)* ***(S)-DPPBA*** *and c)* ***(R)-DPPBA*** *upon excitation of 355 nm laser pulses at 4.5 × 10¹⁵ photons cm⁻².*

The initial samples were exposed to saturating vapours of ethyl acetate and methanol during 24 hours at room temperature. The absorbance of the samples after solvent vapour annealing was recorded (Figure 12a, b and c), then their photoconductivity was measured to analyse any changes in aggregation. The thin films show the presence of aggregates, predominantly J-aggregate, as explained above in the spectroscopy part. No big differences were observed in absorbance, but slight changes in scattering.

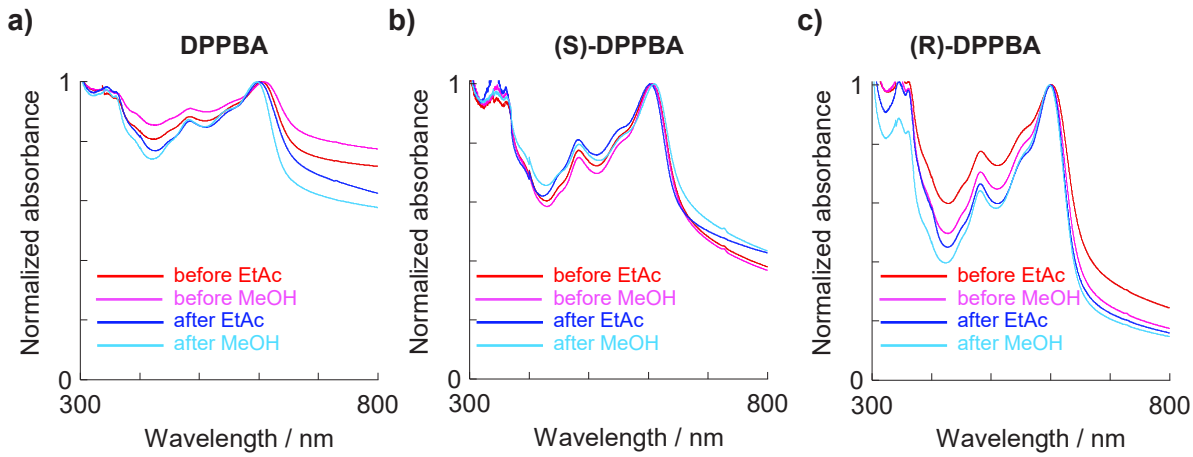

Figure 12: *UV-Vis spectra of thin films before and after exposure to ethyl acetate and methanol.*

Interestingly, the photoconductivity of **DPPBA** was different after solvent annealing in ethyl acetate (Figure 13a), a solvent promoting aggregation. The photoconductivity value increased from 5.0 x 10^{-5} $cm^2V^{-1}s^{-1}$ to 7.4 x 10^{-5} $cm^2V^{-1}s^{-1}$ (Table 1, entry 1), emphasizing the importance of strengthening the H-bonds. On the other hand, methanol annealing did not have any effect on photoconductivity (Figure 13b) for **DPPBA** (Table 1, entry 2). It seems that annealing with methanol has low impact on changing the H-bonding aggregation.

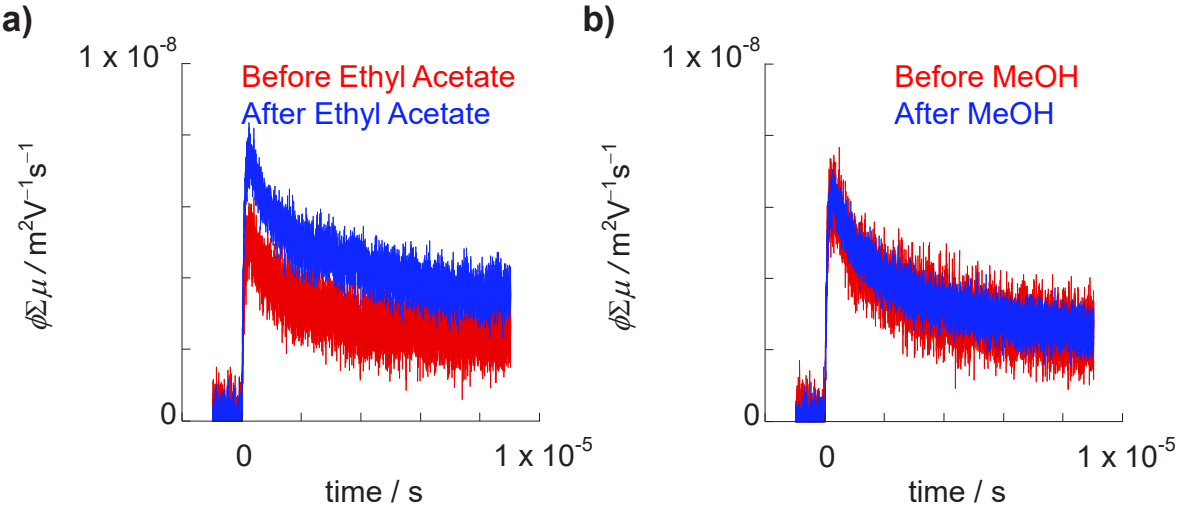

Figure 13: *Kinetic traces of conductivity transients observed for **DPPBA** upon excitation of 355 nm laser pulses at 4.5 × 10^{15} photons cm^{-2} a) before (red) and b) after (blue) solvent (ethyl acetate or methanol) annealing for 24 hours.*

Since solvent annealing with methanol vapour did not show any effects in changing photoconductivity, a different experiment was performed. The thin film cast from ethyl acetate (Figure 14a) was soaked in methanol and dried at room temperature. This treatment changes the decay rate and the recombination process. It

seems that disconnecting H-bonds by methanol causes these differences. Nevertheless, the UV spectra show slight differences (Figure 14b) and other experiments and techniques to study the changes in molecular packing will be performed in the future to understand this effect.

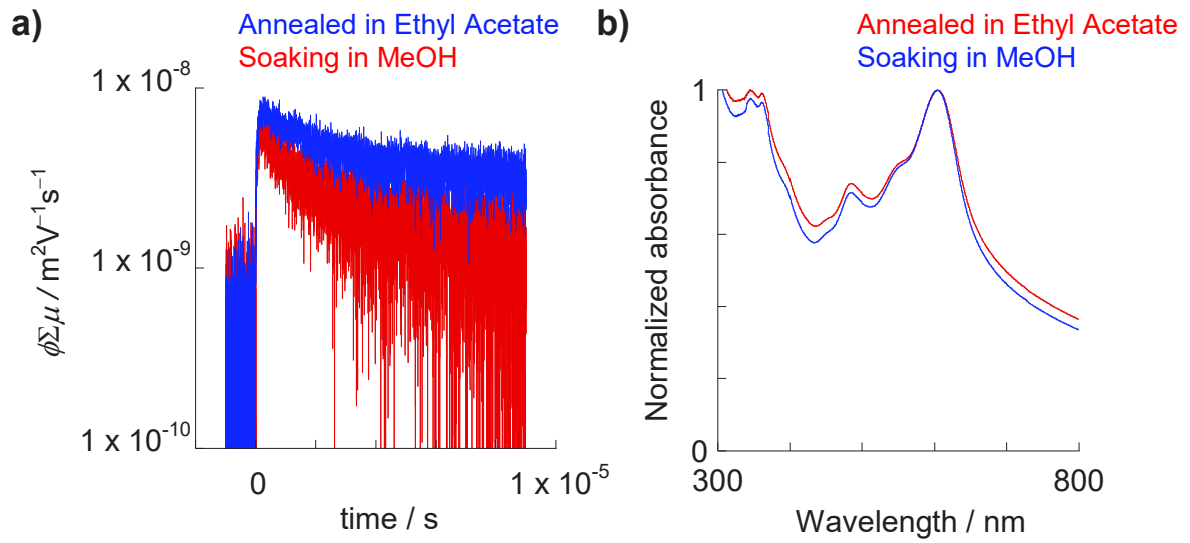

Figure 14: *Comparison of (a) kinetic traces of conductivity transients observed for* ***DPPBA*** *annealed in ethyl acetate (blue) and after being soaked in methanol (red); (b) Comparison of UV absorption spectra of* ***DPPBA*** *annealed in ethyl acetate (red) and after being soaked in MeOH.*

Regarding the chiral derivatives **(S)-** and **(R)-DPPBA**, no differences in photoconductivity were found when the thin films cast from chloroform were exposed to solvent vapour of ethyl acetate or methanol (Figure 15a and 15b). This suggests that solvent vapour annealing is not efficient to favour molecular packing and hence charge transport. The presence of a methyl group next to the H-bonding (amide) motif and the lower solubility of both chiral isomers compared to **DPPBA**, might be the reasons of such results. To complete the study of the chiral molecules, like for **DPPBA**, the thin films will be soaked in different solvents. It is important to remark, that slight differences were found between **(S)-DPPBA** and **(R)-DPPBA**: the photoconductivity is slightly superior (Table 1) and the recombination of charge carriers slower for **(R)-DPPBA** than for **(S)-DPPBA**. During our synthesis and characterization process, we observed that the solubility of **(R)-DPPBA** was higher than that of (**S)-DPPBA**, which resulted into less intense aggregate signals observed by UV-Vis, and lower CD signals. This effect is very interesting and we will continue exploring the differences in photoconductivity between both enantiomers.

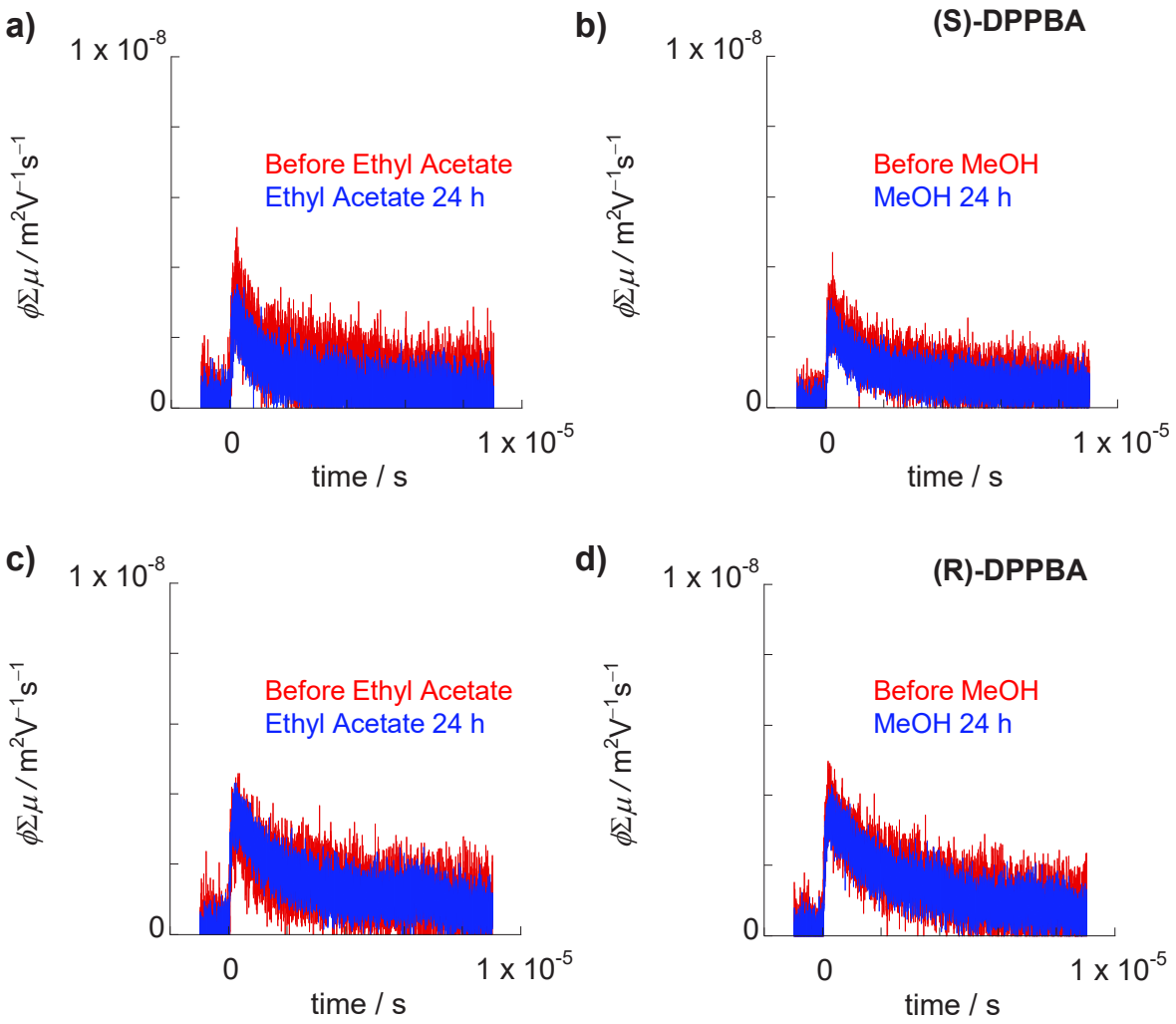

Figure 15: *Kinetic traces of conductivity transients observed for* ***(S)-DPPBA*** *(a) and (b) and for* ***(R)-DPPBA*** *(c) and (d) upon excitation of 355 nm laser pulses at 4.5 × 10^{15} photons cm^{-2} before (red) and after (blue) solvent (ethyl acetate or methanol) annealing for 24 hours.*

Table 1: *Photoconductivity values for chloroform drop cast films of* ***DPPBA****,* ***(S)-DPPBA*** *and* ***(R)-DPPBA*** *before and after solvent annealing.*

Samples (before solvent exposure)	$\phi\Sigma\mu$ /$cm^2V^{-1}s^{-1}$	Samples (after solvent exposure, 24h)	$\phi\Sigma\mu$ /$cm^2V^{-1}s^{-1}$
DPPBA (EtOAc)	5.0×10^{-5}	DPPBA (EtOAc)	7.4×10^{-5}
DPPBA (MeOH)	6.1×10^{-5}	DPPBA (MeOH)	6.5×10^{-5}
(S)-DPPBA (EtOAc)	3.1×10^{-5}	(S)-DPPBA (EtOAc)	2.6×10^{-5}
(S)-DPPBA (MeOH)	2.7×10^{-5}	(S)-DPPBA, (MeOH)	2.4×10^{-5}
(R)-DPPBA (EtOAc)	3.2×10^{-5}	(R)-DPPBA (EtOAc)	3.4×10^{-5}
(R)-DPPBA (MeOH)	3.8×10^{-5}	(R)-DPPBA (MeOH)	3.8×10^{-5}

As mentioned in chapter 2, the **DPP** semicarbazone derivatives, **DPPSC** and **BrDPPSC**, were also evaluated. Thin films of both derivatives were cast from chloroform and ethyl acetate directly. For these compounds, no differences in the photoconductivity values were observed (Figure 16) despite the different morphologies and aggregation state. The charge carrier lifetime was much lower than for the bisamide derivatives. In this case, it seems that there is no morphology dependence for photoconductivity. This result gives us an idea regarding the attachment of the H-bonding groups directly to the peripheral thiopene rings.

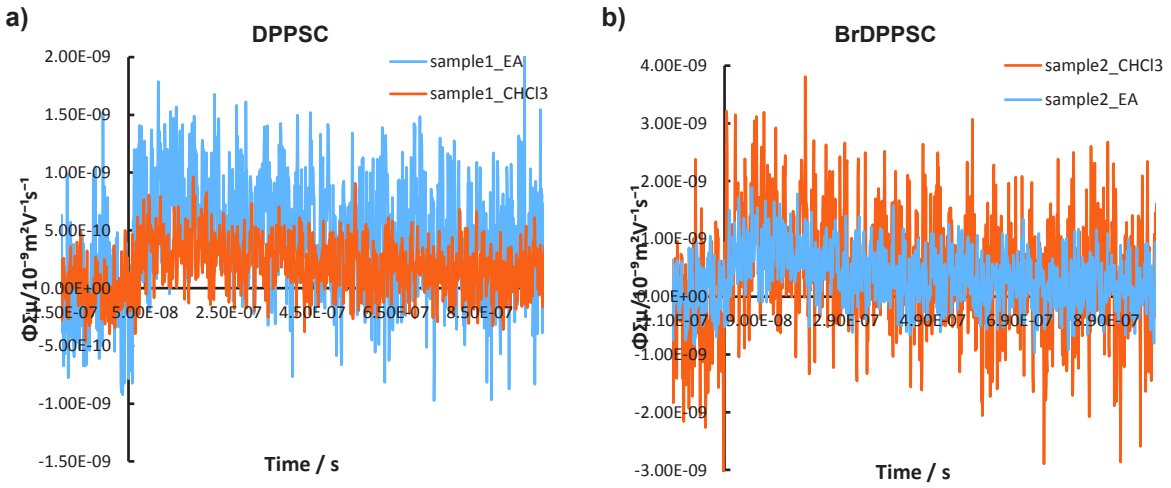

Figure 16: *Kinetic traces of conductivity transients observed for drop cast films of a)* ***DPPSC****. b)* ***BrDPPBA*** *upon excitation of 355 nm laser pulses at 4.5 × 10^{15} photons cm^{-2}.*

If we compare the amide derivatives with the semicarbazone systems of chapter 2, we can conclude that a flexible linker between the electroactive core and the H-bonding group improves the transport properties. These results give us very useful information to keep on expanding our library and synthesizing different **DPP** analogues with flexible linkers in the peripheral thiophenes, with urea or semicarbazone H-bonding motifs attached to the **DPP** lactam rings.

Regarding the FP-TRMC measurements performed for the amide derivatives, we can conclude that the photoconductivity of the achiral derivative **DPPBA** is superior to that of the chiral analogues, with longer lifetime charge carriers and lower recombination decay. Although the chiral derivatives show very interesting morphologies, the presence of the methyl group next to the amide H-bonding functionality seems to hinder the pathways for charge transport. Therefore, we will take this information into consideration to design other chiral analogues.

Interestingly, some differences were observed between the chiral enantiomers, a fact that we will continue to study in depth with electrodeless techniques.

VI. Conclusions and perspectives

In summary, two **DPP** derivatives containing amide functions attached to the **DPP** core have been synthesized. Currently, the reaction conditions are being optimized with microwave irradiation. Product and sub-product isolation and identification are also under investigation by recycling gel permeation chromatography (recycling GPC).

Self-assembly, optical and electronic properties have been studied. UV absorption spectra revealed the presence of J-aggregates signals more intense compared to those of the semicarbazone **DPP** studied in the previous chapter. FT-IR spectra confirmed the presence of H-bonds between the side chains. With the addition of methanol, it is possible to know that the aggregates are formed by H-bonding. Further UV spectroscopy studies also confirmed it through dilution and temperature variation in several solvents.

Solution in different solvents were analyzed by TEM microscopy. Different structures in all solvents were found. In a general point of view, **(S)-DPPBA** tends to form longer fibrillar or lamellar structures than the achiral bisamide. The latter self-assembles into fibers that overlap, sometimes forming twisted structures. The supramolecular structures formed are either in the shape of straight tapes or fibers. The structure obtained from **(S)-DPPBA** are networks mostly often twisted or helical tapes.

Charge transport was also studied by (FP-TRMC). In this case, the achiral derivative shows higher photoconductivity values as well as charge carrier lifetime with slower recombination kinetics compared to the chiral derivatives. Solvent vapor annealing with a self-assembly promoting solvent, showed an increase of photoconductivity. On the other hand, the exposure to methanol did not show any effect on photoconductivity. However, when the samples were soaked into methanol, a dramatic decrease in photoconductivity was observed, highlighting the importance of H-bonds.

Even though the enantiomers did not show significant difference under the conditions used for this study, the small difference between them seems very interesting and it is being investigated at the moment.

With these studies, we have obtained valuable information to continue expanding our library. For example, the direct attachment of H-bonding groups to the peripheral thiophene groups does not seem like a promising strategy, while having flexible alkyl tails between the semiconducting core and the H-bonding functionalities yields better results. Regarding the chirality effect, we have observed that adding chiral centers next to the H-bonding motif hinders charge transport and therefore, they should be placed further apart.

References

[1] T. Aida, E. W. Meijer, S. I. Stupp, *Science* **2012**, *335*, 813–817.
[2] S. Militzer, T. M. P. Tran, P. J. Mésini, A. Ruiz-Carretero, *ChemNanoMat* **2018**, *4*, 790–795.
[3] Y.-T. Tsai, K.-P. Tseng, Y.-F. Chen, C.-C. Wu, G.-L. Fan, K.-T. Wong, G. Wantz, L. Hirsch, G. Raffy, A. Del Guerzo, et al., *ACS Nano* **2016**, *10*, 998–1006.
[4] S. K. P. Velu, M. Yan, K.-P. Tseng, K.-T. Wong, D. M. Bassani, P. Terech, *Macromolecules* **2013**, *46*, 1591–1598.
[5] G. Ghosh, M. Paul, T. Sakurai, W. Matsuda, S. Seki, S. Ghosh, *Chem. - Eur. J.* **2018**, *24*, 1938–1946.
[6] "Supramolecular Chirality in Self-Assembled Systems - Chemical Reviews (ACS Publications)," can be found under https://pubs.acs.org/doi/abs/10.1021/cr500671p, **n.d.**
[7] X. Shang, I. Song, H. Ohtsu, Y. H. Lee, T. Zhao, T. Kojima, J. H. Jung, M. Kawano, J. H. Oh, *Adv. Mater.* **2017**, *29*, 1605828.
[8] A. P. H. J. Schenning, P. Jonkheijm, E. Peeters, E. W. Meijer, *J. Am. Chem. Soc.* **2001**, *123*, 409–416.
[9] F. Würthner, Z. Chen, F. J. Hoeben, P. Osswald, C.-C. You, P. Jonkheijm, J. v Herrikhuyzen, A. P. Schenning, P. P. van der Schoot, E. W. Meijer, *J. Am. Chem. Soc.* **2004**, *126*, 10611–10618.
[10] J. Liu, Y. Zhang, H. Phan, A. Sharenko, P. Moonsin, B. Walker, V. Promarak, T.-Q. Nguyen, *Adv. Mater.* **2013**, *25*, 3645–3650.
[11] R. B. Zerdan, N. T. Shewmon, Y. Zhu, J. P. Mudrick, K. J. Chesney, J. Xue, R. K. Castellano, *Adv. Funct. Mater.* **2014**, *24*, 5993–6004.
[12] T. He, P. Leowanawat, C. Burschka, V. Stepanenko, M. Stolte, F. Würthner, *Adv. Mater.* **2018**, *30*, 1804032.
[13] M. Stolte, S.-L. Suraru, P. Diemer, T. He, C. Burschka, U. Zschieschang, H. Klauk, F. Wurthner, *Adv Mater* **2016**, *26*, 7415–7422.
[14] K. Dhbaibi, L. Favereau, M. Srebro-Hooper, M. Jean, N. Vanthuyne, F. Zinna, B. Jamoussi, L. D. Bari, J. Autschbach, J. Crassous, *Chem. Sci.* **2018**, *9*, 735–742.
[15] P. A. Hume, J. P. Monks, F. Pop, E. S. Davies, R. C. I. MacKenzie, D. B. Amabilino, *Chem. – Eur. J.* **n.d.**, *0*, DOI 10.1002/chem.201802610.
[16] S. Rieth, Z. Li, C. E. Hinkle, C. X. Guzman, J. J. Lee, S. I. Nehme, A. B. Braunschweig, *J. Phys. Chem. C* **2013**, *117*, 11347–11356.
[17] Y. Zhou, C. X. Guzman, L. C. Helguero-Kelley, C. Liu, S. R. Peurifoy, B. Captain, A. B. Braunschweig, *J. Phys. Org. Chem.* **2016**, *29*, 689–699.
[18] C. X. Guzman, R. M. K. Calderon, Z. Li, S. Yamazaki, S. R. Peurifoy, C. Guo, S. K. Davidowski, M. M. A. Mazza, X. Han, G. Holland, et al., *J. Phys. Chem. C* **2015**, *119*, 19584–19589.
[19] D. Ley, C. X. Guzman, K. H. Adolfsson, A. M. Scott, A. B. Braunschweig, *J. Am. Chem. Soc.* **2014**, *136*, 7809–7812.
[20] S. R. Peurifoy, C. X. Guzman, A. B. Braunschweig, *Polym. Chem.* **2015**, *6*, 5529–5539.
[21] S. Militzer, T. M. P. Tran, P. J. Mésini, A. Ruiz-Carretero, *ChemNanoMat* **n.d.**, *0*, DOI 10.1002/cnma.201800192.
[22] S. Ghosh, S. Cherumukkil, C. H. Suresh, A. Ajayaghosh, *Adv. Mater.* **2017**, *29*, 1703783.
[23] A. Ruiz-Carretero, T. Aytun, C. J. Bruns, C. J. Newcomb, W.-W. Tsai, S. I. Stupp, *J. Mater. Chem. A* **2013**, *1*, 11674.

[24] W.-W. Tsai, I. D. Tevis, A. S. Tayi, H. Cui, S. I. Stupp, *J. Phys. Chem. B* **2010**, *114*, 14778–14786.
[25] G. Eaton, M. C. R. Symons, P. P. Rastogi, *J. Chem. Soc. Faraday Trans. 1 Phys. Chem. Condens. Phases* **1989**, *85*, 3257–3271.
[26] T. Ghosh, J. Panicker, V. Nair, *Polymers* **2017**, *9*, 112.
[27] S. Ghosh, R. Raveendran, A. Saeki, S. Seki, M. Namboothiry, A. Ajayaghosh, *ACS Appl. Mater. Interfaces* **2019**, *11*, 1088–1095.
[28] W. Matsuda, T. Sakurai, G. Ghosh, S. Ghosh, S. Seki, *J. Photopolym. Sci. Technol.* **2018**, *31*, 91–99.
[29] Y. Tsutsui, H. Okamoto, D. Sakamaki, K. Sugiyasu, M. Takeuchi, S. Seki, *J. Phys. Chem. Lett.* **2018**, *9*, 3639–3645.

Experimental

Synthesis

<u>Compound 1</u>: N-hexyl-6-hydroxyhexanamide

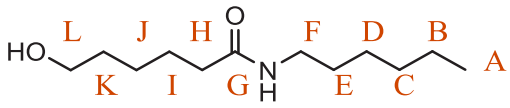

A solution of hexylamine (18.02g, 176.3 mmole) was stirred at ambient temperature. To this was added ξ-caprolactone (13.42 g, 116.3 mmole) dropwise. The mixture was then stirred for 90 min. at 130 °C and cooled down at room temperature. The reaction mixture was dissolved in DCM (50 ml) and washed with a 1 M solution of HCl, then with a solution of $NaHCO_3$. The organic phase was dried with $MgSO_4$, filtrated and concentrated under reduced pressure. The crude was recrystallized (75% ethyl acetate/cyclohexane) to afford **compound 1** as white crystals (16.92 g, 68%).

^{1}H NMR (400 MHz, CD_3OD) : δ [ppm] 3.63 (t, *J* = 6.6 Hz,2H,H_L), 3.15 (t, *J* = 7,1 Hz, 2H, H_F), 2.18 (2H, t, *J* = 7.5 Hz, H_H), 1.67 (m, 2H, H_I), 1.58 (m, 2H, H_K), 1.49 (m, 2H, H_E), 1,41 (m, 2H, H_J), 1.30 (m, 6H, H_B, H_C and H_D), 0.91 (t, *J* = 6.6 Hz, 3H, H_A),

^{13}C NMR (400 MHz, CDCl3) : δ [ppm] 173.4 (C_G), 62.11 (C_L), 39.54 (C_F), 36.55 (C_H), 32.27 (C_K), 31.48 (C_D), 29.52 (C_E), 26.6 (C_C), 25.43 (C_I and C_J), 22.53 (C_B), 13,99 (C_A).

Elemental analysis. Found : C, 67.06; H, 11.67; N, 6.50. Calculated : C, 66.93; H, 11.70; N, 6.50%.

<u>Compound 2:</u> 6-(hexylamino)-6-oxohexyl methanesulfonate

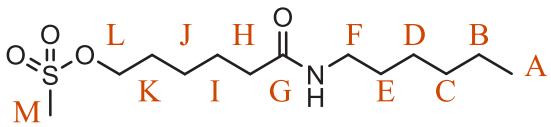

A solution of N-hexyl-6-hydroxyhexanamide (2.8 g, 13 mmol), of NEt_3 (2.8 g, 28 mmol), in anhydrous THF (45 ml) was stirred under argon at 0°C. Methanesulfonyl chloride (3.5 g, 28 mmol) was added dropwise. The mixture was stirred at ambient temperature for 30 minutes, poured in iced water (100 ml) and extracted with DCM (3 x 25 mL). The organic phase was dried by $MgSO_4$, filtrated and concentrated under reduced pressure. The crude was chromatographed on silica (EtOAc) to afford **compound 2** as a white solid (3,1 g, 82%).

^{1}H NMR (400 MHz, CD_3OD) : δ [ppm] 5.45 (s, 1H, NH), 4.23 (t, *J* = 6.6 Hz,2H,H_L), 3.24 (t, *J* = 7,1 Hz, 2H, H_F), 3.01 (s, 3H, H_M), 2.18 (2H, t, *J* = 7.5 Hz, H_H), 1.78 (m, 2H, H_I), 1.68 (m, 2H, H_K), 1.47 (m, 4H, H_E and H_J), 1.29 (m, 6H, H_B, H_C and H_D), 0.91 (t, *J* = 6.6 Hz, 3H, H_A),

^{13}C NMR (400 MHz, CDCl3) : δ [ppm] 172.52 (C_G), 70.00 (C_L), 39.69 (C_F), 37.53 (C_M), 36.56 (C_H), 31.60(C_D), 29.76 (C_E), 29.03 (C_K), 26.72 (C_C), 25.14 (C_I and C_J), 22.69 (C_B), 14.15 (C_A).

Elemental analysis. Found : C, 53.71; H, 9.34; N, 4.75. Calculated : C, 53.21; H, 9.28; N, 4.77.

<u>Compound 1'</u>: (S)-N-(heptan-2-yl)-6-hydroxyhexanamide

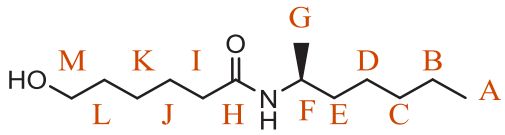

A solution of (S)-(+)-2-aminoheptane (11.34 g, 98.4 mmol) was stirred at room temperature. ξ-caprolactone (7.49 g, 65.6 mmole) was added dropwise. The mixture was stirred for 4 hours at 130°C and cooled down at ambient temperature. The reaction mixture was dissolved in DCM (300 ml) and washed with aqueous HCl (1M) and with aqueous NaHCO3. The organic phase was dried with $MgSO_4$ and concentrated under reduced pressure. The crude chromatographed on silica (EtOAc) to afford **compound 1'** as a limpid oil (10.77 g, 61%).

^{1}H NMR (400 MHz, CDCl3) : δ [ppm] 5.20 (m, 1H, NH), 3.98 (q, *J* = 6.5 Hz, 1H, H_F), 3.66 (t, 2H, H_M), 2.16 (t, 2H, HI), 1.58-1.67 (m, 6H, , H_J, H_K and H_L), 1.41 (m, 2H, H_E), 1.29 (m, 6H, H_B, H_C and H_D), 1.11-1.13 (d, 3H, H_G), 0.88 (t, 3H, H_A)

^{13}C NMR (400 MHz, CDCl3) : δ [ppm] 172.43 (C_H), 62.45 (C_M), 45.22 (C_F), 36.99 (C_M), 36.91 (C_E), 32.37 (C_I), 31.77 (C_D), 25.79 (C_K), 25.48 (C_C), 25.42 (C_J), 22.65 (C_B), 21.09 (C_G), 14.09 (C_A).

Elemental analysis found : C = 67.91%; H = 11.82%; N = 6.14%. Calculated : C = 68.08%; H = 11.87%; N = 6.11%

<u>Compound 2'</u>: (S)-6-(heptan-2-ylamino)-6-oxohexyl methanesulfonate

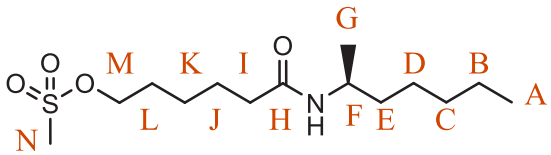

A solution of N-hexyl-6-hydroxyhexanamide (4 g, 17.4 mmol), of NEt_3 (5.29 g, 52.3 mmol), in anhydrous THF (65 ml) was stirred under argon at 0°C. Methanesulfonyl chloride (6 g, 52.3 mmoles) was added dropwise. The mixture was stirred at room temperature overnight, mixed with iced water (150 ml) and extracted with DCM (3 x 25 mL). The organic phase was dried ($MgSO_4$) and concentrated under reduced pressure. The crude was purified by gel silica chromatography (EtOAc) to yield **compound 2'** as a white solid (5.18 g, 77%).

^{1}H NMR (400 MHz, $CDCl_3$) : δ [ppm] 5.13 (m, 1H, NH), 4.16 (t, *J* = 6.5 Hz, 1H, H_M), 3.90 (m, 2H, H_F), 2.93 (s, 3H, H_G), 2.08 (t, *J* = 6.5 Hz, 2H, H_I), 1.71 (m, 2H, H_L), 1.61 (m, 6H, H_J), 1.38 (m, 2H, H_E), 1.21 (m, 6H, H_B, H_C and H_D), 1.04 (d, 3H, H_G), 0.81 (t, *J* = 6.1 Hz, 3H, H_A)

^{13}C NMR (400 MHz, CDCl3) : δ [ppm] 172.4 (C_H), 62.5 (C_N), 45.2 (C_F), 37.0 (C_M), 36.9 (C_E), 32.4 (C_I), 31.8 (C_D), 25.8 (C_K), 25.5 (C_C), 25.4 (C_J), 22.7 (C_B), 21.1 (C_G), 14.14 (C_A).

Elemental analysis found: C = 54.75%; H = 9.60%; N = 4.60%. Calculated: C = 54.69%; H = 9.51%; N = 4.56%

<u>DPPBA:</u> 6-(1,4-dioxo-5-(7-oxotridecyl)-3,6-di(thiophen-2-yl)-4,5-dihydropyrrolo[3,4-c]pyrrol-2(1H)-yl)-N-hexylhexanamide

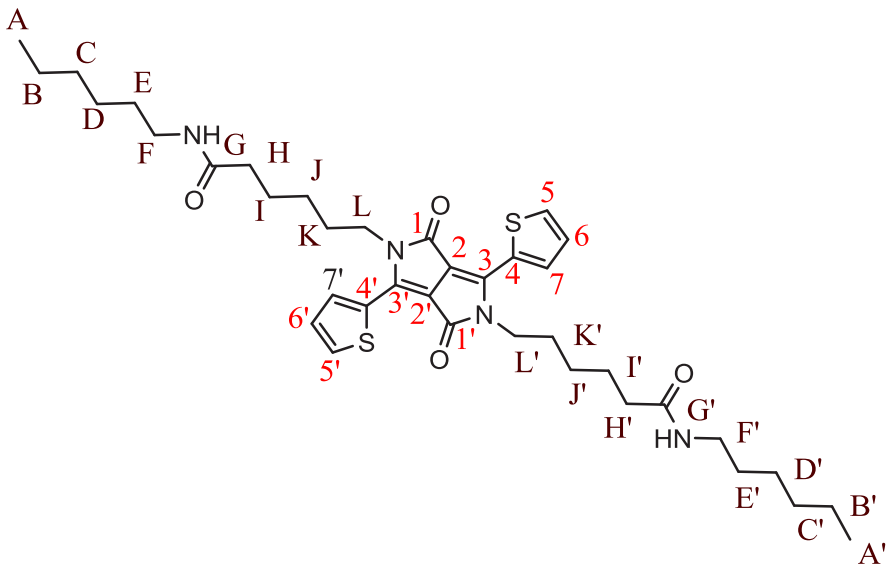

A solution **TDPP** (2 g, 6.8 mmol) in anhydrous DMF (150 ml) was stirred under argon at 120 °C. $CsCO_3$ (5.4 g, 16.5 mmol) was added progressively. The mixture was stirred for 1 h at 120 °C and a solution of **3** (12.24 g, 42 mmol) in anhydrous DMF was added dropwise. The solution was stirred overnight at 120 °C, cooled down at RT and mixed with distilled water (600 ml). The mixture was extracted with DCM (3 x 50 mL). The organic phase was dried ($MgSO_4$) and the solvent removed under vacuum. The crude was purified by column chromatography (DCM/cyclohexane 50/50) to afford the desired compound as a dark purple solid (438 mg, 9%).

^{1}H NMR(400 MHz, CD_2Cl_2) δ [ppm]: 8.91 (dd, *J* = 4, 1.1Hz, 2H, H_5 and $H_{5'}$), 7.66 (dd, *J* = 5, 1.1 Hz, 2H, H_7 and $H_{7'}$), 7.29 (dd, *J* = 5, 4 Hz, 2H, H_6 and $H_{6'}$), 5.48 (m, 2H, NH), 4.09 (t, *J* = 7.7Hz, 4H, H_L and $H_{L'}$), 3.23 (q, *J* = 6.7 Hz, 4H, H_F and $H_{F'}$), 2.18 (t, *J* = 7.6 Hz, 4H, H_H and $H_{H'}$), 1.71-1.78 (m, 8H, H_I, $H_{I'}$, H_K and $H_{K'}$), 1.47 (m, 8H, H_E, H_J, $H_{E'}$ and $H_{J'}$), 1.28 (m, 12H, H_B,H_C, H_D, $H_{B'}$,$H_{C'}$and $H_{D'}$), 0.89 (t, *J* = 6.9 Hz, 6H, H_A and $H_{A'}$)

^{13}C NMR (400 MHz, CD_2Cl_2) δ [ppm]: 172.73 (C_G and $C_{G'}$), 161.53 (C_1 and $C_{1'}$), 140.16, 135.42 (C_5 and $C_{5'}$), 130.99 (C_7 and $C_{7'}$), 129.79 ($C_4$and $C_{4'}$), 128.80 ($C_6$and $C_{6'}$), 107.82 ($C_2$and $C_{2'}$) 42.01 (C_F and $C_{F'}$), 39.68 (C_F and $C_{F'}$), 36.74 (C_H and $C_{H'}$), 31.62

(C_D and $C_{D'}$), 29.79 (C_E and $C_{E'}$), 29.73 (C_K and $C_{K'}$), 26.74 (C_C and $C_{C'}$), 26.53 (C_J and $C_{J'}$), 25.40 (C_I and $C_{I'}$), 22.71 (C_B and $C_{B'}$), 14.17 (C_A and $C_{A'}$)

Elemental analysis found : C = 64.88%; H = 7.88%; N = 8.06%. Calculated : C = 65.67%; H = 7.83%; N = 8.06%

HRMS (ESI+) m/z: 695.3673 (MH+); calcd for $C_{38}H_{55}N_4O_4S_2$ (MH+): 695.3659

(S)-DPPBA: N-((S)-heptan-2-yl)-7-(5-(6-(((S)-heptan-2-yl)amino)-6-oxohexyl)-1,4-dioxo-3,6-di(thiophen-2-yl)-4,5-dihydropyrrolo[3,4-c]pyrrol-2(1H)-yl)heptanamide

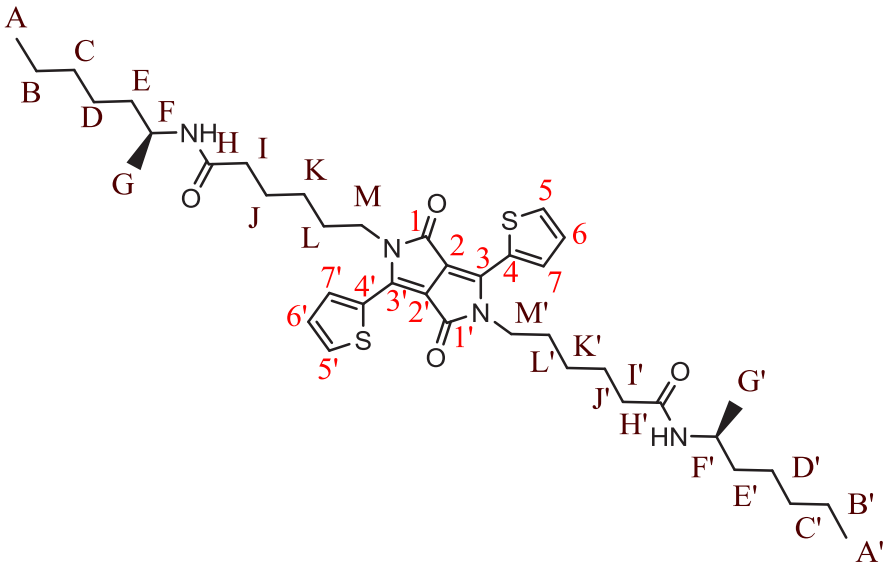

A solution **TDPP** (650 mg, 2 mmoles) was stirred under argon in anhydrous DMF (15 ml) at 120°C. To this was added cesium carbonate (2.17 g, 6.62 mmol) was added progressively portion by portion. The mixture was stirred for 1h at 120°C then a solution of (S)-6-(heptan-2-ylamino)-6-oxohexyl methanesulfonate (2 g, 6.5 mmol) in anhydrous DMF was added drop by drop. The solution was stirred overnight at 120°C, cooled at room temperature and mixed with distilled water (600ml). The crude was extracted DCM. After collecting the organic phase, the solvent was removed under vacuum and the product was purified by column chromatography (50% :DCM : 50% :cyclohexane) to afford **(S)-DPPBA** (150 mg, 10%).

^{1}H NMR (400 MHz, CD_2Cl_2) δ [ppm]: 8.90 (dd, *J* = 4, 1.1Hz, 2H, H_5 and $H_{5'}$), 7.65 (dd, *J* = 5, 1.1 Hz, 2H, H_7 and $H_{7'}$), 7.29 (dd, *J* = 5, 4 Hz, 2H, H_6 and $H_{6'}$), 5.22 (m, 2H, NH), 4.09 (t, *J* = 7.7Hz, 4H, H_M and $H_{M'}$), 3.97 (m, 4H, H_F and $H_{F'}$), 2.15 (t, *J* = 7.6 Hz, 4H, H_I and $H_{I'}$), 1.78 (m, 4H, H_L and $H_{L'}$), 1.71 (m, 4H, H_J and $H_{J'}$), 1.47 (m, 4H, H_K and $H_{K'}$), 1.39 (m, 4H, H_E and $H_{E'}$), 1.28 (m, 12H, H_B,H_C, H_D, $H_{B'}$,$H_{C'}$and $H_{D'}$), 1.11 (d, 6H, H_G and $H_{G'}$), 0.89 (t, *J* = 6.9 Hz, 6H, H_A and $H_{A'}$)

^{13}C NMR (500 MHz, CD_2Cl_2) δ [ppm]: 172.05 (C_H and $C_{H'}$), 161.52 (C_1 and $C_{1'}$), 140.15 (C_3 and $C_{3'}$), 135.43 (C_5 and $C_{5'}$), 130.96 (C_7 and $C_{7'}$), 129.80 (C_4 and $C_{4'}$), 128.81 (C_6 and $C_{6'}$), 107.82 (C_2 and $C_{2'}$), 45.27 (C_F), 42.04 (C_M), 37.11 (C_E), 36.93 (C_I), 31.83 (C_D),

29.72 (C_L), 26.54 (C_K), 25.86 (C_C), 25.47 (C_J), 22.73 (C_B), 21.19(C_G), 14.18 (C_A and $C_{A'}$).

Elemental analysis. Found: C, 66.01; H, 8.07; N, 7.63%. Calculated: C, 66.45; H, 8.09; N, 7.75

HRMS (ESI+) m/z: 723.3981 (MH+); calcd for $C_{38}H_{55}N_4O_4S_2$ (MH+): 723.3972

Chapter 4: Monoamide-functionalized thiophene-capped diketopyrrolopyrrole derivatives. Gelation studies.

Summary

This chapter deals with **DPP** derivatives forming organogels. As an introduction, we show how this type of self-assembly, especially its fibrillar morphology, has been exploited in the literature for organic electronics. By taking into account the low solubility of the diamides **DPP** derivatives of the previous chapter, we designed new **DPP** derivatives bearing only one amide on a lactam and a branched alkyl chain (ethylhexyl or butyloctyl) on the other lactam. We describe their synthesis and we show that these compounds gel *trans*-decalin or cyclohexane for concentrations above 5 mg/mL.

The following sections of the chapter deal with the study of the butyloctyl derivative **BOTDPPma**. In a first part, the phase diagram of **BOTDPPma**/*trans*-decalin is mapped out by rheology and turbidimetry. This phase diagram presents two regimes: at low concentration, the gels have a classical texturation with fibrils of high aspect ratio. At high concentrations, the gels form fibrils and spherulites, as evidenced by polarized optical microscopy. SEM allowed visualizing how the spherulites are embedded in the fibrils network.

The shapes of the aggregates were measured by freeze-fracture TEM and by SAXS. The TEM images showed that the fibrils have a diameter of about 7 nm with low polydispersity. The SAXS intensities are fitted with a model of heterogeneous cylinder with 3 different shells. The measured outer diameter (70.4 ± 2 Å) is consistent with that measured by TEM. The different thicknesses and the scattering lengths density found provide a realistic model of the packing of the molecules inside the cylinders. The core of this cylinder has a scattering length density close to that of the solvent, and an alternative model of tubes is also consistent with the data.

I. Introduction

Organogels have been developed first for their rheological properties and now give rise to research in many domains.[1–6]. Regarding organic electronics, semiconducting organogels possess interesting electronic properties that can be used for solar cells, transistors or sensor devices[7,8]. Organogelators are well dispersed and form fibrils with high aspect ratio, which remain after the solvent is removed (xerogel). Such structures have large specific area. It can be exploited to develop large donor-acceptor interfaces and favour exciton dissociation. The fibrillar morphology favors the transport of charges to the electrodes. This concept was first illustrated in 2008 by Sugiyasu et al. who developed a self-sorted organogel system by combining a P-type and an N-type semiconducting organogelators (Figure 1a).[9] During gelation, both molecules self-assemble independently into nanofibers which interconnect creating p-n heterojunctions points (Figure 1b). This system generates a photocurrent (Figure 1c).

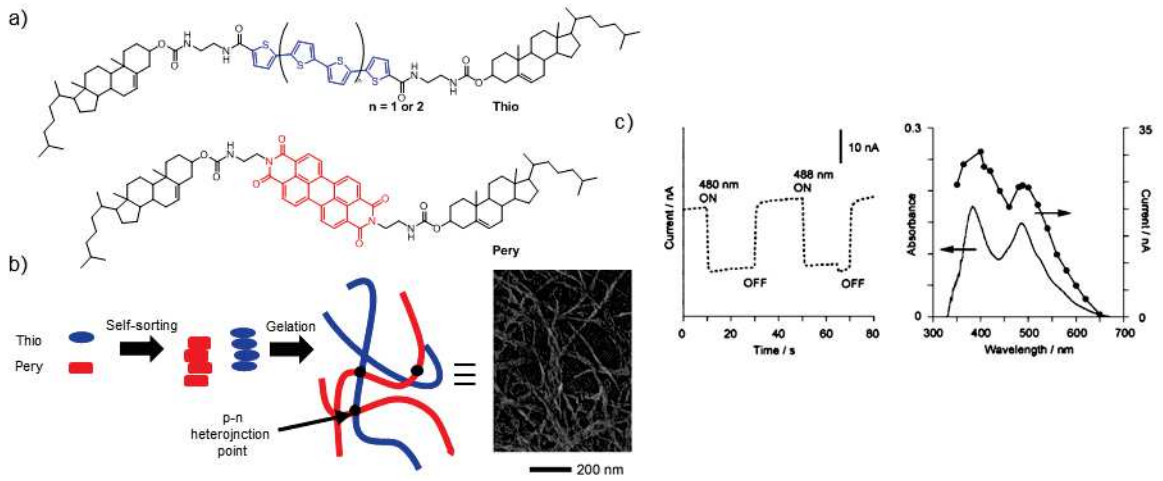

Figure 1: *a) Chemical structure of P-type gelator based on oligothiophene and N-type gelators based on perylene; b) Concept of self-sorting gelation with p-n heterojunctions; c) On the left: photoelectrochemical response, on the right: absorption spectrum (full line), and photocurrent action (pointed line) spectrum of the cast film prepared from self-sorting gel on an ITO electrode: applied potential) 0.2 V vs Ag/AgCl.*

Recently Prasantkumar et al. presented another combined self-sorting gel system where the fibers of P-type and N-type semiconductors were coaxially aligned forming p-n heterojunctions[10] (figure 2). Such assembly between P-type and N-types fibres are advantageous in terms of domains size. Previous studies showed that a diffusion length of excitons between 5 and 10 nm is optimal for the separation of the mobile charge carriers[11]. The diameters of the semiconducting fibers are fully in this range.

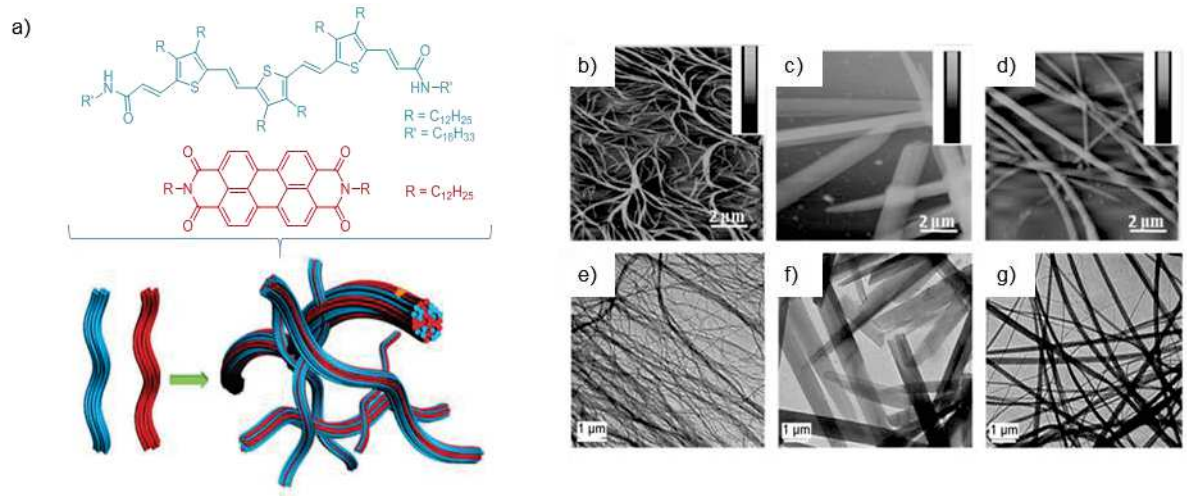

Figure 2: *a) trithienylenevinylene (TTV, P-type) and perylene bisimide (PBI, N-type) derivatives with representation of coaxial assembly; AFM images of b) TTV, c) PBI and d) TTV/PBI coaxially mixed (1:1 molar ratio); TEM images of e) TTV, f) TTV/PBI coaxially mixed (1:1 molar ratio) (n-decane solution with c = 5 x 10^{-5} M).*

Organogels are therefore perceived as efficient tools in the field of organic electronics. But some challenges need to be addressed. To start, there is no known rule for making an organogelator. Structural requirements to achieve gelation are unpredictable although many information regarding gelators helped narrowing some chemical functions essential to make them. These functions are exposed in the following figure.

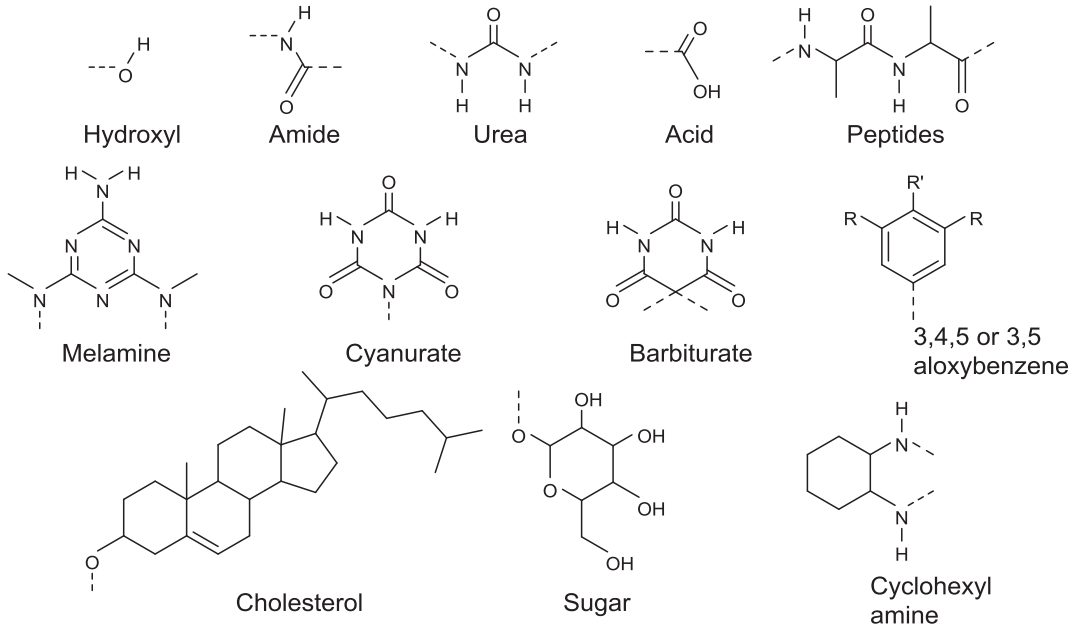

Figure 3: *Chemical structure required for gelation.*

The second difficulty is that the semi-conducting properties of the gel depend on the packing of the molecules within the fibers. For example, charge transport relies

on a good π-stacking. Our group showed that a dendronized naphthalene based gelators cannot transport charge, because the naphthalene units do not stack properly[12].

Among semiconducting organogelators, several type of organic molecules were studied for their charge mobility, conductivity and their self-assembly properties. Organogelators based on thiophene are widely studied for their optoelectronic, redox, and charge transport properties. Stupp and co-workers developed an organogelator based on dendrons rod-coil architecture (Figure 4) with oligothiophene moieties.[13] They gel toluene and self-assemble into nanoribbons, according to electron and atomic force microscopy analysis. The conductivity measured for this molecule is 7.9×10^{-5} $S.cm^{-1}$ in thin films.

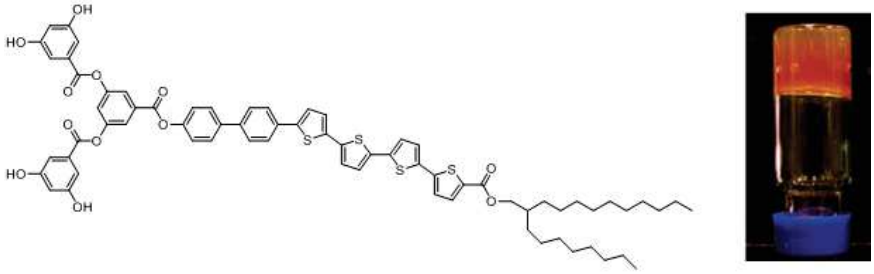

Figure 4: *Chemical structure of the Dendron based organogelator and gel made in toluene.*

Prasanthkumar et al. reported the organogelators TTV 4 and TTV 5 (Figure 5a), based on thienylenevinylene with terminal amides[14]. These compounds gel non-polar solvents like hexane, cyclohexane and decane and are dissociated in chloroform. Their minimum charge carrier mobilities ($\Sigma\mu_{min}$) were measured by flash-photolysis time-resolved microwave conductivity (FP-TRMC). It was 1.5×10^{-2} $cm^2.V^{-1}.s^{-1}$ for TTV 4 and 4×10^{-2} $cm^2.V^{-1}.s^{-1}$ for TTV 5 on films prepared from chloroform solutions. When prepared from chloroform/decane solution the minimum charge carrier mobilities rose up to 6.0×10^{-2} $cm^2.V^{-1}.s^{-1}$ for TTV 4 and 7.2×10^{-2} $cm^2.V^{-1}.s^{-1}$ TTV 5. This improvement was attributed to the hydrogen bonds triggered gelation. A quaterthiophene functionalized by bis(trialkoxybenzamide) was developed by Pratihar et al[15]. This compound gels non-polar solvents by forming fibrillar structures. Pulse radiolysis time resolved microwave conductivity (PR-TRMC) technique allowed measuring charge mobilities around 0.03 $cm^2.V^{-1}.s^{-1}$. These values remain however lower than the mobility exhibited by poly(3-hexyl thiophene) (P3HT) which was 0.1 $cm^2.V^{-1}.s^{-1}$.[16] The same group also developed two oligo(thienylenevinylene) molecules (OTV1 and OTV2), forming gels in non-polar solvents[17] (Figure 5b). The conductivity is $6.45.10^{-4}$ $S.cm^{-1}$ for OTV 1 and $4.83.10^{-4}$ $S.cm^{-1}$ for OTV2, which shows that it is influenced by the extension of conjugation length. It can be increased by iodine doping up to $1.02.10^{-2}$ S. cm^{-1} for OTV 1 and 4.83 $S.cm^{-1}$ for OTV2.

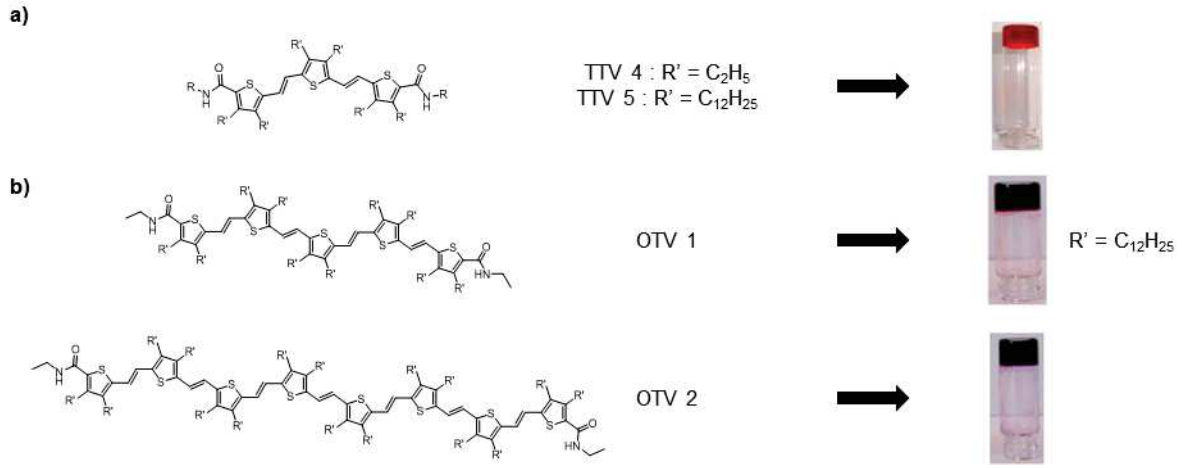

Figure 5: *a) Chemical structures of TTV 4 and TTV 5 with gel sample made with decane; b) Chemical structures of OTV 1 and OTV 2 with gels made in decane.*

Another family of semiconducting gelators that has attracted scientist interest are those based on tetrathiafulvene (TTF). Some of them are able to form conductive single crystals, some of them can form fibers, as in the following examples. Narulli et al. coupled TTF with a dipeptide (Figure 6a).[18] The compound forms gels in chloroform, ethyl acetate and acetone. Conductivity measurements of the xerogels deposited on glass surface were performed before and after doping with TCNQ. Results went from $1.9.10^{-10}$ $S.cm^{-1}$ before doping to $3.6.10^{-4}$ $S.cm^{-1}$ after doping due to strong intermolecular charge transfer between the dipeptide TTF and the doping agent. Recently Draper et al. also made a TTF dipeptide molecule forming hydrogels[19] (Figure 6b). The conductivity of the xerogel was measured on thin film after being doped with iodine vapour. A current response around 0.5 nA was measured for an applied tension of 4 V. The current was also measured on a dried solution sample after dopping. A current of 120 nA was generated for the same tension applied for the xerogel. Around the same period, Lang et al. synthesized an amphiphilic TTF molecule which forms gels in ethanol, methanol, DMSO and n-butanol[20] (Figure 6c). The formation of fibers was confirmed by SEM images and allowed a conductivity of 10^{-4} $S.cm^{-1}$.

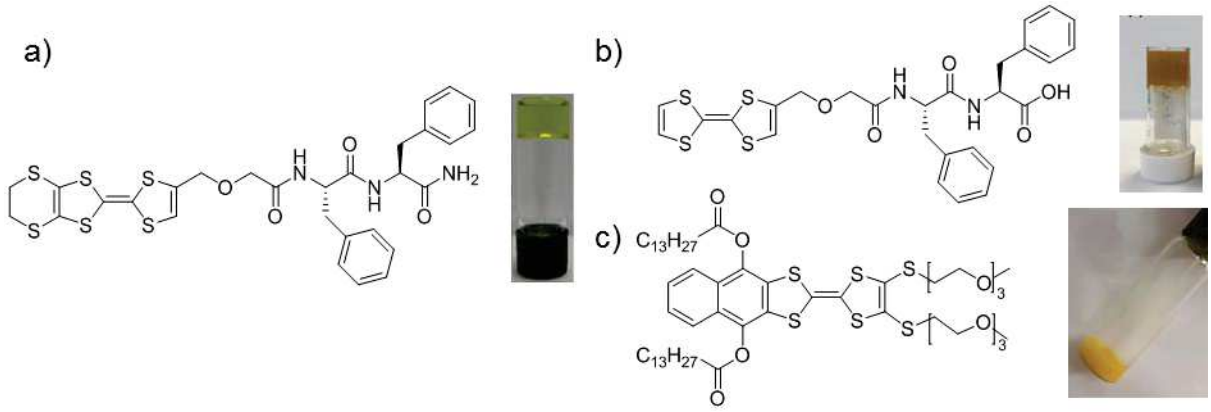

Figure 6: *Chemical structure of (a) a dipeptide* TTF based organogelator with gel in chloroform; (b) *a dipeptide* TTF based hydrogelator with hydrogel sample; (c) an amphilic TTF organogelator with gel sample in DMSO.

Semiconducting organogelator based on naphthalene diimide were also reported in the literature. Recently, naphthalene diimide molecules linked with dipeptides moieties were developed by Nandi et al[21] (Figure 7). They gel a mixture of chloroform and methylcyclohexane. SEM studies revealed these compounds form intertwined nanofibers. These compounds exhibit conductivities of 7.10^{-6} $S.cm^{-1}$ and $5.3.10^{-8}$ $S.cm^{-1}$ as measured by current-voltage studies. Basu reported a dipeptide naphthalene diimide hydrogelator.[22] Their compound showed a photocurrent value from 0.073 to 1.16 µA in gel state whereas aggregate samples only exhibited photocurrent response of 4 nA.

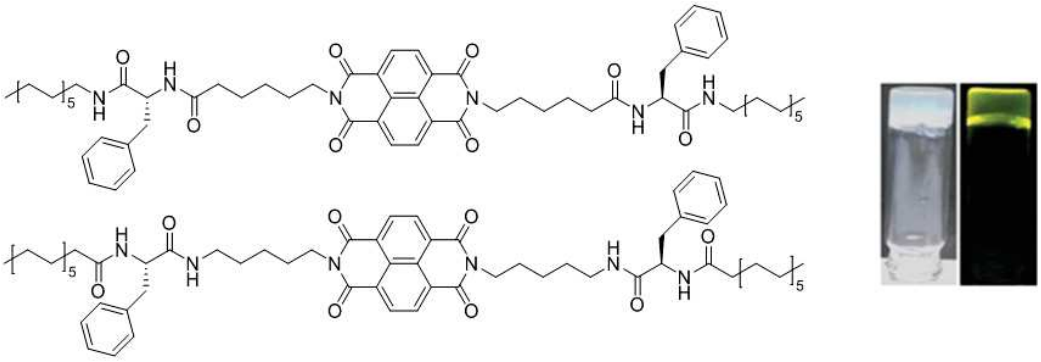

Figure 7: *Chemical structure of naphthalene diimide with gel samples made in chloroform-methylcyclohexane mixture (5:95) in day light and under UV light at 365 nm.*

Perylene bisimide (PBI) are another kind of semiconductor which have shown the ability to form gelation in various solvents[9,23,24]. PBI is one of the rare n-type semiconductor forming organogels. The first PBI organogelator was introduced by Li et al. in 2006[25] They obtained a PBI structure with terminal aromatic amides by combining perylene tetracarboxylic acid bisanhydride with two aminoethylbenzamide units (Figure 8). This molecule forms transparent gels in aliphatic and aromatic solvents, and opaque gels in dioxane, THF, dibutyl ether and trimethylamine. AFM microscopy showed the presence of nanofibers, with left or right handed helicities despite the achiral nature of the PBI units. This behavior was attributed to the formation of hydrogen bonds directing π-π stacking between the monomer units. Pulse-radiolysis time-resolved microwave conductivity (PR-TRMC) analysis, gave the sum of the isotropic electron and hole mobility (ΣµTRMC) of 0.052 $cm^2.V^{-1}.s^{-1}$ which compared to liquid crystalline phase of small PBI molecules[26] (0.007 $cm^2.V^{-1}.s^{-1}$) is more efficient.

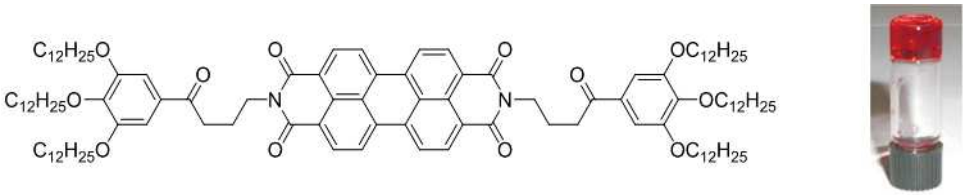

Figure 8: *Chemical structure of PBI organogelator with gel sample in toluene.*

Regarding diketopyrrolopyrrole, there is up to today only six examples of gelators mentioned in the literature which were presented in the introduction chapter.

The objective of this PhD work was to create new DDP semiconducting organogelators, which could also be used for electronic devices applications. The semicarbazone and achiral bisamide DDP presented in the previous chapters were tested as organogelators. But these compounds are not soluble enough and do not dissolve in heated solvent. This observation suggest the molecules need to be more soluble either by adding alkyl chains or making **DPP** molecules with only one amide function, to decrease the strength of intermolecular interactions. This is why we developed monoamides (Figure 9). These molecules are a combination of the two previous families mentioned in the previous chapter. These molecules are N-alkylated on one nitrogen with an amide chain that was previously used to synthesize the bisamide **DPP** (Chapter 3). The other nitrogen of the **DPP** core is alkylated either with a ethylhexyl either with butyloctyl branch chains, like in the semicarbazon **DPP**s (Chapter 2). Studies made on these compounds were more focused on the making of organogels and their self-assembly properties.

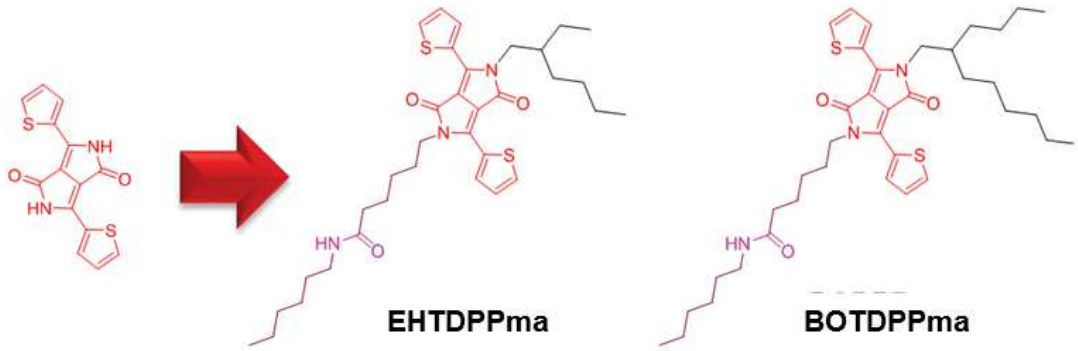

Figure 9: *Chemical structure of the targeted monoamide* ***DPP*** *derivatives.*

II. Synthesis

The synthesis of these molecules is similar to the one of the bisamide **DPP**, with one more alkylation step reaction (scheme 1). The thiophene dyketopyrrolopyrrole is first mono N-alkylated with ethylhexyl bromide or butyloctyl mesylate with yields of 30%. A second N alkylation is performed with the amide chain. The final products **EHTDPPma** and **BOTDPPma** are obtained with yields of 22% and 34% respectively at the scale of 70 and 155 mg.

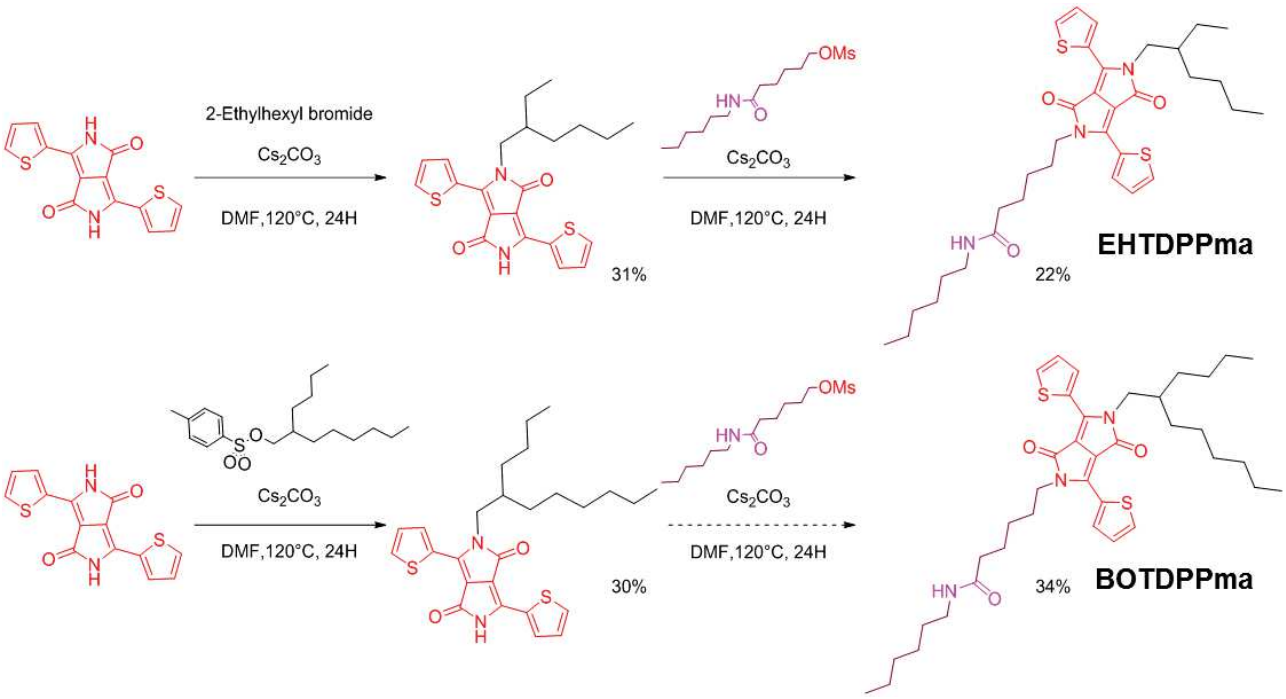

Scheme 1: *Synthetic steps towards* ***EHTDPPma*** *and* ***BOTDPPma.***

III. Gelation testing

The ability of these molecules to form organogels was checked by inverted tube tests: the compounds were mixed with different solvents, heated up to boiling point for five minutes and then let cool down at room temperature (Figure 10).

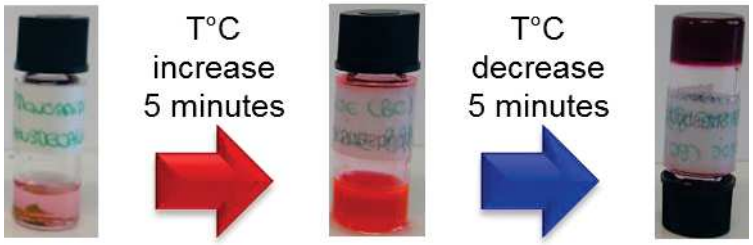

Figure 10: *inverted tube test.*

The results are mentioned in table 1 and 2. **EHTDPPma** precipitates in cyclohexane and forms gels in *trans*-decalin at concentrations from 20 $mg.mL^{-1}$ to 5 $mg.mL^{-1}$. Below 5 $mg.mL^{-1}$, it forms precipitates. In chloroform, chlorobenzene, toluene, ethyl acetate, the product instantly dissolves at room temperature.

Table 1: *Solubility of* ***EHTDPPma*** *: P: precipitate, G : gel; S : solution; - : not tested.*

Solvent	20 mg/ml	10 mg/ml	6,6 mg/ml	5 mg/ml	4.54 mg/ml	3.33 mg/ml
Cyclohexane	P	P	P	P	P	P
Trans-decalin	G	G	G	G	P	P
Chloroform	S	S	S	S	S	S
Chlorobenzene	S	S	-	-	-	-
Toluene	S	-	-	-	-	-
Ethyl acetate	S	-	-	-	-	-

BOTDPPma gels cyclohexane and *trans*-decalin at concentrations from 20 $mg.mL^{-1}$ to 3.33 $mg.mL^{-1}$. In the other solvents, the product is soluble at room temperature.

Table 2: *Solubility of* ***BOTDPPma*** *: P: precipitate, G : gel; S : solution; - : not tested.*

Solvent	20 mg/ml	10 mg/ml	6,6 mg/ml	5 mg/ml	4.54 mg/ml	3.33 mg/ml	2.22 mg/ml
Cyclohexane	G	G	G	G	G	G	-
Trans-decalin	G	G	G	G	G	G	G
Chloroform	S	-	-	-	-	-	-
Chlorobenzene	S	-	-	-	-	-	-
Toluene	S	-	-	-	-	-	-
Ethyl acetate	P	-	-	-	-	-	-

IV. Study of the sol-to-gel transitions and mapping of the phase diagram

1. Study by Rheology

A gel is defined by a solid-like behaviour. Therefore, rheology is essential to characterize properly a gel. Among the quantities measured by rheology, we are interested in two of them: the viscosity and the complex modulus.

The complex shear modulus is

$$G^*(\omega) = \frac{\sigma(\omega)}{\varepsilon(\omega)}$$

where ω is the shear pulsation, and

$$G^*(\omega) = G'(\omega) + iG''(\omega)$$

The real part *G′* is the elastic modulus and *G″* is the viscous or loss modulus. A gel is characterized by a solid-like behavior, which is translated by the fact that *G′* > *G″* for all frequencies. This condition can be verified for liquids at high frequencies, but not at low frequencies. The solid must verify this condition even for low values of ω.

Such a behaviour is illustrated figure 11. At fixed temperature, *G′* and *G″* were measured for a gel of **BOTDPPma** in *trans*-decalin at 20 mg.mL^{-1} over three decades of frequencies. The storage modulus *G*' is constant at 3.10^3 Pa and higher for all the probed frequencies than the loss modulus *G*'' of 2.10^2 Pa (Figure 11). Such variation of both modulus is typical of organogels.

In order to measure the temperature of transition, *G** is measured as a function of temperature. The sol-to-gel transition, according to the model of Winter and Chambon,[27–30] is reached when *G″*/*G′* is independant of temperature. In the case of organogelators, this criterion is never observed, because the initial sol does not contain yet the object increasing the viscosity: the formation of the aggregates coincides with the formation of the network. So for organogelators, the gel-to-sol transition is taken as the point where *G″* and *G′* cross over.

Such a determination of the transition temperature is shown in the following figure (on the right). The sample (*C* = 20 mg/mL) was cooled and *G″*/*G′* are measured at a given frequency for each temperature. At high temperature *G″* > *G′*, which indicates that the mixture is a liquid. At 70 °C, *G″* = *G′*, which marks the temperature of gel formation. Below this temperature *G′* > *G″* indicating the behaviour of a solid, and the regime of the gel. For all these experiments, the cross over point has been extrapolated to null strain σ, because a high strain may disrupt the gel and shift the apparent cross over.

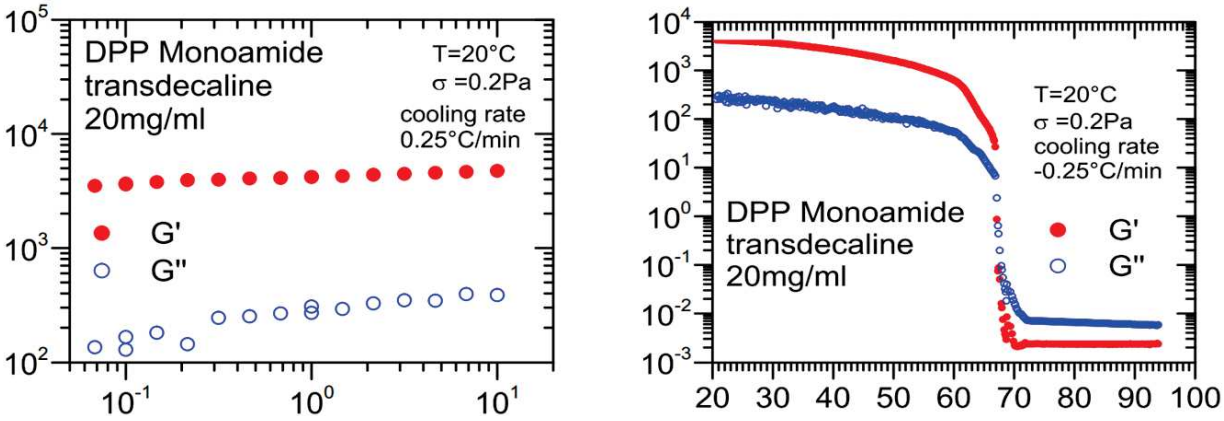

Figure 11: *rheological measurements of the* ***BOTDPPma*** *gel in trans-decalin.*

The measurements are performed when the sample is cooled and when it is heated. Indeed, the gel formation and the melting of the gel occur at different temperatures. The same experiments are done with samples at different concentration. The transition temperatures vary with concentration and are the basis to establish the phase diagrams (see below).

2. *Turbidity*

The rheological measurements were completed by turbidimetry. This technique consists in measuring the light intensity transmitted by a sample (at an angle close to 0°). When heterogeneities appear in the mixture, they scatter light at different angles and the transmitted intensity decreases. This technique can follow the formation of gels,[31,32] because when the gels form, heterogeneities also form and can even opacify them. The technique is useful to track other events that take place after gel melting, like liquid-liquid phase separations.[33]

The same gel samples studied by rheology were studied in a home-made turbidimeter (made by D. Collin) and the intensities were recorded when the temperature was decreased and increase again. Such a curve is shown in the following figure.

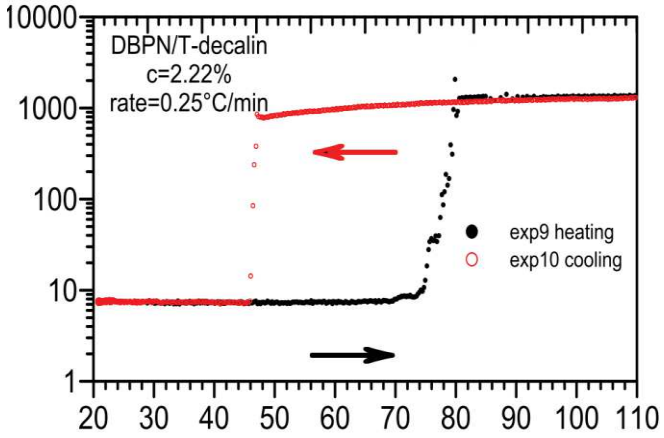

Figure 12: *Turbidity measurments of* ***BOTDPPma*** *gel in trans-decalin C = 20 mg/ml.*

The intensity shows a sharp decrease, when the mixture is cooled and a sharp increase when it is heated back. The cooling and heating rates were the same as in the rheological experiments. For the samples with low concentrations (from 2.22 to 10 mg/mL) these jumps occur at the sol-gel transition and the gel-sol transitions temperatures as measured by rheology.

At higher concentrations (> 10 $mg.mL^{-1}$), the intensity increases at the same temperature than the gel-to-sol transition as measured by rheology. But, upon cooling the intensity decreases at temperature below the sol-to-gel transition. The gel forms first, without significant decrease of the intensity, which proves that the gel contains only a few or small heterogeneities. Therefore, the elastic network itself is not detected by optical measurements. Then, larger objects form below the transition, once the gel is formed

.

In order to visualize these heterogeneities, we have followed the formation and melting of gels by optical microscopy. The gels were prepared in thin capillaries and

observed by polarized light microscopy, while they were heated or cooled at the same heating and cooling rate than in rheology and turbidity analysis.

When the solution is cooled and when the temperature reaches the sol-gel transition, nothing is visible. It is not surprising, since for many organogelators, the size of the fibrils is below the wavelength of visible light. When the temperature reaches the temperature where the turbidity increases, the optical microscopy (OM) images revealed the formation of spherulites, identified by their typical Maltese cross pattern in polarized light (Figure 13). These spherulites were observed for concentrations higher than 10 $mg.mL^{-1}$, but not below.

The spherulites themselves are few and not connected with each other. They do not form a network and therefore cannot account for the elasticity of the network.

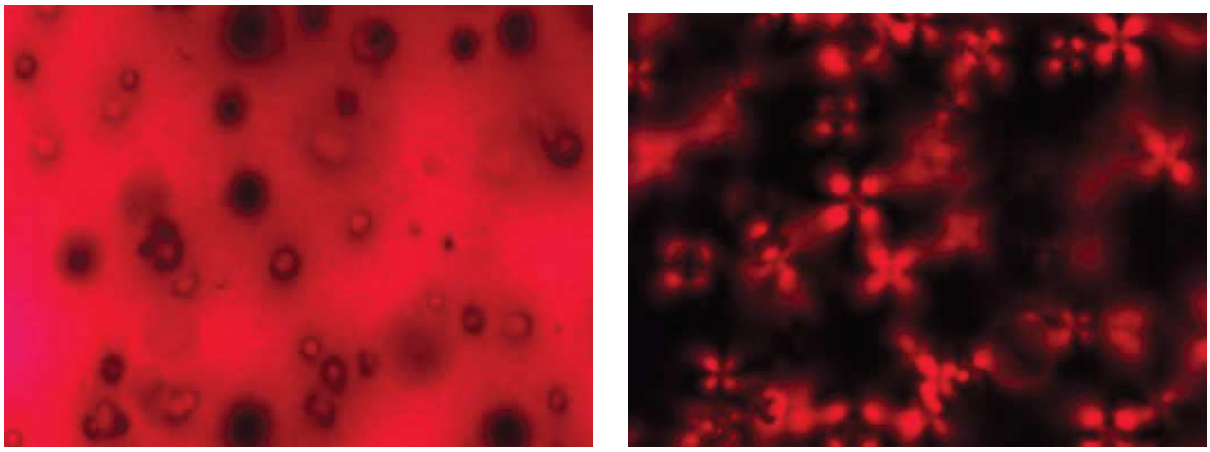

Figure 13: *Optical microscopy images of* ***BOTDPPma*** *gel in trans-decalin; C= 20mg/ml.*

A phase diagram was established by comparing rheology, turbidity and microscopic measurements with gel in *trans*-decalin at different concentrations (Figure 14). In the heating phase, all events occur at the same temperature: the gel-to-sol transition and decrease of the turbidity.

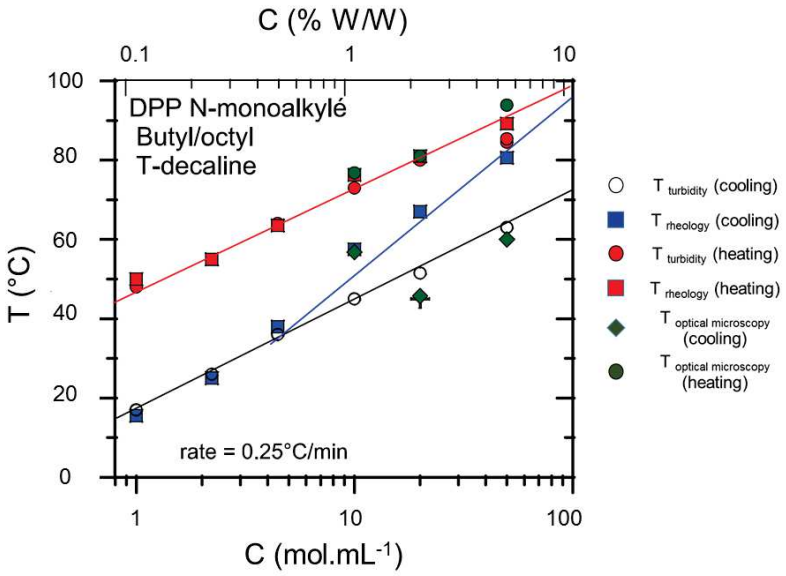

Figure 14: *C-T Phase diagramm of* ***BODPPma****/trans-decalin.*

In the cooling phase, the curves are more complex:

At c > 10 mg.mL^{-1}), two events are observed: the sol-to-gel transition at a given temperature, and at a lower temperature, the formation of crystalline spherulites.

At lower concentrations, the sol-to-gel transitions occur at the same temperature measured by turbidimetry. The increase of turbidimetry can be due to the formation of spherulites. However we have not observed them by microscopy. They can also be due to smaller particles or particles different than spherulites.

In conclusion the phase diagram is complex and shows two different regimes. Its type is unprecedented in the domain of gelators. It is still under investigation and will be the topic of a publication.

3. DSC

The different regimes could not be explored by microDSC because because this apparatus went down and was not replaced during the Ph. D. But we tried to study the two transitions during the cooling process by regular differential scanning calorimetry. We tested the highest concentration (50 mg.mL^{-1}) because it has the highest gap between the sol-to-gel temperature found by rheology and the one found by turbidimetry. But DSC is less sensitive and must operate at higher cooling rate to detect thermic peaks. At the lowest rate that can be applied (1 °C/min), the peaks are not detected and at higher rate only one event is visible (Figure 15, green curve).

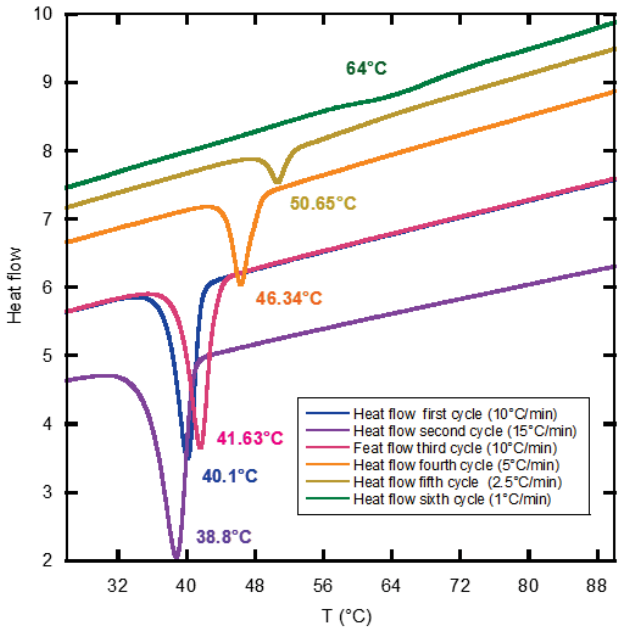

Figure 15: *DSC curves of* ***BOTDPPma*** *during cooling process; (C = 50 mg.mL^{-1}).*

V. Structural studies

1. Electron Microscopy

The shape and the size of the supramolecular structure in the gels in cyclohexane and *trans*-decalin were analyzed by TEM (Figure 16). This technique requires samples thin enough to allow the transmission of the electron beam (typically less than 80 nm). When the sample is a solid, it can be cut into thin slices with a microtome; when it is liquid, a thin film can be formed in a holey grid. The gels are difficult to observe since they form only thick films, and they are too soft to be sliced. For this reason, we implemented the technique of freeze fracture.[34] It consists in freezing the sample with high freezing rates, so the solvent remains amorphous. The sample is kept at low temperature and fractured. The fracture occurs in the planes of least resistance, especially the planes containing the structures. The fracture is successful when the solvent is amorphous and does not feature any crystal structure: only the aggregates are visible. The sample is processed by shadowing one side of the gel and recovering this replica by a carbon film. The advantage of the technique is that the objects are observed in their native form, surrounded by the solvent. The technique is therefore well suited to study organogels.[35–37] The main inconvenient is the resolution, limited to the size of the metal particles sputtered during the shadowing step.

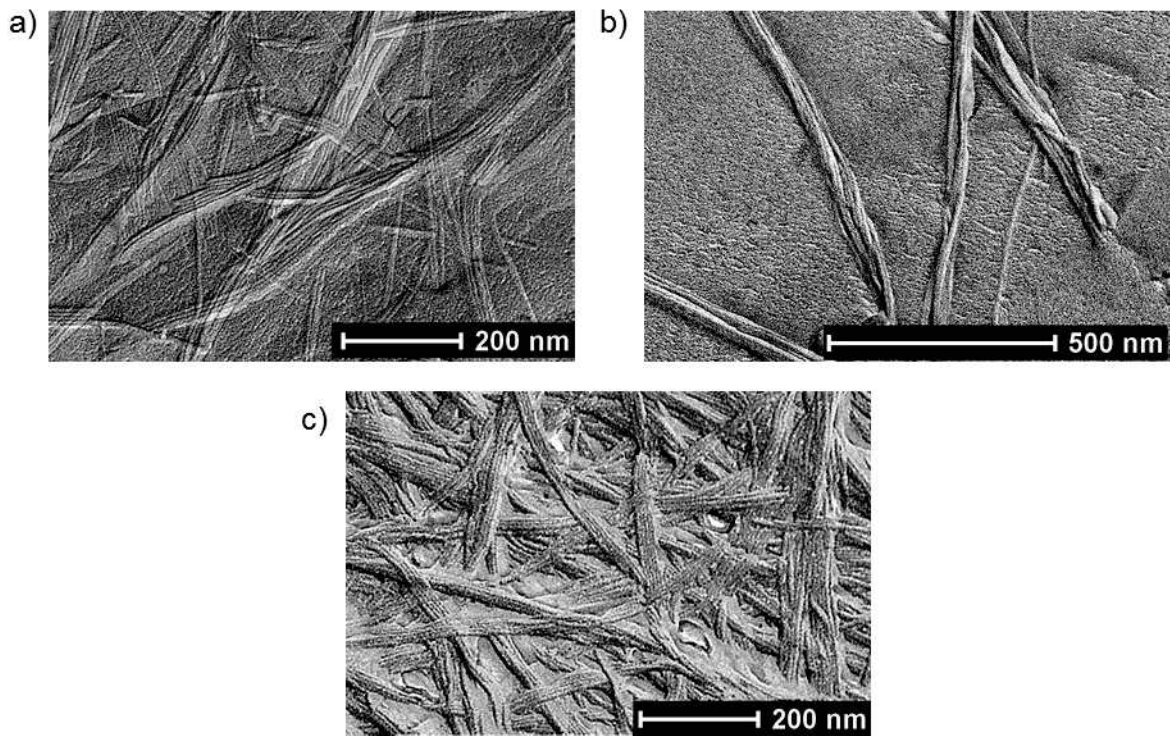

Figure 16: *TEM images of (a)* ***BOTDPPma*** *in trans-decalin (C= 2.22 mg/ml); (b)* ***EHTDPPma*** *in trans-decalin (C= 5 mg/ml); (c)* ***BOTDPPma*** *in cyclohexane (C= 20 mg/ml).*

In freeze-fractured samples, the micrographs show networks of nanofibers for both **BOTDPPma** and **EHTDPPma** molecules, in *trans*-decalin and cyclohexane. The diameters of the fibers are around 7 nm and their lengths several micrometers. The diameters have a low polydispersity.

The shape and the size of the structures are the same in both solvents. They are also the same for both molecules. When the concentration increases, the fibers tend to pack together and their network becomes more dense (Figure 16b and 16c).

The observed field in TEM is rather limited, a few micrometers. For this reason, it is not possible to visualize large object like the spherulites. In optical microscopy, the spherulites can be observed, but not the network of fibers. In order to visualize both components, we have explored the overall structure of gels by scanning electron microscopy. We have first observed samples at low concentrations with no spherulites detected by OM. Figure 17 shows the example of the gel of **BOTDPPma** in *trans*-decalin at 4 mg/mL.

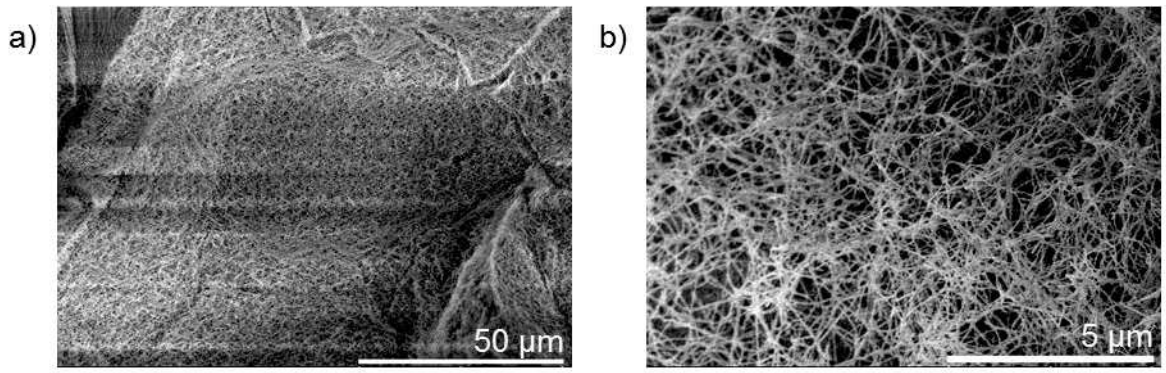

***Figure 17**: SEM picture of a gel of **BOTDPPma** in TD at 4 mg/mL. Left: large field; Right: near field.*

The structure of the gel is quite homogeneous over distances of about 100 µm (Figure 17a). The only areas that show less density are cracks, probably due to the sample handling (stress cracking during freezing or during removal of the solvent). An enlargement of the gel shows the entangled fibrillar network (Figure 17b).

At higher concentration, the samples show large structures, embedded in the gel. They are denser that the gel network. They can be identified as spherulites by many areas with periodical arrays proving their crystalline nature (Figure 18 left and right, black arrows).

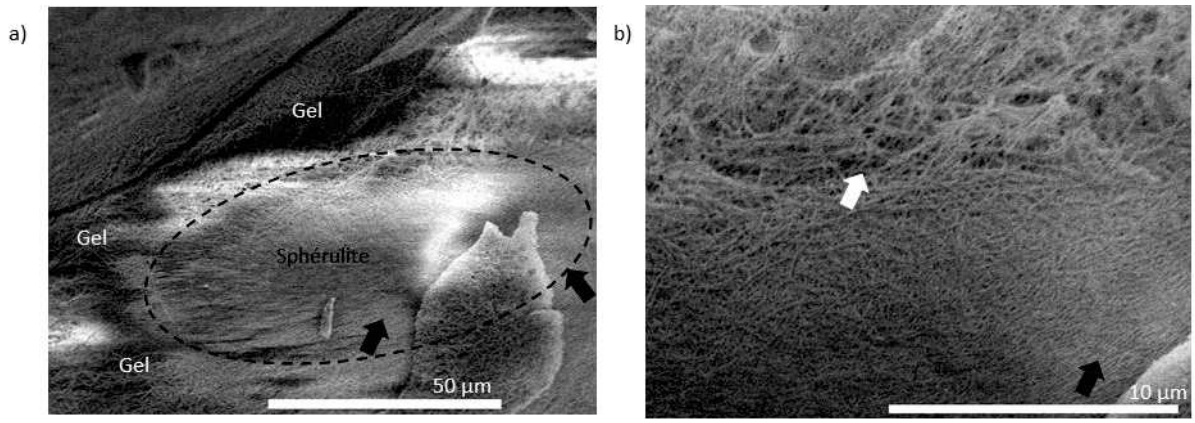

***Figure 18:** Gels of **BOTDPPma** in TD at 50 mg/mL. (a) identification of the spherulite and the surrounding gel. arrows: area with periodical and parallel streaks showing their crystallinity. (b) enlargement showing the spatial transition between spherulite with cristalline array (black arrow) and loose network (white arrow).*

The observations by SEM confirm the presence of spherulites for high concentrations. Like for OM, the spherulites were not visible at low concentration, which also suggests the presence of two regimes in the phase diagram. We tried to observe the concentrated sample at 80 °C, when the gel is formed but not the spherulites. Unfortunately, evaporation of the solvent turned the gel into a xerogel.

2. *Study by small angle scattering X-ray*

SAXS measurements are needed to probe the inner structure of the self-assemblies. We measured the intensity scattered by **BOTDPPma** in *trans*-decalin (50 mg/mL). The experimental curve is showed in the following figure.

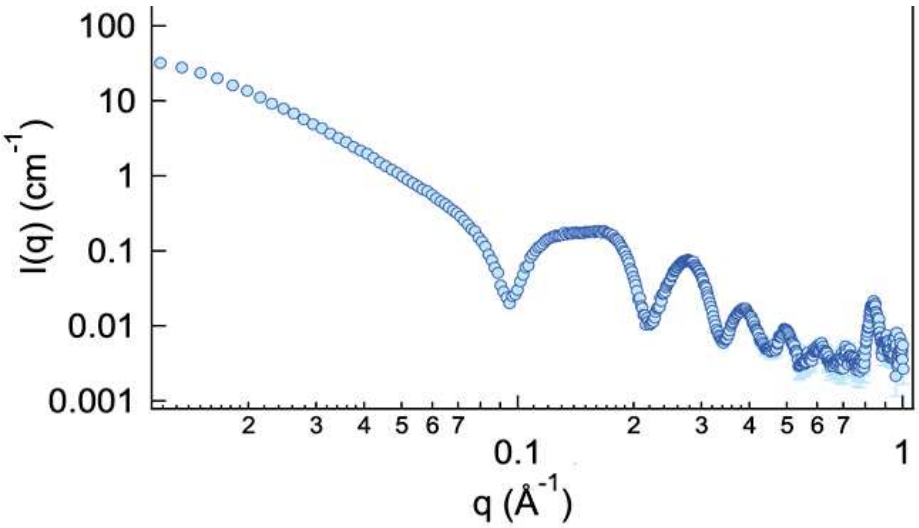

Figure 19: *Intensities scattered by a sample of* ***TDPPMonoBO*** *in trans-decalin (50 mg/mL).*

The intensity scattered by the sample writes:

$$I(q) = \phi_V \Delta\rho^2 V_P P(q) S(q) \qquad (1)$$

where Φ_V is the volume fraction of the particles, V_p is the volume of one particle (cm^3), $\Delta\rho$ is the contrast (cm^{-4}), $P(q)$ is the dimensionless form factor, normalized to 1 when q tends to 0, $S(q)$ is the structure factor, reflecting the correlations between particles. When they are no correlations between particles $S(q) = 1$. For a homogeneous particle, the contrast between the solvent and the particles arises form the difference of scattering lengths between the solvent and the particle: $\Delta\rho = (\rho-\rho_s)^2$. In X-ray the scattering length density (SLD) is given by

$$\rho = \frac{0.282.10^{-12}}{v} ZN$$

where v is the partial molar volume of the scattering element ($cm^3.mol^{-1}$), Z its number of electrons, N is Avogadro's number (mol^{-1}). When the particle is homogeneous, ρ has the same value throughout the particle, and is calculated by considering the molecule as the only scattering element. The particle can be heterogeneous because different part of the molecule self-associate to form areas with different SLD. In this case the scattering elements are the different part of the molecules. We have appraised the different molar partial volumes, either with a software or with the

incremental volume from literature[38] and we have calculated the different corresponding SLD. The different parts of the molecules are identified in scheme 2, and their corresponding SLD ρ given in table 3.

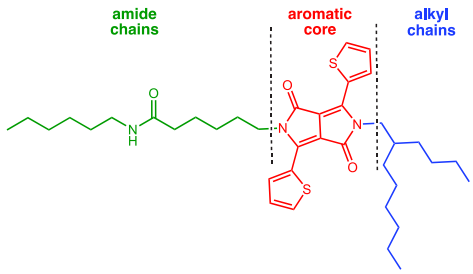

Scheme 2: *Different parts of* ***BOTDPPma*** *considered for the calculation of the SLD.*

Table 3*: Scattering length densities of* ***BOTDPPma*** *and of its different parts. [a]parts considered as dense as a solid.*

Part	estimated volume *v* ($cm^3.mol^{-1}$)	Z	Scattering length density ρ (10^{10} cm^{-2})
amide chains[a]	157.0	111	12.02
aromatic core[a]	120.7	152	21.39
alkyl chains	226.9	97	7.26
Whole molecule	504.6	360	12.1
trans-Decalin			8.39

The experimental curve shows a line at low *q* values, and a series of oscillations at higher *q* values that correspond to the form factor of the cross section. At 0.8 $Å^{-1}$, the curve shows a Bragg peak, that comes from a crystalline-like array of the compound within the particles. This crystalline feature of the organogels has been already described by different authors, [35,39].

The scattered intensity was compared to different models. Models of homogeneous cylinders do not account for the shape of the oscillations. Models with two shells were not satisfactory either.

The curves were fitted with a three shells cylinder model depicted by figure 20. The three layers have different scattering lengths densities and thicknesses.

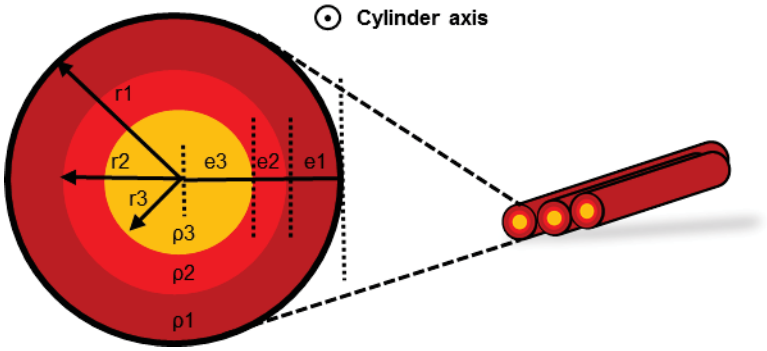

Figure 20: *Three shells models: definition of the parameters.*

In this model, e_i represents the thickness of each layer:

e_3=R_3-R_2, e_2=R_2-R_3 and e_1= R_1-R_2.

The intensity scattered by such cylinders, if they are long in regard with their diameters (L > 10R_1) is given by equation (2)

$$I(q) = \phi_V \frac{4\pi^2}{R_1^2} \frac{1}{q^3} \left[R_1(\rho_1 - \rho_s) J_1(qR_1) + R_2(\rho_2 - \rho_1) J_1(qR_2) + R_3(\rho_3 - \rho_2) J_1(qR_3) \right]^2 \qquad (2)$$

where J_1 represents the Bessel function of first kind and first order. In this expression V_p and $\Delta\rho$ and $P(q)$ are no longer apparent. It can be written as in form of (1), but the equation would become unnecessarily long and $\Delta\rho$ must be expressed as a volume fraction average of the scattering lengths. Here the solvent is *trans*-decalin; its scattering length density is $8.39.10^{10}$ cm^{-2}.

The best fits with this model reproduced most of the oscillations of the experimental curve. Discrepancies appear in the low q region. They are due to the interparticle correlations. The objects cannot be considered as isolated and isotropic in respect with each other, but they often are parallel, as shown by TEM micrographs. This amounts to introducing a structure factor S(q). We followed the same strategy that our group has applied to other gelators:[37] we considered pairs of parallel cylinders. The form factor is therefore multiplied by the factor (3) where $2R_1$ represents the distance between the centers of both cylinders.

$$\left[1 + 2J_1(2qR_1)\right] \qquad (3)$$

In the fits, it is necessary to introduce 3 shells to reproduce both the oscillations at medium and high q. The levelling of the first oscillation can be accounted by pairing the cylinders. The model with two shells was satisfactory provided the cylinders were not in contact, but have a small gap which supports that there is a layer with a density close to that of the solvent. The final fit is given in the following figure.

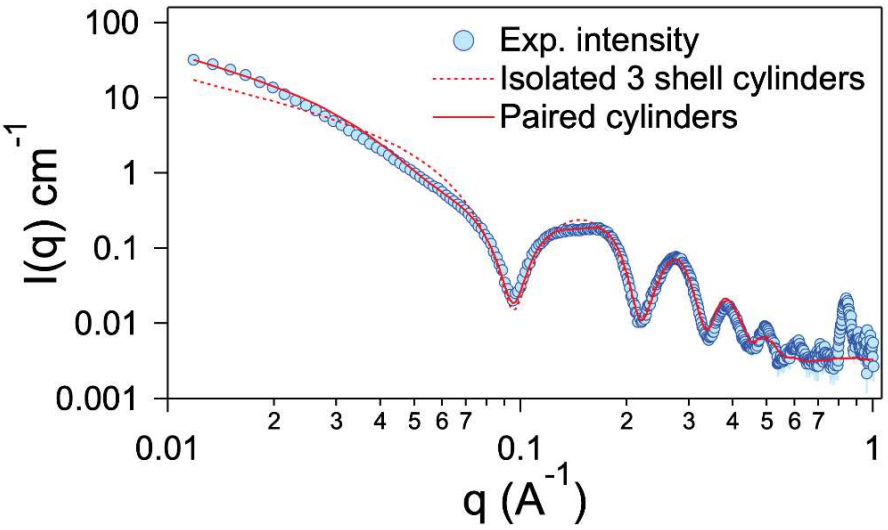

Figure 21: *Experimental intensities and best fit form equation 2 and 3.*

The results of the fits are summarized in the table 4.

Table 4*: Scattering length densities of* ***BOTDPPma*** *and of its different parts.*

Thicknesses of the layers (Å)	values (Å)	Scattering length density	values(10^{10} cm^{-2})
e_1	4.3	ρ_1	6.44
e_2	9.7	ρ_2	13.92
e_3	21.0	ρ_3	8.08
outer radius	35.2		

Figure 22 shows a model that can be proposed from the fitted parameters.

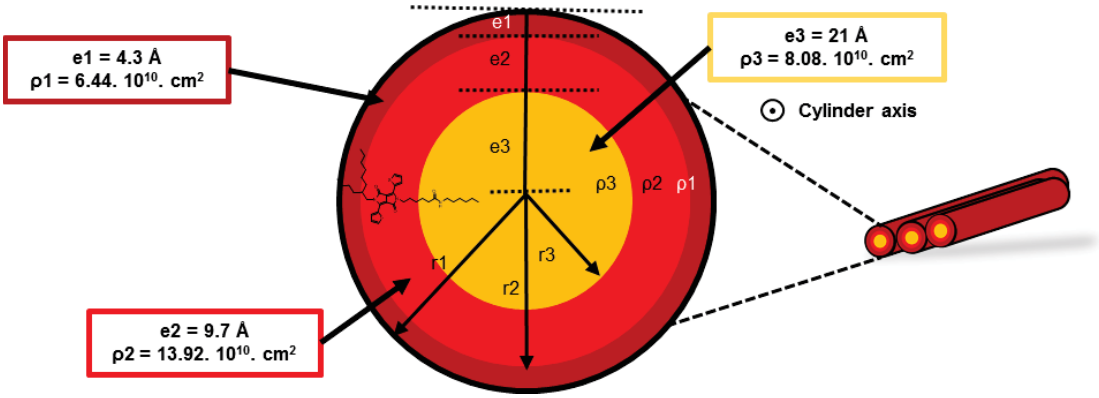

Figure 22: *Possible internal structure of the fibrils of* ***BOTDPPma*** *: model of 3 shells cylinders.*

In the found model, the middle shell has the largest scattering density. The ρ values of the two other shells are quite low. The found value ρ of the outer shell 6.44 10^{10} cm^{-2} is close to he one estimated (7.26). The thickness of this layer is 4 Å, which is

consistent with the alkyl chains turned toward the outside of the cylinders. The second layer has the largest ρ value. It yields most of the observed intensities of the curve. Its value is lower than that found by estimation, which shows that the estimate molar volumes are probably too high or the packing looser. Indeed, the molar volumes of heteroaromatic cycles are rather hard to estimate from incremental calculation. Moreover, the packing of the aromatic part may be looser than we had surmised. In our estimation, we have stated a crystalline packing, justified by the Bragg peaks observed. However a looser packing can be considered.

The main issue of this model is the low ρ value of the core of the cylinder. It is significantly lower than that of the value estimated for the amides. This ρ value corresponds to a very low density (about 0.85) for the amides in the core. It excludes any dense packing, but suggests an amorphous state. The ρ_3 value is also very close to that of the solvent. Therefore, the model of the tube (Figure 23), where the core of the cylinder is filled with solvent cannot be ruled out.

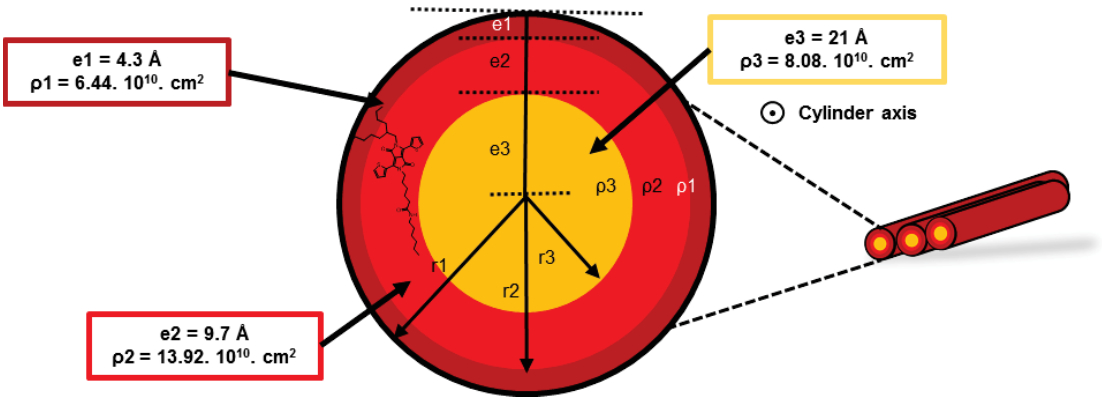

Figure 23: *Other possible internal structure of the fibrils of* ***BOTDPPma*** *: model of tube.*

In summary the aggregates are not homogeneous and show different densities. A multishell model must be implemented to fit the curves. The curves were fitted without polydispersity in diameters, which show a very narrow distribution of the diameters, consistent with the observations by TEM. The formation of bundles is clearly proved by the levelling of the first peak. This study will be completed by small-angle neutron scattering (SANS) studies, to clearly choose one model. Indeed, in SANS, the contrast with the solvent is higher; therefore the inner shell should be erased if empty, but a model a plain cylinder should prevail if it contains compound. Moreover the contrast of some of the shells can be extinguished with mixtures of deuterated and protonated solvents.

VI. Conclusion

New monoamides **DPP** molecules (**EHTDPPma** and **BOTDPPma**) were developed. These molecules form gels in *trans*-decalin and cyclohexane. Gel behaviour was also confirmed by rheology analysis. Cryo TEM images revealed the formation of nanofibers with external diameters of 7 nm and several micrometers lengths. SAXS measurements revealed these fibers are actually full cylinders with 3 layers or tubes with two layers.

A phase diagram was made for **BOTDPPma** gels in *trans*-decalin. Several transitions states were observed at different concentrations during cooling process. Rheology and turbidimetry analysis revealed the presence of one liquid-gel transistion state between 1 and 10 mg/mL. Two transitions states were observed from 10 mg/ml to 50 mg/mL. A first Liquid-gel transition was detected by rheology measurements while a second transition was detected by turbidimetry analysis. Visible by optical microscopy with polarized light, the formation of spherulites suggests that a fraction of the gelator crystallize at high concentration. Such phenomenon did not occur for gel samples with concentration below 10 mg/mL. These spherulites were also observed by SEM microscopy. The images revealed crystalline zone were the fibbers are perfectly organized. For the gels, areas the fibbers are randomly oriented. The optoelectronic properties of these organogelators will be studied to see if they can be potential candidate for making organic devices.

Since these molecules form cylinders with diameters under 10 nm, we intend to encapsulate them with **BHPB-10**, another organogelator developed by our group (Figure 24a). Previous studies made by our groups revealed gel formation in *trans*-decalin in which **BHPB-10** forms nanotubes with inner diameters around 30 nm (Figure 24b).

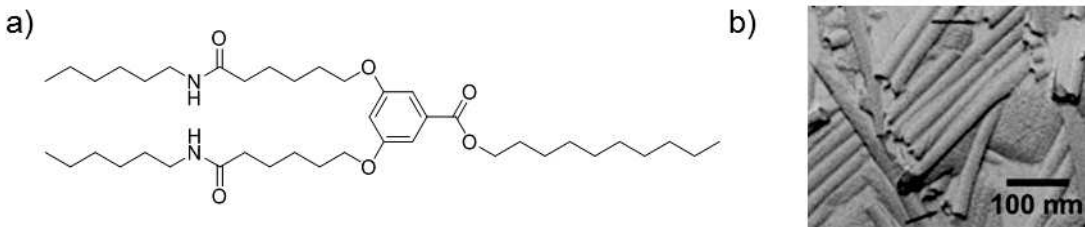

Figure 24: *a) Chemical structure of* ***BHPB-10****; b) SEM image of* ***BHPB-10*** *in trans-decalin.*

The idea is to prepare gels in *trans*-decalin in which both gelators and are mixed. The solution would be first warmed up until both gelator are dissolved. The solution is then cooled down until gelation is observed. This is where the phase diagram plays a major role. In order to achieve encapsulation, a few conditions are required: from a mechanistic point of view, the fibbers of **BOTDPPma** need to be made first before the nanotubes of **BHPB-10**. Therefore, the gelation temperature of **BOTDPPma** needs to

be at least 10 to 20 °C higher than the one of **BHPB-10**. To give a concrete example, for a **BHPB-10** gel sample with a concentration of 0.1% (w/w) which gelation occur at 47°C, the concentration of **BOTDPPma** needs to be at least 2.2% (20 mg/mL) since gelation occur at 70 °C according to rheology measurements (Figure 11 and 14). The encapsulation we target relies on heterogeneous nucleation: we expect to grow the nanotubes f BHPB-10 from the fibrils. To study the nucleation it is necessary to make precise thermoanalysis of the mixtures. This experiment will be performed as soon as the new µDSC machine is settled. If the sheathing of **BOTDPPma** fibers succeeds, these systems could be beneficial for charge transfer in organic devices. They can avoid avoiding charge recombination when p-type and n-type semiconducting fibers are entangled since BHPB-10 nanotubes would play the role of an insulator hence isolating the charges and transferring them more easily to the electrodes.

References:

[1] J. H. Van Esch, B. L. Feringa, *Angew. Chem., Int. Ed.* **2000**, *39*, 2263–2266.
[2] R. G. Weiss, P. Terech, *Molecular Gels. Materials with Self-Assembled Fibrillar Network*, Springer, Dordrecht, The Netherlands, **2006**.
[3] N. M. Sangeetha, U. Maitra, *Chem. Soc. Rev.* **2005**, *34*, 821–836.
[4] K. J. Skilling, F. Citossi, T. D. Bradshaw, M. Ashford, B. Kellam, M. Marlow, *Soft Matter* **2014**, *10*, 237–256.
[5] A. R. Hirst, B. Escuder, J. F. Miravet, D. K. Smith, *Angew. Chem., Int. Ed.* **2008**, *47*, 8002–8018.
[6] A. Dawn, T. Shiraki, S. Haraguchi, S. Tamaru, S. Shinkai, *Chem. Asian J.* **2011**, *6*, 266–282.
[7] A. Ajayaghosh, V. K. Praveen, C. Vijayakumar, *Chem. Soc. Rev.* **2008**, *37*, 109–122.
[8] S. S. Babu, S. Prasanthkumar, A. Ajayaghosh, *Angew. Chem. Int. Ed.* **2012**, *51*, 1766–1776.
[9] K. Sugiyasu, S. Kawano, N. Fujita, S. Shinkai, *Chem. Mater.* **2008**, *20*, 2863–2865.
[10] S. Prasanthkumar, S. Ghosh, V. C. Nair, A. Saeki, S. Seki, A. Ajayaghosh, *Angew. Chem. Int. Ed.* **2015**, *54*, 946–950.
[11] O. V. Mikhnenko, P. W. M. Blom, T.-Q. Nguyen, *Energy Environ. Sci.* **2015**, *8*, 1867–1888.
[12] M. Diebold, E. Christ, L. Biniek, L. Karmazin, B. Heinrich, C. Contal, S. Ghosh, P. J. Mesini, M. Brinkmann, *J. Mater. Chem. C* **2019**, 10.1039.C9TC04402G.
[13] B. W. Messmore, J. F. Hulvat, E. D. Sone, S. I. Stupp, *J. Am. Chem. Soc.* **2004**, *126*, 14452–14458.
[14] S. Prasanthkumar, A. Saeki, S. Seki, A. Ajayaghosh, *J. Am. Chem. Soc.* **2010**, *132*, 8866–8867.
[15] P. Pratihar, S. Ghosh, V. Stepanenko, S. Patwardhan, F. C. Grozema, L. D. A. Siebbeles, F. Würthner, *Beilstein J. Org. Chem.* **2010**, *6*, 1070–1078.
[16] H. Dong, X. Fu, J. Liu, Z. Wang, W. Hu, *Adv. Mater.* **2013**, *25*, 6158–6183.
[17] S. Prasanthkumar, A. Gopal, A. Ajayaghosh, *J. Am. Chem. Soc.* **2010**, *132*, 13206–13207.

[18] S. K. M. Nalluri, N. Shivarova, A. L. Kanibolotsky, M. Zelzer, S. Gupta, P. W. J. M. Frederix, P. J. Skabara, H. Gleskova, R. V. Ulijn, *Langmuir* **2014**, *30*, 12429–12437.
[19] E. R. Draper, B. Dietrich, C. Brasnett, S. Sproules, T. O. McDonald, A. M. Seddon, D. J. Adams, *Macromol. Rapid Commun.* **2018**, *39*, 1700746.
[20] X. Liang, L. Wang, K. Jeong, M. Lee, *Chinese Chemical Letters* **2019**, *30*, 123–126.
[21] N. Nandi, K. Gayen, A. Banerjee, *Soft Matter* **2019**, *15*, 3018–3026.
[22] K. Basu, B. Mondal, A. Das Mahapatra, N. Nandi, D. Basak, A. Banerjee, *J. Phys. Chem. C* **2019**, acs.jpcc.9b04414.
[23] F. Würthner, C. Bauer, V. Stepanenko, S. Yagai, *Adv. Mater.* **2008**, *20*, 1695–1698.
[24] P. Pratihar, S. Ghosh, V. Stepanenko, S. Patwardhan, F. C. Grozema, L. D. A. Siebbeles, F. Würthner, *Beilstein J. Org. Chem.* **2010**, *6*, 1070–1078.
[25] X.-Q. Li, V. Stepanenko, Z. Chen, P. Prins, L. D. A. Siebbeles, F. Würthner, *Chem. Commun.* **2006**, 3871–3873.
[26] M.-A. Muth, G. Gupta, A. Wicklein, M. Carrasco-Orozco, T. Thurn-Albrecht, M. Thelakkat, *J. Phys. Chem. C* **2014**, *118*, 92–102.
[27] F. Chambon, H. H. Winter, *Polym. Bull.* **1985**, *13*, 499–503.
[28] H. H. Winter, F. Chambon, *J. Rheol.* **1986**, *30*, 367–382.
[29] F. Chambon, H. H. Winter, *J. Rheol.* **1987**, *31*, 683–697.
[30] K. Te Nijenhuis, H. H. Winter, *Macromolecules* **1989**, *22*, 411–414.
[31] P. Terech, D. Pasquier, V. Bordas, C. Rossat, *Langmuir* **2000**, *16*, 4485–4494.
[32] F. Placin, J.-P. Desvergne, J.-C. Lassègues, *Chemistry of Materials* **2001**, *13*, 117–121.
[33] E. Christ, C. Blanc, A. Al Ouahabi, D. Maurin, R. Le Parc, J.-L. Bantignies, J.-M. Guenet, D. Collin, P. J. Mésini, *Langmuir* **2016**, *32*, 4975–4982.
[34] M. Schmutz, P. J. Mésini, in *Handbook of Cryopreparation Methods for Electron Microscopy* (Eds.: A. Cavalier, D. Spehner, B.M. Humbel), Francis And Taylor CRC Press, New-York, **2008**, pp. 411–430.
[35] R. Schmidt, F. B. Adam, M. Michel, M. Schmutz, G. Decher, P. J. Mésini, *Tetrahedron Letters* **2003**, *44*, 3171–3174.
[36] N. Diaz, F. X. Simon, M. Schmutz, M. Rawiso, G. Decher, J. Jestin, P. J. Mésini, *Angew. Chem. Int. Ed.* **2005**, *44*, 3260–3264.
[37] F.-X. Simon, T. T. T. Nguyen, N. Díaz, M. Schmutz, B. Demé, J. Jestin, J. Combet, P. J. Mésini, *Soft Matter* **2013**, *9*, 8483–8493.
[38] D. W. Van Krevelen, K. Te Nijenhuis, in *Properties of Polymers (Fourth Edition)*, Elsevier, Amsterdam, **2009**, pp. 71–108.
[39] P. Terech, D. Meerschaut, J.-P. Desvergne, M. Colomes, H. Bouas-Laurent, *Journal of Colloid and Interface Science* **2003**, *261*, 441–450.

Experimental:

Cryo-SEM microscopy

The gel has been observed by cryo-SEM technique. A piece of the gel was placed on a cryo-holder and quickly plunged into a nitrogen slush in the cryopreparation chamber of a Quorum PT 3010 machine. Subsequently, the sample is transferred under vacuum into the chamber attached to the microscope. There, the frozen sample is fractured with a razor blade. A slight etching at -70°C is performed to render the morphology more visible. The sample is eventually transferred in the FEG-cryoSEM (Hitachi SU8010) and observed at 1keV at -150°C

Synthesis

<u>Compound 1:</u> 2-(2-ethylhexyl)-3,6-di(thiophen-2-yl)-2,5-dihydropyrrolo[3,4-c]pyrrole-1,4-dione

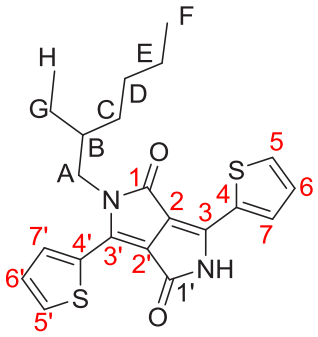

A solution **TDPP** (3 g, 10 mmol) was stirred under argon in anhydrous DMF (250 ml) at 120°C. CCO_3 (3.27 g, 10 mmol) was added progressively. The mixture was stirred for 1 h at 120 °C then 2-ethylhexyl bromide (3 g, 10 mmol) was added dropwise. The solution was stirred overnight at 120 °C, was cooled at RT and mixed with distilled water (2.5 L). The crude was extracted DCM. The organic phase was dried with $MgSO_4$ and solvent under vacuum. The crude was purified by column chromatography (THF/cyclohexane : 10/90). **Compound 1** was afforded as a dark red solid (1.3 g, 31%).

^{1}H-NMR (400 MHz, CD_2Cl_2) δ [ppm]: 8.85 (d, J = 4 Hz, 1.1 Hz, 1H, H_5); 8.62 (s, 1H, NH); 8.39 d, J = 4 Hz, 1H, $H_{5'}$); 7.67 (d, J = 5.1 Hz, 1H, H_7); 7.62 (dd, J = 5.1 Hz, 1H, H7'); 7.30 (t, J = 5 Hz, 1H, H_6); 7.25 (t, J = 5 Hz, 1H, $H_{6'}$), 4 (m, 2H), 1.86 (m, 2H), 1.33-1.25 (m, 8H, H_C, H_D, H_E and H_G), 0.87 (m, 6H, H_F and H_H).

^{13}C NMR (126 MHz, CDCl3) δ [ppm]: 162.60 ($C_{1'}$), 161.80 (C_1), 141.03 (C_3 and $C_{3'}$), 136.65 (C_5), 135.62 ($C_{5'}$), 132.22 (C_6), 131.01 ($C_{6'}$), 139.99 (C_4 and $C_{4'}$), 129.15 (C_7), 128.52 ($C_{7'}$), 108.71 ($C_{2'}$), 108.47 (C_2), 46.03 (C_A), 39.24 (C_B), 30.36 (C_C), 28.49 (C_D), 23.67 (C_G), 23.21 (C_E), 14.18 (C_F), 10.64 (C_H).

HRMS (ESI+) m/z: 413.1346 (MH+); calcd for $C_{22}H_{25}N_2O_2S_2$: 413.1352.

<u>Compound 1'</u>: 2-(2-butyloctyl)-3,6-di(thiophen-2-yl)-2,5-dihydropyrrolo[3,4-c]pyrrole-1,4-dione

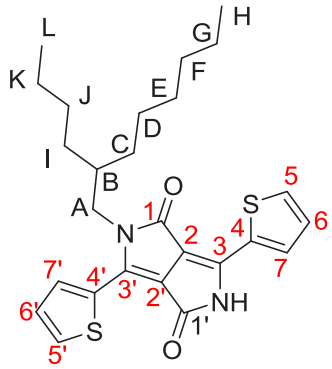

A solution **TDPP** (1 g, 3.3 mmol) in anhydrous DMF (25 ml) was stirred under Ar at 120 °C. $CsCO_3$ (2.72 g, 8.3 mmol) was added progressively. The mixture was stirred for 1 h at 120 °C and a solution of the mesylate (3.4 g, 9.9 mmol) in anhydrous DMF was added dropwise. The solution was stirred for five hours at 120 °C, cooled down at ambiante temperature and mixed with distilled water (250 ml). The mixture was extracted with DCM. The organic phase was dried with MgSO4, and the solvent removed under vacuum. The product was purified by column chromatography (DCM/cyclohexane : 50/50). **Compound 1'** was afforded as a dark red solid (0.432 g, 30%).

^{1}H NMR (500 MHz, Chloroform-d) δ [ppm]: 9.54 (s, 1H, NH), 8.86 (dd, *J* = 3.9, 1.1 Hz, 1H, H_5), 8.39 (dd, *J* = 3.9, 1.1 Hz, 1H, $H_{5'}$), 7.67 (dd, *J* = 5.0, 1.2 Hz, 1H, H_7), 7.62 (dd, *J* = 5.0, 1.0 Hz, 1H, $H_{7'}$), 7.30 (dd, *J* = 5.0, 3.8 Hz, 1H, H_6), 7.24 (dd, *J* = 5.0, 3.8 Hz, 1H, $H_{6'}$), 4.04 (d, *J* = 7.8 Hz, 2H, H_A), 1.92 (m, 1H, H_B), 1.42 – 1.13 (m, 18H, H_C, H_D, H_E, H_F, H_G, H_I, H_J and H_K), 0.94 – 0.77 (m, 6H, H_H and H_L).

^{13}C NMR (126 MHz, CDCl3) δ [ppm]: 162.64 ($C_{1'}$), 161.81 (C_1), 141.05 (C_3 and $C_{3'}$), 136.67 (C_5), 135.53 (C_5 and $C_{5'}$), 132.11 5 (C_6 and $C_{6'}$), 130.01 (C_4 and $C_{4'}$), 129.16 (C_7), 128.87 ($C_{7'}$), 111.05 ($C_{2'}$), 108.22 (C_2), 46.38 (C_A), 37.90 (C_B), 31.91 (C_C), 31.28 (C_I), 31.28 (C_F), 29.82 (C_E), 28.54 (C_J), 26.32 (C_D), 23.16 (C_K), 22.78 (C_G), 14.23 (C_L), 14.18 (C_H).

Elemental analysis. Found : C, 66.26; H, 7.04; N, 5.97. Calcd for $C_{26}H_{33}N_2O_2S_2$: C, 66.63; H, 6.88; N, 5.98.

HRMS (ESI+) m/z: 469.1961 (MH^+); calcd for $C_{26}H_{33}N_2O_2S_2$ (MH+): 469.1978

EHTDPPma: 6-(5-(2-ethylhexyl)-1,4-dioxo-3,6-di(thiophen-2-yl)-4,5-dihydropyrrolo[3,4-c]pyrrol-2(1H)-yl)-N-hexylhexanamide

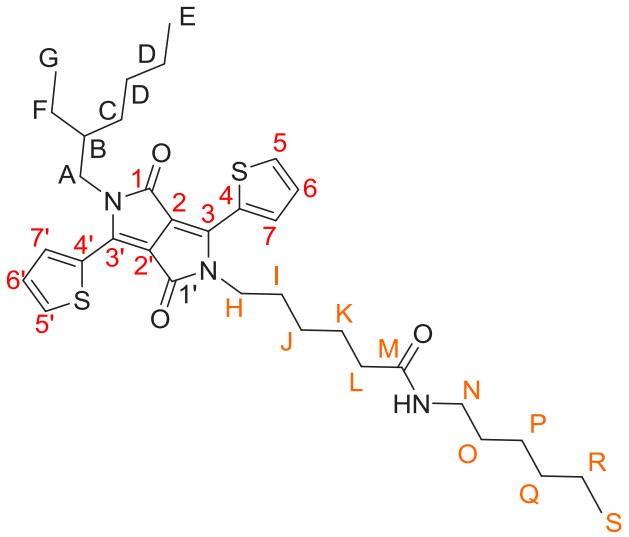

A solution **compound 1** (200 mg, 0,5 mmol) in anhydrous DMF (75 ml) was stirred under Ar at 120°C. $CsCO_3$ (160 mg, 0.5 mmol) portion by portion. The mixture was stirred for 1 h at 120°C and a solution of the mesylate (175 mg, 0.6 mmol) in anhydrous DMF (10 ml) was added dropwise. The solution was stirred for 5 h at 120°C, cooled down at RT. The solvent was removed under vacuum and the residue was dissolved in DCM, washed with distilled water and dried with MgSO4. The solvent was removed under vacuum and the crude was purified by column chromatography (Ethyl acetate/heptane 40/60%) to afford the final product (68.3 mg, 22%).

^{1}H-NMR (400 MHz, CD_2Cl_2) δ [ppm]: 8.86 (dd, *J* = 4 Hz, 1.1 Hz, 1H, $H_{5'}$); 8.78 (dd, *J* = 4 Hz, 1H, H_5); 7.56 (d, *J* = 5 Hz, 2H, H_7 and $H_{7'}$); 7.28 (m, 2H, H_6 and $H_{6'}$); 5.45 (m, 1H, NH); 4.09 (t, *J* = 4 Hz, 2H, HA); 4.09 (t, *J* = 4 Hz, 2H, H_H); 3.22 (q, *J* = 6.6 Hz, 2H, H_N); 1.86 (m, 1H, H_B); 2.18 (t J = 7.5 Hz, 2H, H_L); 1.79-1.72 (m, 4H, H); 1.48 (m, 4H, H_J and H_O); 1.26 (m, 16H, H_C, H_D, H_E, H_F, H_P, H_Q and H_R); 0.88 (m, 9H, H_E, H_G and H_S).

^{13}C NMR (126 MHz, CDCl3) δ [ppm]: 172.78 (C_R), 161.86 ($C_{1'}$), 161.51 (C_1), 140.65 (C_3), 140.06 ($C_{3'}$), 135.53 (C_5), 135.28 ($C_{5'}$), 130.84 (C_6), 130.82 ($C_{6'}$), 129.94 (C_4), 129.77 ($C_{4'}$), 128.83 (C_6), 128.50 ($C_{6'}$), 108.06 (C_2), 107.74 ($C_{2'}$), 45.98 (C_A), 41.99 (C_M), 39.66, 39.20, 36.70, 31.60, 30.33, 29.83, 29.76, 29.70, 28.46, 26.72, 26.51, 25.37, 23.62, 23.20, 22.69, 14.15, 10.61.

MS (MALDI) m/z 610.386 (MH^+); calcd for $C_{34}H_{48}N_3O_3S_2$: 610.31

BOTDPPma: 6-(5-(2-butyloctyl)-1,4-dioxo-3,6-di(thiophen-2-yl)-4,5-dihydropyrrolo[3,4-c]pyrrol-2(1H)-yl)-N-hexylhexanamide

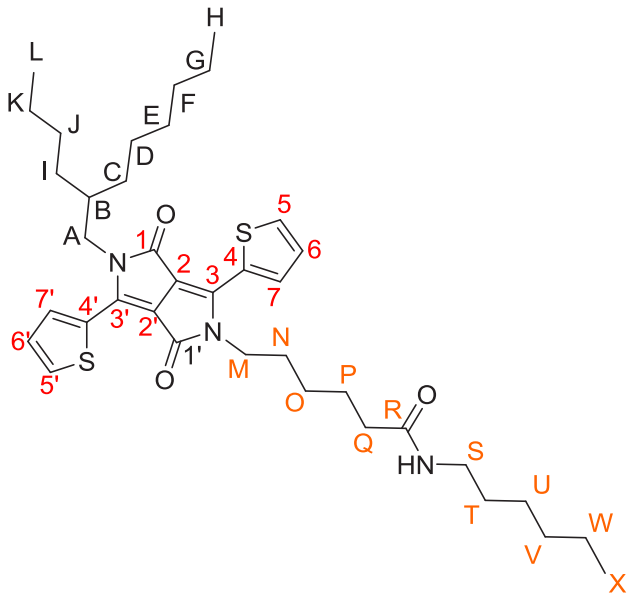

A solution **compound 1'** (220 mg, 0.47 mmol) was stirred under argon in anhydrous DMF (5 ml) at 100°C. $CsCO_3$ (158 mg, 0.47 mmol) was added portion by portion. The mixture was stirred for 1 h at 120 °C and a solution of the mesylate (0.172 g, 84 mmol) in 2 ml of anhydrous DMF was added dropwise. The solution was stirred overnight at 100 °C, cooled down at room temperature and the solvent was removed under vacuum. The residue was dissolved with DCM, washed with water, dried with $MgSO_4$ and the solvent removed under vacuum. The product was purified by column chromatography (DCM/cyclohexane: 50/50) to afford alkylated **TDPP** (155 mg, 34%).

^{1}H-NMR (400 MHz, CD_2Cl_2) δ [ppm]: 8.94 (dd, J = 4 Hz, 1H, $H_{5'}$); 8.83 (dd, *J* = 4 Hz, 1H, H_5); 7.64 (d, *J* = 5 Hz, 2H, H_7 and $H_{7'}$); 7.28 (m, 2H, H_6 and $H_{6'}$); 5.45(m, 1H, NH); 4.09 (t, J = 8Hz, 2H, H_M); 4.02 (d, *J* = 7.9Hz, 2H, H_A); 3.23 (q, *J* = 6.9 Hz, 2H, H_S); 2.18 (t, *J* = 7.6 Hz, 2H, HQ); 1.9 (m, 1H, HB); 1.72-1.79 (m, 4H, H_N and H_P); 1.48 (m, 4H, H_O and H_T); 1.21-1;29 (m, 21H, H_C, H_D, H_E, H_F, H_G, H_I, H_J, H_K, H_U, H_V and H_W); 0.84 (m, 9H, H_H, H_L and H_X).

^{13}C-NMR (400 MHz, CD_2Cl_2) δ [ppm]: 172.74 (C_R), 161.86 ($C_{1'}$), 161.54 (C_1), 140.65 (C_3), 140.07 ($C_{3'}$), 135.54 (C_5), 135.18 ($C_{5'}$), 130.82 (C_6), 130.77 ($C_{6'}$), 129.96 (C_4), 129.79 ($C_{4'}$), 128.84 (C_6), 128.49 ($C_{6'}$), 108.10 (C_2), 107.77 ($C_{2'}$), 46.31 (C_A), 42.00 (C_M), 39.67 (C_S), 37.86 (C_B), 36.73 (C_Q), 31.90 (C_C), 31.62, 31.23 (C_I), 31.00 (C_F), 29.79 (C_E), 29.71, 28.52 (C_J), 26.72, 26.53, 26.29 (C_D), 25.38, 23.20 (C_K), 22.76 (C_G), 22.69, 14.22 (C_L), 14.16 (C_H).

Elemental analysis. Found : C, 68.27; H, 8.34; N, 6.27. Calcd for $C_{38}H_{56}N_3O_3S_2$: C = 68.53; H = 8.32; N = 6.31

HRMS (ESI+) m/z: 666.3770; calcd for (MH+): 666.3763

Summary and general conclusions

In summary, a library of small **DPP** molecules were developed to study the influence of H-bonds on the self-assembly and optoelectronic properties. These molecules were differentiated by several parameters such as the number, the position and the nature of the H-bonding function. The influence of solubility and chirality were also investigated.

UV-visible spectra revealed the formation of aggregates, usually attributed to J-type aggregates, more or less intense depending on the nature of the solvent, concentration and temperature. The signals of the aggregates extended to the near infrared region, which is beneficial for the development of organic electronic devices. Experiments with MeOH addition and FT-IR spectra confirmed the formation of H-bonds and their involvement in the aggregate formation. A major difference exists between the spectra of **DPP** molecules with bisamide arms, and those of **DPP** with semicarbazone. The bisamides have more intense J-aggregate signals. Both types of compounds bear two functions generating two H-bonds, but in the bisamide, they are separated by a spacer.

The morphology of the aggregates, was studied by SEM and TEM microscopy techniques and was found to depend on the nature of the solvent and the deposition technique. Further studies will be performed to see which of these structures are best fitted for making either solar cells or transistor devices.

Charge transport was examined through FP-TRMC measurements for both, semicarbazone and bisamide **DPP** families. The achiral derivative, **DPPBA**, had higher photoconductivity value with longer charge carrier lifetime than the chiral derivatives. Photoconductivity measurements on thin films were performed after solvent vapor annealing. Results revealed that solvents promoting self-assembly positively influence photoconductivity, whereas solvents competing with H-bonds interactions showed no influence at all. The position of the function generating H-bonds interactions also has an impact on charge transport. The values are higher when the H-bonding groups are separated from each other by alkyl chains than when they are directly attached to the thiophene of the main core. The addition of a chiral center next to the H-bonding motif hinders charge transport.

Gel-like materials were obtained in cyclohexane, *trans*-decalin and ethyl acetate for the semicarbazone and bisamide families. SEM and TEM analyses revealed different structures, but these materials were not robust enough to study their mechanical properties. The monoamide **DPP** form genuine gels in cyclohexane and *trans*-decalin. They were studied by rheology measurements. Morphology studies by TEM on cryo-fractured samples revealed the formation of fibrillar structures with an average diameter of 10 nm. Turbidity measurements also showed another phase transition, which is due to the formation of crystalline spherulites, according to polarized light microscopy. A phase diagram was established by rheology and turbidity measurements. It presents two regimes. At low concentration, the gels form with a classical texturation of fibrils. At high concentrations, the gels form fibrils and spherulites.

This project will continue following several perspectives:

The first is the growth of the library of H-bonded semiconductors. Since better photoconductivity was observed for **DPP** molecules with flexible linker between H-bonds motifs and the core, it is interesting to study the influence of the length of the spacer. Therefore, several molecules should be synthesized with different carbon chains (Figure 1) between the amide functions and the **DPP** core. To study further the influence of chirality, we will develop molecules with one or several chiral centers at different positions away from the amide functions (Figure 1). Therefore, the spacing between the chiral centers and the H-bonding moieties is another important parameter to vary.

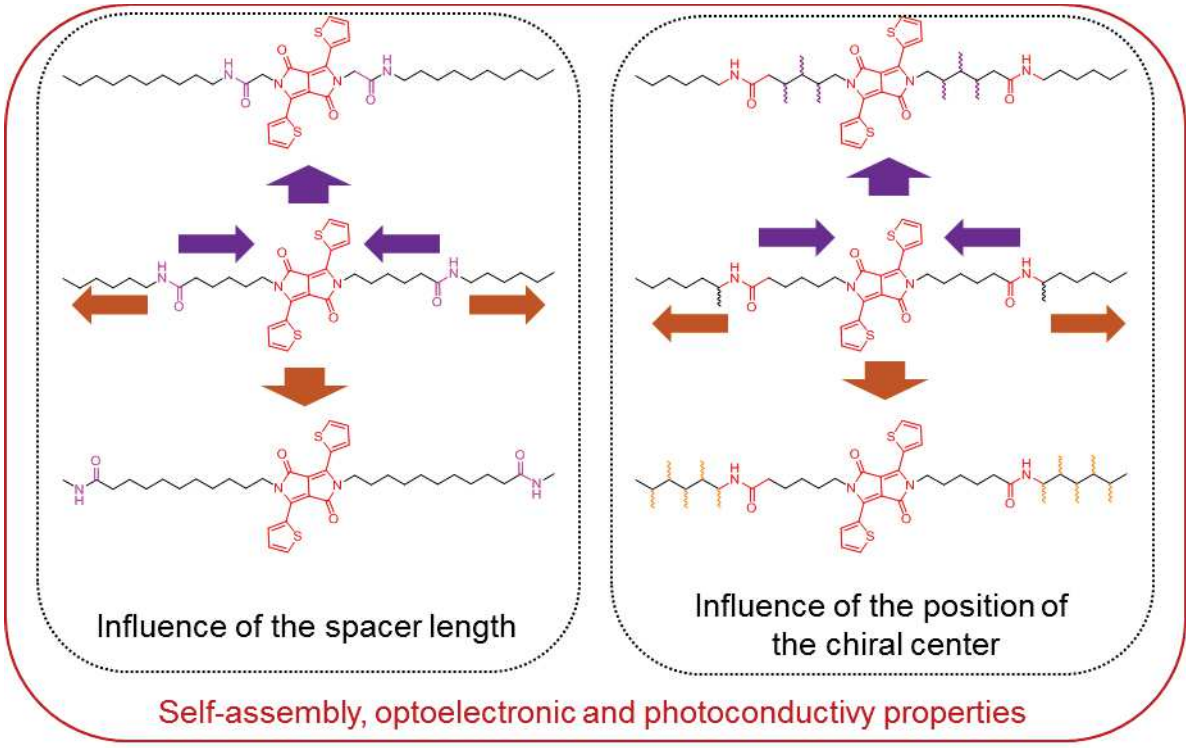

Figure 1: *Suggestion of new bisamide **DPP** molecules to continue the study.*

For the development of new organogelators it seems that monoamide **DPP** molecules are suitable to form gels in apolar solvents. Other monoamide **DPP** will be synthesized with the amide arm attached to different positions of the semiconducting segment (Figure 2a). As shown by previous studies[1] on crystalline structures based on small **DPP** molecules, the presence of alkyl chains influences the packing between the aromatic cores and hence, the device performance of solar cells. **DPP** molecules with one amide arm attached in position 2, 3 or 4 of one thiophene should be interesting whether they form gels or not (Figure 2a). Solubility would be in that case an important parameter to focus on. The alkyl chains attached to the pyrrole rings should be adjusted so that the molecules are entirely dissolved during the heating process but must self-assemble into a supramolecular network trapping the solvent. The use of the ethylhexyl branches could be a good starting point. We synthesized a **DPP** derivative with a monoamide aromatic structure attached to the one of the two thiophenes (Figure 2b). Unfortunately, this compound is soluble in all the solvents tested at room

temperature before heating to the boiling point and does not self-assemble into supramolecular structures. Optoelectronic properties were not studied yet.

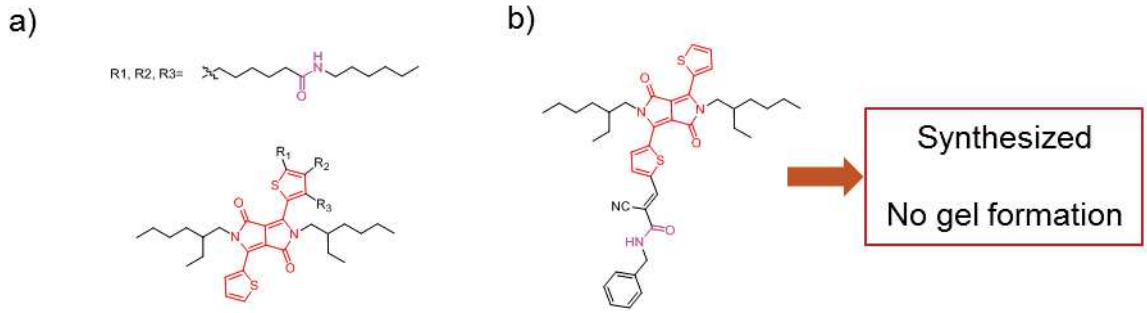

Figure 2: *(a) Suggestion of new monoamide **DPP** molecules as potential organogelators; (b) First monoamide **DPP** synthesized.*

The already existing molecules form gels that quickly collapses under small manual agitation. Regarding the bisamide **DPP**, samples prepared in *trans*-decalin formed a gel like material but the molecules did not dissolve entirely during the gelation heating process. Attaching one or several alkyl chains to the thiophene rings may improve solubility and perhaps form a proper gel (Figure 3).

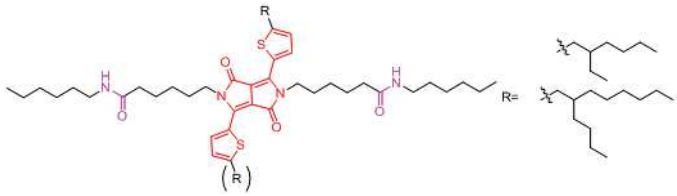

Figure 3: *Suggestion of new bisamide **DPP** molecules as potential organogelators.*

Among the studied molecules, the achiral **DPPBA** is an interesting candidate for the development of solar cell or transistors as observed by photoconductivity measurements. This compound self-assembles into long fibers or ribbons, suitable for mobility. However, their deposition on solid supports by spin coating or drop casting needs to be optimized. The challenge is to organize the structures at the scale of the device. It is vital to obtain long and oriented structures to have optimal charge transport between the electrodes of a specific organic electronic device.

References:

[1] V. S. Gevaerts, E. M. Herzig, M. Kirkus, K. H. Hendriks, M. M. Wienk, J. Perlich, P. Mu, *Chem Mater* **2014**, 11.

Swann MILITZER

Auto-assemblages de dicétopyrrolopyrrole semiconducteurs : impact des liaisons H sur les propriétés électroniques

1 Résumé

La chimie supramoléculaire est un outil attrayant pour contrôler les propriétés optoélectroniques de composés semiconducteur et leur morphologie dans des dispositifs d'électronique organique. Les interactions principales mises en jeu par les semiconducteurs sont les interactions π-π, les liaisons hydrogène étant encore rare. Cependant, il a été démontré qu'après incorporation de liaisons H dans ces composés, les dispositifs plus efficaces qu'avec des molécules de contrôle sans liaison hydrogène. Néanmoins, il n'y a aucun consensus sur l'impact de ces interactions non covalentes puisqu'aucune étude comparative n'a été menée. Pour cette raison, l'objectif de cette thèse est d'étudier l'influence des liaisons hydrogène sur les propriétés d'auto-assemblage et optoélectroniques de petites molécules semi-conductrices modèles ayant le dicétopyrrolopyrrole comme segment électroactif. Ces unités possèdent d'excellentes propriétés électroniques, et en modifiant le cœur conjugué avec différents groupes des liaisons H (position, nombre, force et function) leurs propriétés optoélectroniques ont été améliorées pour les rendre utilisables dans des dispositifs électroniques

Mots clés : semiconducteurs organiques, auto-assemblage, liaison hydrogène.

2 Résumé en anglais

Supramolecular chemistry is an attractive tool to tune the optoelectronic properties of semiconducting compounds and their morphology in organic electronics devices. The main noncovalent interactions in these compounds are π-π stacking and hydrogen-bonding is still scarce. However, it has been demonstrated that the incorporation of H-bonds into semiconductors resulted in more efficient devices than the parent molecules bearing no H-bonding groups. Nevertheless, there is no consensus regarding the impact of such interactions since no comparative studies have been performed. For this reason, the aim of this PhD is to study the influence of H-bonding on the self-assembly and optoelectronic properties of model small molecule semiconductors having diketopyrrolopyrrole as the electroactive segment. Such unit possesses excellent electronic properties, and by modifying its conjugated core with different H-bonding groups (position, number, strength and function) their electronic properties have been improved for its application in electronic devices

Key words: organic semiconductors, self-assembly, hydrogen bonds.